



D1.5: Methods for nonlinear wave forcing and wakes

Néstor Ramos-García, Sergio González-Horcas, Antonio Pegalajar-Jurado, Stavros Kontos, Ozan Gözcü, Henrik Bredmose

DTU

Umut Özinan, Mohammad Youssef Mahfouz

USTUTT

Alessandro Fontanella, Alan Facchinetti, Marco Belloli

POLIMI

March 2022

Disclaimer:



This project has received funding from the European Union's Horizon 2020 Research and Innovation programme under grant agreement No 815083.

Project details:

Duration:
1 Sep 2019 - 28 Feb 2023
Grant agreement:
No: 815083

Document information

| | |
|---------------------------------------|--|
| Deliverable number | D1.5 |
| Deliverable name | Methods for nonlinear wave forcing and wakes |
| Reviewed by | Friedemann Borisade (RAMBOLL) Marco Belloli (POLIMI) Ozan Gözcü (DTU) Reviewed Chapter 6 |
| Date | 29/03/2022 |
| Work Package and Task | WP1, task 1.4: Development of mooring calculation models for accurate and efficient design |
| Lead Beneficiary for this Deliverable | DTU |
| Dissemination Level | Public |

Authors

| Name | Organisation | E-mail |
|--------------------------|--------------|---------------------------------|
| Néstor Ramos-García | DTU | nerga@dtu.dk |
| Sergio González-Horcas | DTU | sgho@dtu.dk |
| Antonio Pegalajar-Jurado | DTU | ampj@dtu.dk |
| Stavros Kontos | DTU | stakon@dtu.dk |
| Ozan Gözcü | DTU | ozgo@dtu.dk |
| Henrik Bredmose | DTU | hbre@dtu.dk |
| Umut Özinan | USTUTT | Oezinan@IFB.Uni-Stuttgart.de |
| Mohammad Youssef Mahfouz | USTUTT | mahfouz@IFB.Uni-Stuttgart.de |
| Alessandro Fontanella | POLIMI | alessandro.fontanella@polimi.it |
| Alan Facchinetti | POLIMI | alan.facchinetti@polimi.it |
| Marco Belloli | POLIMI | marco.belloli@polimi.it |

Version control

| Version | Date | Author | Description of Changes |
|--------------------------|--------------|--|---------------------------|
| [Official versions only] | [yyyy-mm-dd] | | |
| 0.1 | 2021-30-11 | Ramos-García, Horcas, Pegalajar-Jurado, Kontos, Gözcü, Bredmose, Özinan, Mahfouz | Draft for internal review |
| 0.2 | 2022-29-03 | Ramos-García, Horcas, Pegalajar-Jurado, Kontos, Gözcü, Bredmose, Özinan, Mahfouz, Fontanella, Facchinetti, Belloli | Final |
| 0.3 | 2023-31-03 | Ramos-García, Horcas, Pegalajar-Jurado, Kontos, Gözcü, Bredmose, Özinan, Mahfouz, Fontanella, Facchinetti, Belloli | Final Formal edits |

Contents

| | | |
|----------|---|------------|
| 1 | Introduction and outline | 5 |
| 1.1 | People and contributors | 6 |
| 2 | Rapid evaluation of second-order wave loads | 7 |
| 2.1 | The slender body approach | 7 |
| 2.2 | The radiation-diffraction approach in second order wave loads calculation | 7 |
| 2.3 | Numerical speed up by eigenmode decomposition | 8 |
| 2.4 | Results | 9 |
| 2.5 | Conclusion | 14 |
| 3 | Response calculation for a farm with shared mooring | 15 |
| 3.1 | Methodology | 15 |
| 3.2 | Second order wave loads effects | 15 |
| 3.3 | Shared anchor design at Morro Bay | 16 |
| 3.4 | Load analysis | 17 |
| 3.5 | Conclusions | 24 |
| 4 | Investigation of the floating IEA Wind 15 MW RWT using vortex methods: Flow regimes and wake recovery | 25 |
| 5 | Comparative study of the floating IEA Wind 15MW RWT with MIRAS-HAWC2 farm and FAST.Farm | 63 |
| 5.1 | FAST.Farm model of the IEA 15 MW with the WindCrete platform | 63 |
| 5.2 | Simulation load cases and wind fields | 64 |
| 5.3 | Results and discussion | 64 |
| 5.3.1 | Comparison of upwind wind turbines | 64 |
| 5.3.2 | Comparison of downwind wind turbines | 64 |
| 5.3.3 | Comparison of the wake wind fields | 66 |
| 6 | Wind tunnel investigation of the wake of the floating IEA 15 MW RWT | 69 |
| 6.0.1 | Scale turbine design and specifications | 69 |
| 6.0.2 | Measurements | 70 |
| 6.1 | Load cases | 70 |
| 6.2 | Results about wake | 71 |
| 7 | Investigation of the floating IEA Wind 15 MW RWT using vortex methods: Wake impact on downstream turbines under turbulent inflow | 76 |
| 8 | Summary and conclusions | 107 |
| 8.1 | Sub-conclusion on wave forcing | 107 |
| 8.2 | Sub-conclusion on farm response | 107 |
| 8.3 | Sub-conclusion on wake effect of floater motion | 108 |
| 8.4 | Sub-conclusion on comparison between MIRAS-HAWC2 farm and FAST.Farm | 109 |
| 8.5 | Sub-conclusion on wind tunnel wake measurements | 109 |
| 8.6 | Sub-conclusion on floating farm response | 110 |

1 Introduction and outline

Floating wind turbines have special dynamics due to the low-frequency floater motion which results from the mooring system and the restoring forces from hydrostatics and gravity. These motions affect the local inflow dynamics to the blade and also change the wake in comparison to bottom fixed offshore turbines.

Further dynamic effects are added when floating turbines are placed in wind farms. Here, the floater motions effect on the wake may drive motion at the low frequency floater modes of downstream turbines. More direct coupling may also occur, if the turbines share mooring lines. An example of this is shown in Figure 1.

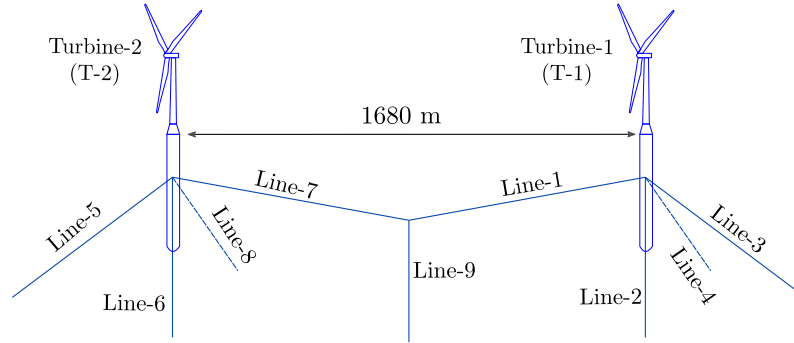


Figure 1: Example of two turbines in a shared anchor configuration (Chapter 3).

These effects are the topic of the present deliverable. It builds on earlier output from COREWIND, namely the WindCrete Spar floater, as designed for the 15 MW IEA Wind reference turbine (Mahfouz *et al.*, 2020a), the mooring configurations of the Morro Bay and the shared mooring method presented in D1.4 (Gözcü *et al.*, 2021). The investigations consist of the following substudies:

- An accelerated method for evaluation of second-order wave loads from Quadratic Transfer Function (QTF) — (Chapter 2)
- A study of dynamic response to a storm sea state for 2-turbine configuration with shared mooring lines. The effect of second-order wave forcing on the low-frequency modes is investigated. (Chapter 3).
- A detailed parametric study of the wake behind an oscillating rotor, carried out with the free MIRAS free vortex code. Chapter 4. An example of the wake behind a rotor with forced harmonic pitch motion is shown in figure 2.
- A comparison of the loads and response for two floating turbines, one in the wake of the other is presented in Chapter 5. Computations are made in MIRAS-HAWC2farm and FAST.farm.
- A wind tunnel test campaign that investigates the wake-flow response of a 1:100 scale model of the IEA 15 MW turbine subjected to imposed platform motion. Chapter 6.
- A detailed MIRAS-based investigation of downwind response in 5-turbine wind farm, where the wake of the upstream turbines can excite resonance along the row. Chapter 7. The computational setup for the 5-turbine configuration is shown in Figure 3.

Conclusions are given as a last chapter. The first MIRAS study has been published in Wind Energy, while the second is currently under review for publication also in Wind Energy.

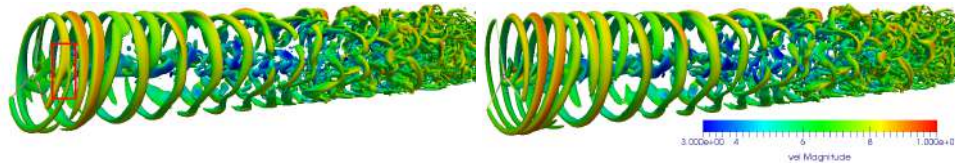


Figure 2: Example of wake behind a rotor with forced harmonic pitch motion (Chapter 4).

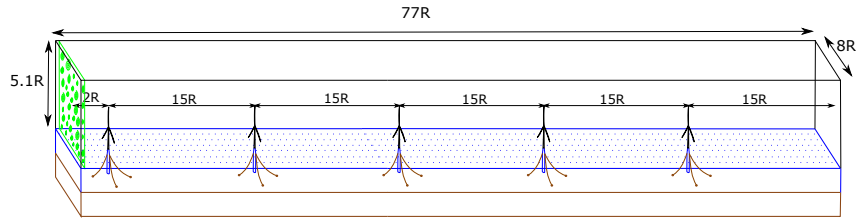


Figure 3: Numerical setup for computations of wake-induced response for 5 turbines in a row (Chapter 6).

1.1 People and contributors

Chapter 2 on accelerated QTF load evaluation has been written by Stavros Kontos and Henrik Bredmose, DTU.

Chapter 3 on response of floating turbines with shared mooring lines has been written by Ozan Gözcü, Stavros Kontos and Henrik Bredmose, DTU.

Chapter 4 and 7 on wake effects and wake-induced response of floating wind turbines has been written by Néstor Ramos-García, Stavros Kontos, Antonio-Pegalajar-Jurado, Sergio González Horcas and Henrik Bredmose, DTU.

Chapter 5 on the comparison between MIRAS and Fast.Farm has been written by Umut Özinan and Mohammad Youssef Mahfouz, University of Stuttgart and Néstor Ramos-García, DTU.

Chapter 6 on the wind tunnel investigation of the wake of the floating IEA 15 MW wind turbine has been written by Alessandro Fontanella, Alan Facchinetti and Marco Belloli, POLIMI.

2 Rapid evaluation of second-order wave loads

Floating wind farms offer great potential of exploiting deep water sites and contributing in the race towards a green transition. To make the technology more cost-competitive against bottom-fixed offshore wind farms, there is a need for floater designs that can be mass produced and are efficient to install. Efficient numerical tools are therefore needed to automate the optimisation of the floater design. Optimisation software are often utilising simplified numerical models that are neglecting second order wave loads to decrease the computational cost. However, these loads are important to include when simulating floating structures with high natural periods (often larger than 100 sec in surge/sway) since the low frequency sub-harmonics can lead to resonance.

We present here an efficient method to calculate second order wave loads based on Quadratic Transfer Functions (QTFs) that can be computed by a potential flow panel solver. The method is presented in details in Bredmose & Pegalajar-Jurado (2020); Pegalajar-Jurado & Bredmose (2020) for the slender body approach and applied on a spar buoy. The QTF based accelerated method has been applied to predict extreme response events for floating wind turbines in combination with a FORM (First-Order Reliability method, Ghadirian *et al.* (2017)) analysis in Freddy J. Madsen (2021).

In the present study, we apply the method in a wind turbine farm context and implement it in Fortran in the HAWC2Farm software (Gözcü *et al.* (2022 -Submitted)), and in Matlab to connect with Matlab-based optimizers. To this end, we benchmark the speed-up benefits and identify the time series length where they become beneficial. In the following subsections we first go through a brief summary of different approaches for calculating wave loads, we present the accelerated method and we apply it to calculate second order wave loads on the WindCrete floater. Finally, we test the accuracy and efficiency of the method and in the following section we investigate the effect of second order wave loads in a shared mooring two turbine wind farm.

2.1 The slender body approach

We can apply the Morison equation 1 to calculate wave loads on structures when they are considered slender. A vertical cylinder in waves is defined as slender when the ratio of its diameter D over the wave length L is smaller than 0.2, ($D/L < 0.2$). The linear hydrodynamic force is then computed by integrating the inertia term of the Morison equation up to $z = 0$

$$F^{(1)} = \int_{-d}^0 \rho \pi R^2 (C_m + 1) u_t^{(1)} dz \quad (1)$$

where d represents the draft and $u_t^{(1)}$ is the first order Eulerian wave particle acceleration. The standard Morison drag force is a second-order term that is defined as:

$$F_{drag}^{(2)} = \int_{-d}^0 \rho R C_D u^{(1)} |u^{(1)}| dz \quad (2)$$

More second order terms can be included as defined in Rainey (1989, 1995).

2.2 The radiation-diffraction approach in second order wave loads calculation

The time domain first order wave excitation loads in a radiation-diffraction analysis are calculated as

$$F_k^{(1)} = \Re \left\{ \sum_{j=1}^N \hat{\eta}_j X_{j,k} e^{i\omega_j t} \right\}, \quad (3)$$

where $k = 1, 2, \dots, 6$ represents the degree of freedom (surge, sway, heave, roll, pitch, yaw), ω_j is the angular frequency, $\hat{\eta}_j = a_o_j e^{-ik_j x}$ are the Fourier coefficients of the free-surface elevation with amplitude a_o and $X_{j,k}$ are the first order wave loads per unit amplitude.

The second order loads consist of contributions from the sum and difference frequencies of pairs of incoming waves. For each pair of frequencies (ω_m, ω_n) two quadratic transfer functions (QTFs) are defined that correspond to the sum (QTF_{mn}^+) and difference (QTF_{mn}^-) frequency loads. Therefore, the second order excitation loads are defined as

$$F_k^{(2)} = \left\{ \sum_{m=-N}^N \sum_{n=-N}^N \hat{\eta}_m \hat{\eta}_n^* QTF_{mn,k}^- e^{i(\omega_m - \omega_n)t} \right\} + \left\{ \sum_{m=-N}^N \sum_{n=-N}^N \hat{\eta}_m \hat{\eta}_n QTF_{mn,k}^+ e^{i(\omega_m + \omega_n)t} \right\}, \quad (4)$$

where the asterisk $*$ represents the complex conjugate and $\hat{\eta}_{-n} = \hat{\eta}_n^*$. Computing the second order wave loads by 4 is computationally expensive for long time series. The symmetry relations of the QTF matrices

$$\begin{aligned} QTF_{mn,k}^+ &= QTF_{nm,k}^+, \\ QTF_{mn,k}^- &= QTF_{nm,k}^{-*} \end{aligned} \quad (5)$$

can be exploited to accelerate the calculations as in Duarte *et al.* (2014).

2.3 Numerical speed up by eigenmode decomposition

The accelerated method of calculating second-order inviscid hydrodynamic loads has been described in detail in Bredmose & Pegalajar-Jurado (2020); Pegalajar-Jurado & Bredmose (2020) for the slender body approach. Here we describe the application of the method on the QTFs determined by a frequency domain potential flow panel code.

For fixed x and t the double sums in 4 can be expressed as the following quadratic matrix product

$$F_k^{(2)} = \left[\dots \hat{\eta}_m e^{i\omega_m t} \dots \right] (\Re(\mathbf{Q}) + i\Im(\mathbf{Q})) \begin{bmatrix} \vdots \\ \hat{\eta}_n e^{i\omega_n t} \\ \vdots \end{bmatrix}, \quad (6)$$

where \Re, \Im denote the real and imaginary parts of the matrix

$$\mathbf{Q} = \begin{bmatrix} QTF_{mn,k}^+ & QTF_{mn,k}^- \\ QTF_{mn,k}^- & QTF_{mn,k}^+ \end{bmatrix} \quad (7)$$

The \mathbf{Q} matrix is symmetric and square and can be diagonalized by eigenmode decomposition

$$F_k^{(2)} = \sum_{j=1}^{2N} \left[\dots \hat{\eta}_m e^{i\omega_m t} \dots \right] \mathbf{V}_{\Re,j} \lambda_{\Re,j} \mathbf{V}_{\Re,j}^T \begin{bmatrix} \vdots \\ \hat{\eta}_n e^{i\omega_n t} \\ \vdots \end{bmatrix} + i \sum_{j=1}^{2N} \left[\dots \hat{\eta}_m e^{i\omega_m t} \dots \right] \mathbf{V}_{\Im,j} \lambda_{\Im,j} \mathbf{V}_{\Im,j}^T \begin{bmatrix} \vdots \\ \hat{\eta}_n e^{i\omega_n t} \\ \vdots \end{bmatrix} \quad (8)$$

Next, we recast the product of the Fourier coefficient vector and the eigenvector V of each mode into a bracketed sum.

$$F^{(2)} = \sum_{q=1}^{n_{modes}} \lambda_{\mathfrak{X},q} \left[\sum_{m=-N}^N V_{\mathfrak{X},qm} \hat{\eta}_m e^{i\omega_m t} \right]^2 + i \sum_{q=1}^{n_{modes}} \lambda_{\mathfrak{S},q} \left[\sum_{m=-N}^N V_{\mathfrak{S},qm} \hat{\eta}_m e^{i\omega_m t} \right]^2 \quad (9)$$

We can interpret those sums as pseudo time series where the eigenvector is applied as a transfer function to the Fourier coefficients. Consequently we can compute them by FFT at a $O(n \log n)$ cost. To approximate 9 we can truncate the active modes in a similar way as in Singular Value Decomposition (SVD) and evaluate the second order force at $O(n \log n)$ cost.

2.4 Results

We evaluated the performance of the accelerated method on the WindCrete spar-buoy floater. We used a mild and a severe sea state based on a Pierson-Moskowitz as in table 1. The QTFs are computed on a 100×100 frequency grid and the eigenvectors that act as pseudo transfer functions are interpolated to the full frequency vector. We implemented the accelerated method in FORTRAN and Matlab and we compared its efficiency and accuracy with the double sum method

| SS | Description | $H_s(m)$ | $T_p(s)$ |
|----|------------------------|----------|----------|
| 1 | Mild | 1.67 | 8.0 |
| 2 | Severe (50-year storm) | 10.90 | 16.0 |

Table 1: Selected sea states.

In Figure 4 the computational time in FORTRAN is plotted as function of time series length for the two sea states. We can see that there is no significant difference in computational time between the two sea states as expected. However, the number of modes for accurate results can be sea state dependant. The accelerated method scales with $O(n)$ cost and the double sum method with $O(n^2)$ as expected. For a one hour time series and 8 modes the accelerated method is approximately 2.5 time faster than the double sum but the two methods perform very similarly when 30 modes are selected. In the accelerated method the computational effort is spent in the calculation of the IFFT of the pseudo time series for each mode whereas the double sum method relies on for loops which are very fast in FORTRAN.

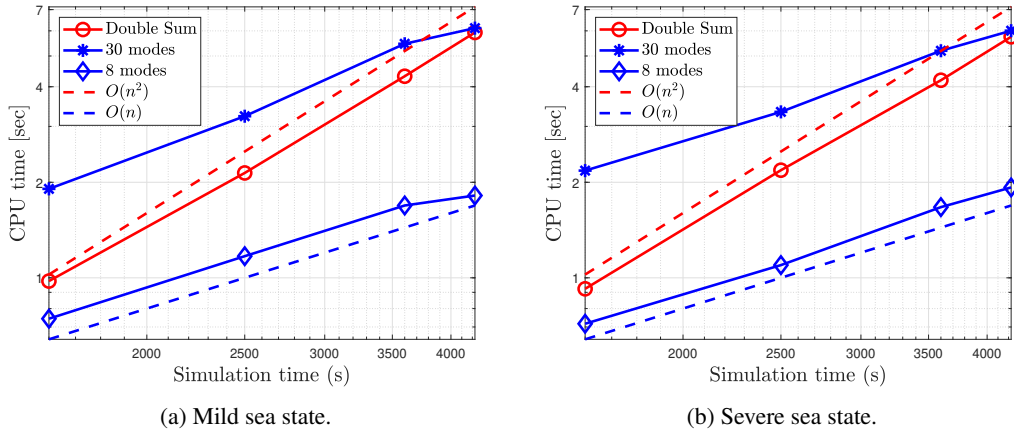


Figure 4: FORTRAN computational time versus time series length.

In Figure 5 the same comparison is made but using Matlab. For a one hour time series in Matlab the accelerated method is approximately 4.3 and 13.6 times faster than the double sum method for 30 and 8 modes respectively. Matlab and FORTRAN have almost the same computational cost when computing FFTs but for loops in Matlab are very expensive.

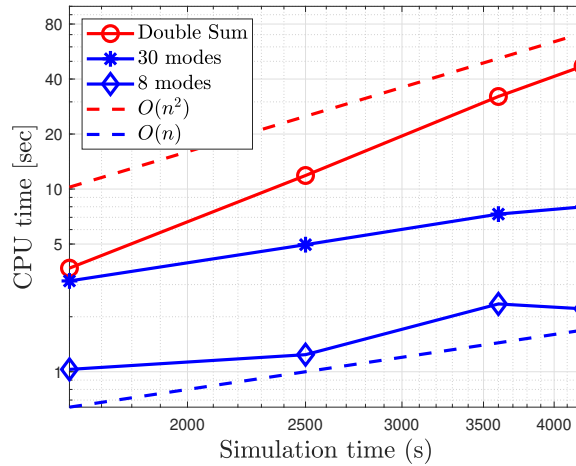


Figure 5: Matlab computational time versus time series length.

In Figure 6 the error $\mathcal{E} = (\sigma_{2sum} - \sigma_{Acc})/\sigma_{2sum}$ is plotted for the two sea states as a function of simulation time. Figures 7 and 8 present the loads for the two sea states. The left column of sub-figures shows a portion of the loads time series of each degree of freedom and the right column presents the corresponding PSD functions.

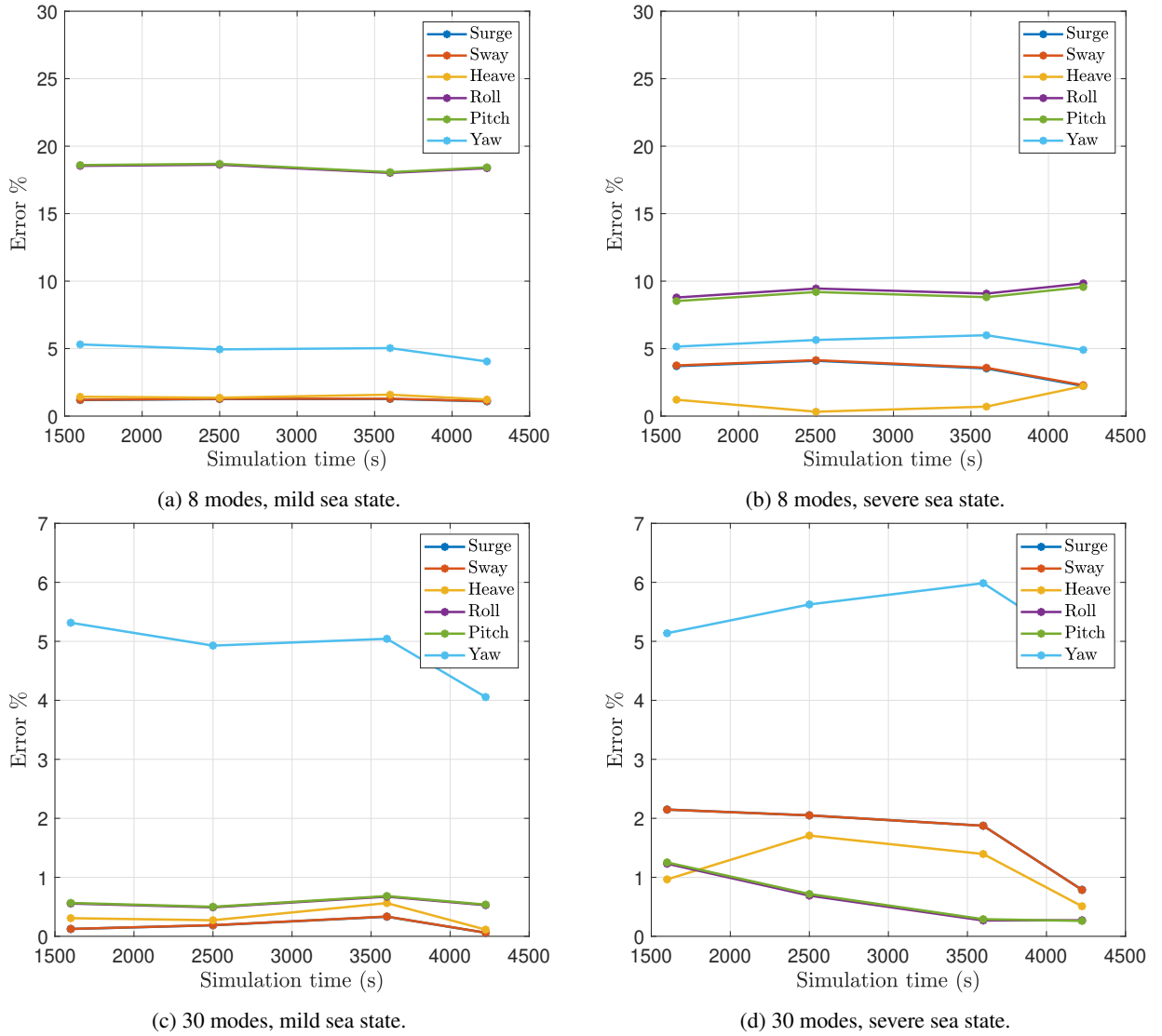


Figure 6: Error versus time series length.

For 8 modes the error of the three translations is below 5% for both sea states. For roll and pitch the error is around 18% for the mild sea state and 10% for the severe sea state. The higher than expected errors in these degrees of freedom can be attributed to discontinuities in the corresponding QTFs. We intend to update these results using new QTFs from a more accurate panel code simulation. When using 30 modes the errors drop below 1% for all degrees of freedom except yaw due to discontinuities of that QTF. That is attributed to numerical noise since there is no forcing in yaw in a potential flow context.

In Figures 7, 8 we present the loads for the mild and severe sea state respectively. We compare the double sum method with the accelerated method with 8 modes. The agreement is reasonably good but the accelerated method underpredicts the loads in the pitch and roll dofs. The accuracy of the method is improved when 30 modes are used.

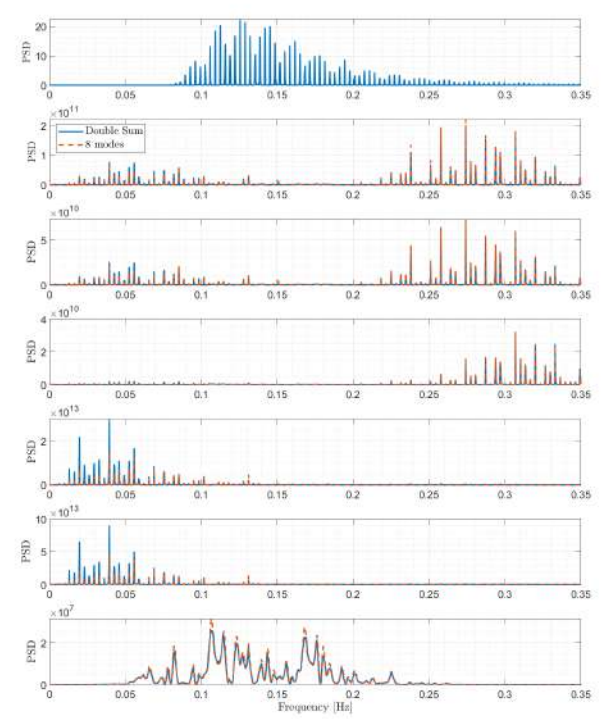
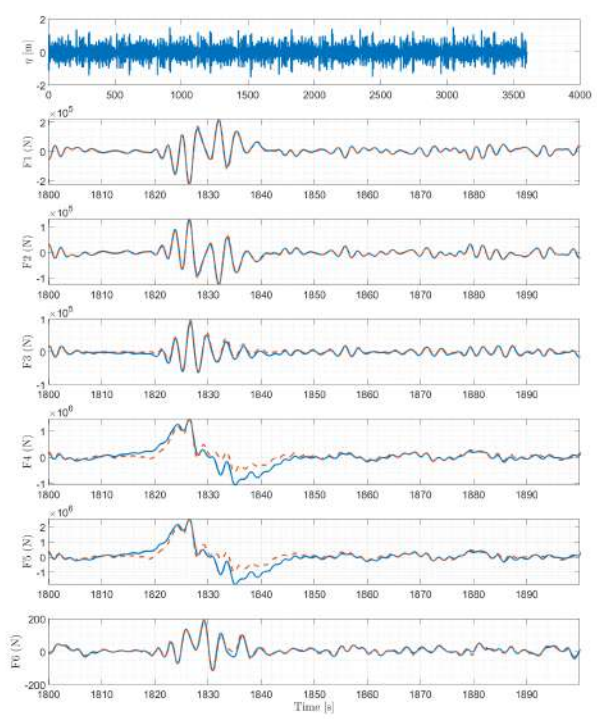


Figure 7: Loads for mild sea state. DOF order as in 3.

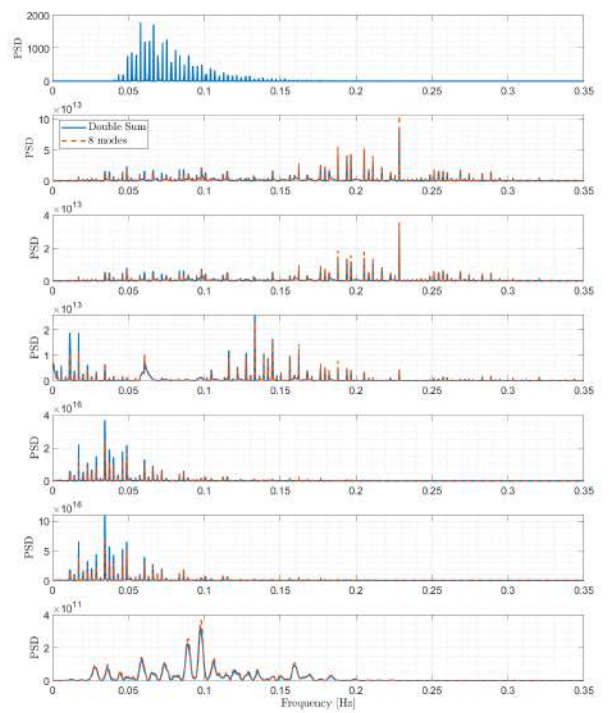
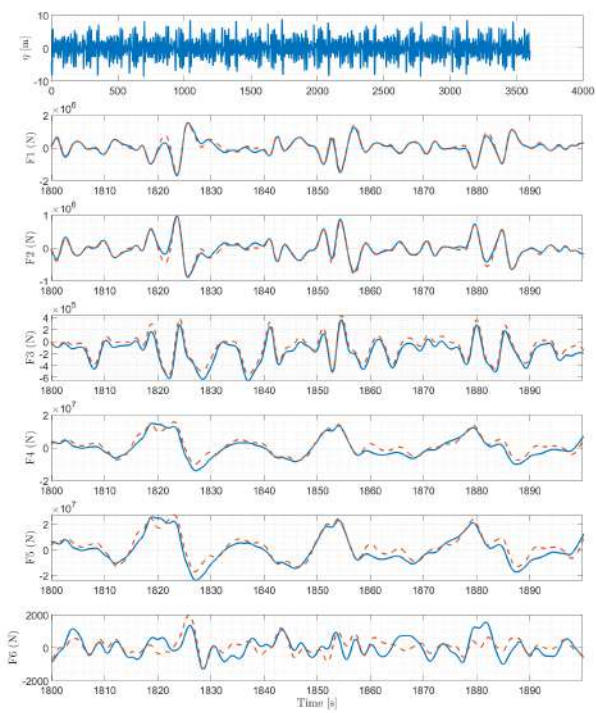


Figure 8: Loads for severe sea state. DOF order as in 3.

2.5 Conclusion

The accelerated method offers good accuracy when 30 modes are selected at an improved computational cost. The efficiency is significantly improved in a Matlab based implementation (92% and 72% computational cost decrease for a 3600 sec time series for 8 modes and 30 modes respectively). In the FORTRAN implementation the computational cost was decreased by 60% for a 3600 sec time series for 8 modes. However, there was a 24% increase in computational time compared to the double sum solution when 30 modes were used for the same time series, due to the low for-loop cost in FORTRAN. Therefore if the response calculation is fast (as in an optimization tool) the accelerated method offers considerable speed gains. Furthermore, since it is QTF based, allows for load calculation on any floater geometry without the limitations of the slender-body approach. If on the other hand a complex hydro-aero-elastic code is used to calculate the response, the gains of the second order loads calculation contribute less to the total cost, since the main effort is spent on computing the response.

3 Response calculation for a farm with shared mooring

Floating wind farms provide the possibility to capture wind resources located in deep water sites and are becoming increasingly competitive in the offshore wind energy market. Contrary to Oil and Gas applications where platforms are moored individually, shared mooring designs could be utilised within a wind farm to decrease installation costs. It is therefore important to be able to model the new system dynamics that arise from shared mooring lines and/or anchors. Furthermore, experience from Oil and Gas platforms shows that second order wave excitation forces can induce large slow-drift motions. As a result, we will use HAWC2Farm to investigate the response of a two turbine shared mooring design and the influence of second order wave loads. The current study builds on the deliverable by Gözcü *et al.* (2021) where the mode shapes and natural frequencies of several shared mooring designs were identified and compared. To demonstrate the capabilities of the HAWC2Farm software we simulate the Design Load Case (DLC) 6.1 that considers a parked turbine under 50-year extreme wind and waves. The setup of this load case leads to a wave dominated response that will allow the influence of the second order wave loads to be more apparent. However, wind drag loads on the tower and the nacelle are also included.

3.1 Methodology

The modeling of the shared mooring design is done in HAWC2Farm, an extension of the aero-servo-hydroelastic wind turbine analysis code HAWC2 Larsen & Hansen (2020). HAWC2 uses a multi-body dynamic formulation, where the wind turbine is composed of bodies that consist of several linear Timoshenko beam elements. Nonlinear structure effects due to body rotation or deformation are introduced through coupling constraints that connect individual bodies. The aerodynamics modeling is based on blade element momentum theory (BEM) Aagaard Madsen *et al.* (2020) and turbulent inflow is generated using the Mann model. The controller is defined as an external dynamic link library (dll). The hydrodynamic loads are computed either through the Morison equation in its full form, or by using the WAMIT Lee (1995) frequency response functions for the radiation and diffraction forces combined with the Morison drag. We used HAWC2's coupling with WAMIT Borg *et al.* (2016) in the following simulations and the second order wave loads are computed through the double sum formulation 4 and without the accelerated method as introduced in Chapter 2. The mooring lines are modeled dynamically using non-linear beam elements with hydrodynamic drag, added mass and buoyancy forces Hansen & Zahle (2011). Clump weights and buoys are included as point mass with linear and quadratic viscous damping terms. Mooring lines can be shared through the constraint equations in the multibody formulation. The extension of the model to include shared mooring lines/anchors is detailed at Gözcü *et al.* (2021).

3.2 Second order wave loads effects

The second order wave loads are proportional to the square of the wave amplitudes and are created by the interaction of a pair of regular waves with frequencies (ω_m, ω_n) . This interaction results at difference-frequency loads at the $|\omega_m - \omega_n|$ frequency. Similarly, there is a high frequency contribution at the $\omega_m + \omega_n$ frequency known as sum-frequency loads.

The difference-frequency loads can excite the slow-drift motion of slacked moored floating structures. A wave pair of equal frequencies results in a zero frequency (constant) contribution. The sum of all the constant contributions produces the mean wave drift load that causes a mean static offset of the floating structure.

Sum frequency loads affect stiffer structures (e.g., fixed bottom monopiles or tension-leg platforms) and can cause ringing.

In the following simulations we used the radiation-diffraction approach for calculating the second order wave loads as summarised in subsection 2.2. The double-sum method was used with QTFs computed by WAMIT on a 50×50 frequency grid with $f_{min} = 0.04$ Hz and $f_{max} = 0.35$ Hz.

3.3 Shared anchor design at Morro Bay

The case study that we will be focusing on uses the IEA 15 MW reference wind turbine Bredmose *et al.* (2020) with the WindCrete spar floater Mahfouz *et al.* (2020b) at the Morro Bay site. The water depth of the site is 870 m and the properties of the floater and tower can be found in Mahfouz *et al.* (2020a). The single turbine design is moored with four taut mooring lines, that attach to the four fair-leads on the floater with delta lines, as shown in Figure 9. The shared anchor design is shown in Figure 10. The two turbines are 7 rotor diameters apart and there is no buoyancy element at the connection that leads to the shared anchor. The mooring line properties are summarised in table 2 and are common between the single and the two turbine designs. The dynamic properties of both designs have been analysed and the natural frequencies and mode shapes are identified and presented in Gözcü *et al.* (2022 -Submitted).

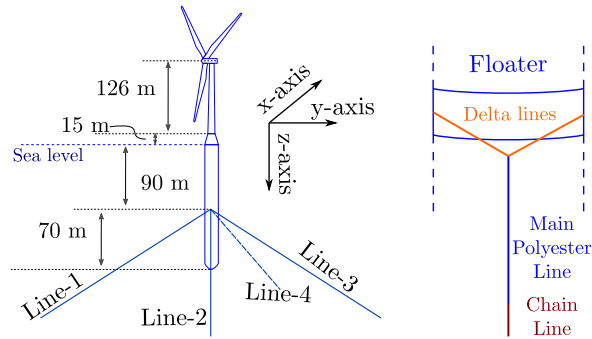


Figure 9: Single turbine design with 4 mooring lines and mooring line sections at Morro Bay. Figure from Gözcü *et al.* (2022 -Submitted)

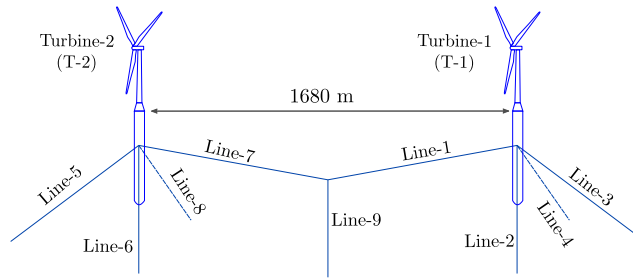


Figure 10: Shared anchor design with 2 turbines in Morro Bay site. Figure from Gözcü *et al.* (2022 -Submitted)

In Figure 11 the eigenfrequencies of the single turbine and the shared mooring design are presented. For completeness, the figure includes all three shared mooring designs that were analysed in Gözcü *et al.* (2022 -Submitted). The one we chose for this case study is the Design-5 since its eigenfrequencies in all degrees of freedom except from yaw, are very close to the single turbines eigenfrequencies.

| | Delta line | Main polyester | Chain line |
|----------------------|--------------------|--------------------|--------------------|
| Length [m] | 50.0 | 1020.8 | 183.7 |
| Diameter [mm] | 90 | 205 | 85 |
| Equivalent D [mm] | 162 | 164 | 171 |
| Dry mass [kg/m] | 161.0 | 28.6 | 179.6 |
| Axial stiffness [kN] | 6.92×10^5 | 2.68×10^5 | 7.71×10^5 |

Table 2: Properties of mooring line sections at Morro Bay.

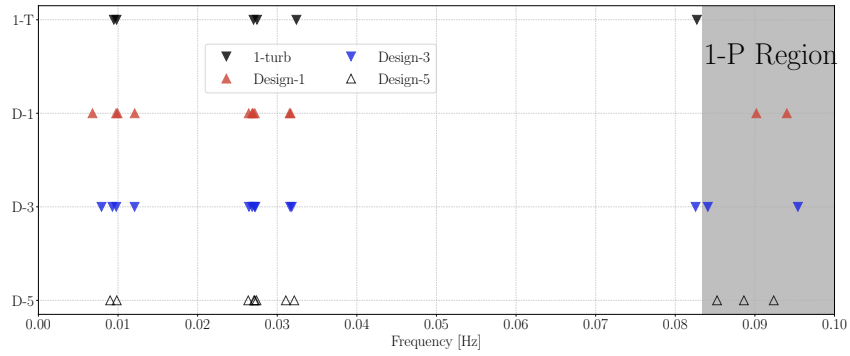


Figure 11: Frequencies for single turbine (1-T), Design-1 (D-1), Design-3 (D-3) and Design-5 (D-5). The gray region represents the turbine 1-P region. Figure from Gözcü *et al.* (2022 -Submitted)

3.4 Load analysis

The turbines responses and loads are computed by HAWC2 for DLC61 where the maximum mooring line forces can occur. Figure 12 shows the environmental conditions and turbine state for DLC6.1 load simulations. Summarising here, the wind direction used is -8,8 deg and the wave direction is -30, 0, 30 deg. Based on the Design Basis Vigara *et al.* (2019) for the Morro Bay site we selected two sea states generated with a Jonswap spectrum with $H_s = 9.9$ m, $T_p = 16$ sec, $\gamma = 1$, and $H_s = 9.9$ m, $T_p = 18$ sec, $\gamma = 1$, respectively. The simulations are run with the first order hydrodynamic models and the second order hydrodynamic models. Since the Wamit model has no viscous drag model, a separate model is used to compute the drag forces on the floaters. Although, the wave loads computed by the first order model is linear, there are still nonlinear effects due to drag model which is nonlinear.

| DLC61 | | Parked in 50-year extreme wind | |
|-----------------------|---|--------------------------------|-------------------|
| Assessment | Extreme – normal event | Safety factor | 1.35 ² |
| Description | Simulation of parked turbine with idling rotor and yaw error at a wind speed with 50-year recurrence period and turbulence intensity of 11%. Six seeds per yaw error are used. The combination of extreme wind and wave conditions shall be such that the global extreme environmental action has a combined recurrence period of 50 years. This needs to be repeated at 3 water depths of MSL, HAT +storm surge and LAT-storm surge if the water level that results in the largest loads is not known. | | |
| Simulation setup | Length: At least 600 s (1 hour is recommended) Wind: V50 Yaw: -8/+8 deg Turbulence: 11% intensity, 6 seeds per wind speed and yaw error Waves: Stochastic, ESS, EWLR, 50 year nonlinear waves, 3 seeds Shear: Vertical and exponent of 0.11 Gust: None Fault: None | | |
| Total no. simulations | 12 (if fixed water depth) otherwise 36 (for 3 different water depths) | | |
| Post-processing | The average of the extremes values is computed for each load sensor as the characteristic extreme load value. The non-linear waves of height equal to the extreme wave height must be used based on at least 1 hour wave simulation using methods such as given in [5]. If the load simulation length is only 600s, then the extreme wave from a 1-hour wave simulation should be used. For 1-hour load simulations the extreme mean wind speed can be 0.95 of the 10 minute extreme mean wind speed. | | |

Figure 12: DLC61. Table from Natarajan *et al.* (2016).

Each load case uses a unique wave field which means 12 different wave fields used in total. Figure 13 shows the surface elevations over the simulation time and their PSD for two selected wave fields used in the load analyses. One wave field has 18 s period (T-18) and the other one has 16 s period (T-16). Wave fields have most of their energy between 0.035 Hz and 0.14 Hz.

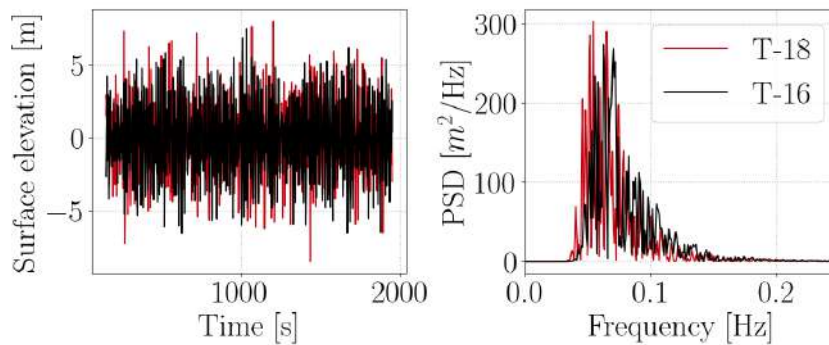


Figure 13: Surface elevations and their PSD for two selected wave fields defined in load analysis.

Table 3 shows the maximum and minimum floater displacements and rotations for different designs (single turbine and shared mooring line) and models with the first order and the second order hydrodynamic models. The displacements are computed from the equilibrium point of the designs for no wind and no wave conditions (Gözcü *et al.* (2021, 2022 -Submitted)). The abbreviations in the plot legends include first the design name (*Single* and *Shared*) and then the hydrodynamic model with "F" for first order hydrodynamic model and "S" for models with second order hydrodynamic model. The effects of second order hydrodynamic loads are not very large for maximum and minimum floater displacements and rotations. The shared mooring line design has larger surge displacements

than single turbine case, yet the sway displacements are similar. The vertical force due to shared mooring lines keeps the heave motion of shared mooring design turbines smaller than the single turbine case. The surge motion of shared turbines are much larger since Line-5 (see figure 10) needs to carry most of the loads alone for both turbines. The mean surge values computed by second order hydrodynamic models are 0.2 m larger than the surge motion results from the first order hydrodynamic models.

Table 3: Maximum and minimum floater motions for both designs with two different hydrodynamic models. The maximum and minimum values are selected among the all time series result.

| | Single-F | | Single-S | | Shared-F | | Shared-S | |
|--------------|----------|-------|----------|-------|----------|-------|----------|-------|
| | max. | min. | max. | min. | max. | min. | max. | min. |
| Surge [m] | 8.22 | -5.32 | 8.51 | -5.68 | 10.82 | -4.03 | 11.41 | -4.48 |
| Sway [m] | 9.19 | -7.91 | 9.08 | -7.77 | 8.09 | -9.36 | 8.07 | -9.39 |
| Heave [m] | 6.94 | -4.64 | 7.14 | -4.02 | 5.99 | -4.98 | 6.66 | -4.45 |
| Pitch [deg.] | 3.79 | -2.58 | 4.34 | -2.83 | 3.52 | -2.38 | 3.89 | -2.80 |
| Roll [deg.] | 5.07 | -4.36 | 4.91 | -4.42 | 4.11 | -3.89 | 4.04 | -3.89 |
| Yaw [deg.] | 3.67 | -3.79 | 3.54 | -4.05 | 3.32 | -3.17 | 3.42 | -3.23 |

Figure 14 shows surge, sway and heave motions time series, PSD and probability of exceeding for the single turbine design with the first order (legend with *First*) and the second order hydrodynamic models (legend with *Second*). The results are from the load case with the maximum surge motion for the single turbine with the second order hydrodynamic model. Two models have similar time series with differences at some peaks, however the difference is more clear in PSD and probability plots in surge direction. The second order hydrodynamic load model has higher energy in low frequencies as seen from the peak at 0.025 Hz which is lower than wave frequencies. This frequency corresponds to the first pitch frequency of the system. The second order hydrodynamic loads also increases the probability of large surge motions compared to the first order hydrodynamic loads. The second order hydro load effects are not visible in sway direction for this load case. The heave results are also close for both models however, the first order hydrodynamic loads have slightly larger peaks in heave PSD results at low frequencies, however it has very similar probability distribution to the second order hydrodynamic model.

Figure 15 shows floater roll, pitch and yaw motions results with similar plots to figure 14 for the load case which gives the maximum pitch motion. The main difference is observed in pitch PSD and probability plots where second order hydrodynamic model has higher energy at the first pitch frequency and higher probability for large pitch rotations than the first order hydrodynamic models. The roll and yaw results for both models look similar in time and in frequency domains.

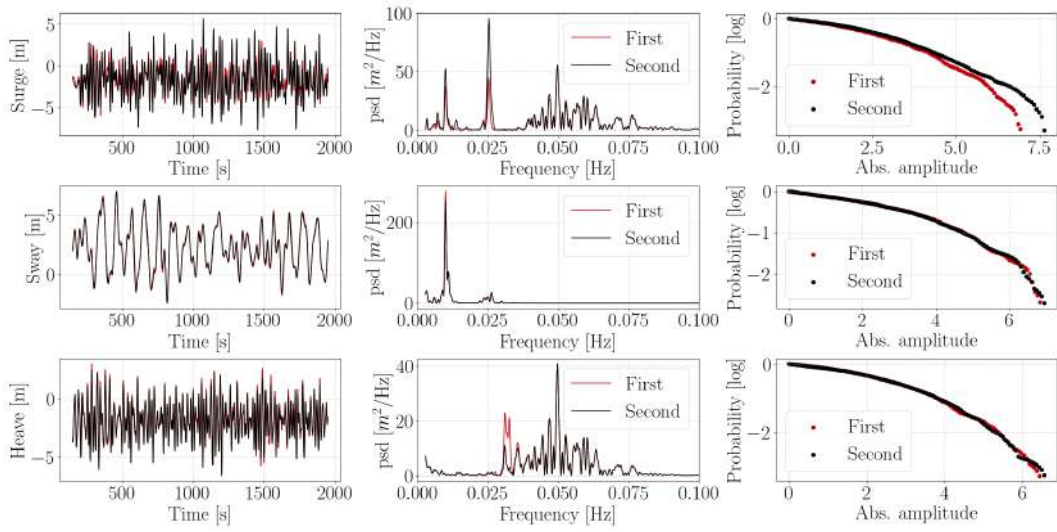


Figure 14: Single turbine design floater surge, sway and heave motions time series, PSD and probability of exceeding plots from the load case with maximum surge motion (30 degree yaw). Results are given for the first order hydrodynamic model (legend with *First*) and for the second order hydrodynamic model (legend with *Second*).

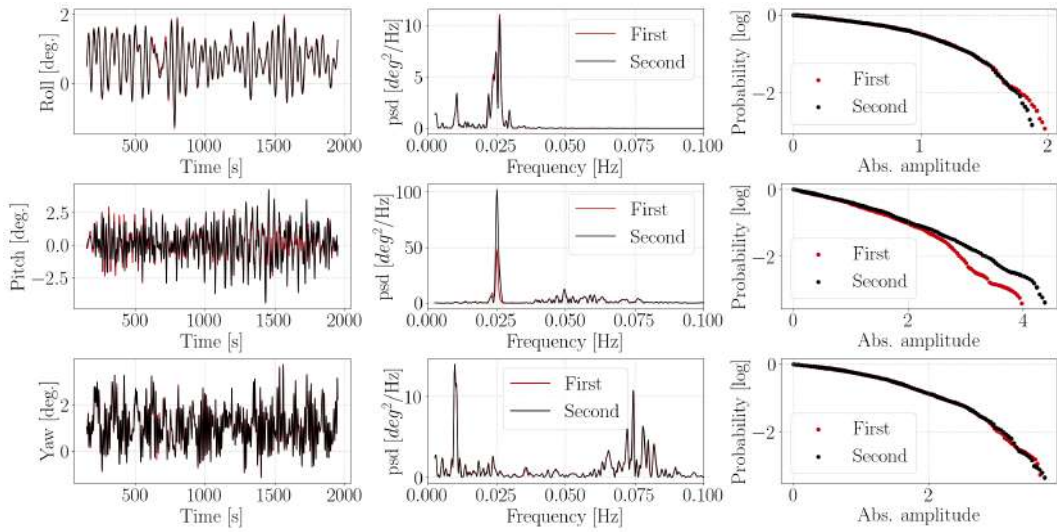


Figure 15: Single turbine design floater roll, pitch and yaw motions time series, PSD and probability of exceeding plots from the load case with maximum pitch motion. Results are given for the first order hydrodynamic model (legend with *First*) and for the second order hydrodynamic model (legend with *Second*).

Figure 16 shows surge, sway and heave results for shared mooring line design model. Results of both turbines with two hydrodynamic models are given. The legends indicate the turbine number as *T1* and *T2* for the first (downwind) and second (upwind) turbine (see figure 10 for turbine numbers). The letters after turbine number indicates the first order (*F*) or second order (*S*) hydrodynamic models. The results are from the load case with maximum surge motion. Although the time signals look different for all three motions, it is hard to see the differences between models in time domain.

On the other hand, PSD and probability plots give better idea about the dynamics of the system. The largest PSD peak occurs in surge direction around first surge natural frequency. Second order hydrodynamic model has larger peaks than the first order model at lower frequencies in surge and heave directions where the large motion probabilities are also higher for second order model than the first order model. The difference between two hydrodynamic models is very small in sway results. The first turbine has higher probability of large sway motion than the second turbine for both hydrodynamic models.

Figure 17 shows floater roll, pitch and yaw rotation results for the load case which gives the maximum pitch motion. The PSD peaks for pitch and roll directions are seen at the first pitch and roll frequencies which are around 0.025 Hz, on the other hand yaw results have a PSD peak around 0.08 Hz which is the first yaw frequency. The second order hydrodynamic model peaks at first roll and pitch frequencies are again larger than the first order hydrodynamic model peaks. The first turbine has higher probability of large roll motions than the second turbine. The pitch probability results of T1 and T2 computed by the second order hydrodynamic model are much closer to each other compared to the results from the first order hydrodynamic model. There is also a slip in roll and pitch results for shared mooring line design which is not observed for the single turbine case. It doesn't look like a strong instability since its slow dynamics. It needs a further investigation with very long simulations to see the value it converges.

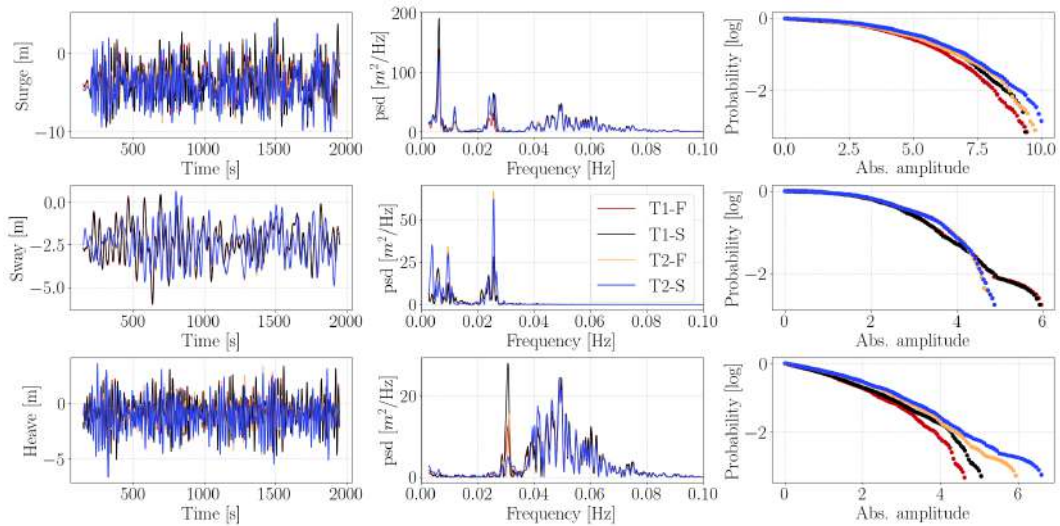


Figure 16: Shared mooring line design floater surge, sway and heave motions time series, PSD and probability of exceeding plots from the load case with maximum surge motion. Results are given for the first order hydrodynamic model (legend with *T1-F* & *T2-F*) and for the second order hydrodynamic model (legend with *T1-S* & *T2-S*).

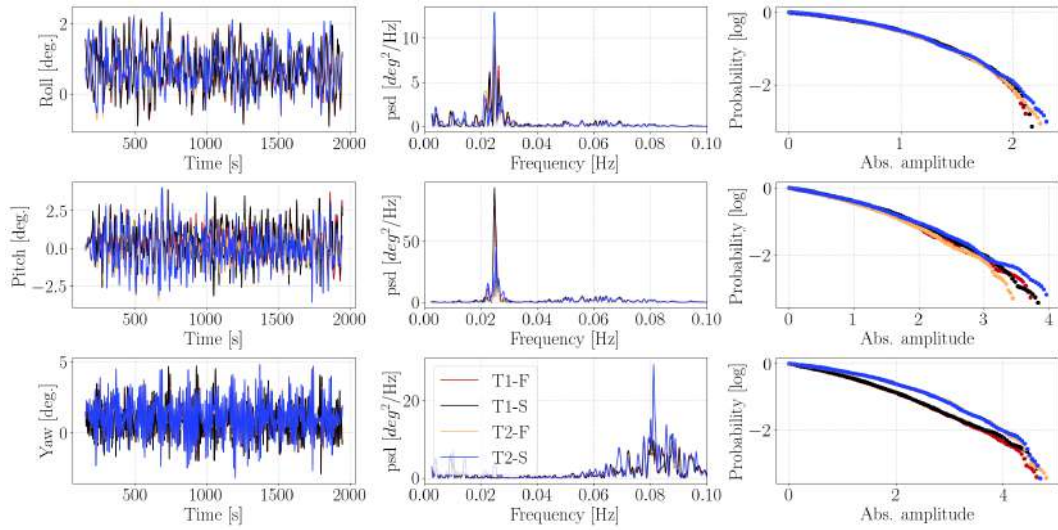


Figure 17: Shared mooring line design floater roll, pitch and yaw motions time series, PSD and probability of exceeding plots from the load case with maximum pitch motion. Results are given for the first order hydrodynamic model (legend with *T1-F* & *T2-F*) and for the second order hydrodynamic model (legend with *T1-S* & *T2-S*).

Table 4 shows the maximum mooring line forces (see figure 9 and 10 for line numbers) for both designs and hydro models. The maximum force values are determined as the average of the maximum values computed for each load simulation (see figure 12 and Natarajan *et al.* (2016)). The effect of second order wave model is not significant for both designs. On the other hand, shared mooring line design has 21 % larger mooring line forces than the single turbine design. The maximum force occurs on Line-5 of shared mooring line design which is the main support line for surge motion of the system together with Line-3.

Table 4: Maximum mooring line forces for both designs and both hydrodynamic models.

| | Single-F | Single-S | Shared-F | Shared-S |
|-------------|----------|----------|----------|----------|
| Line-1 [MN] | 6.15 | 6.19 | 5.61 | 5.65 |
| Line-2 [MN] | 6.07 | 6.05 | 6.10 | 6.08 |
| Line-3 [MN] | 5.67 | 5.64 | 6.45 | 6.38 |
| Line-4 [MN] | 6.01 | 5.97 | 6.02 | 6.00 |
| Line-5 [MN] | | | 7.45 | 7.51 |
| Line-6 [MN] | | | 6.01 | 6.02 |
| Line-7 [MN] | | | 5.60 | 5.64 |
| Line-8 [MN] | | | 5.99 | 6.97 |
| Line-9 [MN] | | | 2.23 | 2.24 |

Table 5 shows the tower top accelerations and tower bottom bending moments for both designs and both hydrodynamic models. The difference between the first order hydrodynamic model and the second order hydrodynamic model is also given for both designs. The coordinate axis for forces are same as the coordinate systems given in figure 9 or figure 10. So, x-moment represents the fore-aft bending in tower and y-moment is in the side-side bending. The z-direction is upward and z-moment represents the torsion for tower. Again the maximum values are determined as the average of all extreme values from each load case. The shared mooring line design has lower fore-aft and side-side tower top accelerations and tower bottom moments than the single turbine design. On the other hand second order wave models give larger tower top accelerations and tower bottom bending

moments than the first order hydrodynamic models. The differences in fore-aft direction are the largest both in accelerations and moments.

Table 5: Mean of maximum tower top accelerations and tower bottom moments for both designs and both hydrodynamic models.

| Tower location | Single-F | Single-S | Diff. [%] | Shared-F | Shared-S | Diff. [%] |
|--------------------------|----------|----------|-----------|----------|----------|-----------|
| Top x-acc. [ms^{-2}] | 1.14 | 1.16 | 1.7 | 0.99 | 0.99 | 0.0 |
| Top y-acc. [ms^{-2}] | 2.00 | 2.15 | 7.5 | 1.94 | 2.09 | 7.7 |
| Top z-acc. [ms^{-2}] | 0.57 | 0.59 | 3.5 | 0.55 | 0.56 | 1.8 |
| Bot. x-mom. [MNm] | 663 | 704 | 6.2 | 646 | 692 | 7.1 |
| Bot. y-mom. [MNm] | 346 | 352 | 1.7 | 309 | 316 | 2.3 |
| Bot. z-mom. [MNm] | 18.5 | 18.4 | -0.5 | 16.2 | 16.2 | 0.0 |

Figure 18 shows tower bottom moment results for single turbine design from the load case with the maximum fore-aft moment. The differences are not visible in time signal but there are some differences in PSD and probability plots in fore-aft (x-Moment) direction. Fore-aft and side-side moments have peaks at the first pitch and roll frequencies. The second order hydrodynamic models have larger peaks than the first order hydrodynamic model in those frequencies. The most important difference is at the fore-aft moment probability plot where the second order hydrodynamic model gives more frequent large moments than the first order hydrodynamic model.

Figure 19 shows tower bottom moment results for the turbines in shared mooring line designs. The results are from the load case which gives the maximum fore-aft moment. The second order hydrodynamic model gives larger PSD peaks at the first pitch and roll frequencies for fore-aft and side-side moments. Apart from the peaks at those frequencies, the PSD results are similar for both hydrodynamic models. The second order hydrodynamic effects result in higher probability of large fore-aft moments than the first order hydrodynamic model, similar to the results for single turbine design given in figure 18. The second turbine probability for large fore-aft moments is higher than the first turbine in both hydrodynamic model. There is no big difference in the probability results of turbines and hydrodynamic models for side-side moment and torsion loads.

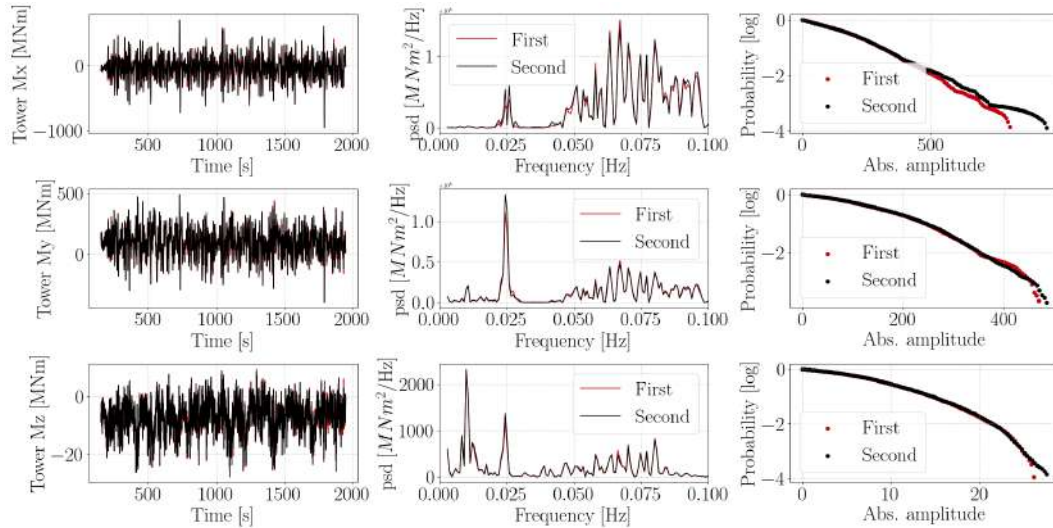


Figure 18: Single turbine design tower bottom moments time series, PSD and probability of exceeding for maximum fore-aft moment load case with the first order and the second order hydrodynamic models.

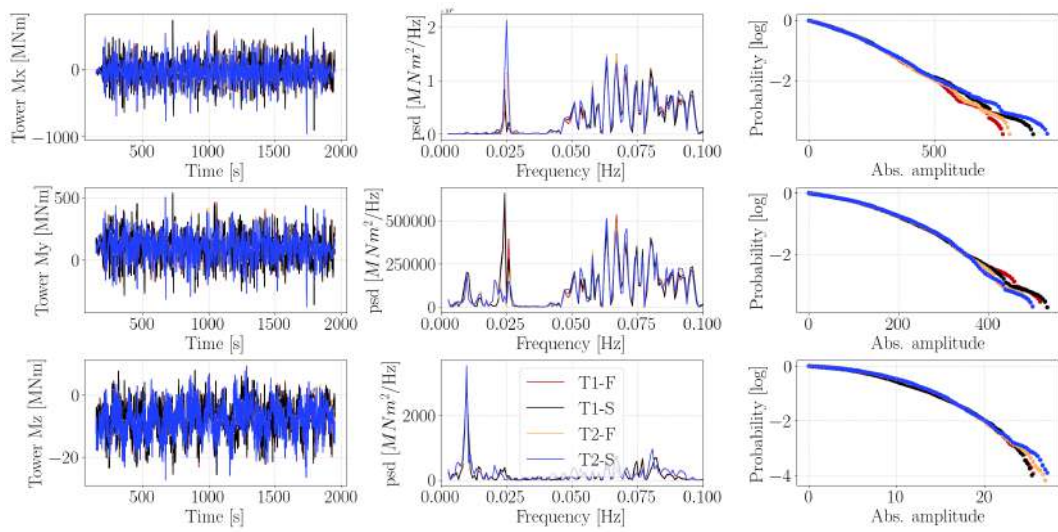


Figure 19: Tower bottom moments time series, PSD and probability of exceeding for turbines in shared mooring line designs. The results are from the maximum fore-aft moment load case with the first order and the second order hydrodynamic models..

3.5 Conclusions

We simulated the DLC6.1 as a case study that shows the capabilities of HAWC2Farm in simulating floating wind turbine farms with shared mooring, under turbulent wind and irregular waves including second order wave loads. Our findings show that second order wave loads are important even in deep water conditions that are typical for floating wind turbines. Furthermore, the response of shared mooring farms are significantly different than individually moored turbines, to the extent that the maximum mooring line loads are increased by 21%. HAWC2Farm is a software solution that allows for detailed examination of the new dynamics that are present in shared mooring designs. As future work, the software will be parallelised and a wake engineering model will be implemented.

4 Investigation of the floating IEA Wind 15 MW RWT using vortex methods: Flow regimes and wake recovery

The wake behind a floating wind turbine is more complicated than for bottom fixed configurations due to the motion of the floating support structure. This motion is driven by low-frequency rotor loads and second-order wave forcing. The motion of the rotor increases the complexity of the aerodynamic loads, since the rotor may move back and forth within its own induced aerodynamic motion. A detailed investigation of these effects therefore requires a numerical approach at a higher fidelity than the BEM (Blade Element Momentum) method, since this approach assume an inflow that is only affected by the turbines quasi-static induction.

In the present section, we therefore investigate the wake characteristics with a free vortex solver, which can describe the detailed local flow around the blade. Comparison is made to the simpler BEM approach too, to assess how well Engineering calculations with such a solver can describe the loads and response.

Since the low-frequency rotor motion results from the motion of the floater, this response will naturally depend on the specific floater and mooring design. The study is therefore conducted as a series of calculations for forced harmonic surge and pitch motion of the floater and rotor with varying frequency and amplitude. The intention is to provide generic results that can represent the response for a variety of floater designs. The study was limited to zero incident turbulence. The extension to include ambient turbulence is presented in Chapter 6.

The main focus of the study are the blade loads and wake recovery, where notable effects from the rotor motion are observed. These effects are further seen to be strongly frequency and amplitude dependent. The wake recovery was found to behave non-monotonously with respect to frequency. This was related to the occurrence of short time intervals between extreme fore-aft blade tip displacements. Finally, for the different cases of amplitude and frequency, the rotor behaviour was characterized between the rotor states, including those of non-conventional propeller state and the vortex ring states.

The study has been published in *Wind Energy* with Open Access and became available online 09 October 2021.

Investigation of the floating IEA Wind 15 MW RWT using vortex methods Part I: Flow regimes and wake recovery

Néstor Ramos-García¹  | Stavros Kontos² | Antonio Pegalajar-Jurado² | Sergio González Horcas¹ | Henrik Bredmose²

¹Aero- and Fluid Dynamics section, Department of Wind Energy, Technical University of Denmark, Building 403, Kgs. Lyngby, DK-2800, Denmark

²Response, Aero-elasticity, Control and Hydrodynamics Section, Department of Wind Energy, Technical University of Denmark, Building 403, Kgs. Lyngby, DK-2800, Denmark

Correspondence

Néstor Ramos-García, Aero- and Fluid Dynamics section, Department of Wind Energy, Technical University of Denmark, Building 403, Kgs. Lyngby DK-2800, Denmark.
Email: nerga@dtu.dk

Funding information

European Union's Horizon 2020 Research and Innovation programme, Grant/Award Number: 815083

Abstract

Floating wind turbines have the potential to enable global exploitation of offshore wind energy, but there is a need to further understand the complex aerodynamic phenomena they can encounter due to floater induced rotor motion. Aerodynamic models traditionally used in the wind energy sector, like the Blade Element Momentum (BEM) theory, may not be capable of capturing the dynamic phenomena that occur when the rotor moves in and out of its own wake. In the present paper, we therefore compare an industry standard BEM-based code to a state of the art vortex solver, to investigate the phenomena in detail and further clarify the capabilities and limitations of both methods. An initial benchmark of the two codes using the IEA Wind 15 MW RWT mounted on the WindCrete spar-buoy floater is carried out. Three different scenarios are taken into account: a bottom-fixed, a floating case, and a floating case subject to regular waves. Growing discrepancies between the codes have been observed with the increasing complexity of the simulations. Moreover, large differences between the wake generated by a bottom fixed and a floating turbine have been observed, with the latter one experiencing a faster recovery. To further explore the floating turbines behaviors that can affect the rotor performance and wake, a systematic investigation of the mean tilt angle influence in the wake development has been carried out. Further, to account for the oscillatory motion of a floating turbine, a parametric study where the floater motion is prescribed in both pitch and surge degrees of freedom (DoF) is designed. The study covers a large variety of scenarios; a wide range of relevant frequencies and amplitudes are taken into account in under and above-rated wind conditions. A total of more than 28 unique cases have been defined and simulated with both fidelity models. The results include the downstream evolution of the wake recovery and intensity of the turbulent disturbances induced by the rotor. The generic nature of the study allows to characterize the flow and performance effects and enables subsequent generalization to floater designs of given natural frequency and motion amplitude. It has been found that the BEM and LL predictions of the maximum loading in the blade root and tower bottom compare quite well, except for the case of large oscillation frequency in above rated

This is an open access article under the terms of the Creative Commons Attribution License, which permits use, distribution and reproduction in any medium, provided the original work is properly cited.

© 2021 The Authors. *Wind Energy* published by John Wiley & Sons Ltd.

conditions, where the BEM method under-predicts the loads. Moreover, the use of a vortex solver makes it possible to look in depth into the wake characteristics, in which large differences are observed between the bottom-fixed and the floating case in non-turbulent inflow conditions. It has been found that the frequency and amplitude of the turbine oscillations can have a strong impact on the recovery of the wake. Moreover, we have found a link between short time intervals of large FA blade tip displacements and a faster break down of the wake. Finally it has been shown that a floating wind turbine with large and fast oscillations can transition between the different rotor states, including the non-conventional propeller and vortex ring states, which are identified and characterized.

KEYWORDS

BEM, floating wind turbine, lifting line, offshore wind, vortex method, wakes

1 | INTRODUCTION

The immense offshore wind resource has the potential to power the world, attracting more and more the attention of both industry and academia. However, the majority of the available offshore wind is located in deep waters, making floating turbines a key technology for the further exploitation of offshore wind energy. Moreover, in contrast with onshore wind, offshore wind generally provides higher wind speeds and lower turbulence levels in free atmospheric flow conditions.^{1,2} Furthermore, regulatory esthetic and noise requirements are much lower, making possible the installation of larger wind turbines.^{1,3,4} The floaters for offshore wind deployment are usually classified into spar-buoys, semi-submersibles, barges, and tension-leg platforms (TLPs). Whereas TLPs are very stiff with respect to floater pitch motion, the other floater types are typically restrained with a catenary mooring system, thus allowing large motions around an equilibrium point in both surge and pitch.

During the design and planning stages of new offshore wind turbines and wind farm development, simulation tools are used to predict the coupled dynamic loads and response of the offshore wind turbine structure.⁵ Such tools are developing very quickly in recent years and vortex solvers have the potential to become a key method due to their flexibility and reliability.^{6–8} With these solvers, it is possible to easily combine different flow and aerodynamic models depending on the degree of complexity required for the case of study. Enumerated in ascending complexity, the aerodynamic models traditionally implemented in the vortex solvers can be classified as Lifting Line (LL), vortex lattice, potential panel, viscous-inviscid panel, and penalization methods. Analogously, one can divide the flow solvers used in prescribed filament wake methods, free wake filament methods, hybrid filament-particle-mesh methods, and particle-mesh methods. For the present investigation a LL model in combination with a hybrid filament-particle-mesh method is used.

Blade Element Momentum theory (BEM), which at the moment is considered as the industry standard, is not capable to accurately simulate complex blade geometries nor complex flow cases, e.g., yaw and shear. Sub-models to account for such complexities need to be implemented and calibrated with higher fidelity codes or even experimental data. For example, it is not yet clear that the current dynamic inflow models are valid under the most severe unsteady effects a floating machine is subject to. Vaal et al⁹ found that dynamic inflow models calibrated for rapidly changing loads were suitable to be used for analyzing surging wind turbines subject to the low frequency oscillations representative of a TLP. It was found that differences between a BEM and an actuator disc model increased with the increasing oscillation frequency. Other studies like the one of Sivalingam et al¹⁰ have observed larger differences of the BEM based predictions compared to unsteady CFD, in line with the observations of Tran and Kim.¹¹ Moreover, previous work of Sebastian and Lackner¹² on floating machines found that slip-stream violations are most likely to occur for the outboard blade sections at low wind speeds or high tip-speed ratios, demonstrating the necessity of higher-fidelity tools. Moreover, the large fluctuations in the local relative velocities seen by the oscillating blades make floating turbines more likely to encounter “off-design” rotor states, i.e., turbulent wake, vortex ring, and propeller states. Note that some of these states have been investigated in detail using high fidelity CFD solvers in Kyle et al¹³ and Lienard et al.¹⁴ These states present a challenge for standard BEM methods since they can violate the momentum balance assumption¹⁵ due to the appearance of local re-circulation areas or due to the large expansion of the wake at high tip speed ratios, which causes the flow field behind the rotor to be governed by turbulent mixing. Despite these challenges, BEM-based methods can be used to predict the onset of vortex ring state in helicopters¹⁶ and wind turbine applications.¹⁷ It is presumed that empirical corrections have to be used to correctly model these flows in BEM. Sørensen et al¹⁸ compared one-dimensional momentum theory against a Navier-Stokes algorithm with an actuator disc method to model the rotor, finding with their simulations that the turbulent wake and vortex ring states were unstable regimes with a very complicated transient phase.

Kopperstad et al¹⁹ studied the wakes of floating wind turbines using an actuator disc LES methodology. They investigated two concepts, a spar buoy and a barge platform, finding that the motion of the barge platform induced a faster wake recovery in both laminar and turbulent inflow conditions. Rockel et al^{20,21} conducted wind tunnel experiments with stereo Particle Image Velocimetry (PIV) to analyze the effect of pitch motion on the wake development of horizontal axis wind turbines. Their results indicate an upward shift of the wake as a result of the turbine being tilted upwards that is consistent with this study. However, contrary to our findings, they report that the wake of the pitching turbine is governed by an increase in the mean vertical component of velocity that decreases the turbulence production, suppresses the entrainment of kinetic energy, and reduces the mean streamwise velocity. Fu et al²² performed laboratory experiments to study the impact of pitch and roll motion on the power output and wake of a horizontal axis wind turbine. Their results, as ours, show a faster wake recovery for the oscillating turbine due to an enhanced turbulent mixing that leads to an increased turbulence kinetic energy.

Floating wind turbines are subject to large periodic oscillations, which can trigger such complex transient phenomena. It is therefore necessary to employ higher-fidelity tools capable to simulate such complex cases and use the obtained knowledge to improve and calibrate the faster engineering methods. Although there is a strong commercial interest in the design of floating wind farms, the use of simplified engineering tools to predict the aerodynamic performance in the more dynamic conditions encountered in oscillatory rotor motion has not yet been verified in detail. Simple methods may miss the required accuracy to model such complex scenarios. The same also applies to wake modeling, where existing engineering methods do not include the effect of the floater motion. This is the purpose of the present study, where the in-house code MIRAS-HAWC2 has been used to perform fully interactive aero-hydro-servo-elastic simulations of the IEA Wind 15 MW Reference Wind Turbine (RWT)²³ mounted on the WindCrete spar-buoy floater²⁴ for different waves and wind conditions. Moreover, the effect of mean tilt in the development of the wake has been investigated, and a detailed parametric study on the rotor performance and the wake properties in prescribed harmonic motion has been carried out. This generic approach allows for characterization of the flows and generalization for various floater types based on natural frequencies and representative motion amplitudes. The study involved more than 28 different cases, including different combinations of wind speed and floater motion. Only the surge translation and the pitch rotation of the floater have been investigated in detail, since these two degrees of freedom are the most relevant in the response of a floating wind turbine to wind loading. For all simulated cases presented in this manuscript, the MIRAS-HAWC2 predictions are compared to those obtained with the BEM method implemented in HAWC2.

The manuscript is divided in four main sections, excluding the introduction. First, the numerical tools used throughout the investigation are presented in the methodology section. Second, the simulation setup is introduced including a definition of the IEA Wind 15 MW RWT, the WindCrete floater, the DTU controller calibration, the test matrix definition, and the computational setup. The results are presented in four independent sections. First, the simulations of the turbine mounted on the WindCrete floater are presented and analyzed. Second, the investigation of the effect of tilt in the wake development is presented. Finally, the parametric study using a prescribed harmonic motion of the floater is presented for pitch and surge degrees of freedom. Conclusions of the study are drawn in a final section.

2 | METHODOLOGY

In this section, the numerical methods involved in the simulations of the present work are introduced. First, details of the vortex solver MIRAS are given in Section 2.1. The integration of the aerodynamic and wake models of MIRAS with the multi-body finite-element solver HAWC2 is then described in Section 2.2. This allowed to account for the rest of the main physics involved in floating wind turbines, namely, the structural dynamics, the actuation of the wind turbine controller, and the effects of the hydrodynamics and the mooring system.

2.1 | MIRAS vortex solver

The in-house vortex code MIRAS,²⁵⁻²⁸ i.e., Method for Interactive Rotor Aerodynamic Simulations, has been the main solver employed to model the rotor aerodynamics and the flow. MIRAS is a multi-fidelity aerodynamic tool for wind turbine and wake analyses. In the herein presented research, the LL module is used as aerodynamic model, while the hybrid filament-particle-mesh method is used to model the flow.

In the LL method, the rotor blades are modeled as discrete filaments, which account for the bound vortex strength and act by releasing vorticity into the flow. This vorticity can be subdivided into trailing vorticity, which is related to span-wise variations of the bound vorticity and shed vorticity, related to time variations of the bound vortex. The bound vortex strength, Γ , is calculated applying the Kutta-Joukowski theorem at the different span-wise stations along the blade as follows:

$$\Gamma = \frac{L}{\rho V_{qc}}, \quad (1)$$

where \underline{L} is the lift force of each aerodynamic section, obtained by interpolation in a set of tabulated airfoil data (C_l, C_d, C_m) as function of the computed angle of attack. Such two-dimensional (or 3D-corrected) airfoil data are the same as the one used in BEM models, making the comparison between such different fidelity tools very straight forward. ρ is the air density at a given temperature, and V_{qc} is the total velocity at the quarter chord of the different blade sections, calculated as follows:

$$\underline{V}_{qc} = \underline{V}_0 + \underline{V}_b + \underline{u}_w + \Delta \underline{u}^b, \quad (2)$$

where \underline{V}_0 is the inflow velocity, \underline{V}_b is the blade motion, \underline{u}_w is the wake induced velocity, and $\Delta \underline{u}^b$ accounts for a bound vortex correction applied to curved blade geometries and detailed in Ramos-García et al.²⁹

Øye's dynamic stall model³⁰ is used to account for the delay in the stall mechanisms due to dynamic inflow changes seen by the airfoils. Moreover, an additional non-circulatory contribution to the computed C_l and C_m ³¹ is included to account for the correct unsteady lift and blade pitch moment in dynamic attached flow. These corrections depend only on the instantaneous acceleration and velocity of the airfoil motion and account for the missing torsional damping incurred when computing the airfoil characteristics at the quarter chord.

$$C_l = C_l + \frac{0.50 c \pi \dot{\alpha}}{V_{qc}}, \quad C_m = C_m + \frac{0.25 c \pi \dot{\alpha}}{V_{qc}}, \quad (3)$$

where $\dot{\alpha}$ is the torsional rate. These non-circulatory terms have been found key throughout the investigation for the simulation of floating turbine in above-rated conditions. A violent torsional instability was observed when the corrections were neglected.

The initial sheet of vortex filaments is transformed into a set of vortex particles which vorticity is later on interpolated into an auxiliary Cartesian mesh. The downstream location of the filament to particle transformation depends on type of case we want to simulate. In this case, due to the aero-elastic nature of the problem and the necessity of small time steps, only one row of vortex filaments has been used. A study on the influence of this distance in a hybrid filament-mesh was previously published in Ramos-García et al.²⁷ The motion of the vortex elements is determined by the velocity of their markers $\underline{u}(\underline{x}_i)$ (filaments endpoints or the particles itself), which is calculated by a superposition of the free-stream velocity \underline{V}_0 and the velocity contributions from all vortex and boundary elements at the marker positions \underline{x}_i ,

$$\frac{d\underline{x}_i}{dt} = \underline{u}(\underline{x}_i) \quad \text{with} \quad \underline{u}(\underline{x}_i) = \underline{V}_0 + \underline{u}_\Gamma(\underline{x}_i) + \underline{u}_{tw}(\underline{x}_i) + \underline{u}_{pw}(\underline{x}_i), \quad (4)$$

where \underline{u}_Γ is the velocity induced by the blade bound vortex, \underline{u}_{tw} is the velocity induced by the filament wake, and \underline{u}_{pw} is the velocity induced by the particle wake, in which the Poisson equation is solved by a high-order regularization method introduced by Hejlesen et al.³² A detailed explanation of the different velocity contributions of Equation 4 and a study on the choice of the time-integration scheme was presented in Ramos-García et al.^{27,28}

The vorticity equation, curl of the Navier-Stokes equation, is used to account for stretching and diffusion of the vortex structures. It describes the evolution of the vorticity of a fluid particle as it moves with the flow, and assuming an incompressible fluid with a constant and uniform viscosity reads

$$\frac{D\underline{\omega}}{Dt} = \frac{\partial \underline{\omega}}{\partial t} + (\underline{u} \cdot \nabla) \underline{\omega} = (\underline{\omega} \cdot \nabla) \underline{u} + \nu \nabla^2 \underline{\omega}. \quad (5)$$

The left-hand side of the equation characterizes the rate of change of the vorticity, including the unsteady term, $\frac{\partial \underline{\omega}}{\partial t}$, and the convection term, $(\underline{u} \cdot \nabla) \underline{\omega}$, which accounts for the changes in vorticity due to the motion of the fluid particle. On the right-hand side, $(\underline{\omega} \cdot \nabla) \underline{u}$ accounts for the vortex stretching and $\nu \nabla^2 \underline{\omega}$ for the vortex diffusion due to viscous effects.

2.2 | Coupled simulations

In order to model the complex environment that a floating wind turbine is subjected to, the inclusion of different physics is required. Together with the rotor aerodynamics modeled with MIRAS (Section 2.1), the effects of the control actuation, the hydrodynamic loading, and the structural response were considered in the present work. This led to a coupled multi-physics problem, which is often referred to as aero-servo-hydro-elasticity in the literature. This problem was handled by the multi-body finite-element software HAWC2.³³ The framework that HAWC2 uses for the solution of the aero-servo-hydro-elasticity problem relies on an augmented form of the floating frame of reference (FFR) formulation (see for instance Shabana³⁴). In FFR, the kinematics of every flexible body is described in a coordinate system which translates and rotates relative to an

inertial system. In this way, each of the flexible components of the models developed within the present work was characterized by two complementary discretizations. On one hand, a set of linear isotropic Timoshenko beam elements was defined. On the other hand, an arbitrary number of bodies was also specified along the component. Those bodies were connected through a set of constraints that allowed to capture the geometrical non-linearities of the structural response under the presence of the aerodynamic loading, the hydrodynamic loading, and the control actuation. At every time step, HAWC2 solved the constrained equation of motion in order to obtain the corresponding generalized coordinates. This solution was performed iteratively, based on a predictor/corrector approach, resulting in a strong coupling between the different physics involved. A Newmark-beta scheme was used for the time-integration.³⁵

Figure 1 illustrates the integration of the MIRAS solver into the HAWC2 *aero-servo-elastic* solution, together with the rest of the physical models concerned by the present work. The aforementioned integration was done through an external Python code: the *DTU coupling*. This outer layer accessed the instances of MIRAS and HAWC2 codes, compiled as shared objects for this purpose. The *DTU coupling* orchestrated the execution of both solvers and managed the transfer of the wind turbine kinematics predicted by HAWC2 and the aerodynamic loads computed by MIRAS. MIRAS loads could then be injected into the built-in *aerodynamic model* of HAWC2, thus replacing the originally computed BEM loads. This allowed to re-use the already existing routines for loads interpolation and the aeroelastic solution of HAWC2, thus simplifying the implementation of the coupling. It should be remarked that the replacement of BEM blade loads by MIRAS loads occurred only once per time step, resulting in a loose aeroelastic coupling for this particular case. The reader is referred to Ramos-García²⁹ for more information regarding the aeroelastic coupling between MIRAS and HAWC2 and for a detailed comparison against in-house fully resolved FSI (Fluid Structure Interaction) simulations and other aeroelastic tools used in the framework of the OC3 and OC4 projects.^{36–38} This type of simulations are labeled in the present work as MIRAS-HAWC2, MIRAS, or simply LL.

Alternatively, the injection of the MIRAS blade loads could be switched off, so that pure BEM simulations could be made for comparison purposes. That type of computations are referred to in this document as HAWC2-BEM, HAWC2, or simply BEM. While BEM is considered a step-down in terms of modeling fidelity with regards to MIRAS, the implementation of the former approach in HAWC2 features several enhancements in order to increase its range of applicability. Those features include a modification to account for the wake expansion and swirl and extended models to handle: dynamic inflow, skewed inflow, shear effect on induction, the effect from large blade deflections, tip loss, and dynamic stall. In the present study, the dynamic stall model of Leishman and Beddoes³⁹ has been employed. The reader is referred to the recent publication of Madsen et al⁴⁰ for more details regarding the BEM implementation of HAWC2. Moreover, it has been found critical to include the effect of rotor motion for the yaw/tilt correction and the dynamic inflow time constants in BEM. It is important to note that during the course of this study, we

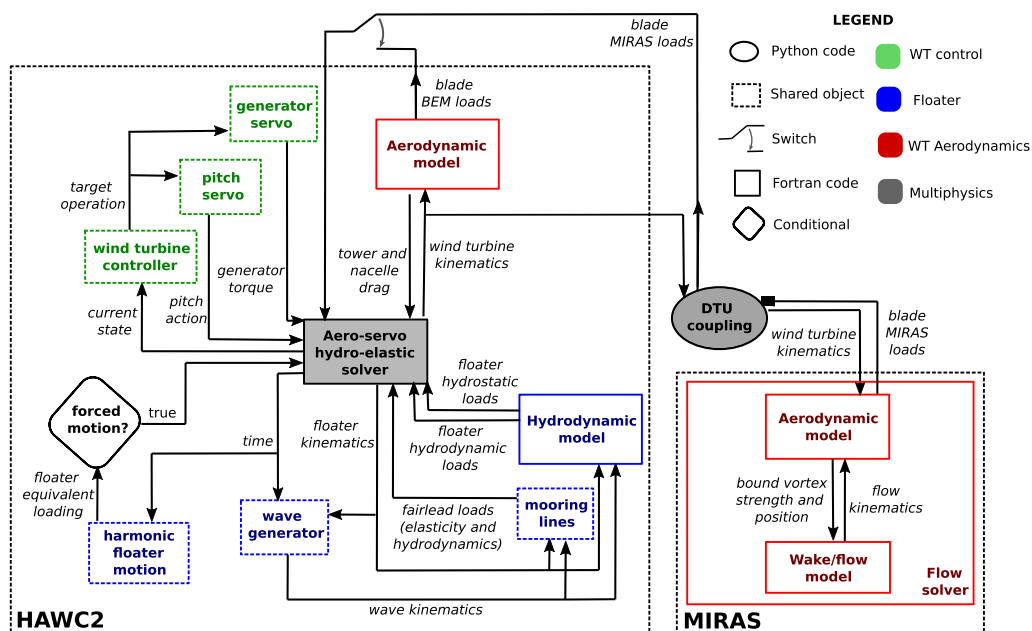


FIGURE 1 Sketch of the different components involved in the simulations [Colour figure can be viewed at wileyonlinelibrary.com]

have seen large differences between MIRAS-HAWC2 and HAWC2-BEM when not using such corrections, especially at high frequencies of the pitch and surge floater motions.

The rest of the physical models involved in the coupled simulations were introduced making use of the standard capabilities of HAWC2. The built-in *hydrodynamic model*, relying on linear wave kinematics from a *wave generator* and the Morison equation,⁴¹ was used to account for the hydrodynamic loads on the floating substructure. This platform also received a set of fair-leads loads coming from a *mooring line model*. This model consisted on a series of elastic bars under the action of hydrodynamic loads and was coded as an external library. As described in Section 3.5, some configurations studied in the present work analyzed particular sea states or floating platform behaviors. Therefore, in some computations, the response of the moored floating wind turbine to wind and wave loads was calculated. In other simulations, the hydrodynamic and mooring modules were disabled, and the motion of the floating platform in different degrees of freedom was forced. This was achieved through the action of an external library, labeled here as *harmonic floater motion*, that computed a set of equivalent concentrated loads to achieve the desired forced motion. The wind turbine control was also handled by a stand alone shared object (*wind turbine controller*), corresponding to the basic implementation of the DTU Wind Energy Controller.⁴² The transformation of the controller output into a new collective blade pitch and a generator torque was steered by two additional libraries, labeled in this document as *pitch servo* and *generator servo*.

3 | CHOICE OF SIMULATION CASES

This section describes cases of study presented, including the IEA Wind 15 MW RWT turbine, the WindCrete spar-buoy floating platform, the DTU Wind Energy Controller (WEC) calibration, and the prescribed floater motion.

3.1 | IEA Wind 15 MW Reference Wind Turbine

The wind turbine chosen for this investigation is the recently released IEA Wind 15 MW RWT, especially designed for offshore applications and extensively described in Gaertner et al.²³ Some key figures are given in Table 1.

3.2 | WindCrete

WindCrete is a monolithic concrete spar-buoy that includes the tower and the floater in a continuous single piece. The advantage of such monolithic construction is the absence of joints between the tower and the floater, which leads to an increased fatigue resistance. The tower is a truncated cone with a constant thickness of 0.4 m and a height of 129.495 m resulting in a hub height of 135 m. A tapered transition piece connects the tower to a cylindrical spar with a diameter of 18.6 m and a length of 135.7 m. The bottom of the spar buoy is closed by a hemisphere of the same diameter. The total draft of the WindCrete is 155 m, and the total mass is $3.9805 \cdot 10^7$ kg including ballast. The main dimensions of the WindCrete are summarized in Figure 2, where the different DoF are also sketched. The station keeping system consists of three single crowfoot catenary mooring lines with 120° spacing. The rigid-body natural frequencies of the WindCrete floater with the IEA Wind 15 MW turbine are presented in Table 2, and more details about the floater can be found at Mahfouz et al.²⁴ and Vigara et al.⁴³

The structural modeling of WindCrete is based on the multibody formulation of HAWC2 where the structure is an assembly of bodies and each body is an assembly of Timoshenko beam elements. The hydrodynamic loads are based on the Morison equation that is suitable for slender

TABLE 1 Key figures for the IEA Wind 15 MW Reference Wind Turbine²³

| Parameter | Value |
|--|----------------|
| Rated power | 15 MW |
| Rated wind speed | 10.59 m/s |
| Turbine class | IEC Class 1B |
| Rotor diameter | 240 m |
| Design tip-speed ratio | 9.0 |
| Rotor speed range | 5.00–7.56 rpm |
| 3P excitation range | 0.250–0.378 Hz |
| First blade flapwise natural frequency | 0.555 Hz |
| First blade edgewise natural frequency | 0.642 Hz |

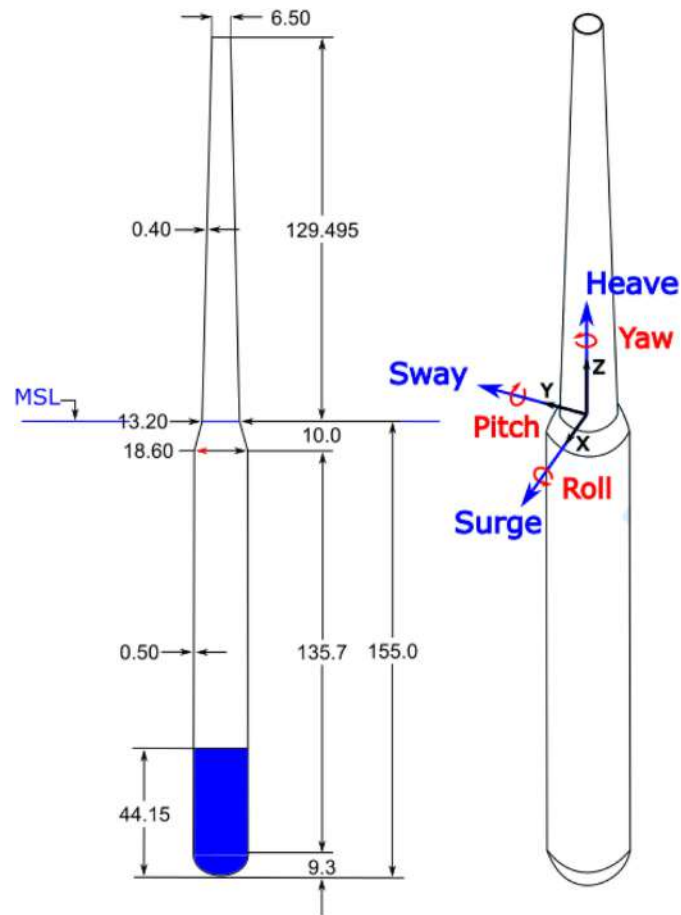


FIGURE 2 WindCrete Sketch with dimensions in meters²⁴ [Colour figure can be viewed at [wileyonlinelibrary.com](https://onlinelibrary.wiley.com)]

structures. The buoyancy loads calculation is based on the integration of the external water pressure on the submerged body. The mooring lines are modeled by a dynamic modeling approach using a general cable element formulation that includes hydrodynamic drag and buoyancy forces. In the paper, the herein presented floating wind turbine is compared against a fixed machine, in which the motion of the floater is eliminated. Practically, the floater has been clamped at the tower interface in the HAWC2 structural solver. This configuration is referred throughout the paper as a bottom-fixed turbine.

3.3 | DTU controller calibration

The HAWC2 model of WindCrete uses the DTU Wind Energy Controller.⁴² Using an onshore controller on a floating wind turbine can lead to blade pitch instability for above rated wind speeds. Such instability is directly related to the coupling of the tower motion and the blade pitch control.⁴⁴ Therefore, the controller was tuned using HAWCStab2 Version 2.16a.⁴⁵ The assumed partial-load poles (torque controller) were set to a natural frequency of 0.05 Hz, with 70% critical damping. The full-load poles (blade pitch controller) were set to 0.011 Hz natural frequency (half the floater's pitch frequency) and 70% critical damping. The control strategy combines constant power (90%) and constant torque (10 %); therefore, a linear interpolation between them is used to compute the generator torque limits. Such control strategy causes small variations in power in above rated wind conditions. The stability of the WindCrete with the new controller settings was first confirmed by doing a HAWC2 step-wind

TABLE 2 Rigid-body natural frequencies of the WindCrete floater, mounting the IEA Wind 15 MW wind turbine²⁴

| Degree of freedom | Natural frequency [Hz] |
|-------------------|------------------------|
| Surge | 0.01221 |
| Heave | 0.03052 |
| Pitch | 0.02441 |
| Yaw | 0.09155 |

test and simulations with steady wind above rated wind speed. The allowed max low-pass filtered tower top acceleration was increased in order to avoid shut down during the initial transient where the turbine undergoes large accelerations in the forced prescribed motion cases described in the following.

3.4 | Prescribed floater motion

The aerodynamic behavior of floating wind turbines is generally more complex than for bottom-fixed machines, mainly because the rotor experiences a significant motion due to the floating support structure and its interaction with the waves. From an aerodynamic point of view, the most relevant floater motions are those that result in an oscillation of the rotor in the direction of the wind. Assuming no misalignment, those motions correspond to the angular displacement of the platform referred to as *pitch* and to its translatory displacement in *surge*.

To investigate the effects of the floater motion on the rotor aerodynamics, parametric studies were carried out for pitch and surge. For each of these two DoFs, the displacement of the floater was prescribed as a sinusoidal function with user-defined amplitude and frequency. In the prescribed surge cases, the entire system translates back-and-forth along the X axis (see Figure 2), whereas in the prescribed pitch cases, it rotates around the point of flotation, located at the mean water level. We note that the instantaneous center of rotation of the structure is located below water, due to the very low center of mass of spar-buoy floaters. The choice of the present coordinate system, however, is common practice when modeling floating wind turbines.

The amplitude and frequencies of the two parametric studies have been chosen to cover a representative range of the pitch and surge motion of a floating wind turbine. In this way, the investigation can be generalized beyond the spar-buoy floater. For pitch (Table 3), the frequency study is carried out at 0.01419, 0.02838, 0.05676, and 0.11352 Hz with a pitch amplitude of 6.38°. The first two frequencies are representative of the surge and pitch natural frequency of floating platforms, whereas the last two frequencies represent wave peak frequencies in storm and normal conditions. Moreover, an amplitude study was performed for 3.19°, 6.38°, and 12.7° with a frequency of 0.02441 Hz, which is the pitch natural frequency of the WindCrete floater (see Table 2). Here, the first amplitude is representative of strong motion under turbine operation, while the two next are stronger cases, selected to study the amplitude effect beyond normal operation.

For surge (Table 4), the frequency study was carried out for the same frequencies as the pitch study and an amplitude of 15 m. The amplitude study includes surge amplitudes of 5, 10, and 15 m at a frequency of 0.01419 Hz, which is close to the surge natural frequency for the WindCrete platform (see Table 2). The surge amplitude of 5 m is representative of motion in operation, while the 10 and 15 m amplitudes can be regarded as extreme cases, selected to enhance the motion effects.

All the cases with prescribed floater motion were simulated in below- and above-rated wind conditions, i.e. 8 m/s (tip-speed ratio $\lambda = 9.0$) and 15 m/s ($\lambda = 6.33$), respectively. The given λ values are for steady conditions, as the use of an active torque control makes the tip speed ratio change in time.

3.5 | Computational setup

In the present study, we have used the knowledge obtained from earlier discretization studies performed with MIRAS, for example, in Ramos-García et al.,^{25,27} in order to define the blade discretization. MIRAS-LL simulations employ a bound vortex discretized with 40 straight segments following a cosinus distribution, where the root and the tip region have a higher point density. The influence of the HAWC2 structural model fidelity of the blade on the response, loads, and stability of large turbines has been analyzed in Gözcü and Verelst.⁴⁶ A $28R \times 4R \times 4R$ Cartesian mesh has been employed in all cases, with a constant spacing of 3 m in the x, y, and z directions which adds up to a total of approximately 29 million cells. This cell size has been chosen to be equal to the one used to resolve the wake behind the complex multi-rotor turbine in van der Laan.⁴⁷ In that paper, the wake behind the Vestas multi-rotor concept was simulated and compared by different fidelity numerical models, including the MIRAS-FLEX5 coupling. The MIRAS-FLEX5 simulations used the same hybrid filament-particle-mesh solver as the present one obtaining a good agreement with the predictions of EllipSys3D LES-AL-FLEX5 for both mean velocities and turbulent intensity in the near and the far wake. A generally good agreement was also obtained with experimental short-range WindScanners data. The turbine hub is located at a position of 1.125R

TABLE 3 Test matrix for the prescribed harmonic pitch motion

| | Floater pitch frequency [Hz] | Floater pitch period [s] | Floater pitch amplitude [deg] |
|-----------------|------------------------------|--------------------------|-------------------------------|
| | 0.01419 | 70.472 | |
| Frequency study | 0.02838 | 35.236 | 6.38 |
| | 0.05676 | 17.618 | |
| | 0.11352 | 8.809 | |
| | | | 3.19 |
| Amplitude study | 0.02441 | 40.967 | 6.38 |
| | | | 12.7 |

TABLE 4 Test matrix for the prescribed harmonic surge motion

| | Floater surge frequency [Hz] | Floater surge period [s] | Floater surge amplitude [m] |
|-----------------|------------------------------|--------------------------|-----------------------------|
| | 0.01419 | 70.472 | |
| Frequency study | 0.02838 | 35.236 | 15 |
| | 0.05676 | 17.618 | |
| | 0.11352 | 8.809 | |
| | | | 5 |
| Amplitude study | 0.01419 | 70.472 | 10 |
| | | | 15 |

from the water level. So the distance from the ground to the blade tip when pointing straight down is 15m. All simulations have been carried out for 1,400 s of simulated time with a time step size of 0.025 s, which results in 56,000 time steps. Note that the chosen time step gives an azimuthal discretization under normal turbine operation of 0.8° to 1.1° , depending on the tip speed ratio. This means that approximately 450 time steps per revolution are simulated in below rated conditions while 330 time steps per revolution are simulated in the above-rated cases. In the extreme cases, where large instabilities are encountered, the time step is reduced by a factor of 2 to 0.0125 s. This temporal discretization is usually employed in HAWC2 stability analysis, giving accurate results even for the most dynamic load cases and instability studies as in Volk et al.⁴⁸ Each MIRAS simulation uses two-hundred 2.8 GHz processors on a Linux cluster, with an approximate computational time per case of 50 h. A free boundary condition is used in all directions but the ground plane, where a no-through condition is used.²⁹ An eight-order stencil is used to spatially discretize the vorticity equation. Moreover, a particle re-meshing every time step is used to maintain a smooth field, which is forced to remain divergence free by applying a periodic re-projection of the vorticity. The flow has been extracted every time step in 22 planes perpendicular to the flow direction (YZplanes), from 1R upstream to 20R downstream the rotor plane. Moreover, a single XZ plane is extracted. This plane contains the stream-wise direction and the height and is located at the rotor center. For reducing the necessary storage space, such planes are defined using 64×64 cells with a constant spacing and are written out as binary files. This means that in the YZ plane, the velocity extraction mesh is 2.5 times coarser than the computational mesh and in the XZ plane, the extraction mesh is 17.5 times coarser. Moreover, unless stated otherwise, only the last 700 s of the simulated time are used for the flow analysis, disregarding the first 700 s in order to avoid transients.

4 | SIMULATIONS OF THE IEA WIND 15 MW RWT MOUNTED ON THE WINDCRETE

An initial comparison between the HAWC2 standalone and the MIRAS-HAWC2 solvers is carried as a check of the aero-hydro-servo-elastic coupling. Three cases for the operating turbine are taken into account, in increasing degree of complexity: bottom-fixed turbine, floating turbine without waves, and floating turbine with waves. First, a comparative study between the solvers predictions of rotor integral and blade distributed quantities is carried out in what follows. Second, a comparison between the wake generated by a fixed and a floating turbine is presented. Note that all cases analyzed use the controller calibration described in Section 3.3.

4.1 | Turbine performance analysis.

Figure 3 depicts the mean in-plane and out-of-plane forces, F_x and F_y , respectively, and their standard deviation over the last 300 s of simulated time for winds speeds of 8 and 15 m/s, with tip-speed ratio of $\lambda = 9.0$ and 6.33, respectively. An excellent agreement is observed regarding the

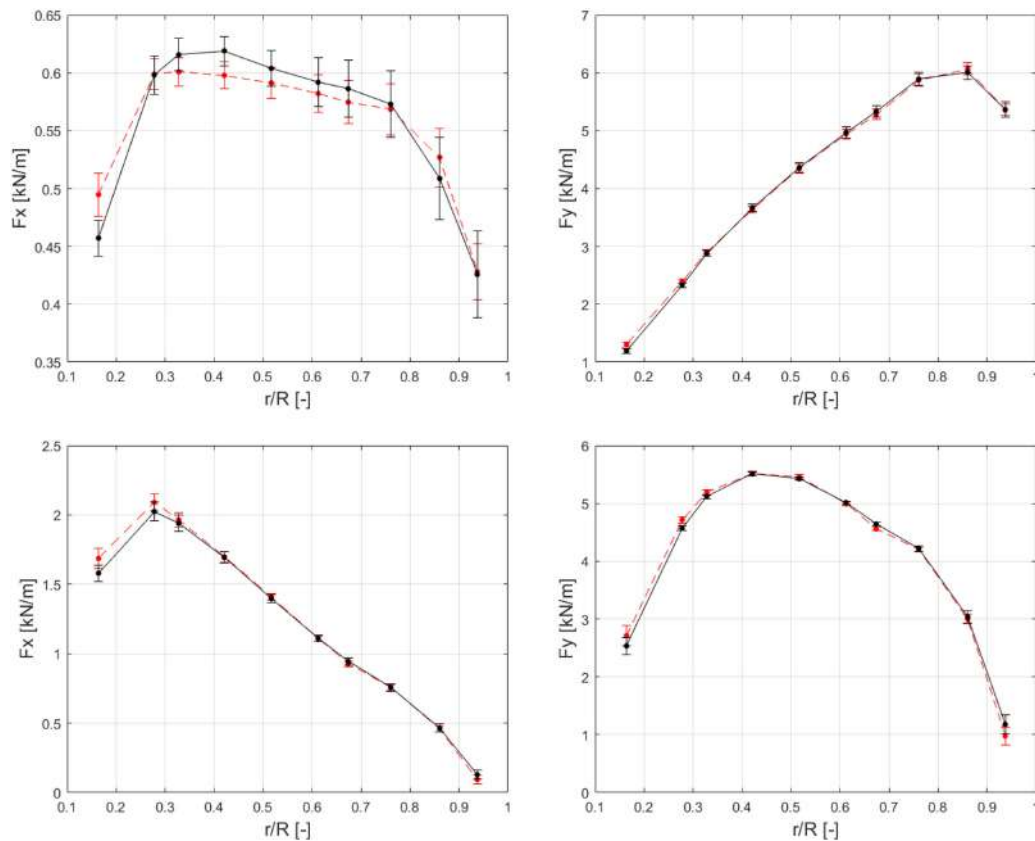


FIGURE 3 Mean and standard deviation of the in-plane and out-of-plane forces on blade one for the bottom-fixed IEA Wind 15 MW RWT. HAWC2-BEM in dashed red lines and MIRAS-HAWC2 in solid black lines (top, 8 m/s; bottom, 15 m/s) [Colour figure can be viewed at wileyonlinelibrary.com]

out-of-plane force distribution in below-rated wind conditions, although larger relative differences appear in the in-plane component, especially around the root and mid-span regions. It is also remarkable that the LL method predicts a larger standard deviation of the loading in the tip vicinity. This is most probably related to the ground modeling in MIRAS, which is not accounted for in the lower fidelity solver. The proximity of the ground when the tip of the blades is pointing downwards creates a variation in the loading due to a ground effect. This has been confirmed by performing a simulation where the ground is not taken into account which shows a lower standard deviation of the loading. At 15 m/s, differences between the codes predictions of the in-plane force component are drastically reduced, while a good agreement is maintained for the out-of-plane one.

In terms of rotor performance predictions for the bottom-fixed IEA Wind 15 MW RWT, the BEM method under-predicts the mean power by a 1.4 %, while an excellent agreement is obtained for the thrust force at a wind speed of 8 m/s. At a wind speed of 15 m/s, differences in thrust and power between the codes are reduced to less than 0.1 %.

A comparison of the HAWC2-BEM and MIRAS-HAWC2 predicted forces and displacements in below-rated conditions without waves are shown in Figure 4. For clarity, only the last 700 s are depicted. A really good agreement is obtained between the codes in terms of the power and thrust variation in time. In general, the BEM method consistently under-predicts the mechanical power by less than 0.5% and slightly over-predicts the mean thrust force. Regarding the tower-top side-side (state pos x) and fore-aft (state pos y) displacements, there is a very small under-prediction of the first one and an over-prediction of the latter one by the BEM method probably related to the difference in thrust and aerodynamic damping.

At a wind speed of 15 m/s, Figure 5, differences in the time signals predicted by the solvers increase, although the computed mean values of all investigated quantities remain very similar. In this case, HAWC2-BEM consistently under-predicts both loads and displacements. Looking at

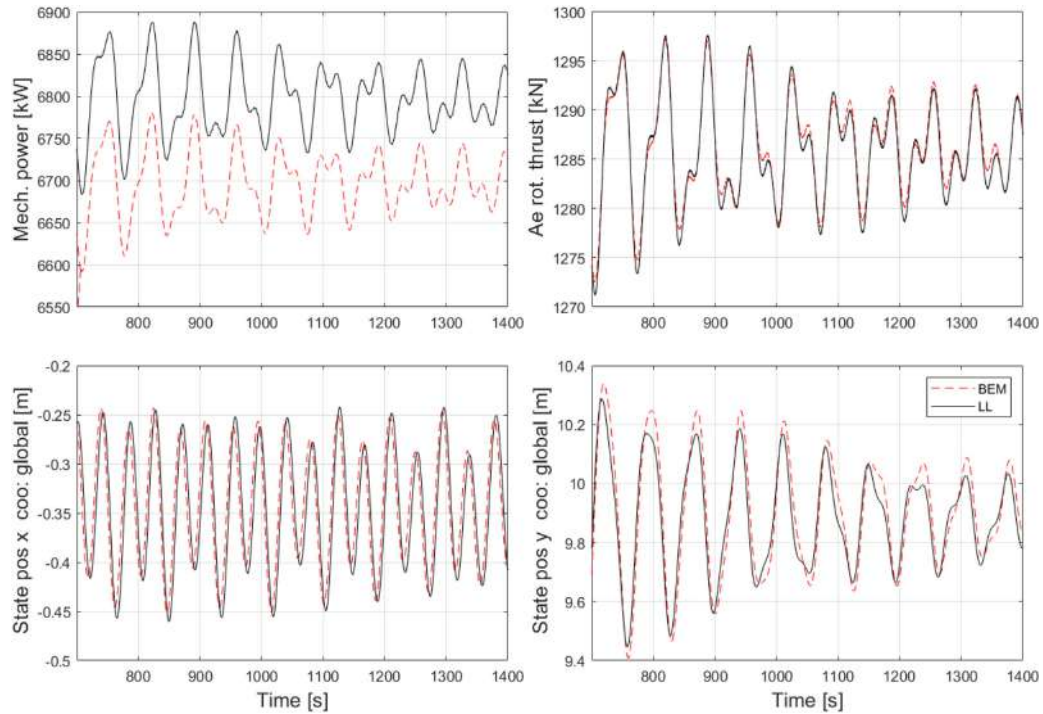


FIGURE 4 Floating IEA Wind 15 MW RWT mounted on the WindCrete platform without waves, comparison between BEM and LL simulations (8 m/s wind speed) [Colour figure can be viewed at wileyonlinelibrary.com]

the spectral distribution of the thrust signal, Figure 6, there are some notable differences. The higher aerodynamic loads predicted by MIRAS leads to a dynamic behavior where the blade loading is more important in the overall turbine behavior, with the most important aerodynamic frequencies related to the blade passing, i.e., 3P and 6P, showing up in the spectral analysis of the thrust force. This frequencies are not clearly observed in the BEM simulations. In BEM, the power spectra density is dominated by the low frequency motion of the platform, over-predicting the peak value at the surge natural frequency of the floater (0.014 Hz) and under-predicting the pitch peak value (0.021 Hz).

A further comparison between the codes is carried out for multiple cases where regular waves are taken into consideration. The results obtained in below-rated conditions for the cases with 2 and 6 m Airy waves, with periods of 6 and 10 s, respectively, exhibited an excellent agreement between the codes (figures not included for the sake of brevity). However, a different picture is seen once the wind speed is increased to 15 m/s, as can be appreciated in Figure 7 where the turbine is subject to 2 m waves with a 6 s period. Differences between BEM and LL predictions increase considerably, with the BEM method predicting larger extreme loads, in terms of both the minimum and maximum values of thrust and power. This could be related to the different aerodynamic damping predicted by the codes since the system response at the floater natural frequencies is very sensitive to it. Moreover, the turbine undergoes larger oscillations in the BEM simulations, particularly in the fore-aft direction (state pos y), where the BEM method over-predicts the maximum amplitude of the motion by more than a 50% compared to the LL values. In general, it has been found that differences between BEM and LL simulations are more sensitive to variations in the motion frequency than in its amplitude, with BEM predictions deviating considerably from the LL predictions at high wave frequencies.

A spectral analysis of the thrust signal has been carried out to gain a better insight into the cases with regular waves at high wind speeds. As expected, the more distinct peak in the frequency domain appears exactly at the wave frequency, i.e., 0.16 and 0.10 Hz for the 2 and 6 m wave case, respectively. However, a striking difference between the codes is that the BEM simulations have a peak at the surge natural frequency, approximately at 0.014 Hz for the 2 m wave case, as can be seen in Figure 8 left. Since the wind is steady, and the wave is regular and at a frequency far from the surge natural one, there should be no load excitation, and the peak has to be due to a transient. It shows more in the BEM case since there is less aerodynamic damping and the transient survives for a longer time. An overall good agreement between the codes is obtained for the case with 6 m regular waves except for the low frequency range, as seen in Figure 8 right.

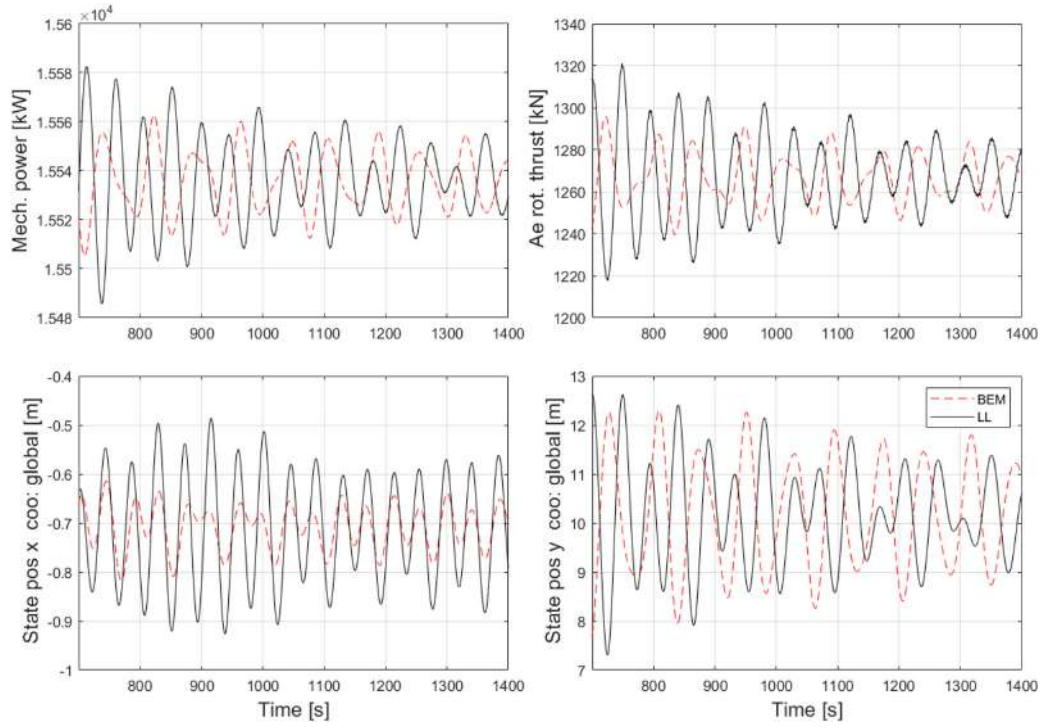


FIGURE 5 Floating IEA Wind 15 MW RWT mounted on the WindCrete platform without waves, comparison between BEM and LL simulations (15 m/s wind speed) [Colour figure can be viewed at wileyonlinelibrary.com]

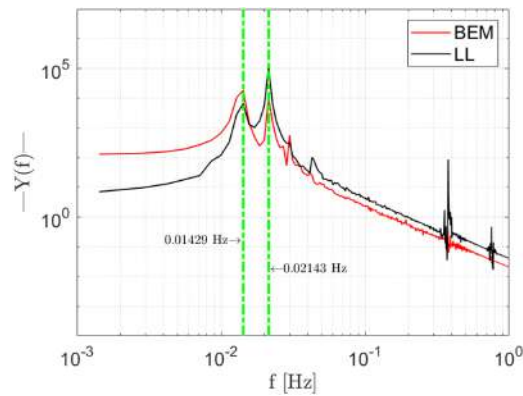


FIGURE 6 Spectral analysis of the thrust signal predicted for the floating IEA Wind 15 MW RWT mounted on the WindCrete platform without waves. Comparison between BEM and LL simulations (15 m/s case) [Colour figure can be viewed at wileyonlinelibrary.com]

4.2 | Wake analysis

A comparison of the wakes generated by the bottom-fixed and the floating IEA Wind 15 MW RWT in below-rated conditions is presented in what follows. A low wind speed case is selected because it features the largest differences between the wakes. At 8 m/s, the turbine is operating at an

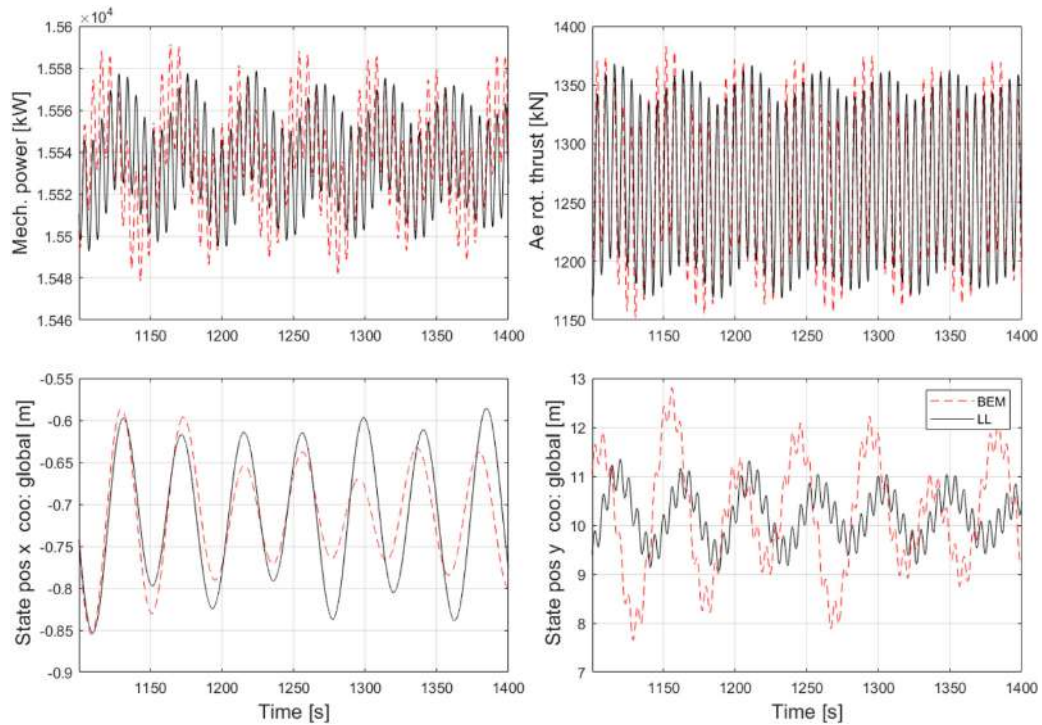


FIGURE 7 Floating IEA Wind 15 MW RWT mounted on the WindCrete platform and subject to regular waves with 2 m height and period of 6 s. Comparison between BEM and LL simulations (15 m/s case) [Colour figure can be viewed at wileyonlinelibrary.com]

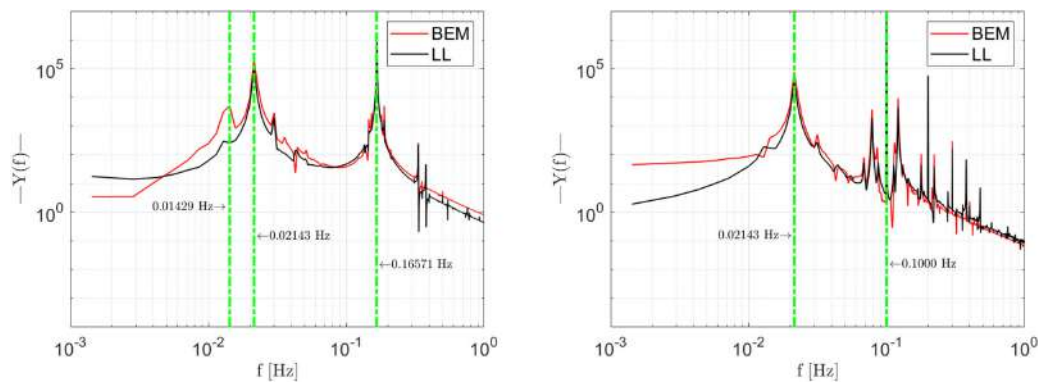


FIGURE 8 Spectral analysis of the thrust signal predicted for the floating IEA Wind 15 MW RWT mounted on the WindCrete platform and subject to regular waves with (left) 2 m height and period of 6 s and (right) 6 m height and period of 10 s. Comparison between BEM and LL simulations (15 m/s case) [Colour figure can be viewed at wileyonlinelibrary.com]

optimal tip speed ratio for extracting maximum power. Note that only small differences have been observed when comparing the wake of the floating cases with and without waves (for the considered cases) and, therefore, such comparison is not presented here.

Figure 9 shows stream-wise velocity and turbulence intensity contours at multiple downstream locations, i.e., 2, 4, 6, 10, 14, 16, 18, and 20R downstream the rotor plane. The wake generated by a bottom-fixed turbine with a non-turbulent inflow, depicted in the top sub-figures, remains

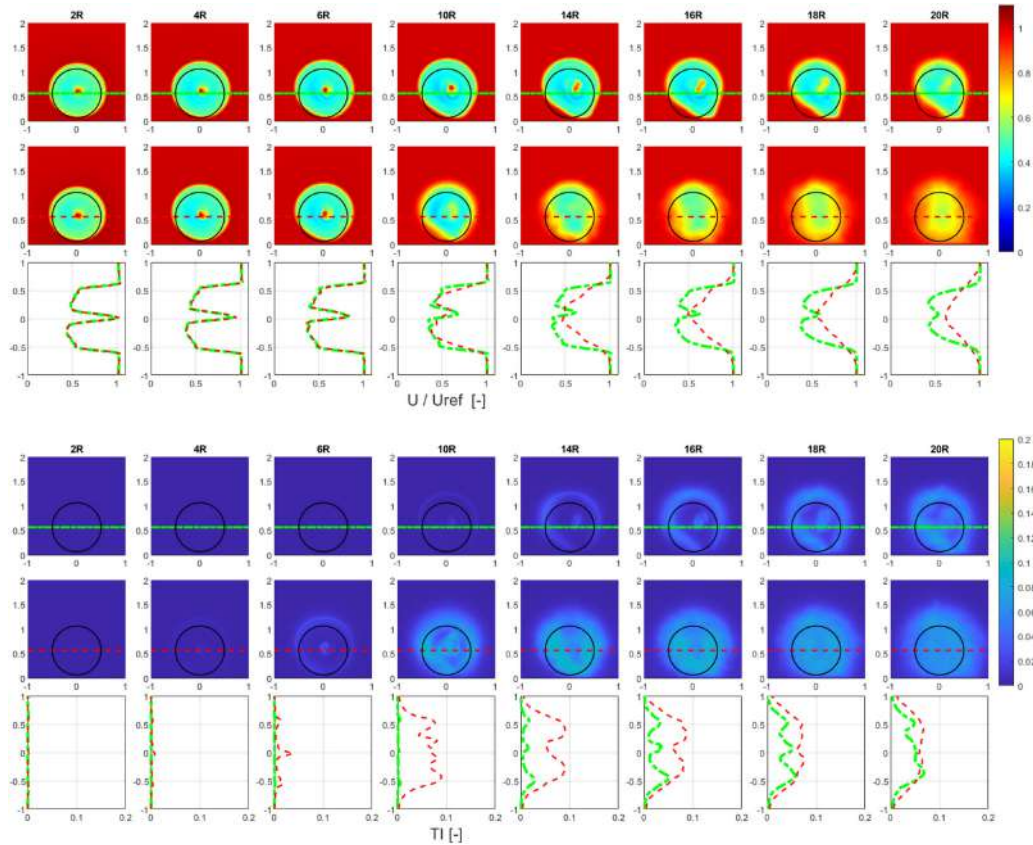


FIGURE 9 Comparison between the (top-figure) mean stream-wise velocity and (bottom-figure) turbulent intensity in the wakes generated by the bottom-fixed and the floating IEA Wind 15 MW RWT at different downstream distances from the rotor plane. Mean stream-wise velocity and turbulence intensity contours on multiple YZ planes downstream the rotor plane (top sub-figures) bottom-fixed case and (mid sub-figures) floating case. (bottom sub-figures) profiles along the horizontal marked line drawn at hub height where green represents the bottom fixed case and red depicts the floating one [Colour figure can be viewed at wileyonlinelibrary.com]

undisturbed for a longer distance compared to the one generated by a floating turbine, which is depicted in the mid sub-figures. The later one reaches a Gaussian distribution between 10 to 14 R downstream the rotor plane. However, it is observed that for the wake generated by the bottom-fixed turbine the Gaussian shape is first reached further downstream than 20 R . This can be further explained by looking at the turbulence intensity contours. The floating turbine generates more mixing in the flow, developing a higher turbulence level which helps promoting a faster break down of the strong vortex structures. Note that at far downstream positions the turbulence intensity profile of both wakes becomes very similar. Contrary to what is observed in the present work Kopperstad et al.¹⁹ spar-buoy concept showed a quite similar wake recovery as in the bottom fixed case.

In an effort to define a set of simplified quantities that can describe the wake characteristics, we introduce the wake velocity recovery, Equation 6, and the integrated turbulence intensity, Equation 7. These terms are used throughout the manuscript to characterize the wake in a simple manner. Figure 10 depicts such quantities as function of the downstream distance from the rotor plane for the bottom fixed and the floating cases. Note that the area of integration is defined by the rotor disk excluding the hub region, which is approximately 0.1 R . This figure confirms what was already shown in the previous analysis, the faster recovery of the wake of a floating wind turbine in laminar inflow conditions, which is tied to the higher TI level produced by the motion of the floater. For example, at a distance of 12 R , the wake recovery is increased from 0.47 for the bottom fixed case to 0.56 for the floating case.

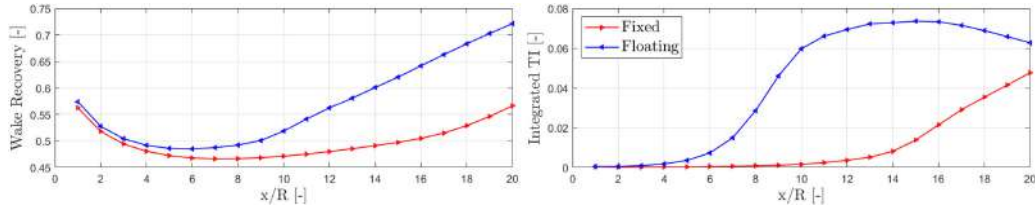


FIGURE 10 Integrated wake quantities for the bottom-fixed and floating IEA Wind 15 MW RWT at a wind speed of 8 m/s. (left) Wake velocity recovery; (right) integrated turbulent intensity [Colour figure can be viewed at wileyonlinelibrary.com]

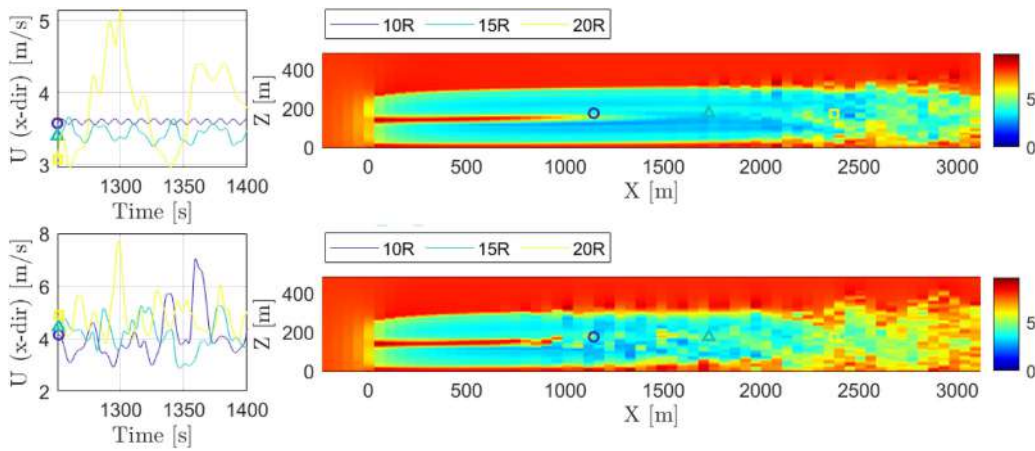


FIGURE 11 (Left) Time variation of the stream-wise velocity at three different downstream locations; (right) instantaneous stream-wise velocity contours on a XZ plane crossing the turbine center at the simulation time of 1,250 s. Comparison between (top) the bottom-fixed and (bottom) the floating IEA Wind 15 MW RWT [Colour figure can be viewed at wileyonlinelibrary.com]

$$\text{Wake Recovery} = \frac{\int_A U dA}{\int_A U_0 dA} \quad (6)$$

$$\text{Integrated TI} = \frac{\int_A TI dA}{A} \quad (7)$$

Figure 11 shows the time variation of the hub height stream-wise velocity for the last 150 s of simulated time at three different downstream locations 10, 15, and 20 R and the instantaneous stream-wise velocity contours in an XZ plane crossing through the center of the rotor at the simulation time of 1,250 s. This figure gives a very good overview of the floater influence in the wake development. Large differences can be seen between the velocity contours of both cases and more especially between the time signals at the 10 and 15 R locations, with pronounced low-frequency oscillations for the floating case.

5 | INVESTIGATION OF THE EFFECT OF MEAN TILT IN THE WAKE DEVELOPMENT

Due to the mean aerodynamic thrust on the rotor, a mean operational pitch angle should usually be considered for floating wind turbines. This results in a larger operating mean tilt angle, when compared to their bottom-fixed counterparts. In order to understand how the mean rotor tilt angle affects the wake development, stream-wise velocity contours for different downstream located YZ planes behind the bottom-fixed IEA Wind 15 MW RWT with 0°, 10°, 15°, and 30° of tilt are presented in Figure 12. From the figure, it is clear that a positive tilt angle, defined with

the rotor facing upwards, deflects the wake towards higher altitudes. This is consistent with the findings of Wise and Bachynski,⁴⁹ who also pointed out the similarity with the well-known horizontal deflection from yaw-misalignment.

It is also very interesting to see how the wake curls up forming a mushroom shape in its cross-sectional cut for large tilt angles, which further helps bending the wake away.

To more easily quantify the wake properties for the different tilt cases, Figure 13 shows the computed wake recovery and the integrated turbulence intensity, computed following Equations 6 and 7. From the figure, it is clear that the larger the tilt angle, the faster the wake recovers. Note that with a tilt angle of 30°, almost 90% of the wake is recovered at the 20R downstream location. We also note that this tilt angle is not realistic for a floating wind turbine, but it is included here for completeness. On top of the upwards motion of the wake, the wake stretching towards a mushroom shape breaks down the cylindrical wake form and promotes its recovery. Differences between the different tilt cases are already notable at the closest downstream station in the plot (1 R), and they increase with the downstream distance. For example at $x/R = 12$, a change from 0° to 10° tilt increases the wake recovery from 0.45 to 0.52. In the far wake, the differences start to decrease. Regarding the integrated TI, it is interesting that the 30° tilt case shows the higher values up to 14 R, after that there is an inversion of the trend and this case has the lowest integrated TI in the far wake. This effect is mostly related to the wake moving away from the integrated area and not to the wake dissipation itself.

6 | INVESTIGATION OF THE EFFECT OF FLOATER HARMONIC MOTION IN PITCH

In order to isolate the aerodynamic effects related to the different DoFs, we first force a prescribed harmonic pitch motion of the floater, which is a very relevant DoF for a floating wind turbine from an aerodynamic point of view. Note that all cases presented use the DTU Wind Energy

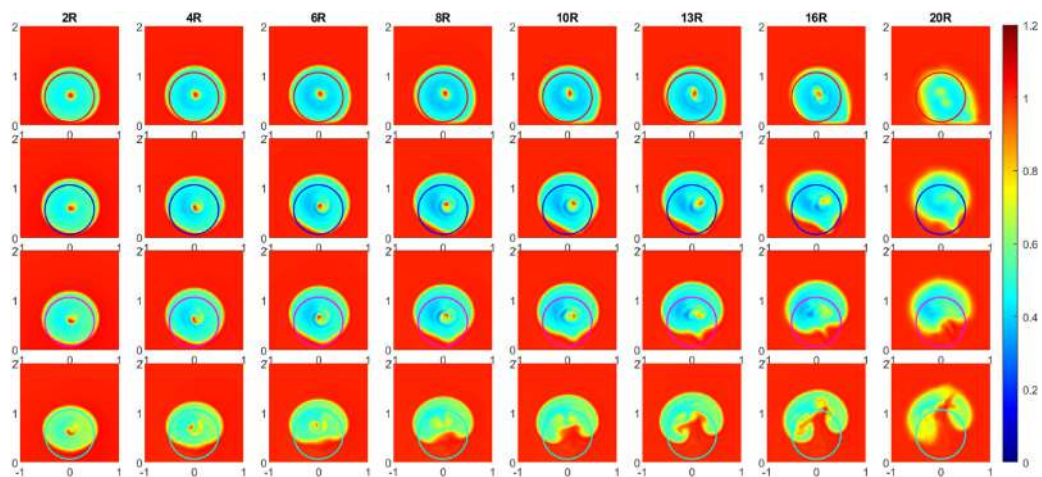


FIGURE 12 Mean stream-wise velocity contours on different YZ planes downstream the rotor plane for the bottom-fixed IEA Wind 15 MW RWT with tilt angles (from top to bottom) 0°, 10°, 15°, and 30° at a wind speed of 8 m/s [Colour figure can be viewed at wileyonlinelibrary.com]

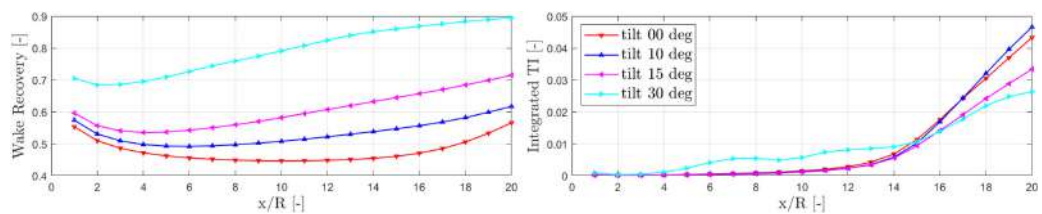


FIGURE 13 Integrated wake quantities for the bottom-fixed IEA Wind 15 MW RWT with 0°, 10°, 15°, and 30° tilt angles at a wind speed of 8 m/s. (Left) Integrated wake velocity recovery; (right) Integrated Turbulent Intensity [Colour figure can be viewed at wileyonlinelibrary.com]

Controller calibrated as described in Section 3.3. All cases are simulated in below- and above-rated conditions, i.e., wind speeds of 8 and 15 m/s, respectively.

The test matrix for the harmonic pitch motion is presented in Table 3. The investigation is divided in five parts. First, a turbine load performance analysis is carried out. Key turbine quantities like rotor rotational speed, blade pitch, mechanical power, and aerodynamic thrust are presented and analyzed for the last pitching cycle of the floater. We have chosen to present the mechanical power at the shaft and not the aerodynamic one since the latter is partially used to accelerate the inertia of the rotor and such contribution is not felt at the shaft. The depicted power is therefore calculated as the shaft moment multiplied by the rotational speed. This study is combined with a qualitative wake analysis where three-dimensional iso-vorticity contours are investigated for six different time instants during the last pitching cycle to cover the complete turbine oscillation, i.e., t_1 , t_2 , t_3 , t_4 , t_5 , and t_6 . Ring distributions of the in-plane and out-of-plane blade forces are shown for selected cases in order to better understand the turbine behavior under such dynamic conditions. Second, a similar study is carried out for the extreme frequency cases. Such cases display a very different turbine behavior compared to the lower frequency ones, and it is therefore for the sake of clarity that they are presented in a different section. Third, an analysis of the different rotor states along the last pitching cycle is carried out in order to further characterize the aerodynamic behavior of a floating turbine. Fourth, a comparative study of the maximum blade root and tower base bending moments for all simulated cases is shown. Fifth and last, a quantitative wake study is performed with focus on the wake recovery.

6.1 | Turbine behavior and iso-vorticity comparison in pitch

The variation of key turbine quantities over the last pitching cycle for three different frequencies in below-rated conditions is presented in Figure 14. MIRAS-HAWC2 results are compared to the standalone HAWC2 simulations with the in-built BEM aerodynamic module. The BEM solver tends to under-predict the maximum attained power and thrust for the low and mid frequency cases. Such maximum values appear in the second half of the forward motion of the floater as it enters negative floater pitch values. For example, at the frequency of 0.01419 Hz, the power is under-predicted by approximately a 10%. However, a different trend is observed for the 0.05676 Hz case. For this case, the pitch control is active in the last half of the forward motion and beginning of the backwards one which could explain the change in tendency. Regarding the minimum loading region, there is a general tendency for the BEM method to slightly under-predict the thrust during the first part of the backwards motion, $\approx t_6 - t_1$, and considerably over-predict it during the second part, $\approx t_1 - t_2$. It is in this region where the relative error between the code

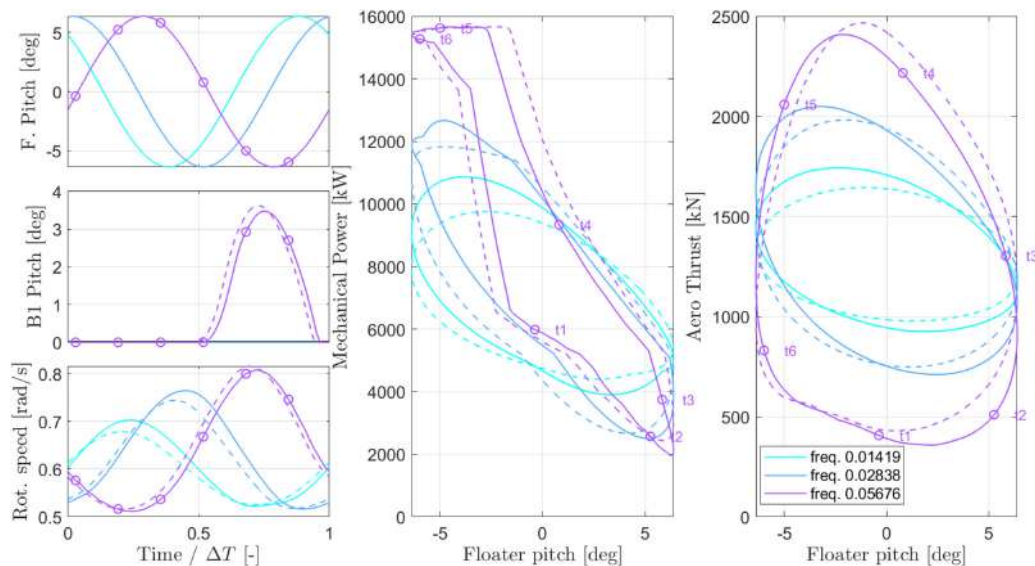


FIGURE 14 Aerodynamic quantities for the last cycle of a prescribed pitching motion of the floater with an amplitude of 6.38° and different frequencies. Wind speed of 8 m/s. Solid lines represent MIRAS-HAWC2 simulations, while dashed lines represent HAWC2-BEM [Colour figure can be viewed at wileyonlinelibrary.com]

predictions is largest. As it shown in what follows, this is a sign of the BEM method not accurately capturing the rotor aerodynamics in local vortex ring state, observed between the times t_1 and t_2 .

The vorticity iso-contours of the 0.05676 Hz case for the six different marked times are depicted in Figure 15. This case is chosen because it is the highest frequency case in the set and it shows the most distinguishable wake effects. It can be appreciated in the figure how at t_1 and t_2 the upward pointing blades are striking the wake generated by the previous passing blade, at the same time as the two tip vortices merge into one, increasing its total thickness. This is an initial evidence of local vortex ring state isolated to the tip region. Note that the large flexibility of the IEA Wind 15 MW RWT blades could have a strong impact in its aerodynamic behavior, with the outer part of the blades bent forward and making them less prone to hit their own wake during the backwards motion, and vice-versa during the forward motion. Focusing on the iso-vorticity contour at t_3 , it is clearly appreciated how once the turbine starts moving forward the thicker tip vortex (formed by a combination of two) splits back into two separate ones. For clarity, a red box is drawn to highlight these effects for times t_1 , t_2 , and t_3 . Note that for the rest of the selected times, the near wake does look more conventional although one can discern how the merged tip vortices travel downstream.

Figure 16 shows a ring distribution of the MIRAS predicted F_x and F_y forces in blade one. Sub-figures to the left represent the force distributions over the first half of the last pitching cycle; meanwhile, sub-figures to the right depict the second half. The colored outer ring represents the direction of the floater motion, red represents backward motion, and blue features the forward one. Moreover, the sub-figure on the top of each ring distribution shows the variation of the floater pitch and the root bending moments for blade one over the non-dimensionalized time, $(t - t_0)/(t_f - t_0)$. Here, t_0 is the start time of the last pitch cycle, and t_f is the final time. M_x is the flap-wise root bending moment, and M_y is the chord-wise root bending moment. Finally, the small gray band in the top sub-figures during the second half of the pitch cycle highlights simulated time non-included in the ring distribution.

During the backwards motion of the floater, approximate time from 0.00 to 0.17, the in-plane forces reach a plateau near zero loading along the span. The out-of-plane force displays slightly larger values near the tip and small negative values in the mid and in-board regions, which is yet another indication of the vortex ring state. This can be explained by the gathering of vortex structures in the root region which induces a negative inflow velocity at the blade. Focusing on the root bending moments, it is interesting that the chord-wise component, M_y , reaches a maximum during the transition from backward to forward motion of the turbine and vice-versa, non-dimensional times of 0.29 and 0.79, respectively. Regarding the flap-wise component, M_x , its maximum absolute value appears in accordance with the maximum out-of-plane blade loading, attained between non-dimensional times of 0.63 and 0.67. The minimum value of M_x is predicted during the backward motion, non-dimensional time of 0.08, and it is again in accordance with the minimum out-of-plane blade loading.

In what follows, we present the frequency study in above-rated wind conditions. Key quantities are shown in Figure 17. As expected, the blade pitch control is active in all cases. In general, it is seen that differences between the codes predictions are large for the 0.05676 Hz case while they are quite small in the lower frequency cases. Focusing on the 0.05676 Hz case, the LL simulations predict a speed up of the rotor due to the generator servo action while maintaining a lower blade pitch, which adds a time offset in comparison to BEM. In this case, the predicted power is quite different between the codes. Especially during the backwards motion of the floater, $\approx t_6 - t_1 - t_2$, where the BEM method tends

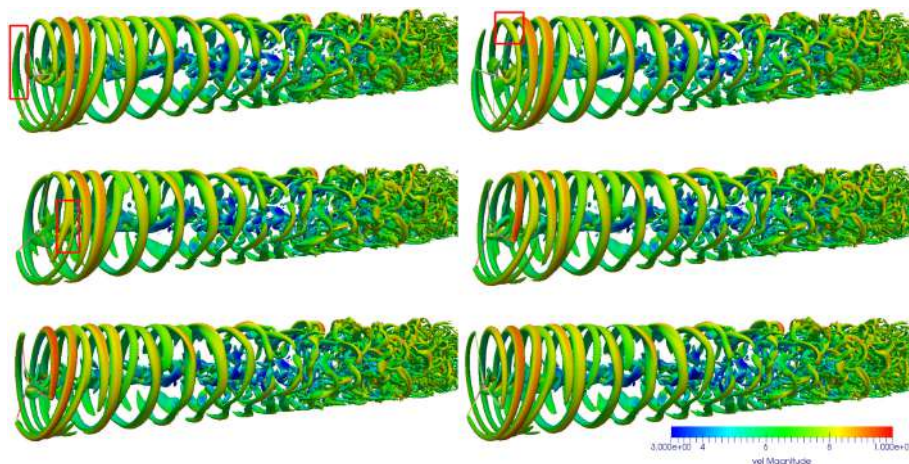


FIGURE 15 Three-dimensional vorticity contours at six selected times over the last cycle of a floater prescribed pitch motion with 6.38° amplitude and a frequency of 0.05676 Hz. From left to right and top to bottom, t_1 , t_2 , t_3 , t_4 , t_5 , and t_6 . Wind speed of 8 m/s [Colour figure can be viewed at wileyonlinelibrary.com]

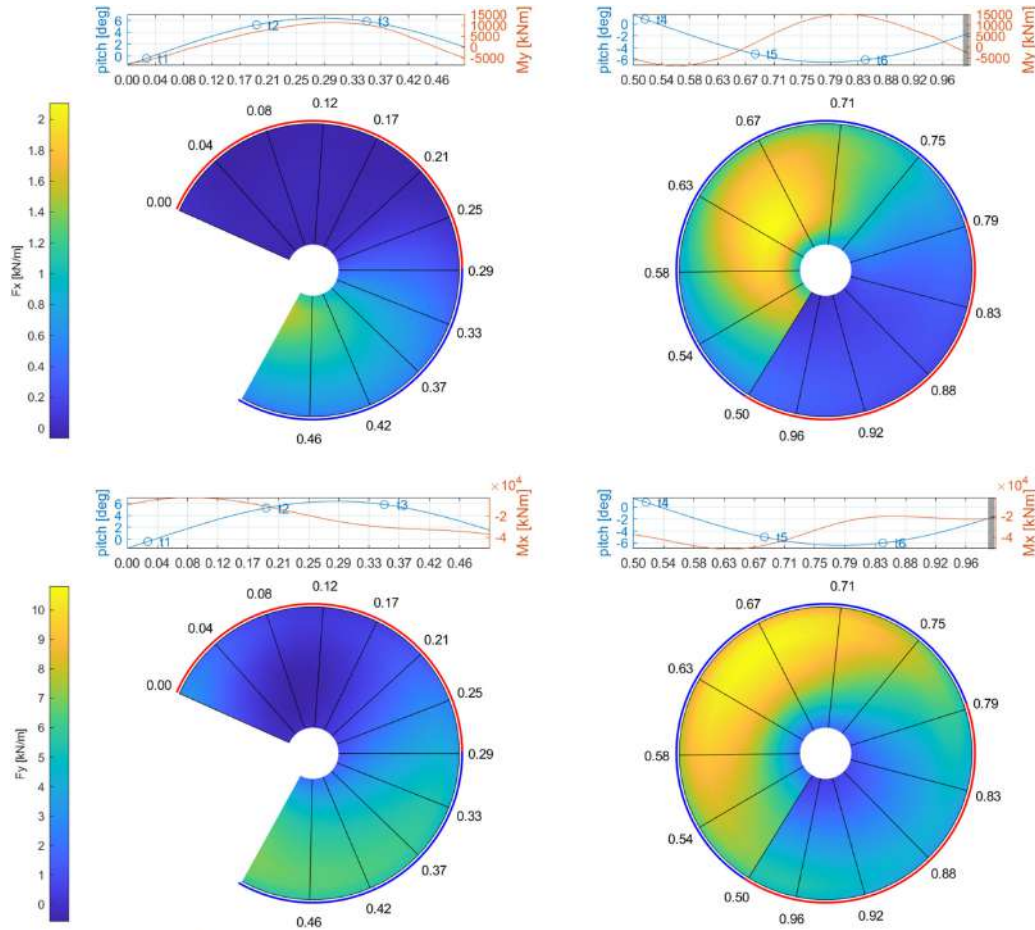


FIGURE 16 Annular distribution of the (top) in-plane force, F_x , (bottom) out-of-plane force, F_y , for the last cycle of a prescribed pitch motion of the floater with an amplitude of 6.38° and a frequency of 0.05676 Hz. Wind speed of 8 m/s. Blade 1 [Colour figure can be viewed at wileyonlinelibrary.com]

to consistently under-predict the power up to a 9 % respect to LL at t_2 . Differences in thrust are large, with a clear under-prediction of the maximum thrust by the BEM code when the floater starts moving forward, $\approx t_3$, and a constant offset between the codes during the complete backwards motion, $\approx t_6 - t_1 - t_2$.

Analyzing the iso-vorticity contours for the 0.05676 Hz case in above-rated wind conditions, depicted in Figures 18, there are clear differences compared to the 8 m/s case. The blade tip is not that highly loaded, and therefore, the tip vortex is not as concentrated; it seems to be distributed along a larger span region. This is highlighted with a red box in the t_3 snapshot. We thus emphasize that in this case, the blades are far from entering local vortex ring state. As it is shown in Section 6.3, the rotor remains in normal turbine operation state during the complete cycle. It is remarkable that during the forward motion of the floater the maximum out-of-plane blade loading appears in the mid-span region, as shown in the ring distributions of Figure 19. This creates a particular span-wise variation of the bound vortex circulation which produces a double tip vortex structure, which can clearly be appreciated in the t_4 , t_5 , and t_6 iso-vorticity snapshots. Note that during the forward motion of the floater all blade tips are subjected to negative F_x and F_y loads. This is due to the servo action, pitching the blades towards feather, combined with the effect of blade torsion, which helps deloading the tip by reducing the effective angle of attack.

We next investigate the amplitude dependence of the floater pitch motion at the fixed frequency of 0.024421 Hz. Pitching amplitudes of 3.19° , 6.38° , and 12.76° are considered in below-rated wind conditions. Key selected sensors are shown in Figure 20 for the BEM and LL

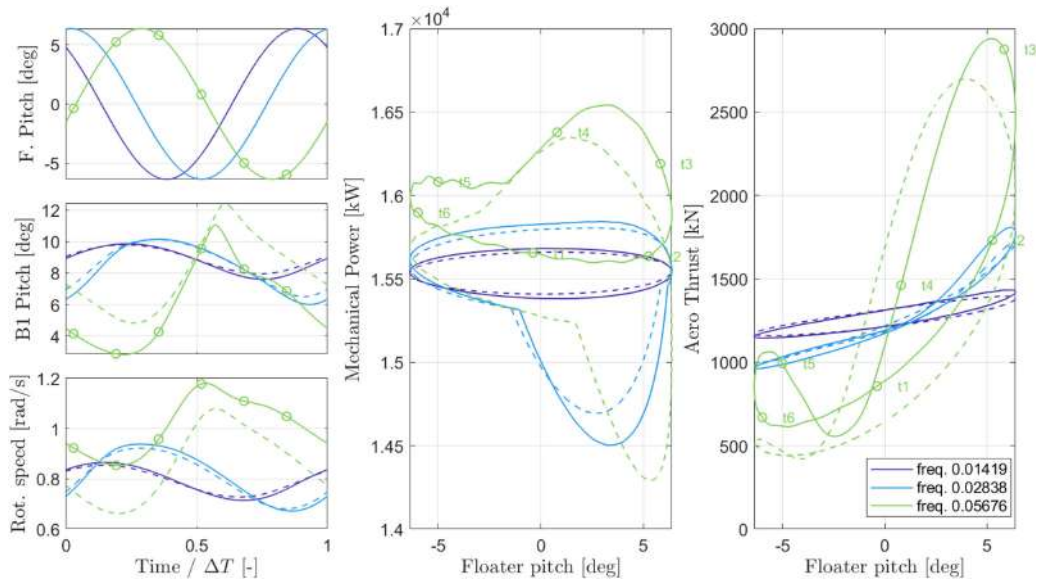


FIGURE 17 Aerodynamic quantities for the last cycle of a prescribed pitching motion of the floater with an amplitude of 6.38° and different frequencies. Wind speed of 15 m/s. Solid lines represent MIRAS-HAWC2 simulations, while dashed lines represent HAWC2-BEM [Colour figure can be viewed at wileyonlinelibrary.com]

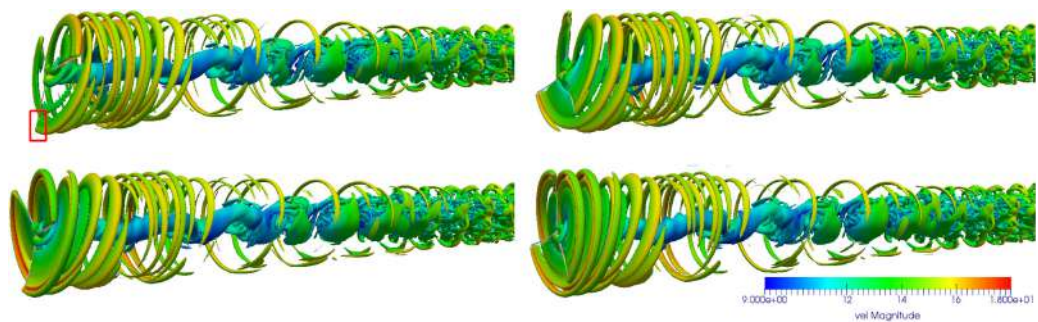


FIGURE 18 Three-dimensional vorticity contours at six selected times over the last cycle of a floater prescribed pitch motion with 6.38° amplitude and a frequency of 0.05676 Hz. From left to right and top to bottom, t_3 , t_4 , t_5 , and t_6 . Wind speed of 15 m/s [Colour figure can be viewed at wileyonlinelibrary.com]

simulations. It is interesting here to investigate the change in shape of the load loop for the 12.76° case compared to the lower amplitudes motions. This change is similarly captured by both solvers although small differences in thrust between t_6 and t_1 can be linked to a more aggressive blade pitch actuation in the LL simulations. Another remarkable difference between the solver predictions appears during the second half of the backward motion of the floater, $\approx t_3 - t_4$, which, judging from the iso-vorticity contours presented in Figure 21, is related to the upwards pointing blade entering its own wake in what can be identified as local vortex ring state. This phenomenon is highlighted with a red box in the t_3 and t_4 iso-vorticity snapshots.

Results for the different amplitude cases at the wind speed of 15 m/s are presented in Figure 22. The largest differences between the codes are observed in the 12.76° amplitude case. The maximum thrust is strongly under-predicted by the BEM code by a 10 %, while the minimum power is over-predicted by a 3 %. It also is interesting that during the beginning of the forward motion of the floater, $t_5 - t_6$, there appears a bump in the power and thrust. This is mostly related to the action of the controller switching quickly from below-rated to above-rated regulation,

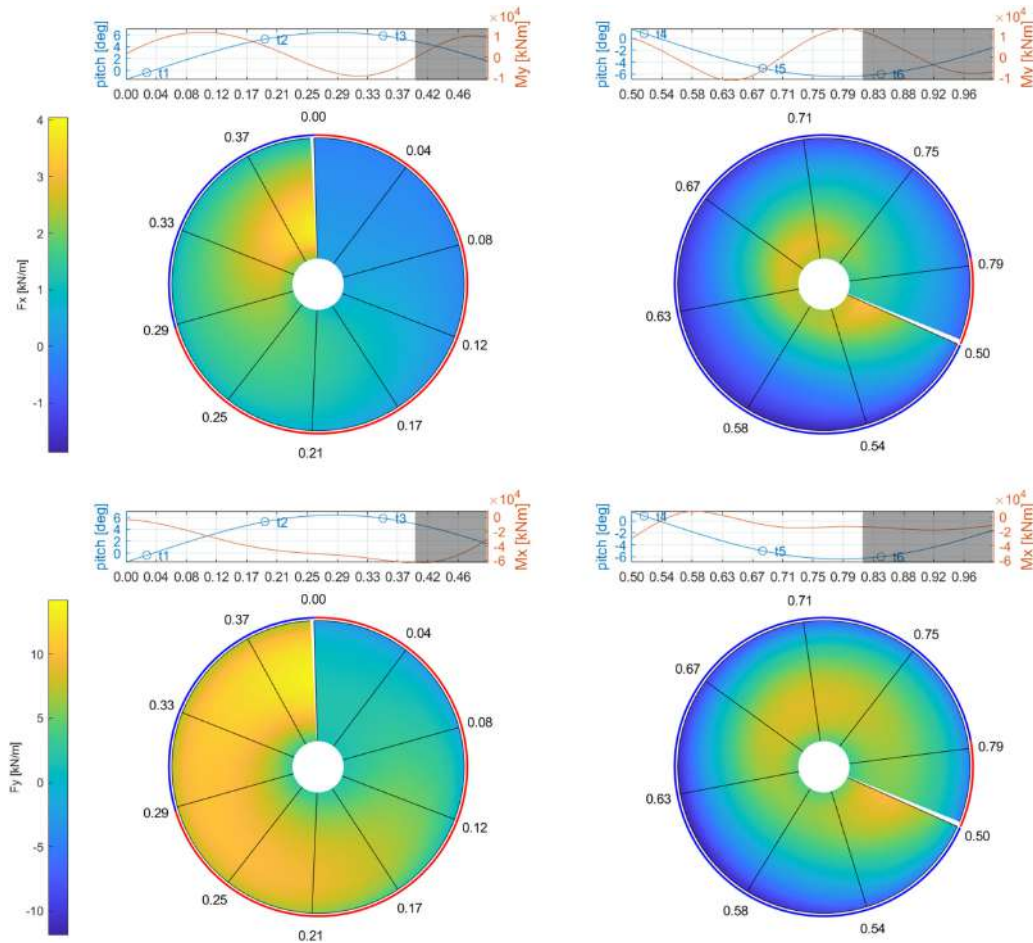


FIGURE 19 Annular distribution of the (top) in-plane force, F_x , and (bottom) out-of-plane force, F_y , for the last cycle of a prescribed pitch motion of the floater with an amplitude of 6.38° and a frequency of 0.05676 Hz. Wind speed of 15 m/s. Blade 1 [Colour figure can be viewed at wileyonlinelibrary.com]

which increases the rotational speed and pitches the blade towards stall. This sudden change is predicted by both codes. However, the LL predicts a steeper response, probably due to the fact that it predicts larger load variations.

For the sake of brevity, and since they do not provide new insight in our investigation, the iso-vorticity contours for these cases are not included.

6.2 | Turbine behavior and iso-vorticity comparison for extreme cases in pitch

As it is shown in the analysis of maximum bending moments, Section 6.4, the cases where the floater motion is prescribed with a frequency of 0.11352 Hz, representative of the wave loads in harsh sea states, and an amplitude of 6.37° displays the most extreme loads. These cases are presented in a different section in order not to mask the analysis of the moderate cases. It is important to mention that, in order to take a less conservative approach in the simulation of such extreme cases, the controller over-speed thresholds that trigger the safety system and the wind turbine shut-down were deactivated. Such thresholds would trigger an automatic shut down of the turbine after a few seconds in order to prevent damages to the machine.

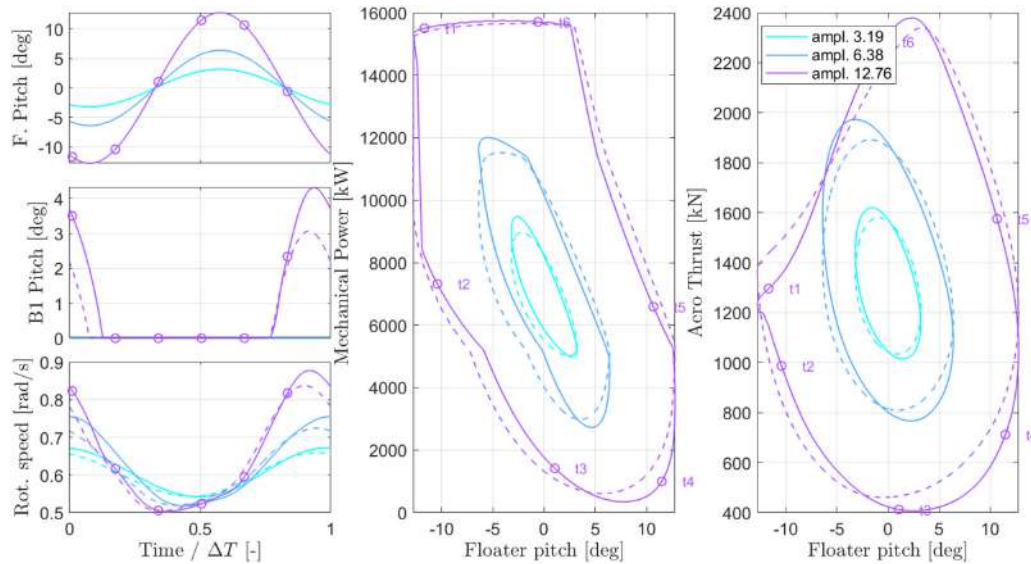


FIGURE 20 Aerodynamic quantities for the last cycle of a prescribed pitching motion of the floater with a frequency of 0.02441 Hz and different amplitudes. Wind speed of 8 m/s. Solid lines represent MIRAS-HAWC2 simulations, while dashed lines represent HAWC2-BEM [Colour figure can be viewed at wileyonlinelibrary.com]

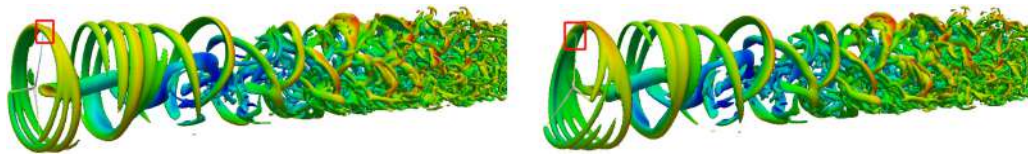


FIGURE 21 Snap-shots of three-dimensional vorticity contours over the last cycle of a floater prescribed pitch motion with amplitude 12.7 degrees and frequency 0.02441 Hz. (Left) t_3 and (right) t_4 . Wind speed of 8 m/s [Colour figure can be viewed at wileyonlinelibrary.com]

An over-speeding of the rotor has been observed for the MIRAS-HAWC2 simulations at 8 m/s, with the largest differences between the codes observed in the thrust prediction during the backwards motion of the turbine, as shown in Figure 23 where BEM under-predicts the minimum thrust by more than a 25 % while the maximum thrust is under-predicted by approximately a 7%. Differences in power are kept below 3 % throughout the complete cycle. In this case, the rotor seems to transition between different states, as it is shown in Section 6.3.

Analyzing the iso-vorticity contours, Figure 24, it can be appreciated that during most of the backwards motion of the turbine, $t_3 - t_4 - t_5$, the rotor is operating inside its own wake, while it is generating a negative thrust force, a clear sign of a global propeller state. At the same time, large negative angles of attack can be observed from the ring distribution in Figure 25, a clear indication of negative stall in the root region between times $t_4 - t_5$. Moreover, a negative aerodynamic power, which is not translated into the mechanical power at the shaft, is predicted around t_3 slowing down the rotor. It can be appreciated in the iso-vorticity contours at t_6 that the newly generated tip vortex by the upwards pointing blade, highlighted in a red box, is released downstream of the tip vortex created by the previous passing blade. Once the turbine starts moving forward, the thrust force becomes positive but the rotor blades continue hitting the previously released vortex structures. During this first half of the forward motion, $t_1 - t_2$ approximately, it is observed that the airfoil sections near the blade root enter stall, as seen in Figure 25. Note that the lower and upper limits of the color-bar are truncated at -12° and 14° , respectively, these values are representative of the static stall aoa in the vast majority of the airfoils that the blade mounts. It is important to emphasize here that the dynamic stall methods implemented in both the BEM and the LL solvers should be capable of quite accurately model the physics of this case. It is only in the second half of the forward motion and beginning of the transition to the backward motion, $\approx t_2 - t_3$, that the rotor leaves behind its own wake and appears to be in normal operation. Notice that the very long, slender, and flexible blades lag behind during the first part of the backward motion, $\approx t_3 - t_4$. The opposite occurs, but to a lesser extent, during the beginning of the forward motion. Unfortunately, as the rotor is immersed inside its own wake the blade

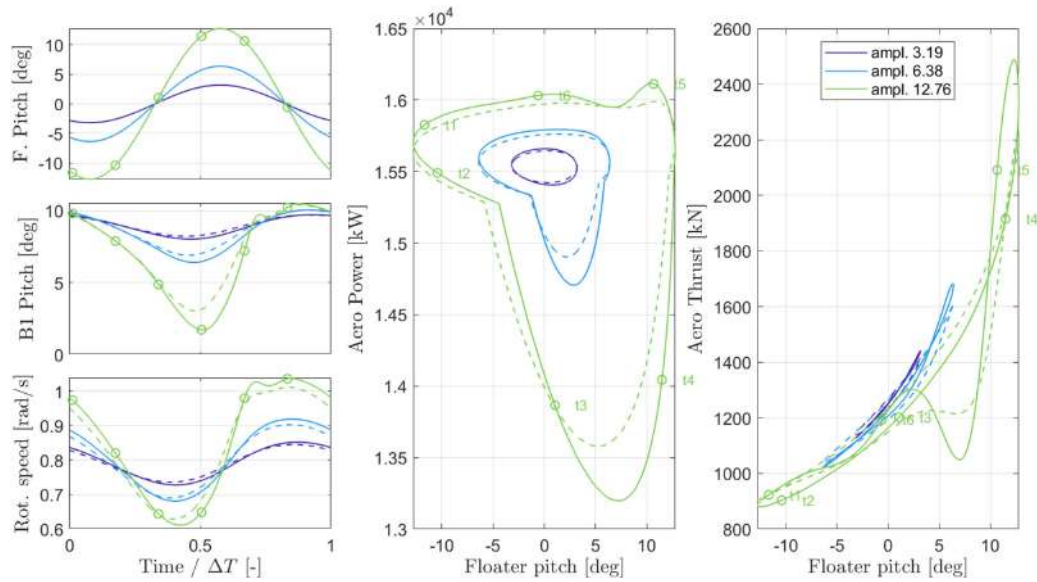


FIGURE 22 Aerodynamic quantities for the last cycle of a prescribed pitching motion of the floater with a frequency of 0.02441 Hz and different amplitudes. Wind speed of 15 m/s. Solid lines represent MIRAS-HAWC2 simulations, while dashed lines represent HAWC2-BEM [Colour figure can be viewed at [wileyonlinelibrary.com](https://onlinelibrary.wiley.com)]

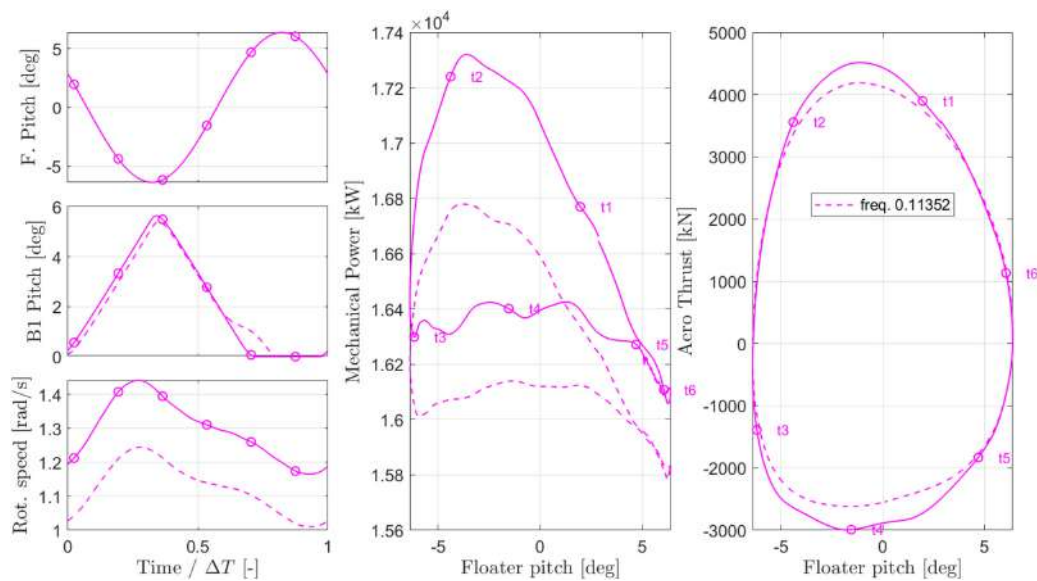


FIGURE 23 Aerodynamic quantities for the last cycle of a prescribed pitching motion of the floater with an amplitude of 6.38° and a frequency of 0.11352 Hz for a wind speed of 8 m/s. Solid lines represent MIRAS-HAWC2 simulations, while dashed lines represent HAWC2-BEM [Colour figure can be viewed at [wileyonlinelibrary.com](https://onlinelibrary.wiley.com)]

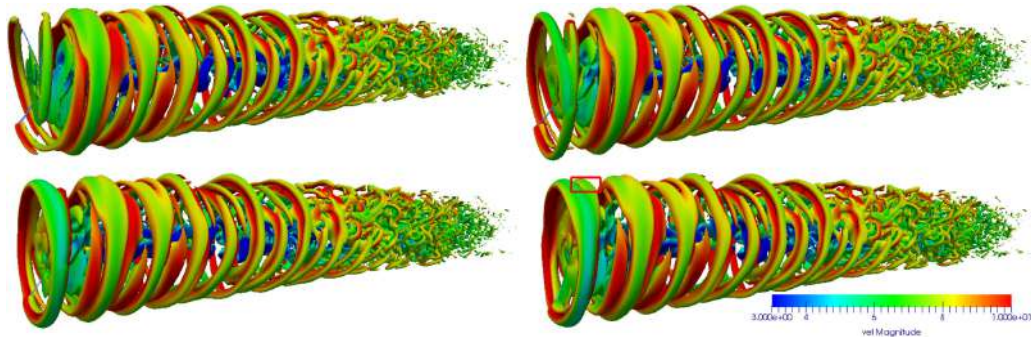


FIGURE 24 Three-dimensional iso-vorticity contours over the last cycle of a floater prescribed pitch motion with an amplitude of 6.38° and a frequency of 0.11352 Hz for a wind speed of 8 m/s. From left to right and top to bottom, t_3 , t_4 , t_5 , and t_6 [Colour figure can be viewed at wileyonlinelibrary.com]

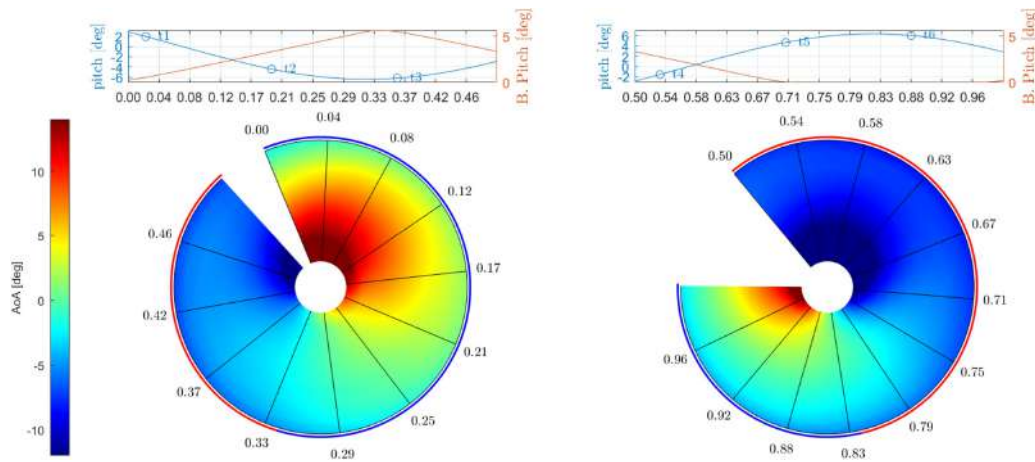


FIGURE 25 Annular distribution of the angle of attack during the last cycle of a prescribed pitch motion of the floater with an amplitude of 6.38° and a frequency of 0.11352 Hz. Wind speed of 8 m/s. Blade 1 [Colour figure can be viewed at wileyonlinelibrary.com]

deflections cannot be clearly seen in the iso-vorticity plots. Figure 26 is introduced to more clearly show the variation in the blade deflections in relation to the floater motion. Mark that the studied t_1 , t_2 , t_3 , t_4 , t_5 , and t_6 times are highlighted with a pink rectangle.

At 15 m/s, the rotor is over-speeding in both fidelities, pure HAWC2 and MIRAS-HAWC2. Generally, differences between the codes are much larger than observed for the 8 m/s case. Regarding the generated wake, depicted in Figure 27 for times t_2 and t_5 , it appears to be formed by much smaller turbulent structures which seem to be triggered by the quick blade deflections. Looking at the ring distributions of the angle of attack presented in Figure 28, the higher free-stream velocity has induced a larger region of the disc under positive stall while the negative stall area has been considerably reduced.

6.3 | Rotor state analysis in pitch

As seen from the previous results, the rotor operates in strongly varying inflow conditions during the pitch motion cycle. Following Lienard et al¹⁴ and Eggleston and Stoddard,⁵⁰ we now utilize the inflow velocity ratio V_c/V_n , to analyze the rotors transition between the different rotor states. V_c is the velocity normal to the rotor plane, computed as $V_c = -(V_w \cos(\theta) - \dot{\theta} l_{HT})$, mind the negative sign in accordance with helicopter notations.

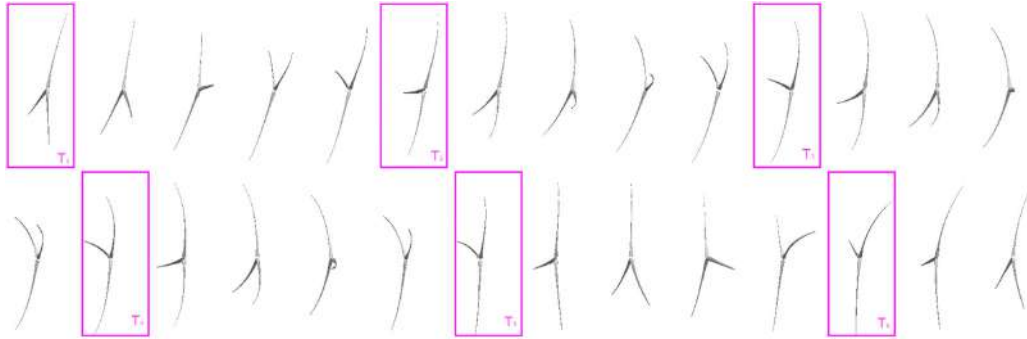


FIGURE 26 Rotor geometry for the last cycle of a prescribed pitch motion of the floater with an amplitude of 6.38° and a frequency of 0.11352 Hz. Wind speed of 8 m/s [Colour figure can be viewed at wileyonlinelibrary.com]



FIGURE 27 Three-dimensional iso-vorticity contours over the last cycle of an extreme floater motion at 15 m/s. With an amplitude of 6.38° and a frequency of 0.11352 Hz. (Left) t2 and (right) t5 [Colour figure can be viewed at wileyonlinelibrary.com]

V_w is the wind speed, and l_{HT} is the distance from the center of the turbine pitch rotation to the hub center, in this case 135 m. θ is the floater pitch angle, and $\dot{\theta}$ is the floater angular velocity. V_h is a theoretical induced velocity calculated as

$$V_h = \text{sgn}(T) \sqrt{\frac{|T|}{2\rho S}} \quad (8)$$

where T is the turbine thrust at a given time, S is the rotor area, and ρ is the air density. The use of the total turbine thrust T and the calculation of V_c at the hub height simplifies this expression, making it useful to capture trends in the turbine operation but not an accurate way to identify the different rotor states in rotatory movements of the turbine.

From actuator disc theory, a rotor can operate in different states,⁵¹ i.e., propeller state (PPS), turbine state (TBS), turbulent wake state (TWS), vortex ring state (VRS), and propeller break state (PBS). If energy is added to the fluid, the rotor normally operates in PPS, with a contracting stream-tube, and a resulting propulsion producing thrust force which is directed upstream. In TBS, the rotor extracts energy from the flow, exhibiting a stream-tube that expands downstream the rotor plane. With increasing loading of the turbine (axial induction factor), the rotor can transition to TWS, in which there is a reverse flow region at the exit of the stream-tube which progresses towards the rotor plane. The turbine is releasing very strong vortices that move very slowly downstream, violating the assumptions of inviscid and irrotational flow of the actuator disk model. When the reverse flow reaches the actuator disk, the rotor enters VRS, blocking the flow through the rotor. If the axial induction factor of the rotor is larger than unity, it can enter PBS, also known as the reverse thrust state, where power is added to the flow. But, contrary to what occurs in PPS, the thrust created is directed downstream.

The computed inflow velocity ratio over the last pitching cycle for all the prescribed pitch cases considered in this work is depicted in Figure 29. An arrow has been drawn to indicate the loop direction, which is the same for all cases. An unusual effect is observed in the simulations with a pitch frequency of 0.11352 Hz in under-rated conditions, the most extreme case. The rotor does not seem to enter the VRS transitioning from the TWS, as it has been previously reported by other researchers in simulations without active turbine control.^{14,50} It abruptly jumps from the TBS to the PPS and then smoothly transitions down to what can be called an inverted vortex ring state. The rotor exits the VRS entering again the PPS during the last part of the backward motion of the floater. When the floater transitions to forwards motion, there is again an abrupt jump down to TBS. The abrupt jumps of the inflow velocity ratio from PPS to TBS or vice-versa happen for thrust values in the vicinity of zero. The inflow velocity ratio is inversely proportional to the square root of the rotor thrust. Therefore, when the thrust is close to zero, the ratio becomes

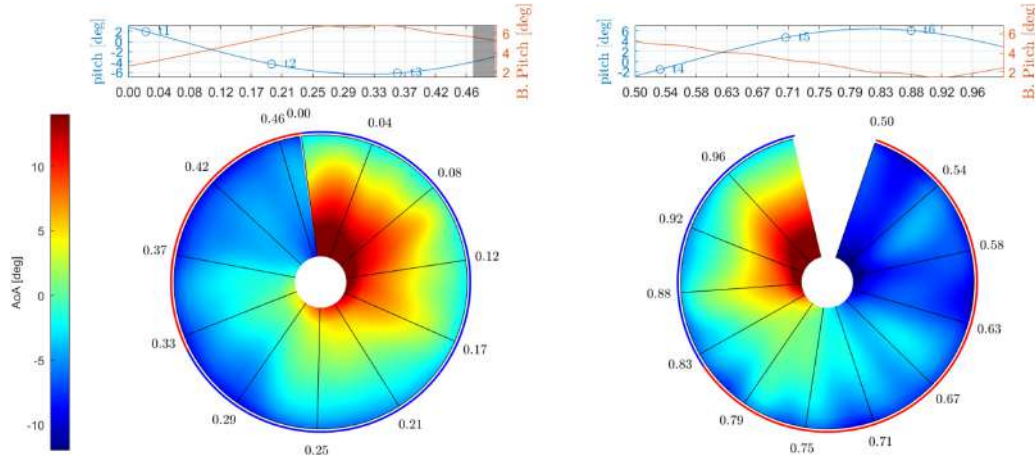


FIGURE 28 Annular distribution of the angle of attack during the last cycle of a prescribed pitch motion of the floater with an amplitude of 6.38° and a frequency of 0.11352 Hz. Wind speed of 15 m/s. Blade 1 [Colour figure can be viewed at [wileyonlinelibrary.com](#)]

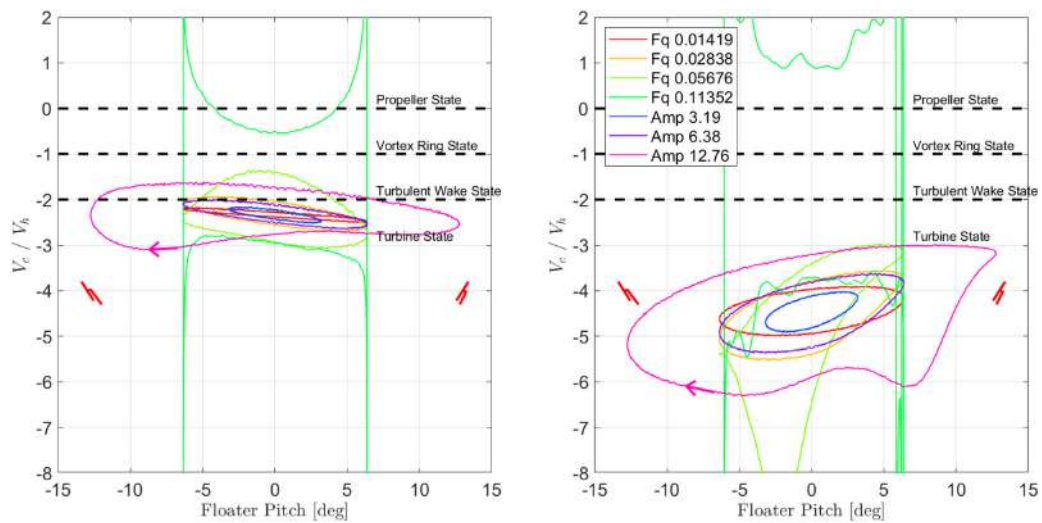


FIGURE 29 Computed inflow velocity ratio for all the harmonic pitch cases with active turbine control (left) 8 m/s and (right) and 15 m/s cases [Colour figure can be viewed at [wileyonlinelibrary.com](#)]

a large absolute number. Note that, for the rest of the considered cases, the rotor seems to be far from entering a global VRS. In many cases, it is operating in TWS during part of the backwards motion, and as previously shown during the analysis of the iso-vorticity contours, the top part of the rotor can enter local VRS. At 15 m/s, the rotor operates in normal turbine state in all cases but for the extreme frequency, where it operates in PPS during the full backwards motion. The spikes observed during the transition to forward motion are related to the blade instabilities that make the turbine thrust jump from positive to negative values and vice-versa multiple times.

To further investigate this phenomena, a set of cases where the rotor is close to enter VRS have been simulated with the controller turned off. The wind speed of 8 m/s has been selected since it has been found that the rotor is more prone to enter non-conventional operation states at lower wind speeds. The rotational speed was fixed to 0.6025 rad/s, and the blade pitch was set to 0°, following the turbine normal operation

points. As can be seen in Figure 30, for a pitching frequency of 0.07804 Hz, the rotor transitions smoothly between the states TBS-TWS-VRS. However, if the frequency is higher, the rotor enters PPS, and it transitions abruptly down to TBS as it has been previously shown. This can happen multiple times during the backwards motion of the floater, as seen for the 0.11352 Hz case, in which the wind speed is lower than the velocity generated by the motion of the turbine, i.e., positive V_c , and if the thrust is negative, i.e., negative V_h , the inflow velocity ratio becomes negative but the relative wind seen by the rotor is coming from downstream. Therefore, it can be said that the turbine is operating in an inverted fashion, in which it can transition again between all states, as seen during part of the backwards motion for the 0.11352 Hz case.

Note that the flexibility of the blades and tower should add an extra velocity term to the inflow velocity ratio calculation, which is not taken into account in our analysis for the sake of simplicity.

6.4 | Maximum blade and tower loading in pitch

The thrust variations associated with the pitch motion naturally alters the structural loads. Bar diagrams with the maximum attained blade root and tower base bending moments, BRBM and TBBM, respectively, are shown in Figure 31. A comparison between the MIRAS-HAWC2 and HACW2-BEM predictions shows that for most of the cases the higher fidelity model predicts just slightly larger maximum values of the blade root bending moments. However, for the extreme cases, i.e., pitching frequency of 0.11352 Hz, the difference is much larger, especially in above-rated conditions. Such large differences are accentuated in the tower base bending moments, mostly for the side-side component. Note that, as an exception, the BEM method generally over-predicts the fore-aft tower base bending moment, except for the extreme case. It is observed that increasing the frequency or the amplitude of the prescribed floater motion raises the maximum moments. The only exception is the maximum torsional tower bending moment at the wind speed of 15 m/s, which seems to be almost invariant to frequency or amplitude changes (disregarding the extreme frequency case). Moreover, under-rated wind conditions exhibit the larger maximum blade root bending moments, except for the extreme case and the LL prediction of the flap-wise component in the 0.05676 Hz case.

6.5 | Wake analysis in pitch

The influence of the turbine motion in the downstream development of the wake is studied in what follows. First, the integrated wake velocity recovery, Equation 6, and the integrated turbulence intensity, Equation 7, are plotted as function of the downstream distance to the rotor plane in Figure 32. In this case, a prescribed harmonic pitch motion with 6.38° amplitude and three different frequencies are compared to the

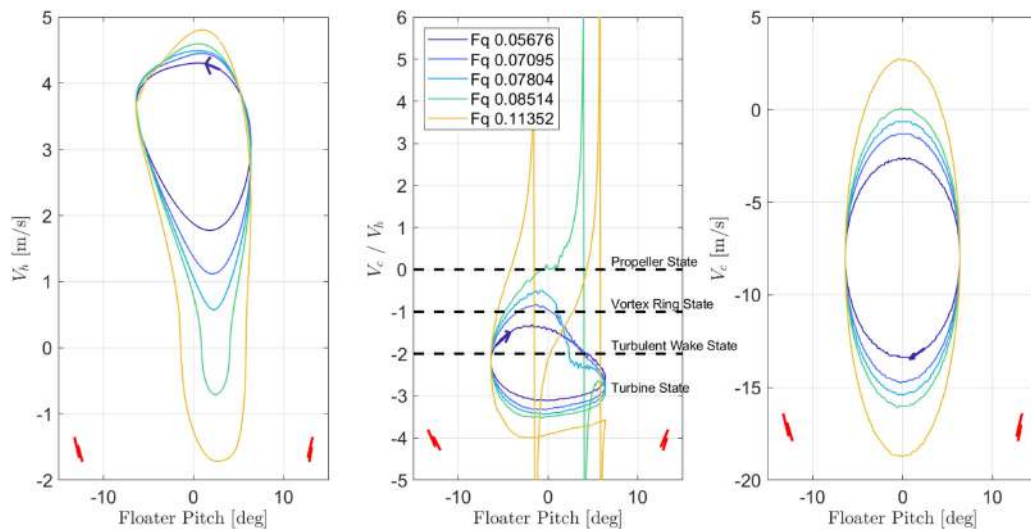


FIGURE 30 (Left) theoretical induced velocity, V_h , (middle) inflow velocity ratio, V_c/V_h , and (right) normal velocity to the rotor plane V_c for selected harmonic pitch cases with the controller turned off. Wind speed of 8 m/s [Colour figure can be viewed at wileyonlinelibrary.com]

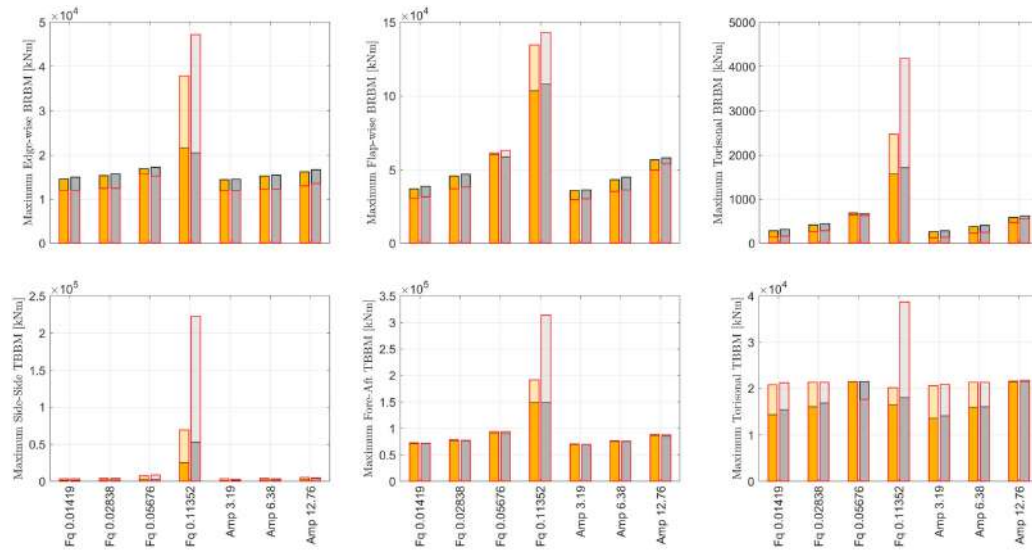


FIGURE 31 Maximum computed (top) blade root and (bottom) tower base bending moments for the prescribed pitching motion of the floater at wind speeds of 8 m/s, black edged bars, and 15 m/s, red edged bars. Bars with amber filling represent HAWC2-BEM, while bars with grey filling represent MIRAS-HAWC2 simulations [Colour figure can be viewed at wileyonlinelibrary.com]

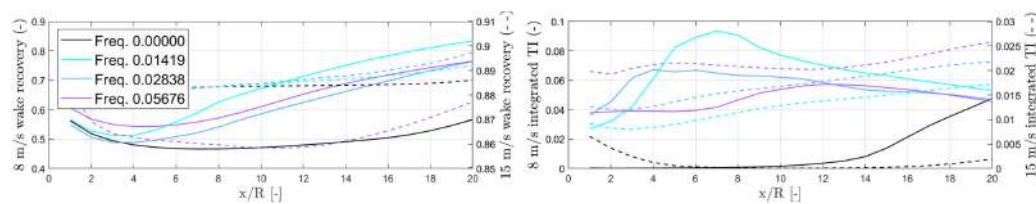


FIGURE 32 Wake analysis for a prescribed pitching motion of the floater with an amplitude of 6.38° and different frequencies at wind speeds of 8 m/s (solid lines) and 15 m/s (dashed lines). (Left) Wake velocity recovery; (right) Integrated Turbulent Intensity [Colour figure can be viewed at wileyonlinelibrary.com]

non-oscillating case (bottom-fixed turbine), referred as Freq. 0.00000. Cases at a wind speed of 8 m/s are depicted in solid lines, while dashed lines represent the cases at 15 m/s. In below-rated conditions, there is a large difference in the wake recovery of the three pitching cases compared to the non-oscillating case, which shows a much slower recovery far downstream and a lower integrated TI. This is in agreement with the experimental observations of Fu et al.,²² who observed a faster wake recovery of a pitching turbine due to an enhanced turbulent mixing that led to a higher turbulence kinetic energy level. Initially, the higher frequency case (0.05676 Hz) shows a better initial recovery compared to the other cases. However, there is a change in tendency and the lowest frequency motion (0.01419 Hz) reaches the best recovery far downstream, approximately 50% that of the bottom-fixed case. Regarding above-rated conditions, the highest frequency case shows the worst wake recovery independently of the downstream location, even worse than the non-oscillating case. This is surprising since the turbulence intensity level achieved is larger than the rest. It was initially assumed that more mixing would accelerate the recovery but this does not seem to hold for this case. The other three cases, including the non-oscillating case, show very similar characteristics in the near wake. Differences grow downstream of the 10R location, with the 0.02838 Hz case displaying the best recovery at the 20R location. Figure 33 shows the integral wake velocity and turbulence intensity for three different amplitudes of the pitch oscillation, at the given frequency of 0.02441 Hz. It is clearly observed that the wake recovery far downstream improves with the increasing amplitude, with the 12.7° case attaining the best recovery 20 R downstream in both below- and above-rated conditions and with an increase from 0.48 to 0.63 in wake recovery at $x/R = 12$ for the motion at 0.02838 Hz at 8 m/s.

In order to assess the influence of large blade motions (including floater oscillation and the blade elastic deformation) in the recovery of the wake, we have investigated the blade fore-aft tip displacement for the cases with a prescribed harmonic pitch motion of the floater. Focusing first

in below rated wind conditions, Figure 34 to the left shows the fore-aft displacement of the tip of blade one over 350 s of simulated time. The peaks where the displacement is larger than 80% of the largest displacement are located and marked in the figure. Large displacements are linked to substantial variations in the blade loading, the wake geometry and the strength of the released tip vortex and can promote a faster break down of the wake structure. Moreover, Figure 34 to the right presents the time interval between consecutive peaks. Thus, each filled up circle represents a peak pair, and it is colored by the mean value of its fore-aft displacement. Note that 1,275 s of simulated time have been used for the peak investigation; the first 125 s have been disregarded to avoid transients. It is observed from the sub-figure to the right that the 0.01419 Hz case has the largest amount of peak pairs with the shortest time between them, approximately 10 s. Followed by the high frequency case, i.e., 0.05676 Hz, with a time interval of approximately 19 s. Finally, in the 0.02441 Hz case, all the peaks appear much more spaced in time, with an interval between 30 and 40 s. A low time interval between high consecutive peaks is an indication of a reduced distance between consecutive tip vortices, which could promote a vortex instability and trigger a faster wake recovery. Our findings are therefore in agreement with the wake velocity recovery results presented with solid lines in Figure 32, left, where the lowest frequency pitch oscillation achieves the fastest wake recovery, followed by the highest frequency oscillation and with the mid-range oscillation presenting the slowest recovery of the three cases. To further support our analysis, we have carried out a similar peak study in above rated conditions, i.e., 15 m/s. Note that in this case, the highest frequency floater oscillation showed surprisingly the worst wake recovery, earlier presented in Figure 32 to the left using dashed lines. This finding is in agreement with the peak analysis depicted in Figure 35 where a minimum peak to peak time interval of approximately 7.5 s is computed for the 0.01419 and 0.02441 Hz cases and almost a three times larger time gap between large tip deflections is recurrently observed for the highest frequency floater oscillation.

7 | INVESTIGATION OF THE EFFECT OF FLOATER HARMONIC MOTION IN SURGE

The test matrix for the harmonic surge motion is presented in Table 4. In general, similar results are observed during the isolated surge translation compared to the pitch rotation; therefore, only selected results are presented in what follows.

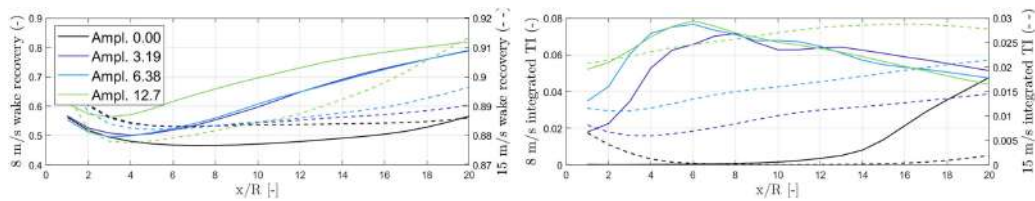


FIGURE 33 Wake analysis for a prescribed pitching motion of the floater with an frequency of 0.02441 Hz and different amplitudes at wind speeds of 8 m/s (solid lines) and 15 m/s (dashed lines). (Left) Wake velocity recovery; (right) Integrated Turbulent Intensity [Colour figure can be viewed at wileyonlinelibrary.com]

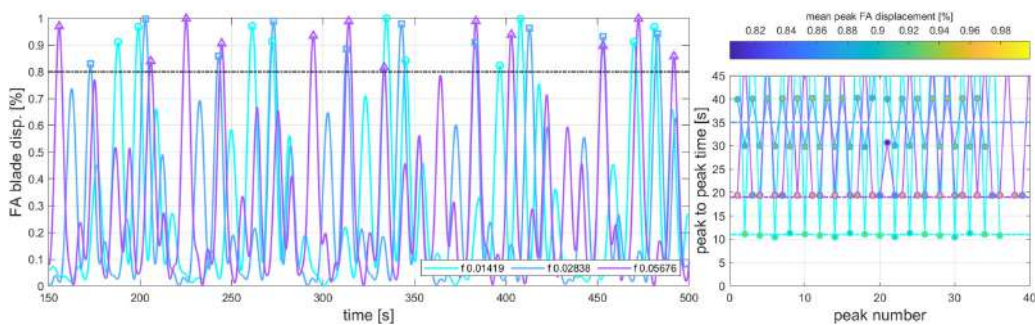


FIGURE 34 Peak analysis of the blade one tip position for a prescribed pitching motion of the floater with an amplitude of 6.38° and different frequencies at a wind speed of 8 m/s [Colour figure can be viewed at wileyonlinelibrary.com]

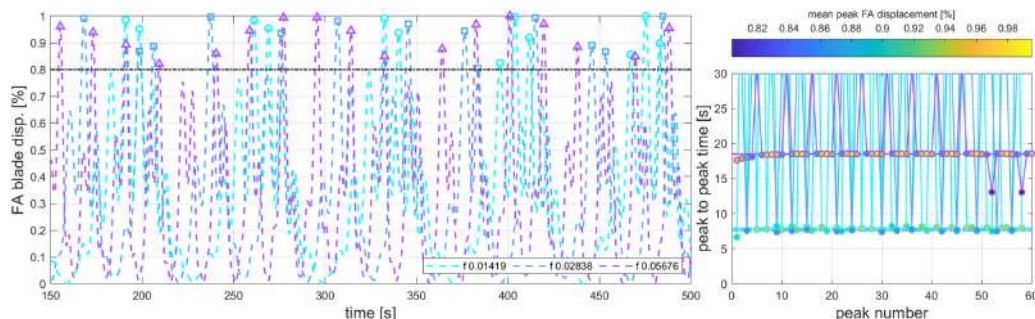


FIGURE 35 Peak analysis of the blade one tip position for a prescribed pitching motion of the floater with an amplitude of 6.38° and different frequencies at a wind speed of 15 m/s [Colour figure can be viewed at wileyonlinelibrary.com]

7.1 | Turbine behavior and iso-vorticity comparison in surge

The influence of the surge frequency in the turbine behavior is herein presented for a wind speed of 8 m/s and an amplitude of 15 m. The key sensors presented in Figure 39a show an almost identical picture as the pitch study in below-rated conditions. Even so, the wake has a very different structure due to the translatory nature of the movement, as seen in Figure 36. The iso-vorticity snap-shot at t_1 shows the wake during the floater backward motion, while at t_5 it is depicted during the forward motion. In the latter one, a wider spacing between the newly released tip vortices and the ones released by the previous passing blade is observed. Merging of tip vortices during part of the backwards motion is observed, with the thickness of the vortices facilitating the merging although there are no clear signs of direct blade-vortex interaction. As it is shown in Section 7.3, the turbine operates in turbulent wake state during most of the rearward movement.

Results for a surge motion with an amplitude of 15 m and frequencies of 0.01419, 0.2838, and 0.05676 Hz in above-rated conditions are presented below. The change in selected rotor quantities over the last cycle is summarized in Figure 39b. A fairly good agreement between the solvers is obtained at the lower frequencies; however, large discrepancies are seen at 0.05676 Hz. In this case the width of the thrust loop predicted by LL is narrower than for the equivalent pitch case. And generally, differences between the BEM and LL simulations are much larger. Notice how BEM under-predicts both the maximum and the minimum power and thrust compared to the LL solution. Iso-vorticity contours for two selected times, i.e., t_1 and t_4 , are reproduced in Figure 37.

Selected sensors for the amplitude surge study at the frequency of 0.01419 Hz and a wind speed of 8 m/s are presented in Figure 39c. The largest differences in absolute terms between the codes are observed during the forward motion of the blade, $t_1 - t_2 - t_3$. Again, such differences grow with the increasing amplitude of the surge. In general, smaller differences are appreciated during the backward motion, $t_4 - t_5 - t_6$, although these differences are larger in relative terms. The BEM method consistently under-predicts the height of the power and thrust loops by up to a 20% and 17%, respectively, for the highest amplitude case. Three-dimensional iso-vorticity contours are shown in Figure 38 for the selected times t_2 and t_5 . A very distinctive wake shape is simulated in this case, The tip vortex structures seem to dissipate faster and do not reach the far wake. An accordion effect is clearly observed when comparing the wake during the forward, t_2 , and backward, t_5 , motion of the floater.

The final study regarding the surge DoF focuses on an amplitude variation in above-rated conditions. Surge amplitudes of 5, 10, and 15 m are considered, and key outputs are presented in Figure 39d. Again in this case, the LL solver predicts a larger loop height compared to the BEM predictions. With differences up to 10% in power and 15% in thrust. As expected, the differences in power between BEM and LL predictions are reduced compared to the below-rated case. The iso-vorticity contours for the 15 m amplitude case at times t_1 and t_5 are shown in Figure 40. The tip vortex is very stable compared to the previous cases in below-rated conditions, remaining unaltered quite far downstream. It is surprising that even the root vortex remains almost unaltered until the end of the computational domain.

7.2 | Turbine behavior and iso-vorticity comparison for extreme cases in surge

A very similar behavior of the rotor is observed for the below-rated case with a surge frequency of 0.11352 Hz as for the equivalent pitch case and therefore the results are not included for the sake of brevity.

At 15 m/s, the surging rotor presents a very abrupt flap-wise instability at 1.45 Hz, probably flutter. And as shown in Figure 41, large blade deformations generate a more chaotic wake than the one observed in the equivalent pitch case (Figure 27). This large discrepancies with the

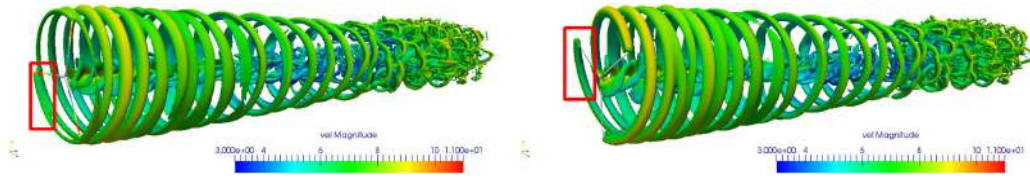


FIGURE 36 Three-dimensional iso-vorticity contours over the last cycle of a floater prescribed surge motion with an amplitude of 15 m and a frequency of 0.05676 Hz. (Left) t1 and (right) t5. Wind speed of 8 m/s [Colour figure can be viewed at wileyonlinelibrary.com]

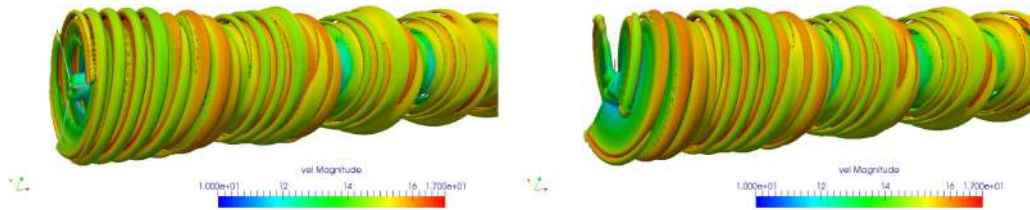


FIGURE 37 Three-dimensional iso-vorticity contours over the last cycle of a floater prescribed surge motion with an amplitude of 15 m and a frequency of 0.05676 Hz. (left) t1 and (right) t4. Wind speed of 15 m/s [Colour figure can be viewed at wileyonlinelibrary.com]

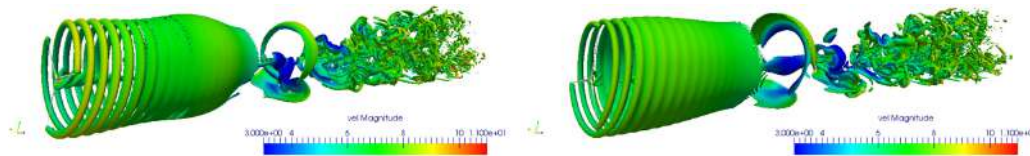


FIGURE 38 Three-dimensional iso-vorticity contours over the last cycle of a floater prescribed surge motion with an amplitude of 15 m and a frequency of 0.01419 Hz. (Left) t2 and (right) t5. Wind speed of 8 m/s [Colour figure can be viewed at wileyonlinelibrary.com]

floaters motion in pitch can clearly be appreciated in the angle of attack ring distributions presented in Figure 42, where on top of the positive stall region in the vicinity of the root (already seen in the pitch cases), an extreme behavior is observed in the tip region during most of the backward motion where the outer part of the blade enters and exits negative stall at a very high frequency rate. Fairly similar loads are predicted by both fidelity codes although it is very difficult to assess if this very challenging scenario is correctly captured by the current levels of fidelity. The codes can probably predict the onset of the aeroelastic instability, but what is very challenging is the prediction of its amplitude.

7.3 | Rotor state analysis in surge

The variation of inflow velocity ratio, V_c/V_t , over the last surge cycle is presented in Figure 43. In surge, V_c is computed as $V_c = -(V_w - \dot{x})$, where x is the prescribed surge position. Since surge is a translatory motion, in the present analysis, it is assumed that the full rotor is moving with the same velocity. Therefore, the inflow velocity ratio is a more accurate way to identify the different rotor states than during a pitch rotation. Focusing first on the 0.05676 Hz case in below-rated conditions, it is hereby confirmed that the rotor does not enter VRS, remaining in TWS during most of the backward motion. Regarding the extreme case, frequency of 0.11352 Hz, the general behavior of the rotor is very similar to the equivalent pitch case, and it will not be further discussed. At a wind speed of 15 m/s, cases with a frequency of 0.05676 Hz and lower exhibit a rotor operating in turbine state. For the 0.11352 Hz case, the rotor is operating in PPS during most of the backward motion of the turbine with the large blade deflections triggering sharp transitions between TBS and PPS.

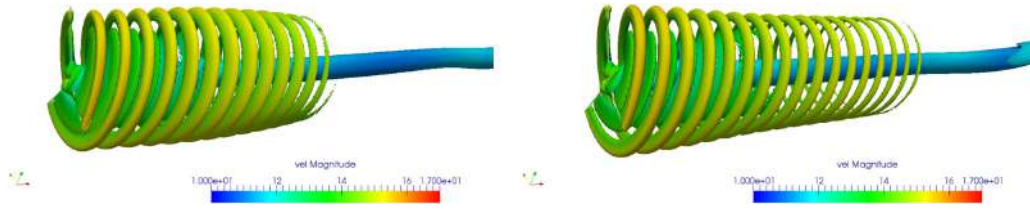


FIGURE 39 Aerodynamic quantities for the last cycle of a prescribed surge motion of the floater. Solid lines represent MIRAS-HAWC2 simulations while dashed lines represent HAWC2-BEM. (a) Amplitude of 15 m and different frequencies. Wind speed of 8 m/s. (b) Amplitude of 15 m and different frequencies. Wind speed of 15 m/s. (c) Frequency of 0.01419 Hz and different amplitudes. Wind speed of 8 m/s. (d) Frequency of 0.01419 Hz and different amplitudes. Wind speed of 15 m/s [Colour figure can be viewed at wileyonlinelibrary.com]

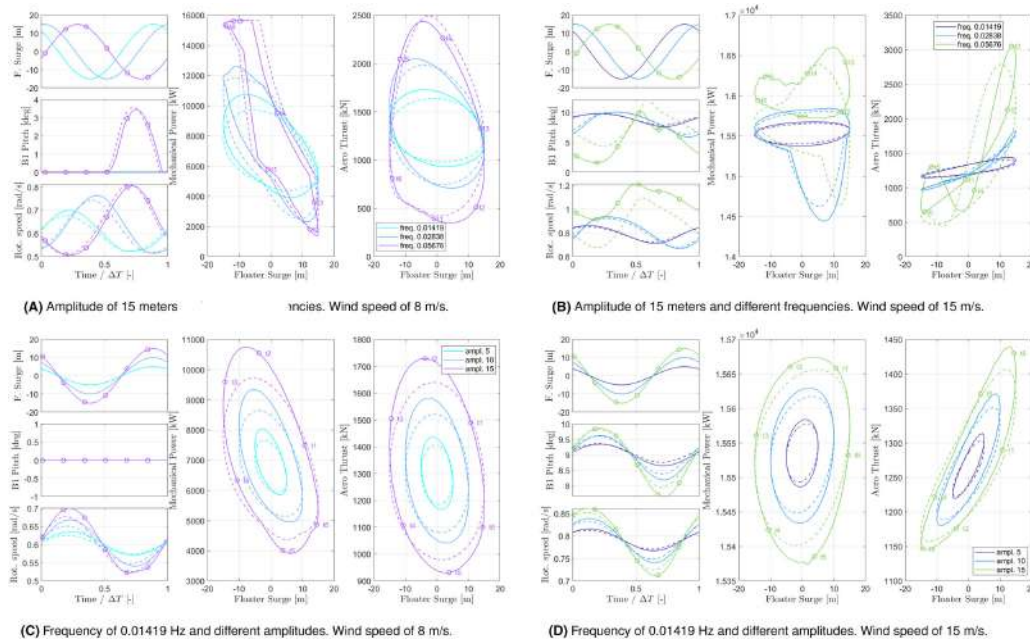


FIGURE 40 Three-dimensional iso-vorticity contours over the last cycle of a floater prescribed surge motion with and amplitude of 15 m and a frequency of 0.01419 Hz. (Left) t1 and (right) t5. Wind speed of 15 m/s [Colour figure can be viewed at wileyonlinelibrary.com]

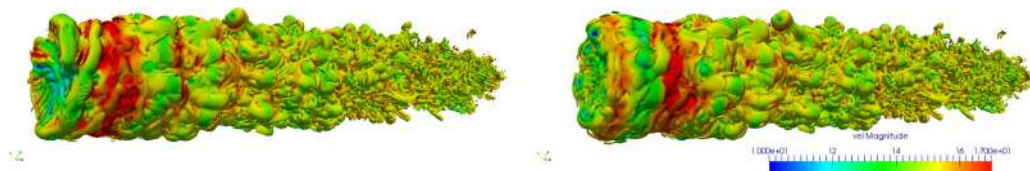


FIGURE 41 Three-dimensional vorticity contours over the last cycle of an extreme floater prescribed surge motion at 15 m/s. Amplitude of 15 m and a frequency of 0.11352 Hz. (Left) t3 and (right) t6 [Colour figure can be viewed at wileyonlinelibrary.com]

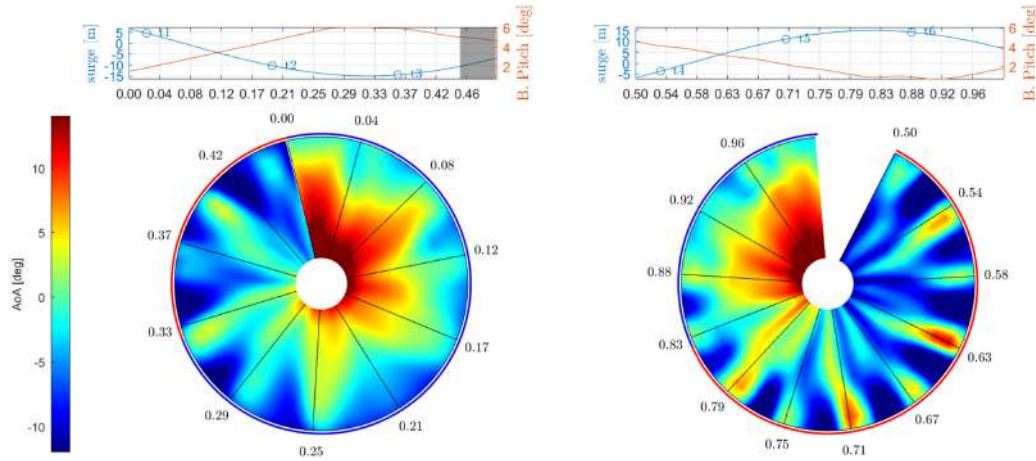


FIGURE 42 Annular distribution of the angle of attack during the last cycle of a prescribed surge motion of the floater with an amplitude of 15 m and a frequency of 0.11352 Hz. Wind speed of 15 m/s. Blade 1 [Colour figure can be viewed at wileyonlinelibrary.com]

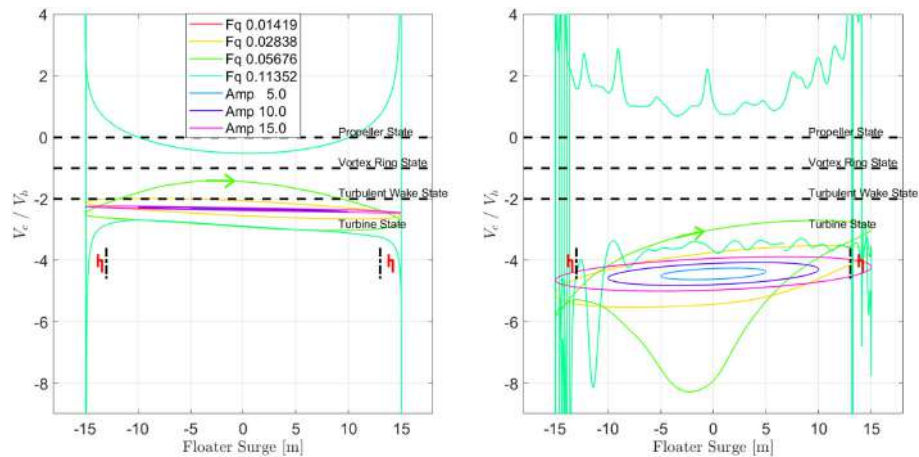


FIGURE 43 Computed inflow velocity ratio for the harmonic surge cases: (left) 8 m/s and (right) 15 m/s cases [Colour figure can be viewed at wileyonlinelibrary.com]

7.4 | Maximum blade and tower loads in surge

The analysis of maximum blade root and tower base bending moments showed very similar trends as for the pitch DoF, previously shown in Figure 31. Therefore, the results are not included in the interest of brevity.

7.5 | Wake analysis in surge

Regarding the influence of the surge frequency in the recovery of the wake, our investigation shows a very similar picture as in the pitch case with small variations as seen in Figure 44. At $x/R = 12$ for the motion at 0.01419 Hz, the wake recovery increases from 0.48 to 0.71 due to the surge motion in the 8 m/s case. The main differences to the pitch case are observed in the amplitude investigation, depicted in Figure 45 for a

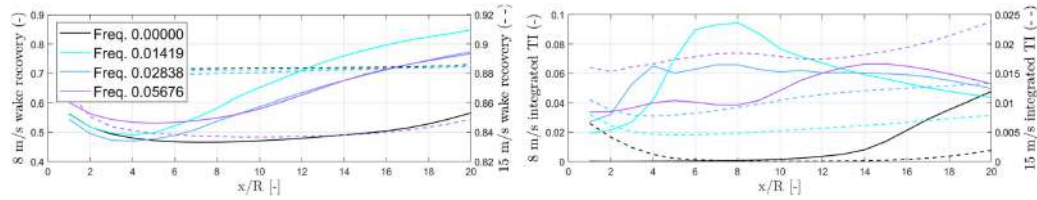


FIGURE 44 Wake analysis for a prescribed surge motion of the floater with an amplitude of 15 m and different frequencies at wind speeds of 8 m/s (solid lines) and 15 m/s (dashed lines). (Left) Wake velocity recovery; (right) Integrated Turbulent Intensity [Colour figure can be viewed at wileyonlinelibrary.com]

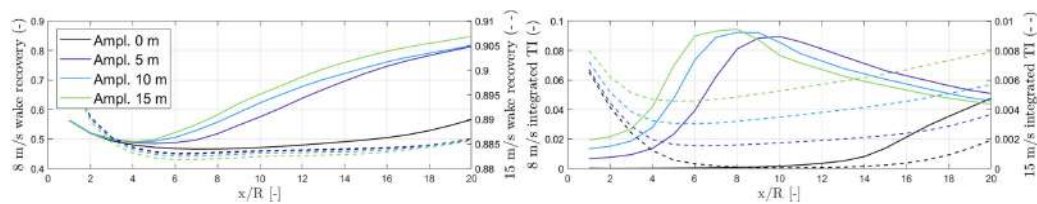


FIGURE 45 Wake analysis for a prescribed surge motion of the floater with a frequency of 0.02441 Hz and different amplitudes at wind speeds of 8 m/s (solid lines) and 15 m/s (dashed lines). (Top) Wake velocity recovery; (bottom) Integrated Turbulent Intensity [Colour figure can be viewed at wileyonlinelibrary.com]

prescribed surge motion with amplitudes of 5, 10, and 15 m at a frequency of 0.01419 Hz, in the vicinity of the natural frequency of the WindCrete floater. Here, we can observe larger differences than for the pitch case in above-rated conditions, i.e., 15 m/s. In the surge case, the amplitude of the motion does not seem to have as strong effect in the recovery of the wake although the TI level is clearly affected by it, contrary to what has earlier been observed during the pitch study.

8 | CONCLUSION

A detailed investigation of the floating IEA Wind 15 MW reference wind turbine and its wake has been carried out under a large variety of conditions. The main numerical approach relied on the in-house multi-fidelity vortex solver MIRAS, equipped with a LL aerodynamic model and coupled with the multi-body finite-element solver HAWC2. The investigation was divided in four parts: (i) simulations of the turbine mounted on the WindCrete floater; (ii) study of the effect of mean tilt in the wake development; (iii) parametric study under prescribed platform pitch; and (iv) under prescribed surge motion of the assembly. Throughout the investigation, the turbine behavior predicted by the MIRAS-HAWC2 coupling has been compared against the HAWC2-BEM lower fidelity method. In HAWC2-BEM, the aerodynamic loads were estimated with the BEM approach, which is considered an industry standard, while the same structural model was kept. The systematic comparison of MIRAS-HAWC2 and HAWC2-BEM approaches allow to assess the influence of the accuracy of the aerodynamic modeling under a large variety of floating conditions.

The aero-hydro-servo-elastic simulations showed the largest differences between the codes for high wind speeds under regular waves. Regarding the influence of the wave characteristics, in general, it has been found that differences between BEM and LL methods are more sensitive to variations in wave frequency than in wave amplitude, with the BEM predictions deviating considerably from the LL solution at high wave frequencies, where BEM over-predicts the maximum amplitude of the motion by more than a 50%.

The analysis of the effect of mean tilt in the wake development has confirmed that a positive tilt angle deflects the wake upwards, promoting the wake stretching and helping break down the cylindrical wake shape, which leads to a faster wake recovery. The recovery has been quantified as function of the downwind position for three tilt angles. For a tilt angle of 10° , the recovery is 0.52 at a distance of 12 rotor radii, relative to a value of 0.45 for the 0° case.

During the parametric study under prescribed pitch motion, it was found that the largest relative differences between the codes appear during the backward motion of the rotor, where the BEM method can violate the momentum balance assumption. The largest absolute differences between the codes have generally been found at the maximum thrust and power values during the forward motion of the turbine. Regarding the

rotor flow, it has been observed that the outer part of the blades are more prone to local vortex ring state in below-rated conditions and high frequency motions. Wake recovery is enhanced by the pitch motion, since the rotor motion accelerates the mixing and breakdown of the tip vortices. A relation between short time intervals of large FA blade tip displacements and a faster break down of the wake has been demonstrated. For the case of 0.02838 Hz pitch motion at 6.38° amplitude, the wake recovery at a 12 R distance downstream increased from 0.48 to 0.63 at 8 m/s. It was further found that in terms of the wake recovery, slow oscillations have shown to be more beneficial than high frequency ones. The latter ones can produce a stronger and more stable wake, which recovers slower than in the steady case without motion. This effect is more pronounced in the surge motion, in which the delay is maintained in the far wake, contrary to what was observed for the pitch case. It has been shown that a pitching wind turbine can transition throughout all possible rotor states. Moreover, inverted rotor states have been identified and defined during a cycle with high frequency pitch motion. In this regime, negative thrust and strong blade oscillations can occur during the motion cycle. While the structural loads generally compared quite well between the BEM and vortex code results, this case showed substantial differences.

Regarding the surge investigation, it has been found that a surging rotor has, in general, a very similar behavior to a pitching one. Surge motion of 15 m amplitude at 0.01419 Hz increased the wake recovery from 0.48 to 0.71 at $x = 12R$ and 8 m/s. However, there are clear differences in the generated wake due to the translatory nature of the surge movement. The wake of a surging turbine seems to be less prone to local vortex ring state compared to the wake of a pitching turbine. Additionally, an accordion-like effect has been clearly identified in some of the presented cases. Regarding the wake recovery, the amplitude of the surge motion does not have a strong effect in the recovery of the wake for the investigated frequencies.

Overall, the study demonstrates the applicability of vortex solvers to supplement and detail the Engineering calculations offered by BEM methods for the loads and energy yield of floating wind turbines. The generic nature of the study allows generalization to arbitrary floater designs, based on their natural frequencies in surge and pitch and the associated typical motion amplitudes. While our choice of a non-turbulent inflow allows for a clear investigation of the motion-induced wake mixing, the inclusion of such inflow turbulence is a natural next step. A further extension includes a detailed study of the turbine response for a second turbine within the wake of the present computations. These effects are subject to our present research and will provide further insight into the performance and wake effects in floating wind farms.

ACKNOWLEDGMENTS

This work was carried out as part of the COREWIND project (<https://corewind.eu>), which has received funding from the European Union's Horizon 2020 Research and Innovation programme under Grant Agreement No. 815083. This funding is gratefully acknowledged. The authors would also like to acknowledge the support from the Department of Wind Energy, Technical University of Denmark. The authors would like to thank Georg Pirrung for his contribution to the further development of the dynamic inflow model in the BEM solver and for his great insight regarding the instability analysis. We would like to extend our gratitude to our colleagues Fanzhong Meng and David Verelst for their help tuning up the HACW2 model.

PEER REVIEW

The peer review history for this article is available at <https://publons.com/publon/10.1002/we.2682>.

DATA AVAILABILITY STATEMENT

Data available on request from the authors.

ORCID

Néstor Ramos-García  <https://orcid.org/0000-0002-8326-2174>

REFERENCES

1. Breton S-P, Moe G. Status, plans and technologies for offshore wind turbines in Europe and North America. *Renew Energy*. 2009;34(3):646-654.
2. Mostafaeipour A. Feasibility study of offshore wind turbine installation in Iran compared with the world. *Renew Sustain Energy Rev*. 2010;14(7):1722-1743.
3. Ochieng E, Melaine Y, Potts S, et al. Future for offshore wind energy in the United Kingdom: The way forward. *Renew Sustain Energy Rev*. 2014;39:655-666.
4. Colmenar-Santos A, Perera-Perez J, Borge-Diez D, de Palacio Rodríguez C. Offshore wind energy: A review of the current status, challenges and future development in Spain. *Renew Sustain Energy Rev*. 2016;64:1-18.
5. Jonkman J, Musial W. Offshore code comparison collaboration (OC3) for IEA Task 23 offshore wind technology and deployment, technical report NREL/TP-5000-48191, National Renewable Energy Laboratory, 2010.
6. Corniglian R, Harris J, Peyrard C, Capaldo M. Comparison of the free vortex wake and actuator line methods to study the loads of a wind turbine in imposed surge motion. *J Phys: Conf Ser*. 2020;1618:052045.
7. Rodríguez SN, Jaworski JW. Strongly-coupled aeroelastic free-vortex wake framework for floating offshore wind turbine rotors. part 2: Application. *Renew Energy*. 2020;149:1018-1031.

8. Xu BF, Wang TG, Yuan Y, Cao JF. Unsteady aerodynamic analysis for offshore floating wind turbines under different wind conditions. *Philos Trans Royal Soc A: Math Phys Eng Sci.* 2015;373(2035):20140080.
9. Vaal J, Hansen M, Moan T. Effect of wind turbine surge motion on rotor thrust and induced velocity. *Wind Energy.* 2014;17(1):105-121.
10. Sivalingam K, Martin S, Singapore Wala AA. Numerical validation of floating offshore wind turbine scaled rotors for surge motion. *Energies.* 2018;11(10):2578.
11. Tran TT, Kim D-H. Fully coupled aero-hydrodynamic analysis of a semi-submersible fowt using a dynamic fluid body interaction approach. *Renew Energy.* 2016;92:244-261.
12. Sebastian T, Lackner M. Characterization of the unsteady aerodynamics of offshore floating wind turbines. *Wind Energy.* 2013;16:339-352.
13. Kyle R, Lee YC, Früh W-G. Propeller and vortex ring state for floating offshore wind turbines during surge. *Renew Energy.* 2020;155:645-657.
14. Lienard C, Boisard R, Daudin C. Aerodynamic behavior of a floating offshore wind turbine. *AIAA J.* 2020;58(9):3835-3847.
15. Thomas S, Matthew L. Offshore floating wind turbines - an aerodynamic perspective, in *49th Aiaa Aerospace Sciences Meeting Including the New Horizons Forum and Aerospace Exposition - 2011, p. 27 pp., 2011.*
16. Wolkovitch J. Analytical prediction of vortex-ring boundaries for helicopters in steep descents. *J Am Helicopter Soc.* 1972;17(3):13-19.
17. Dong J, Viré A. Predicting the occurrence of the vortex ring state for floating offshore wind turbines. *J Phys: Conf Ser.* 2020;1618:052044.
18. Sørensen JN, Shen WZ, Munduate X. Analysis of wake states by a full-field actuator disc model. *Wind Energy.* 1998;1(2):73-88.
19. Kopperstad KM, Kumar R, Shoele K. Aerodynamic characterization of barge and spar type floating offshore wind turbines at different sea states. *Wind Energy.* 2020;23(11):2087-2112.
20. Rockel S, Camp E, Schmidt J, Peinke J, Cal RB, Hölling M. Experimental study on influence of pitch motion on the wake of a floating wind turbine model. *Energies.* 2014;7(4):1954-1985.
21. Rockel S, Peinke J, Hölling M, Cal RB. Wake to wake interaction of floating wind turbine models in free pitch motion: An eddy viscosity and mixing length approach. *Renew Energy.* 2016;85:666-676.
22. Fu S, Jin Y, Zheng Y, Chamorro LP. Wake and power fluctuations of a model wind turbine subjected to pitch and roll oscillations. *Appl Energy.* 2019;253:113605.
23. Gaertner E, Rinker J, Sethuraman L, Zahle F, Anderson B, Barter G, Abbas N, Meng F, Bortolotti P, Skrzypinski W, Scott G, Feil R, Bredmose H, Dykes K, Shields M, Allen C, Viselli A. Definition of the IEA Wind 15-Megawatt Offshore Reference Wind Turbine, tech. rep., National Renewable Energy Laboratory, 2020.
24. Mahfouz M, Salari M, Hernández S, Vigará F, Molins C, Trubat P, Bredmose H, Pegalajar-Jurado A. COREWIND D1.3: Public design and FAST models of the two 15MW floater-turbine concepts, tech. rep., University of Stuttgart, 2020.
25. Ramos-García N, Sørensen JN, Shen WZ. Three-dimensional viscous-inviscid coupling method for wind turbine computations. *Wind Energy.* 2016;19(1):67-93.
26. Sessarego M, Ramos-García N, Sørensen JN, Shen WZ. Development of an aeroelastic code based on three-dimensional viscous-inviscid method for wind turbine computations. *Wind Energy.* 2017;20(7):1145-1170.
27. Ramos-García N, Hejlesen MM, Sørensen JN, Walther JH. Hybrid vortex simulations of wind turbines using a three-dimensional viscous-inviscid panel method. *Wind Energy.* 2017;20(11):1871-1889.
28. Ramos-García N, Spizet HJ, Sørensen JN, Walther JH. Vortex simulations of wind turbines operating in atmospheric conditions using a prescribed velocity-vorticity boundary layer model. *Wind Energy.* 2019;21(11):1216-1231.
29. Ramos-García N, Sessarego M, Horcas S. Aero-hydro-servo-elastic coupling of a multi-body finite-element solver and a multi-fidelity vortex method. *Wind Energy.* 2020.
30. Øye S. Dynamic stall simulated as a time lag of separation, in *Proc. of EWEC, Thessaloniki, Greece, 1994.*
31. Bæk P. *Unsteady Flow Modeling and Experimental Verification of Active Flow Control Concepts for Wind Turbine Blades.* PhD thesis, Technical University of Denmark, May 2012.
32. Hejlesen M, Rasmussen J, Chatelain P, Walther J. A high order solver for the unbounded poisson equation. *J Comput Phys.* 2013;252:458-467.
33. Larsen TJ, Hansen AM. *HAWC2 - User manual,* July 2015. DTU-Risø-R-1597.
34. Shabana AA. *Computational Dynamics.* Seconded. John Wiley & Sons, Inc; 2001.
35. Newmark NM. A method of computation for structural dynamics. *J Eng Mech ASCE.* 1959;85(EM3):67-94.
36. Manolas D, Riziotis V, Voutsinas S. Assessment of 3D aerodynamic effects on the behaviour of floating wind turbines. *J Phys: Conf Ser.* 2014;555:012067.
37. Popko W, Vorpahl F, Zuga A, et al. Offshore code comparison collaboration continuation (OC4), Phase I - Results of coupled simulations of an offshore wind turbine with jacket support structure, in *the Twenty-second International Offshore and Polar Engineering Conference,* 2012.
38. Robertson A, Jonkman J, Vorpahl F, et al. Offshore code comparison collaboration continuation within IEA wind task 30: Phase II results regarding a floating semisubmersible wind system: Preprint, in *The 33rd International Conference on Ocean, Offshore and Arctic Engineering,* 2014.
39. Leishman J, Beddoes T, W. H. Ltd. A generalised model for airfoil unsteady aerodynamic behaviour and dynamic stall using the indicial method, 1986.
40. Madsen HA, Larsen TJ, Pirrung GR, Li A, Zahle F. Implementation of the blade element momentum model on a polar grid and its aeroelastic load impact. *Wind Energy Sci.* 2020;5(1):1-27.
41. Morison JR, O'Brein MP, Johnson JW, Schaaf SA. The Force Exerted by Surface Waves on Piles. *J Petrol Tech.* 1950;2(05):149-154.
42. Hansen M, Henriksen L. *Basic DTU Wind Energy controller.* Denmark: DTU Wind Energy, 2013. Contract Number: EUDP project Light Rotor; Project Number 46-43028-Xwp3 The report number is DTU-Wind-Energy-Report-E-0028 and not DTU-Wind-Energy-Report-E-0018 as stated inside the report.
43. Vigará F, Cerdán L, Durán R, Muñoz S, Lynch M, Doole S, Molins C, Trubat P, Guanache R. COREWIND D1.2: Design Basis, tech. rep., ESTEYCO, 2019.
44. Larsen TJ, Hanson TD. A method to avoid negative damped low frequent tower vibrations for a floating, pitch controlled wind turbine. *J Phys: Conf Ser.* 2007;75:012073.
45. Henriksen L, Tibaldi C, Bergami L. DTU wind energy technical report, technical report, DTU Wind Energy, 2015.
46. Gözcü O, Verelst DR. The effects of blade structural model fidelity on wind turbine load analysis and computation time. *Wind Energy Sci.* 2020;5(2):503-517.

47. van der Laan MP, Andersen SJ, Ramos García N, et al. Power curve and wake analyses of the vestas multi-rotor demonstrator. *Wind Energy Sci.* 2019; 4(2):251-271.
48. Volk DM, Kallesøe BS, Johnson S, Pirrung GR, Riva R, Barnaud F. Large wind turbine edge instability field validation. *J Phys: Conf Ser.* 2020;1618: 052014.
49. Wise AS, Bachynski EE. Wake meandering effects on floating wind turbines. *Wind Energy.* 2020;23(5):1266-1285.
50. Leble V, Barakos GN. Forced pitch motion of wind turbines. *J Phys: Conf Ser.* 753 022042. 2016;753:022042.
51. Eggleston DM, Stoddard FS. *Wind Turbine Engineering Design.* New York: Van Nostrand Reinhold; 1987.

How to cite this article: Ramos-García N, Kontos S, Pegalajar-Jurado A, González Horcas S, Bredmose H. Investigation of the floating IEA Wind 15 MW RWT using vortex methods Part I: Flow regimes and wake recovery. *Wind Energy.* 2021;1-37. doi:10.1002/we.2682

5 Comparative study of the floating IEA Wind 15MW RWT with MIRAS-HAWC2 farm and FAST.Farm

In this chapter, a comparative study is carried out between different fidelities of farm simulation tools, MIRAS-HAWC2 farm Ramos-García *et al.* (2022) and FAST.Farm Jonkman & Shaler (2020). This work could be the basis for further studies on floating offshore wind farm (FOWF) simulations of different fidelities. The IEA 15MW wind turbine coupled with the WindCrete platform is used within the study. The public design of the FOWT Mahfouz *et al.* (2021) Mahfouz *et al.* (2020b) is modelled in OpenFAST v3.0.0 NREL (2021) which is included in the official release of FAST.Farm. The controllers used in the OpenFAST model and the HAWC2 model, are similar with minor differences to be compatible with each of the tools. Two FOWTs with 15R (rotor radius) distance are set-up. Operation of WTs, and wake wind fields at 10R and 14R are investigated at two turbulence intensity (TI) with a fixed and a floating platform.

Structural and operation differences of the IEA 15MW RWT HAWC2 and OpenFAST models coincides with the outputs found in Rinker *et al.* (2020). In this work, the blades are modelled in both tools without including the full stiffness matrix, using ElastoDyn for OpenFAST and H2-PTNT for HAWC2. Wake and flow modelling of MIRAS is explained in chapter 4 in detail. FAST.Farm makes use of several principles of dynamic wake meandering with additional implementations to negate its shortcomings Shaler & Jonkman (2021). As a result, the high fidelity MIRAS solver is more computationally expensive than the medium fidelity FAST.Farm due to physics involved in its solver. FAST.Farm parameterization and wind farm set-up is shortly explained in the next sub-chapter.

5.1 FAST.Farm model of the IEA 15 MW with the WindCrete platform

The inflow wind and wake modules of FAST.Farm are set-up following the recommendations given by NREL in its documentation. However, to make the results of FAST.Farm and MIRAS more comparable, certain changes on time-step and spatial resolution are made. In the inflow wind module, 2s and 0.25s time step for low- and high-resolution wind interpolation are chosen respectively. Although low-resolution time step can be higher and still capture wake dynamics, this value provides better comparison of wake wind fields between the tools. The low-resolution wind field, which is 720m in width, is divided into 128 spatial nodes in the Y- and Z-directions. The same corresponding spacing is used for the X-direction. For higher computational efficiency, the spacing can be increased even more according to the recommendations. High-resolution wind field has the same spacing as low-resolution which is slightly lower than highest chord length. Figure 20 illustrates the wind farm set-up, where wind turbines are located in the middle of high-resolution areas denoted as white box.

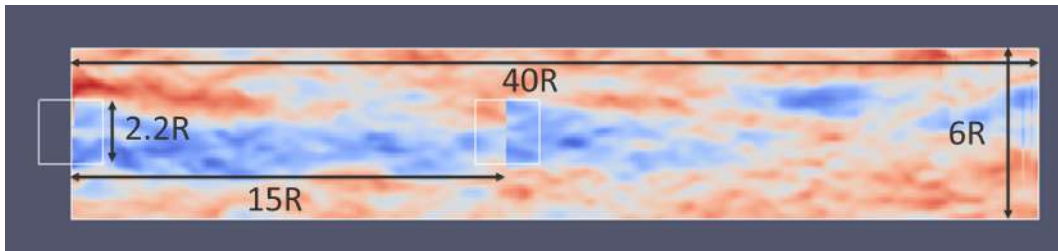


Figure 20: Wind farm set-up in FAST.Farm

Wake dynamics include many calibration parameters that defines wake advection, deflection, near-wake correction, eddy viscosity and wake meandering. These parameters are all taken as *default*, whereas the wake plane parameters are set-up to fit this wind turbine diameter and wind farm size.

5.2 Simulation load cases and wind fields

Load cases chosen for this work are at 8 m/s undisturbed mean wind speed for different TI and platform status and summarized in Table 6. In order to minimize the controller effect on two different simulation models, a below rated wind speed was chosen. Addition of platform motions on the wake wind field and consequently WT2 operation and power production are analysed by comparison. Simulations are carried out at ambient TIs of 7.3% and 14.4% to identify additional effects at varying levels of TI.

Table 6: Load case matrix with permutation of TI and platform status

| Load Case | Wind Speed [m/s] | TI [%] | Platform Status |
|-----------|------------------|--------|-----------------|
| LC 1 | 8 | 7.3 | Fixed |
| LC 2 | 8 | 7.3 | Floating |
| LC 3 | 8 | 14.4 | Fixed |
| LC 4 | 8 | 14.4 | Floating |

A Mann box has been used to define a representative turbulent inflow, which has been scaled to obtain different TI levels. In order to simulate a turbulent inflow in MIRAS, the velocity-based Mann box is transformed into a particle cloud. This cloud is slowly released one diameter upstream the turbine and it develops as it convects downstream towards the rotor plane. The released turbulent particles interact freely with the turbine and its wake. In order to create an equivalent turbulent box that can be used in the FAST.Farm model, the Mann boxes are simulated in MIRAS without turbines and the wake wind field at the 0R location is extracted and used as inflow in FAST.Farm. Wake wind fields at 10R and 14R are extracted and they are used for flow comparison between the tools.

5.3 Results and discussion

5.3.1 Comparison of upwind wind turbines

In the beginning of the simulations, a certain amount of time is needed for wind turbines to start-up and reach operational rotor speeds. Around 500s is sufficient for WT1; however, more time is needed for the wake to reach WT2. Figure 21 shows the comparison of MIRAS and FAST.Farm for WT1 operation, which indicates that both turbines are experiencing the same wind fields without any time delay. It is evident that there are slight differences in rotor speed and generated power, due to the differences in solvers. These differences are consistent with the paper from Rinker Rinker *et al.* (2020).

As expected, rotor speed and power generation of floating cases show higher fluctuations than fixed ones. Statistical analysis of the results are included in the next subsection.

5.3.2 Comparison of downwind wind turbines

The response of the downwind WTs located at 15R are shown in Figure 22. The controller allows rotor speed as low as 5 rpm, which is why similar rotor speeds are observed for LC1 and LC3. There are no blade pitching for both models. When the platform is allowed to float, as in LC2 and LC4, downwind turbines experience higher rotor speeds and larger spikes in power. Unlike WT1, power generations of WT2 are quite different between the tools without any strong indication of similar trends. Therefore, statistical results are investigated in a comparative manner, followed by a closer inspection on the wake wind fields in the next sub-chapter.

Statistics of rotor speed and power are calculated for the last 600 seconds of simulations where the wakes are fully developed. Due to the slight differences of simulation models and tools, there

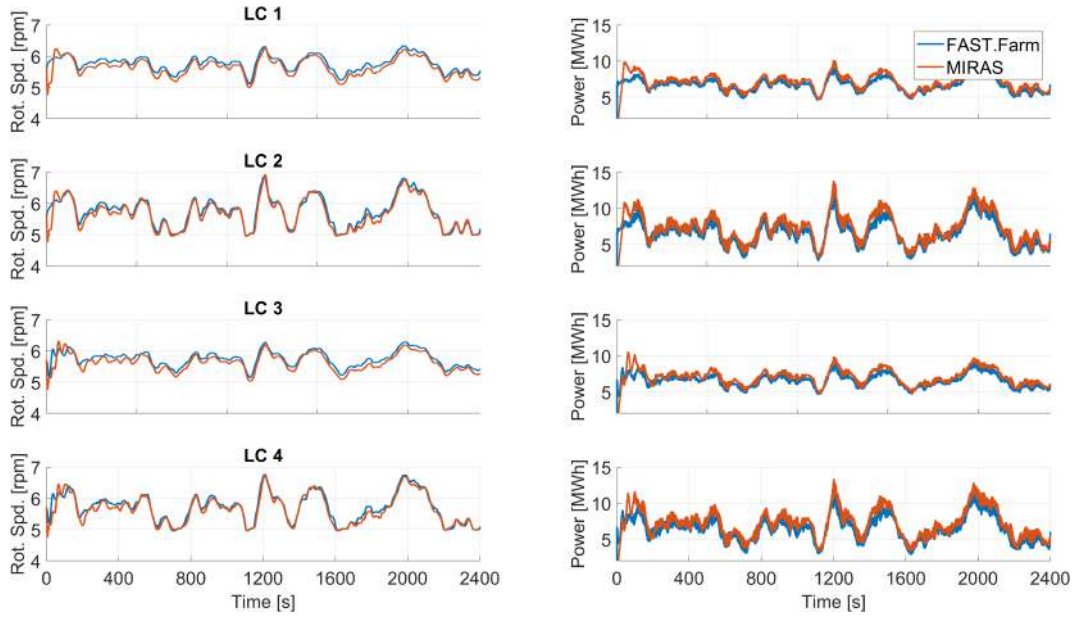


Figure 21: Comparison of MIRAS and FAST.Farm response of WT1

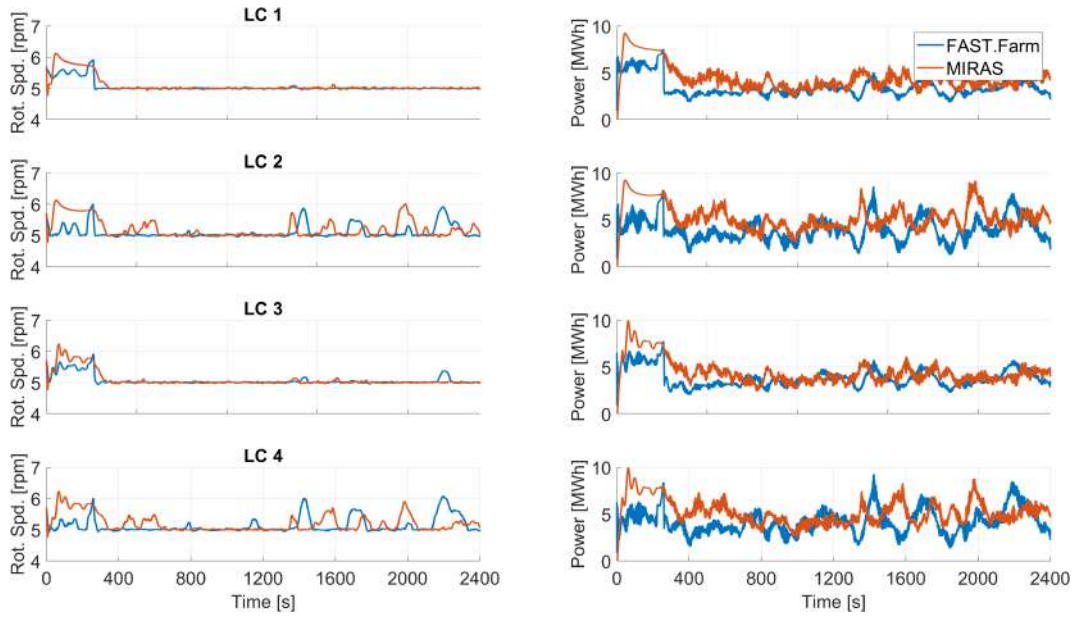


Figure 22: Comparison of MIRAS and FAST.Farm response of WT2

is a 0.1 rpm rotor speed and 0.4 MWh power generation difference between WT1 operation. When downwind WTs are compared, influences from wake and flow modelling as well as previously mentioned differences are summed. Moreover, differences in resulting wake deficit and position would lead to different average power generations. These reasons make it difficult to directly compare the power of downwind turbines between the tools. However, it is observed that WT2 produces up to 14% more power when floating in FAST.Farm simulations, whereas very small difference is observed for MIRAS. These differences are investigated by relating them to wake wind fields in the next sub-chapter.

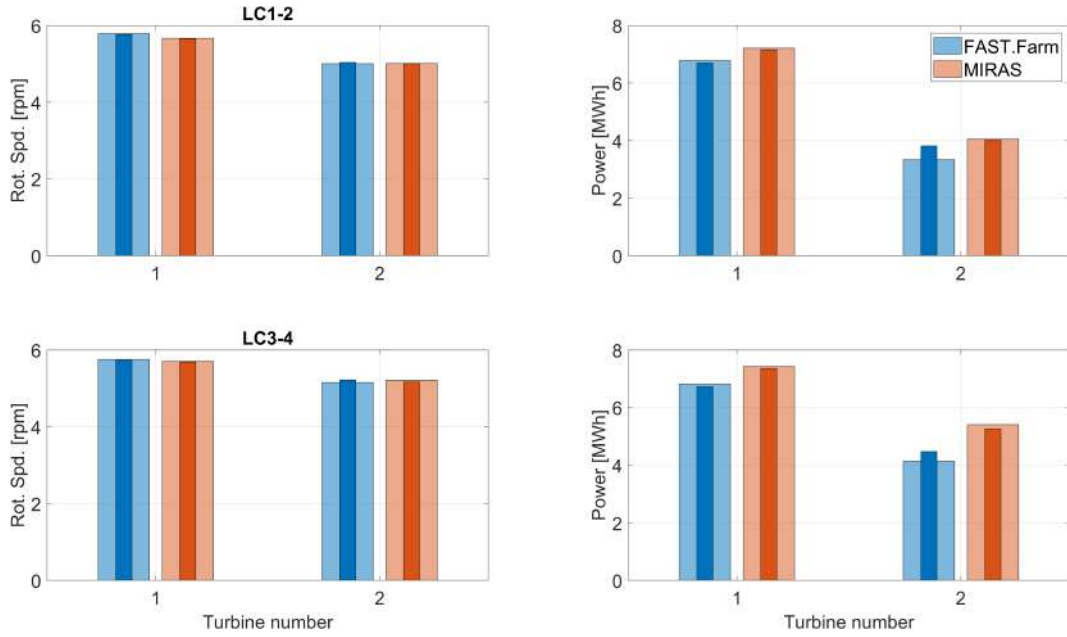


Figure 23: Average (last 600s) of MIRAS and FAST.Farm response for LC1-2 at top and LC3-4 at bottom (large and small bars represent fixed and floating, respectively)

5.3.3 Comparison of the wake wind fields

Within the wind fields presented in this sub-chapter, wind turbines hubs are aligned at 360m in Y-direction and 135m in Z-direction. For each node in the wake wind field, statistics of average wind speed and TI are calculated for the last 600 seconds. In LC1 and LC2, shown in Figure 24, the wake wind field of MIRAS shows more mixing with ambient wind field, less velocity deficit and higher turbulence. This could be traced to the lack of wake added turbulence in FAST.Farm.

In LC3 and LC4, where ambient TI is higher, MIRAS results show once again less velocity deficit. Conversely, FAST.Farm wake wind fields exhibit higher turbulence in the wake as shown Figure 25. The lack mixing in the wake is not as apparent as lower ambient TI cases. If the velocity deficit is over predicted at a spatial node, it is possible that meandering causes higher TI in the wake statistics. This should be further investigated by comparing the wake center position in a larger simulation study. Additionally, there are differences in wind field statistics even further away from the wake zone. This is because MIRAS considers the evolution of the vorticity of fluid particles, whereas FAST.Farm utilizes Taylors' frozen turbulence hypothesis with reduced velocity wake planes.

In all load cases, FAST.Farm wake wind fields exhibit higher deflection of wake in vertical direction. This is a significant difference compared to MIRAS wake wind fields, where wake is still concentrated at hub level. Such a deflection could have significant impact on power generation estimation and should be investigated in a larger study.

Finally, the wake wind field statistics are evaluated in terms of relative difference between the floating and the fixed cases. Mean wind speed difference between the floating and fixed cases for low TI at 10R is given in Figure 26. MIRAS wake wind field difference shows that wake deficit with floating and fixed is shifted slightly upwards for the given operational and environmental conditions. FAST.Farm exhibits more notable deflection in the wake which could be one of the reasons for higher power production in floating load cases.

In the end, this preliminary study shows several interesting differences between MIRAS-HAWC2 farm and FAST.Farm tool when simulating a FOWF. A more extensive simulation study to investi-

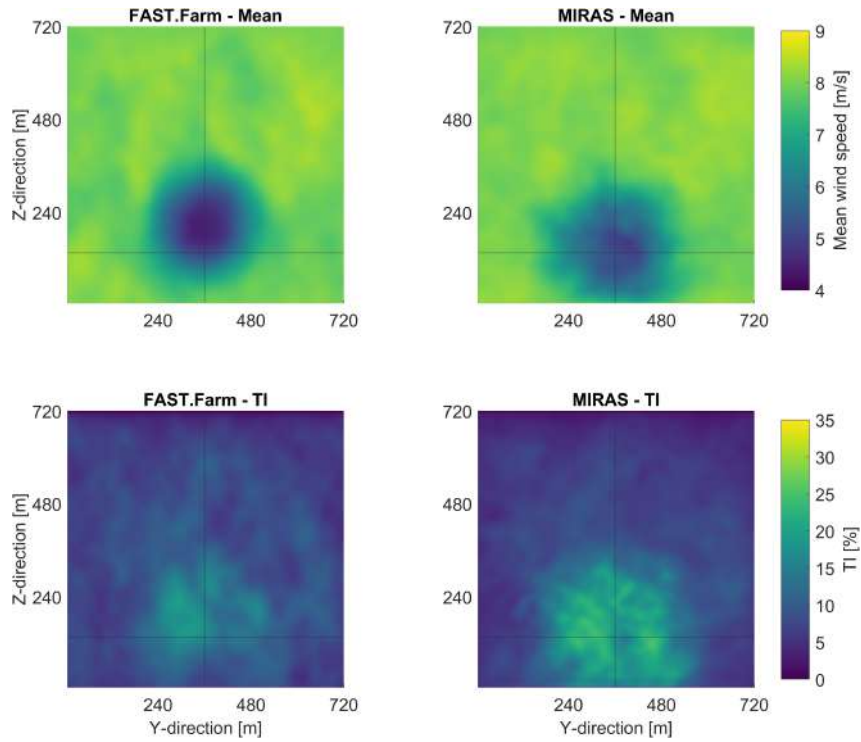


Figure 24: Cross-sectional mean wind speed and TI (last 600s) of MIRAS and FAST.Farm wind fields at 10R for LC2

gate the discussed topics could prove to be useful to better understand when to use a medium and a high fidelity tool. This can be further extended to a blind comparison including a calibration of FAST.Farm parameters to fit the results of MIRAS.

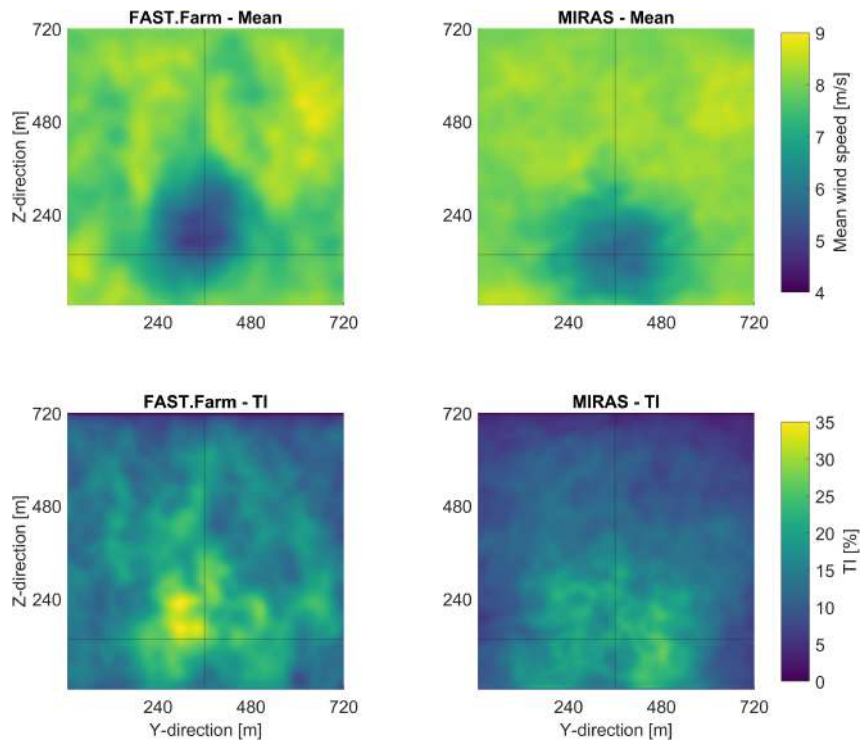


Figure 25: Cross-sectional mean wind speed and TI (last 600s) of MIRAS and FAST.Farm wind fields at 10R for LC4

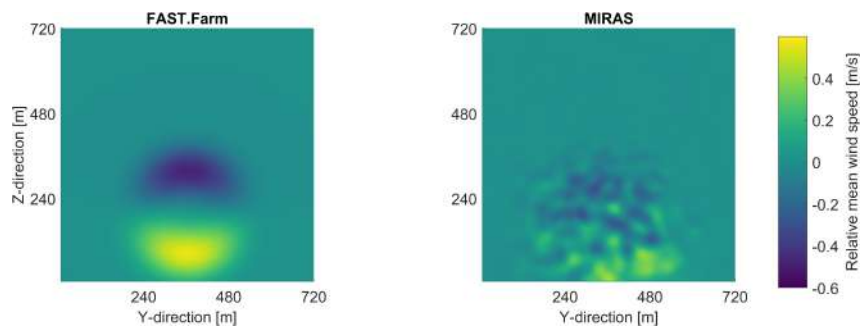


Figure 26: Cross-sectional relative mean wind speed (last 600s) difference of fixed and floating cases for MIRAS and FAST.Farm wind fields at 10R

6 Wind tunnel investigation of the wake of the floating IEA 15 MW RWT

The testing activity was carried out in the atmospheric boundary layer test section of the Politecnico di Milano wind tunnel (GVPM), which has dimensions: 13.84 m wide x 3.84 m high x 35 m long. The test setup is shown in Fig. 27. The turbine was mounted on a 6-DOFs robotic platform to enable forced motion.

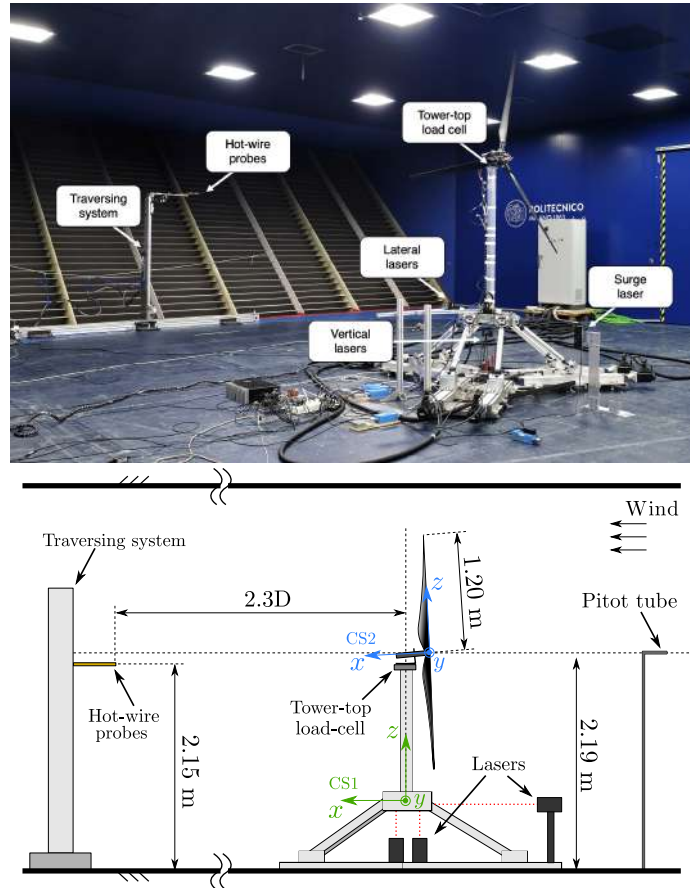


Figure 27: Experimental setup in the Polimi wind tunnel (left) and a schematic of the test setup with the coordinate systems (CS) used for measurements and their analysis (right).

6.0.1 Scale turbine design and specifications

The wind turbine is a 1:100 scale model of the IEA 15 MW. The turbine rotor was scaled to preserve the power C_P and thrust C_T coefficients of the reference turbine despite the reduction of size and a wind speed reduced of a factor of 3. The blade design is carried out to match the lift distribution along the span while preserving the tip-speed ratio. The blade chord is increased with respect to the full-scale rotor of reference preserving the original distribution; the twist distribution is altered to have the target non-dimensional lift force. The turbine tower, of 75 mm diameter, is rigid since the focus is on the effect of rotor motion associated with platform rather than with tower deformability. The turbine has individual blade-pitch control and variable-speed generator control. The blades were built to be rigid to exclude any aeroelastic interaction, which was outside of the scope of this

research. The main properties of the turbine model are resumed in Table 7.

Table 7: Key parameters of the wind turbine model.

| Parameter | Unit | Value |
|----------------|------|-------|
| Rotor diameter | m | 2.400 |
| Blade length | m | 1.110 |
| Hub diameter | m | 0.180 |
| Rotor overhang | m | 0.139 |
| Tilt angle | ° | 5.000 |
| Tower-to-shaft | m | 0.064 |
| Tower diameter | m | 0.075 |
| Tower length | m | 1.400 |
| Nacelle mass | kg | 1.975 |
| Blade mass | kg | 0.240 |
| Rotor mass | kg | 2.041 |
| Tower mass | kg | 2.190 |

6.0.2 Measurements

The measurements taken in the tests are shown in Fig. 27 and are: interface forces between tower-top and nacelle by a 6-components load cell, platform position by laser transducers, 3-components (u , v , and w) wind velocity in the wake by hot-wire probes. The two probes were moved in the cross-wind direction (Y) of CS1, from -1.6 m to $+1.6$ m with a discretization of 100 mm, at a fixed distance $X = 2.3D$, and $Z = 2.15$ m. The undisturbed wind velocity was measured by a pitot tube 7.15 m upstream of the turbine rotor, centerline, and hub height (not visible in the picture of Fig. 27). All measurements were sampled synchronously at 2 kHz and stored at model scale.

6.1 Load cases

The experiment considered two wind turbine functioning conditions resumed in Table 8: one is representative of below rated wind operations, where rotor speed is controlled to achieve the maximum power coefficient; and one for above rated wind, where the blade pitch angle is adjusted to regulate power at its rated value. Active turbine control was not used, and in all tests the blade pitch angle and rotor speed were constant. All tests were performed with constant inflow velocity and the turbulence intensity was around 2%.

Table 8: Wind turbine operating conditions considered in the experiment (CP is collective pitch), C_P and C_T are the power and thrust coefficients measured at steady state.

| Condition | Wind speed [m/s] | Rotor speed [RPM] | TSR [-] | CP [°] | C_P [-] | C_T [-] |
|------------------|---------------------|----------------------|------------|-----------|--------------|--------------|
| Below rated (BR) | 3.0 | 210 | 8.8 | 0.0 | 0.35 | 0.78 |
| Above rated (AR) | 5.0 | 216 | 5.4 | 11.5 | 0.13 | 0.20 |

For cases with motion, the turbine was forced to oscillate alternatively in the surge, sway, roll, pitch, and yaw degree-of-freedom (DOF). When the wind is constant and uniform in space, the effect of sway and heave in terms of apparent wind perceived by rotor is similar: one inclines the

velocity vector in the horizontal plane, and the other in the vertical plane. At the same time, the wind tunnel section is large compared to rotor ($A_{\text{rotor}}/A_{\text{tunnel}} = 0.08$) but its height is comparable to the rotor diameter ($D/h_{\text{tunnel}} = 0.62$) and this is cause of anisotropic blockage. In reason of these two considerations, the turbine was moved only in the sway direction. For every DOF motion was imposed at the frequency of the wave spectrum peak defined for the deployment site of Gran Canaria (i.e., 0.11 Hz corresponding to 3.175 Hz at model scale). It was decided to characterize the wake response for the wave frequency because the large hydrodynamic excitation is likely to produce large motions in this frequency range. Moreover, this complements the wind tunnel measurements of Fontanella *et al.* (2021) that focused on the wake-flow response with low-frequency surge motion.

One value of motion amplitude was considered for any wind condition. In case of surge and pitch, the amplitude was selected to have a normalized maximum apparent wind at hub height $\Delta u_{\text{hh}}/U_{\infty} = 0.05$, and this resulted in (surge below rated = 0.006 m, surge above rated = 0.013 m, pitch below rated = 0.25° , pitch above rated = 0.6°); in case of sway and roll, to to have a maximum wind misalignment at hub height $\alpha_{\text{hh}} = 4^{\circ}$ (sway below rated = 0.011 m, sway above rated = 0.018 m, roll below rated = 0.4° , roll above rated = 0.7°); in case of yaw motion to have a normalized maximum velocity of the rotor edge $\Delta u_R/U_{\infty} = 0.05$, with $\Delta u_R = 2\pi f_m A_m R$ (yaw below rated = 0.3° , yaw above rated = 0.6°).

6.2 Results about wake

This section describes results about hot-wire measurements. Focus of the analysis is the effect of platform motion on the axial velocity. This is examined because, in a wind farm perspective, it defines the inflow conditions for downstream turbines. Results are reported in the CS2 reference system of Fig. 27.

Figure 28 shows the average wake deficit normalized by the free-stream velocity U_{∞} at $X = 2.3D$ for the fixed turbine and with motion imposed at the wave peak frequency (3.175 Hz at model scale) for different DOFs. The wake shape is defined by the turbine operating condition, and it has a double-gaussian profile in below rated wind cases, and a gaussian profile in above rated-cases. In both conditions it is not symmetric with respect to the rotor axis, and velocity is generally lower for negative-Y. This asymmetric behavior was also present in the wake measurements of Fontanella *et al.* (2021), which were with a different rotor but in the same wind tunnel, and this supports the idea it is due to the wind tunnel characteristics more than the wind turbine model or the experimental setup. It can be caused by anisotropic blockage, which hinders the wake expansion on one side more than the other. The velocity at the wake extremities is about 15% higher than the free-stream velocity, and this is a consequence of blockage.

The wake with motion is compared to the fixed turbine case by the average wake deficit for the rotor area, defined as:

$$D_{\text{avg}} = \frac{1}{U_{\infty}} \left(\frac{\sum_{i=1}^N |y_i| U_i}{\sum_{i=1}^N |y_i|} \right), \quad (10)$$

with $y_i = -1.2, \dots, 1.2$, and $N = 25$. The results are reported in Table 9, and show that the average velocity across the rotor is slightly lower with motion compared to the fixed case. In a wind farm perspective, this means the energy in the flow available for a hypothetical floating turbine at 2.3D distance from the upstream unit working in fully-waked condition would be slightly less than in the bottom-fixed case. The bottom panels of Fig. 28 show the wake deficit increment with motion compared to the bottom-fixed case for different Y positions. This information might be used to compute the change in the radial distribution of aerodynamic loads for a waked floating turbine. In below rated wind, the velocity is lower in correspondence of the outer sections of the rotor, and increased outside it; the variation is about the same regardless of the type of motion. In above rated wind, the velocity is decreased between $Y = \pm(0.5-1)$ m, and the largest decrement is with sway, pitch, and yaw motion. Sway has the lowest difference for below rated but the highest difference for the above rated.

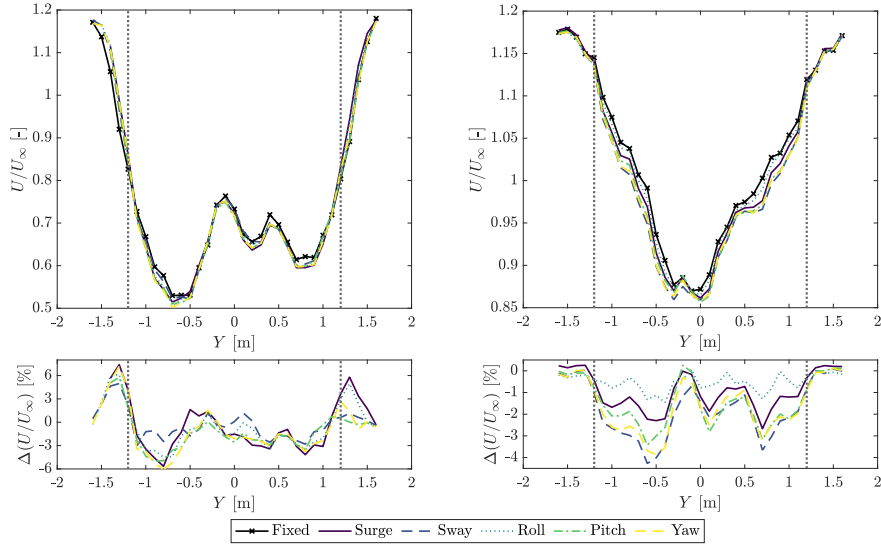


Figure 28: Average wake deficit at $X = 2.3D$ for the fixed case and with different motions, in below rated (top left) and above rated (top right) wind. $\Delta(U/U_\infty)$ is the wake deficit increment with motion with respect to the fixed case (below rated: bottom left; above rated: bottom right). The vertical dotted lines mark the edge of the rotor.

Numerical results of 4 and Fu *et al.* (2019) observed the wake recovery for a pitching turbine is different than in the bottom-fixed case: flow mixing is higher for a floating turbine because increased turbulence due to motion helps promoting a faster break down of the strong vortex structures. In this sense, Fig. 29 complements Fig. 28 by showing the turbulence kinetic energy (i.e., $k = \frac{1}{2}(\sigma_u^2 + \sigma_v^2 + \sigma_w^2)$), where σ_i is the variance of the i -th velocity component) at $X = 2.3D$ for the fixed turbine and with different types of force platform motion at the wave peak frequency. The distribution of k about the Y axis is given by the turbine operating condition and is consistent for the fixed and floating scenario. In below rated wind, most of the turbulence kinetic energy is concentrated around the edge of the rotor, and is associated with tip vortices. In above rated, k is maximum between $Y = -0.5$ - 0 m, which corresponds to the wake center, and the peak is likely associated with root vortices. k is non-symmetric, and is more pronounced at negative- Y . With motion, k is generally lower than for the bottom-fixed case, except at the rotor edge for the above-rated case. The high-frequency platform oscillations caused by response to wave forcing seems to produce a stronger

Table 9: Average wake deficit for the rotor area for the two wind conditions (below rated BR, above rated AR) and different motions at the wave frequency ($f_m = 3.175$ Hz). Δ is the percent change with motion with respect to the fixed case.

| Condition | BR | Δ BR | AR | Δ AR |
|-----------|-------|-------------|-------|-------------|
| | [-] | [%] | [-] | [%] |
| Fixed | 0.667 | - | 1.034 | - |
| Surge | 0.660 | -1.079 | 1.021 | -1.300 |
| Sway | 0.661 | -0.884 | 1.011 | -2.310 |
| Roll | 0.659 | -1.319 | 1.028 | -0.609 |
| Pitch | 0.657 | -1.604 | 1.015 | -1.876 |
| Yaw | 0.657 | -1.589 | 1.013 | -2.117 |

and more stable wake. The lower flow mixing makes the wake recover more slowly than without motion. This agrees with what was observed in 4 for pitch motion at 0.057 Hz (i.e., 1.622 Hz at model scale). The authors noticed that for lower motion frequencies differences between a bottom-fixed and floating turbine are significant for $x/D > 5$, but for higher frequencies the wake recovery is independent of the downstream location.

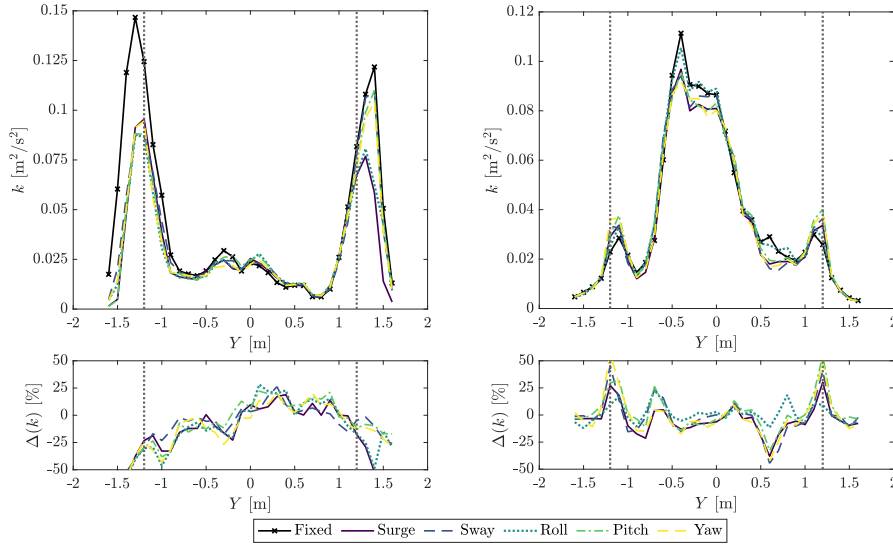


Figure 29: Turbulence kinetic energy at $X = 2.3D$ for the fixed case and with different motions, in below rated (left) and above rated (right) wind. $\Delta(k)$ is the turbulence kinetic energy increment with motion with respect to the fixed case (below rated: bottom left; above rated: bottom right). The vertical dotted lines mark the edge of the rotor.

Velocity fluctuations are expected to happen for different reasons with different types of motion. The dynamic component of the along-wind force (F_x in CS2 of Fig. 27) in one motion cycle for all load cases is shown in Fig. 30. The oscillations amplitude is large with surge and pitch motion, and negligible with all the other types of motion. With surge and pitch, wake-velocity fluctuations occur because of the dynamic inflow created by motion and the oscillating thrust force. With the motion in the other directions, the magnitude of the wind speed perceived by the rotor is similar to the fixed case, and oscillations of the axial velocity in the wake are explained as the effect of wake meandering: the velocity at a downstream location varies periodically because the wake is moved laterally and vertically. This occurs also with pitch and is superposed to the effect of dynamic inflow. The presence and relevance of velocity oscillations in the wake due to motion is assessed from the phase-averaged time series obtained by averaging data of 94 motion cycles. This way of processing data keeps the signal content which has the same periodicity of motion, filtering out the rest. The phase-averaged time series of the axial velocity u at $X = 2.3D$ and at $Y = 0R$ (center of the wake) is shown in Fig. 31. The figure also shows the harmonic component of u at the frequency of motion. In below rated wind the amplitude of velocity fluctuations associated with motion is small, less 1% of U_∞ , and similar in magnitude to the turbulence in the wake of the fixed turbine. In above rated wind the harmonic at the frequency of motion is clearly present with sway, roll and pitch. Sway and roll move the wake along the Y - Z plane and pitch moves the wake in X - Z plane. This may explain the periodically-varying axial velocity. In contrast, it seems that yaw does not move the wake center in a significant way. In wind farm control studies a static yaw is often used for redirecting the wake laterally, however oscillating yaw does not seem an effective way of disturbing the wake direction. The tracking methods for the wake center described by Coudou *et al.* (2018) was applied to measurements with sway and roll, and the wake center position obtained from the algorithm is

constant in time. If the wake core moves, the motion is smaller than the spatial resolution of wake data (i.e., 100 mm, or 10 m full-scale).

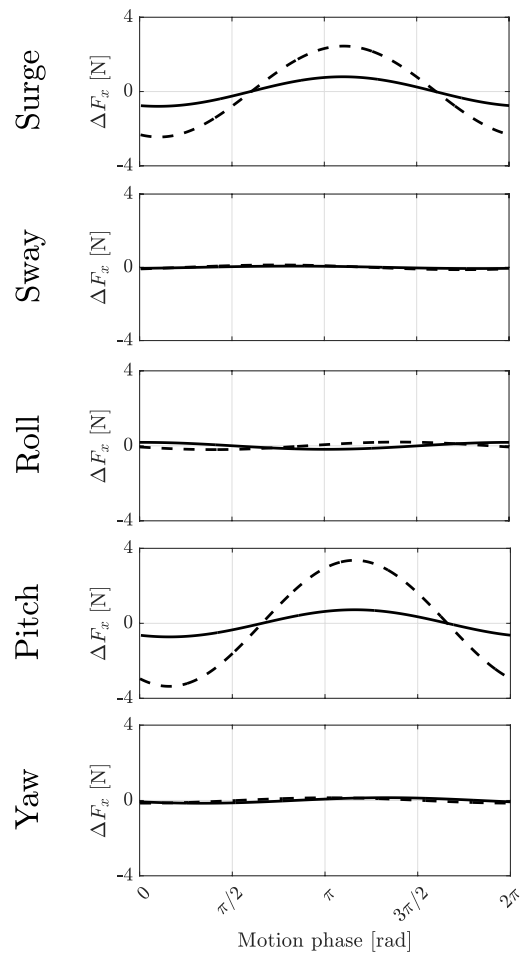


Figure 30: Harmonic component of the dynamic component of the along-wind force at hub (ΔF_x) at the frequency of motion in one period for different type of platform motion Solid line = below rated, dashed line = above rated.

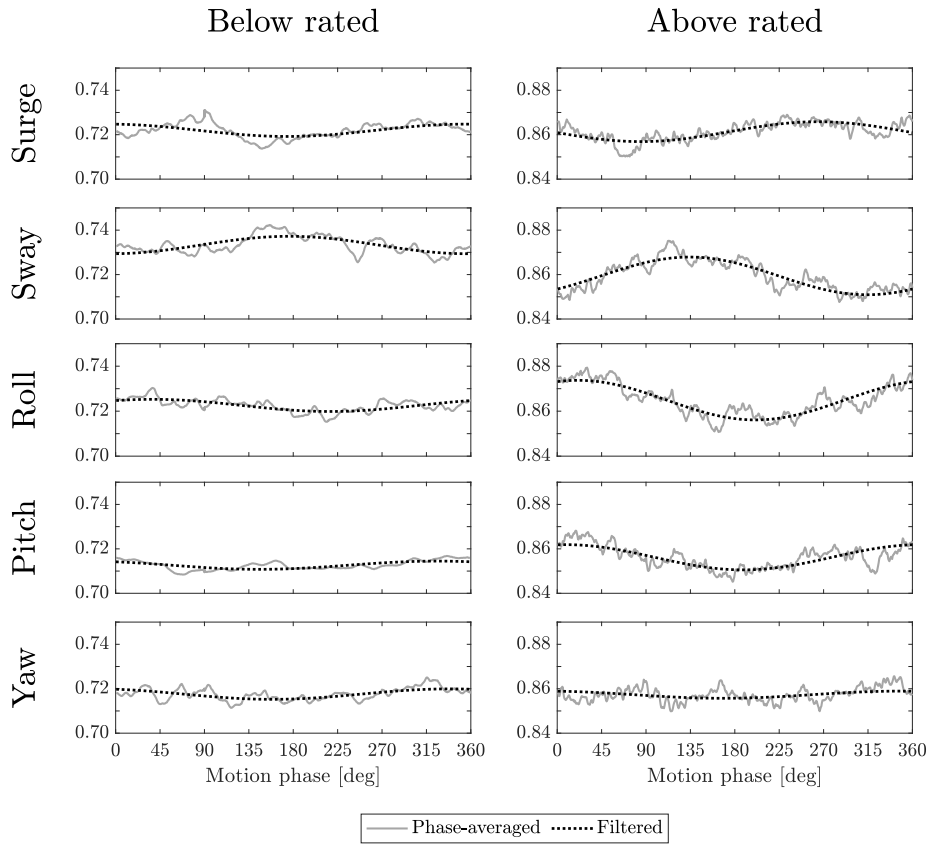


Figure 31: Time series of the axial velocity normalized by the free-stream wind speed u/U_∞ in one motion cycle at $X = 2.3D$ and $Y = 0R$ with different motions and in two wind conditions. Phase-averaged data of 94 motion cycles are compared to the harmonic of the signal at the frequency of motion (“Filtered”).

7 Investigation of the floating IEA Wind 15 MW RWT using vortex methods: Wake impact on downstream turbines under turbulent inflow

From the results of Chapter 4 and 5 it is clear that the wake behind a floating turbine is affected by the low-frequency floater motion. These motions occur at the natural frequencies of the floater. It can therefore be expected, that such frequencies will be common for the individual turbines in a farm. Hence, if the motion from a turbine induces a period perturbation of the wake at such a frequency, one could speculate that this could lead to resonant forcing of a downstream floating turbine.

Such resonance effects are the core of the present investigation, where the response of downstream turbines is studied. First, a tandem configuration is looked at with comparison between response to wakes of a bottom fixed and a floating turbine. The study differs from the one of Chapter 4 by inclusion of ambient turbulence and completely free response to wind forcing.

A second part of the study extends to five turbines in farm, where the resonance effects are investigated. We find that such resonance can occur at above-rated conditions. Further, quantification is made in terms of power and thrust.

The study has been submitted to Wind Energy in August 2021 and accepted 11 April 2022. It has been published with Open Access.

Investigation of the floating IEA wind 15-MW RWT using vortex methods Part II: Wake impact on downstream turbines under turbulent inflow

Néstor Ramos-García¹ | Sergio González Horcas¹ | Antonio Pegalajar-Jurado² | Stavros Kontos² | Henrik Bredmose²

¹Aero- and Fluid Dynamics section, Department of Wind Energy, Building 403, Technical University of Denmark, Kgs. Lyngby, DK-2800, Denmark

²Response, Aero-elasticity, Control and Hydrodynamics section, Department of Wind Energy, Building 403, Technical University of Denmark, Kgs. Lyngby, DK-2800, Denmark

Correspondence

Néstor Ramos-García, Department of Wind Energy, Fluid Mechanics Section, Building 403, Technical University of Denmark, DK-2800 Lyngby Denmark.
Email: nerga@dtu.dk

Funding information

H2020 European Research Council, Grant/Award Number: 815083

Abstract

The manuscript presents a novel numerical investigation on the impact of the wake of a floating IEA wind 15-MW reference wind turbine (RWT) on downstream machines using a state-of-the-art vortex solver coupled to a multi-body code. The coupling enables to account for the flexibility of the different turbine components as well as to include the effect of the controller and the dynamics of the floating support structure. First, the turbine is mounted on the WindCrete spar-buoy platform, and the wake impact on a second turbine positioned at different downstream positions is investigated and compared with the impact of the wake generated by a bottom-fixed machine. It is found that the faster breakdown of the vortex structures triggered by the motion of the floater in the upstream turbine increases the power production of a downstream machine, as well as its mean thrust level relative to normal operation downstream a bottom-fixed machine. It is demonstrated that this effect is drastically reduced with the increase of the turbulence intensity (TI). Further, simulations with a prescribed harmonic motion of the upstream turbine in surge and pitch under different turbulence levels are presented. It is found that the motion of the floater has a strong impact in the generated wake and consequently in the operation of downstream machines. In particular, downstream turbines experienced considerably higher blade loading that led to an increase of the aerodynamic power. Finally, aero-hydro-servo-elastic simulations of five turbines in a row have shown that the interaction between multiple floating machines is more dynamic than between bottom-fixed turbines. This has been mainly observed at high wind speeds, where the pitch and surge motions of the floater in turbines located deep inside the farm can be resonantly excited by the interaction with the wind farm flow. In practice, this means that the power and thrust variations increase with the turbine location depth inside the farm. Overall, the study highlights the importance of an accurate flow and wake modeling for the prediction of turbine-to-turbine interaction in a floating context.

This is an open access article under the terms of the [Creative Commons Attribution-NonCommercial-NoDerivs](https://creativecommons.org/licenses/by-nc-nd/4.0/) License, which permits use and distribution in any medium, provided the original work is properly cited, the use is non-commercial and no modifications or adaptations are made.
© 2022 The Authors. *Wind Energy* published by John Wiley & Sons Ltd.

KEYWORDS

floater, lifting line, offshore, turbine farm, vortex method, wakes, wind turbine

1 | INTRODUCTION

Offshore wind energy has the potential to deliver a huge amount of energy to power the world. Most of the available wind resources at sea are located in deep waters, where bottom-fixed machines are economically not viable. Floating turbines are slowly rising as an alternative with more competitive costs¹⁻³ and a larger energy market, which embraces ocean areas with depths of 60 m or more.⁴ However, the floater-induced rotor motion that a floating wind turbine is subjected to creates new challenges for engineers and researchers.⁵⁻⁷ Moreover, and due to the clustering of turbines usually seen in offshore projects, a better understanding of the physical phenomena that govern the complex interaction between multiple floating turbines through their wakes is necessary. This would allow to continue pushing the technology to new limits. The large turbine oscillations introduced by the floater have the potential to trigger a faster breakdown of the strong vortex structures shed by the turbine blades, thus accelerating the wake recovery. A quicker wake recovery would play a key role in the design of the farm layout, increasing its efficiency, and helping to reduce the economic cost. In summary, that could make floating wind an even more attractive alternative to other energy sources. On the other hand, such level of interaction between turbines that are not fixed to the sea bed can have unwanted effects. It can potentially excite specific motion modes of downstream machines and induce large oscillations, which could increase the ultimate and fatigue loads. There is therefore a high interest to identify, understand, and quantify these phenomena.

During the design of offshore wind turbines and the wind farm development, simulation tools are used to predict the coupled dynamic loads, the response of the offshore wind turbine structure⁸ and the interaction between the turbines. We summarize below different strategies that have been used to simulate the wakes and interaction of floating wind turbines utilizing different computational methods. Huang et al⁹ used an unsteady actuator line (AL) model coupled to a CFD solver to study the wake interaction between two floating offshore turbines. Similarly,¹⁰ performed AL LES (large-eddy simulations) of a floating offshore multi-turbine platform using a prescribed rigid-body motion of the system. Results showed that the floater pitching introduced a vertical wake meandering that was apparent in the periodic oscillations of the blade pitch angle and the thrust of the downstream machine. Johlas et al¹¹ used the same computational tool to better understand the wake effects of floating turbines. Their study showed that differences in the wake shape compared with that of a bottom-fixed machine were linked to mean platform displacements. Moreover, the authors associated turbulence variations to time-varying platform motions. The actuator line model of the blade can be seen as a lower fidelity level relative to a lifting line approach since it relies on a tip correction to correctly simulate the blade loading. Xiao and Yang¹² employed a LES wind field representation combined with the actuator-disk method and a high-order spectral wave potential-flow solver to study the effect of swell- and wave-induced turbine pitch motion on the statistics of wind turbulence and the wind-power extraction rate of a 3×3 floating wind farm. Their results showed that swell-induced turbine pitch motion causes oscillations of the vertical-velocity variance and Reynolds stress. Furthermore, a $\sim 15\%$ increase in magnitude for the vertical-velocity variance around the upper edge of the turbine rotor was observed. Wise and Bachynski¹³ investigated the effects of wakes on the global responses for a floating two-turbine case using the engineering model of FAST.Farm.¹⁴ Moreover, they studied the effects of wake meandering on floating wind turbines by simulating a two-turbine case with three different floaters.¹⁵ Using their dynamic wake meandering model, they found that the yaw motion of the downstream turbine compared with the upstream machine in the semi-subcase was much larger in low turbulence conditions. Binsbergen et al¹⁶ investigated the drivetrain loads caused by induction and wake steering control on two floating wind turbines in a wind farm. Nanos et al¹⁷ studied the influence of vertical wake deflection on the wake behavior and power production of a cluster of two wind turbines through experiments and simulations using an LES flow solver coupled to OpenFAST. Kopperstad et al¹⁸ studied the wakes of floating wind turbines using an actuator disc LES methodology. They investigated two concepts, a spar-buoy and a barge platform, and found that the motion of the barge platform induced a faster wake recovery in both laminar and turbulent inflow conditions. Note that their spar-buoy concept showed a quite similar wake recovery as their bottom-fixed case, contrary to what was observed in study.¹⁹ Manolas et al²⁰ used vortex-based techniques to perform aero-hydro-servo-elastic simulations of floating wind turbines in laminar inflow and compared them with unsteady blade element momentum (BEM) predictions, concluding that in terms of loads, the engineering method was conservative in comparison with vortex-based modeling, similarly to what we have seen in the present study. Moreover, they used their aero-elastic solver to study half-wake effects with a one-way and two-way wake interactions of two NREL 5-MW RWT. Recently, Li et al²¹ investigated the effects of a floating turbine on the wake dynamics using LES. In line with the findings in the present work, they reported that low turbulence levels were key to the appearance of rotor-induced wake meandering, which they linked to the side-to-side motion of a floating turbine.

Our approach allows us to account for more representative offshore floating turbine conditions compared with fully resolved CFD codes, and it can be considered as a fidelity level between the latter ones and the more commonly used engineering models.^{13,15,16}

Experimental studies help to validate and improve numerical models by shedding light in the complex physics of the interaction of floating wind turbines in a wind farm configuration. Rockel et al²² measured the wakes of two floating turbines in tandem using stereoscopic Particle

Image Velocimetry (PIV) to study the influence of pitch motion on the turbine's wake. Jacobsen and Godvik²³ presented full-scale measurements from the Hywind Scotland wind farm and compared the floater responses of a turbine in free wind and a turbine in wake operation. Furthermore, they investigated the influence of atmospheric stability on the floater response. They concluded that in stable atmospheric conditions a clear wake effect with increased floater responses is observed. For neutral and unstable atmospheric stratification hardly any wake effects were seen. Fu et al²⁴ performed wind-tunnel experiments of a horizontal axis wind turbine subject to oscillations in pitch and roll. They showed a faster wake recovery for the oscillating turbine due to an enhanced turbulent mixing that led to a higher turbulence kinetic energy.

Vortex solvers have the potential to become a key method in the simulation of floating wind turbines due to their flexibility, reliability, and high level of detail. One could think about these solvers as a level of fidelity between fully resolved CFD and BEM, although in reality, this can vary significantly depending on the aerodynamic models and flow models employed in the simulation. With vortex solvers it is possible to easily combine different models depending on the degree of accuracy required. Enumerated in ascending complexity, the aerodynamic models traditionally implemented in vortex solvers can be classified as lifting line (LL), lifting surface, potential panel, viscous-inviscid panel, and penalization methods. Analogously, one could divide the flow solvers into: prescribed filament wake methods, free-wake filament methods, hybrid filament-particle-mesh methods, and particle-mesh methods. Our in-house multi-fidelity vortex code MIRAS²⁵⁻²⁸ is used for the present investigation. To the authors' knowledge, this is the first study that simulates the interaction between multiple large-scale floating wind turbines with an aero-hydro-servo-elastic tool that includes the interaction between the atmospheric turbulence and the turbines wakes. More specifically, the wind turbine aerodynamics are simulated with a LL model in combination with a hybrid filament-particle-mesh method. The lifting line is a mathematical method that models the wind turbine blades as formed by discretized vortex lines. On the other hand, the hybrid filament-particle-mesh resolves the vorticity equation, which is obtained by taking the curl of the Navier-Stokes equation, and describes the evolution of the vorticity of a fluid particle as it moves with the flow. In order to extend its modeling capabilities, MIRAS is coupled with the multi-body code HAWC2.²⁹ This coupling is referred to from now on as MIRAS-HAWC2. The use of HAWC2 allows to account for the flexibility of the different turbine components through a multi-body finite-element formulation, as well as the consideration of the controller and the dynamics of the floating support structure.

The present study focuses on the impact of a floating wind turbine wake on the dynamics of downstream machines. It is a continuation of a recent, preceding study,¹⁹ where the MIRAS-HAWC2 model was applied to investigate the wake structure and recovery behind the IEA wind 15-MW RWT³⁰ mounted on the WindCrete spar floater.³¹ The floater and rotor were subjected to prescribed harmonic motion in surge and pitch with varying frequency and amplitude. The interaction of the blade flow and shed tip vortices were examined in detail. It was found that the oscillatory rotor motion generally leads to a faster wake recovery due to the increased mixing, although the opposite effect could also occur for high-frequency motion above-rated wind speed. While the preceding study was carried out without turbulent inflow, we here include the inflow turbulence and further investigate the dynamic effect of the wake on downstream turbines. A central question here is whether the motion of an upstream turbine at a natural frequency can force the response of the same mode for a downstream turbine through the wake. A further question here is whether such forcing can lead to increasing resonance along a row of turbines.

In the present work, a set of aero-hydro-servo-elastic simulations of the IEA Wind 15-MW RWT mounted on a spar floater and in the wake of (a) a bottom-fixed and (b) a floating machine are carried out. We are hereby able to analyze the effect of the floating turbine wake on the power, thrust, and flap-wise root bending moment of downstream turbines. Further, in the tandem configuration, a prescribed harmonic motion in floater surge and pitch is applied to the upstream turbine, which is again simulated with MIRAS-HAWC2. The effect of the prescribed motion on the wake and performance of the downstream turbine is analyzed for different distances between turbines and different turbulence levels. The use of a forced motion in the upstream turbine is preferred over a variation in the wave properties in order to simplify the already complex system.

The present study is divided in two parts, based on the number of turbines considered. First we focus on the direct wake impact on a single downstream machine in a tandem configuration. This is based on simulations of the upstream turbine using MIRAS-HAWC2 and extraction of flow slides every time step at different downstream locations. These slides are introduced as inflow via a turbulence-box approach into a BEM simulation of the downstream turbine. This approach will be referred to as HAWC2-BEM simulation of the downstream turbine. In the present setup, the HAWC2-BEM simulations are two orders of magnitude faster than the MIRAS-HAWC2 and can be run sequentially. The two approaches are benchmarked against each other.

The second part of the study focuses on farm cases, where a cluster of five turbines in a row has been considered. In the framework of the present study, the coupling between MIRAS and HAWC2 has been extended to handle aero-hydro-servo-elastic wind farm simulations. This approach will be referred to from now on as MIRAS-HAWC2 farm. Bottom-fixed as well as floating configurations of the IEA wind 15-MW RWT have been used in an effort to identify the main differences arising from the foundation type, under different wind conditions. The turbines are left to respond freely to the incident wind, with inclusion of a turbulent inflow with 7% turbulence intensity. Emphasis is given to the mean and fluctuating parts of the power and thrust for the downstream turbines along with side-side and fore-aft responses of the floater and tower top. The differences in response between the floating and bottom-fixed configurations are traced back to the floater modes through spectral analysis.

The manuscript is organized as follows. Section 2 describes the solvers used, including the multi-physics solution. Next, Section 3 introduces the different strategies employed to simulate two and five turbines in a row. The numerical models and computational setup is detailed in Section 4, with information about the wind turbine, the spar floater, the control strategy, and domain size. Results for the tandem configurations

are presented in Section 5, with a benchmark of the simplified tandem approach, comparison of downstream response to bottom-fixed and floating turbines and downstream response to harmonic motion of the upstream machine. Finally, in Section 6, the response investigation for five wind turbines in a row is presented. The conclusions drawn in the study are summarized in Section 7.

2 | NUMERICAL METHODS FOR WIND TURBINE SIMULATIONS

In this section, the numerical methods employed to simulate the multi-physics problem of a floating wind turbine are introduced. These account for a hydrodynamic model, a structural model, the controller actuation, an aerodynamic and flow model and the solution strategy to account for their interaction. For brevity, only the latter two components are described here. The reader is referred to Ramos-García et al.³² for more details regarding the formulation and the assumptions made for the computation of the hydrodynamic loads and the integration of the controller in the wind turbine operation.

Concerning the aerodynamic modeling, two distinct levels of fidelity were considered. On one level, an enhanced variant of the well-known BEM theory was employed (Section 2.1). On the other level, the use of the in-house vortex solver MIRAS is suggested in the present study (Section 2.2). While a computational overhead can be attributed to this type of codes, their higher fidelity can provide valuable insight on the physics of the problem. Regardless of the aerodynamic model employed, the integration of the corresponding blade loading into the multi-physics solution was equivalent. More details regarding this are given in Section 2.3

2.1 | BEM method

BEM is an efficient approach for aerodynamic loads computation, and it is considered the current industry standard. It allows to explore a large parametric space of operation and external conditions at an affordable computational cost. In the present work, the enhanced implementation of the BEM method described in Madsen et al.³³ was employed. It features several improvements in order to increase its range of applicability. Those capabilities include a modification to account for the wake expansion and swirl and extended models to handle: dynamic inflow, skewed inflow, shear effect on induction, the effect from large blade deflections, tip loss, and dynamic stall.

2.2 | MIRAS vortex solver

The in-house vortex code MIRAS, standing for Method for Interactive Rotor Aerodynamic Simulations, is a multi-fidelity aerodynamic tool for wind turbine and wake analysis. It allows for a large variety of fidelity levels, and it is written in the programming language Fortran. For the present investigation, the lifting line (LL) module is used as aerodynamic model, while the hybrid filament-particle-mesh module is used to model the flow. In the (LL) method, the rotor blades are modeled as discrete filaments, which accounts for the bound vortex strength and release vorticity into the flow. This vorticity can be subdivided into two types: the trailing vorticity, which is related to span-wise variations of the bound vorticity, and the shed vorticity which is related to time variations of the bound vortex. The bound vortex strength, Γ , is calculated applying the Kutta-Joukowski theorem at the different span-wise stations along the blade as follows:

$$\Gamma = \frac{\underline{L}}{\rho V_{qc}} \quad (1)$$

where \underline{L} is the lift force on each aerodynamic section, obtained by interpolation in a set of tabulated airfoil data (C_l, C_d, C_m) as function of the computed angle of attack. Such two-dimensional (or 3D-corrected) airfoil data are the same as the ones used in BEM models, making the comparison between such different fidelity tools easier. ρ is the air density at a given temperature, and V_{qc} is the total velocity computed at the quarter chord of the different blade sections, computed as follows:

$$\underline{V}_{qc} = \underline{V}_0 + \underline{V}_b + \underline{u}_w + \Delta \underline{u}^b \quad (2)$$

where \underline{V}_0 is the inflow velocity, \underline{V}_b is the blade motion, \underline{u}_w is the wake induced velocity, and $\Delta \underline{u}^b$ accounts for a bound vortex correction applied to curved blade geometries, as detailed in Ramos-García et al.³²

Øye's dynamic stall model³⁴ is used to account for the delay in the stall mechanisms due to dynamic inflow changes seen by the airfoils, practically introducing a time lag of the separation location. Moreover, an additional non-circulatory contribution to the computed C_l and C_m is included to account for the correct unsteady lift and pitch moment in dynamic attached flow as in Bæk.³⁵

The initial sheet of vortex filaments is transformed into a set of vortex particles, and their vorticity is later on interpolated into an auxiliary Cartesian mesh. The downstream location of the filament-to-particle transformation depends on the type of simulation. A study on the influence of this distance in a hybrid filament-mesh was previously published in Ramos-García et al.²⁷ The motion of the vortex elements is determined by the velocity of their markers $\underline{u}(\underline{x}_i)$ (filaments endpoints or the particles itself), which is calculated by a superposition of the free-stream velocity \underline{V}_0 and the velocity contributions from all vortex and boundary elements at the marker positions \underline{x}_i ,

$$\frac{d\underline{x}_i}{dt} = \underline{u}(\underline{x}_i) \quad \text{with} \quad \underline{u}(\underline{x}_i) = \underline{V}_0 + \underline{u}_f(\underline{x}_i) + \underline{u}_{fw}(\underline{x}_i) + \underline{u}_{pw}(\underline{x}_i) \quad (3)$$

where \underline{u}_f is the velocity induced by the blade bound vortex, \underline{u}_{fw} is the velocity induced by the filament-wake and \underline{u}_{pw} is the velocity induced by the particle-wake, in which the Poisson equation is solved by a high-order regularization method introduced by Hejlesen et al.³⁶ A detailed explanation of the different velocity contributions of Equation (3) and a study on the choice of the time-integration scheme was presented in previous studies.^{27,28}

The particles vorticity is interpolated onto a Cartesian mesh, where their interaction is efficiently calculated by an FFT-based method. Moreover, the solver accounts for stretching and diffusive terms in the vorticity transport equation by using a finite difference approach in which the vorticity variations are computed directly on the mesh in combination with a periodic re-meshing of the particles to maintain a smooth field. The vorticity transport equation is obtained by taking the curl of the Navier-Stokes equation and describes the evolution of the vorticity of a fluid particle as it moves with the flow, and assuming an incompressible fluid with a constant and uniform viscosity, it reads

$$\frac{D\underline{\omega}}{Dt} = \frac{\partial \underline{\omega}}{\partial t} + (\underline{u} \cdot \nabla) \underline{\omega} = (\underline{\omega} \cdot \nabla) \underline{u} + \nu \nabla^2 \underline{\omega}. \quad (4)$$

The left-hand side of the equation characterizes the rate of change of the vorticity, including the unsteady term, $\frac{\partial \underline{\omega}}{\partial t}$, and the convection term, $(\underline{u} \cdot \nabla) \underline{\omega}$, which accounts for the changes in vorticity due to the motion of the fluid particle. On the right-hand side, $(\underline{\omega} \cdot \nabla) \underline{u}$ accounts for the vortex stretching and $\nu \nabla^2 \underline{\omega}$ for the vortex diffusion due to viscous effects.

2.3 | Multi-physics solution

In order to model the complex dynamic behavior of a floating wind turbine, the inclusion of different physics is required. Together with the rotor aerodynamics (modeled either with MIRAS or with the BEM method), the effects of the control actuation, the hydrodynamic loading and the structural response have been considered in the present work. This coupled multi-physics problem is often referred to as aero-hydro-servo-elasticity in the literature. In this study, it was handled by the multi-body finite-element software HAWC2,²⁹ which is a commercialized in-house software written in Fortran. The framework that HAWC2 uses for the solution of the aero-hydro-servo-elastic problem relies on an augmented form of the floating frame of reference (FFR) formulation³⁷ and was introduced by the authors in Part I of the present study.¹⁹

Regardless of whether MIRAS or the BEM method was used, the aerodynamic blade loading was accounted for in an analogous manner. In particular, different aerodynamic sections were considered along the blade, where the corresponding loads were computed and subsequently integrated in the solution. We then distinguish in the present work between two different simulation strategies with regard to the fidelity of the aerodynamic model. On one hand, the HAWC2-BEM simulations, where the aerodynamic loading of every section was computed with BEM, and that corresponds to the built-in capabilities of HAWC2. On the other hand, MIRAS-HAWC2 computations rely on the vortex solver MIRAS for the computation of the aerodynamic loading through a loose coupling methodology. The details of that approach were introduced in.³² A comparison with a higher fidelity model (i.e., a fully resolved CFD solver) was also performed in the framework of the aforementioned work, showing a good agreement for the studied aero-elastic simulations.

3 | COUPLING STRATEGIES FOR MULTIPLE WIND TURBINES

As described in Section 2, the multi-physics simulations of each wind turbine relied either on the MIRAS-HAWC2 or the HAWC2-BEM approaches. Since the main focus of the present work is the study of multiple wind turbines, the extension of these methodologies was required. At this point, it is interesting to describe in more detail the two main wind turbine layouts that were studied in the present work:

Tandem configurations Two different tandem layouts are used throughout the manuscript, here understood as the combined simulation of two wind turbines in a row. In the first configuration, depicted in the left side of Figure 1, the upstream turbine is fixed to the sea bottom with a rigid

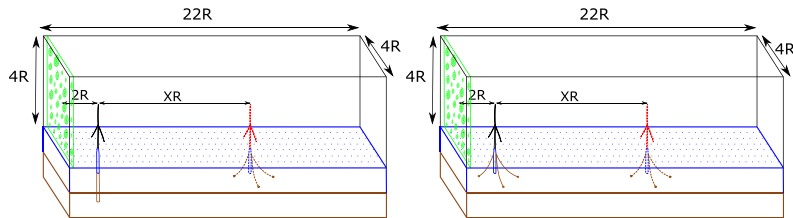


FIGURE 1 Sketch of the simulations setup for tandem configurations: (left) upstream machine fixed to the sea bottom and (right) upstream machine floating

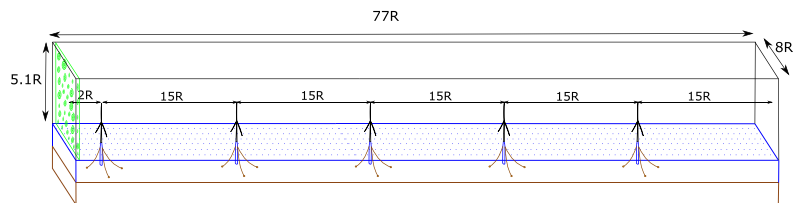


FIGURE 2 Sketch of a MIRAS-HAWC2 farm simulation with five floating wind turbines in a row

monopile. In the second one, depicted in the right side of Figure 1, the first turbine is mounted on a spar-buoy floating platform. Note that in both cases the downstream turbine is modeled as a floating machine.

It should be noted that, for some of the cases simulated in this work, a prescribed motion was imposed to the upstream turbine. This was achieved through the action of an external library, which introduced a set of pre-computed loads in the floating substructure. More details about this procedure can be found in Part I of the present study.¹⁹

Wind farm configuration In the present work, we refer to as *wind farm simulations* to the computations involving more than two machines in a row. Two types of wind farm configurations were also studied. First, the *fixed wind farm*, which accounted exclusively for fixed offshore substructures. In second place, all the wind turbines of a *floating wind farm* were mounted in a spar-type floater as sketched in Figure 2.

The coupling strategies developed in the present work in order to model both tandem configurations and wind farms are described in the subsections below.

3.1 | Coupling strategy for wind farms

All the presented wind farm simulations were computed with the MIRAS-HAWC2 farm tool, which was developed within the framework of the present study. MIRAS-HAWC2 farm can be seen as an extension of the MIRAS-HAWC2 coupling methodology presented in Section 2, and allows multiple turbines. The tool can be used to solve the multi-physics problem of an arbitrary number of wind turbines and can model any user-specified wind farm layout. In practice, it involves the interaction of a single MIRAS simulation, that includes all the modeled wind turbines, with multiple executions of HAWC2. In this way, the coupling between the physics of the different machines is ensured through the wake/flow model. A general diagram of MIRAS-HAWC2 farm is included in Figure 3. At every time step, the alternate execution of MIRAS and the different HAWC2 instances relies on the in-house Python-based DTU coupling architecture. This framework also enables the transfer of information between the solvers (that were compiled as shared objects). For the present work, the implemented coupling strategy can be summarized as:

- The aerodynamic loading on every wind turbine blade, computed by MIRAS through the LL method, is transferred to the corresponding HAWC2 instance. In particular, the sectional forces and moments at every aerodynamic section are considered.

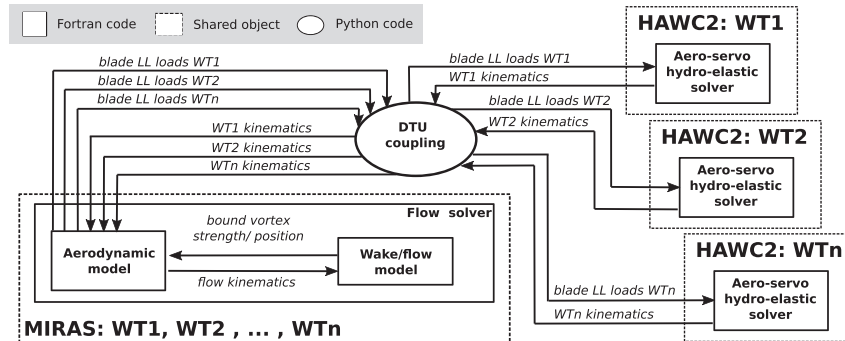


FIGURE 3 Diagram of MIRAS-HAWC2 farm simulations. An arbitrary number n of wind turbines WT is included. *blade LL loads* refers to the sectional aerodynamic loads (forces and moments). *Kinematics* refer to the blade displacements, accounting for both the rigid-body motion at the root and the local translations and rotations of every aerodynamic section

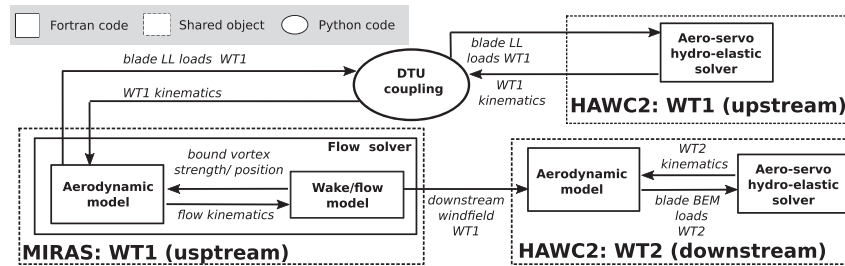


FIGURE 4 Diagram of the simplified tandem methodology, where the upstream wind turbine WT_1 is solved with a MIRAS-HAWC2 approach, and the downstream WT_2 with HAWC2-BEM. *blade LL loads* refers to the sectional aerodynamic loads (forces and moments), computed by means of LL. Analogously, *blade BEM loads* refer to the same quantities, computed by the BEM method instead. *Kinematics* refer to the blade displacements, accounting for both the rigid-body motion at the root and the local translations and rotations of every aerodynamic section

- The updated kinematics of every wind turbine blade, computed by each of the instances of HAWC2, is transferred to the matching blade in the MIRAS simulation. This accounts for both the rigid-body motion of the root and the blade axis translations and rotations at every aerodynamic section.

The reader is referred to Ramos-García et al.³² for more details about the implementation of the DTU coupling tool, as well as a detailed description on how the sectional loads and the blade kinematics are computed.

3.2 | Coupling strategies for tandem configurations

As the tandem configuration can be seen as a particular wind farm case, the MIRAS-HAWC2 farm methodology could be applied without any loss of generality. In that way, both wind turbines would account for a LL-based aerodynamic model. In addition to that approach, the simplified methodology illustrated in Figure 4 was introduced to reduce the computational requirements of simulating interacting turbines. As it can be observed, the approach solves the multi-physics problem of the upstream turbine (WT_1) via the LL-based MIRAS-HAWC2. However, no data transfer through the DTU coupling took place for the downstream turbine (WT_2). Instead, the aerodynamic model used for that wind turbine corresponded to the built-in BEM capabilities of HAWC2. In this way, the *tandem simplified* methodology could be seen as two independent multi-physics simulations: first, a single turbine MIRAS-HAWC2 computation for WT_1 ; second, a HAWC2-BEM simulation of the downstream turbine WT_2 . As illustrated in Figure 4, the velocity field computed in the MIRAS-HAWC2 simulation of WT_1 was extracted at different downstream planes. Such velocities were used to generate a new turbulent field, which was loaded in HAWC2 during the input reading phase of

the WT2 simulation. In this way, the turbine modeled in HAWC2-BEM operated immersed in the wake of the turbine simulated in MIRAS. It should be noted that the MIRAS-HAWC2 simulation could be seen as a precursor computation, allowing for multiple subsequent HAWC2-BEM runs. This is a particularly efficient way to, for instance, assess the influence of the wind turbines distance on the loads of WT2 by means of BEM.

4 | NUMERICAL MODELS AND COMPUTATIONAL SETUP

This section describes the numerical models used in the present investigation, including the models of the wind turbine and the spar-buoy floating platform, the DTU wind energy controller (WEC), and other computational details.

4.1 | Numerical models

The wind turbine chosen for this study is the recently released IEA Wind 15MW RWT.³⁰ This machine, that has a rotor diameter of 240 m, was designed in a collaboration between the National Renewable Energy Laboratory (NREL) and the Technical University of Denmark (DTU). The WindCrete spar-buoy platform was designed in the COREWIND project specifically for the IEA Wind 15-MW RWT. The floater was designed for a maximum static pitch of 4° at the peak thrust and with all natural periods above 30 s for the rigid-body motions of the platform in heave, pitch, and roll as depicted in Table 1. The reader should note that the natural frequencies of the floater under external loads will slightly vary from the equilibrium ones due to, for example, the nonlinear nature of the mooring system. More details about the floater design can be found in previous works.^{31,38} The structural modeling of the WindCrete used in the present investigation was first introduced by the authors in Part I of the present work.¹⁹ As a baseline for the comparison with the floating cases, the same wind turbine mounted on a very stiff monopile is defined in an effort to completely exclude the effects of the substructure's motion. The basic DTU wind energy controller³⁹ has been tuned for floating conditions using HAWCStab2 Version 2.16a.⁴⁰ More details about the controller calibration were first introduced by the authors in Part I of the study.¹⁹

4.2 | Computational setup

In the present study, we have used the knowledge obtained from earlier blade discretization studies performed with MIRAS (for example, Ramos-Garcá et al.^{25,27}). The MIRAS-LL simulations employ a bound vortex discretized with 40 straight segments following a cosine distribution, where the root and the tip region have a higher point density. The influence of the HAWC2 structural model fidelity of the blade on the response, loads, and stability of large turbines has been analyzed in Gözcü and Verelst.⁴¹ The turbine hub is located at a position of 1.125R from the water level, and its wake effect has not been included in the present modeling approach. An eight-order stencil is used to spatially discretize the vorticity equation. Moreover, a particle re-meshing every time step is used to maintain a smooth field, which is forced to remain divergence-free by applying a periodic re-projection of the vorticity. A Mann box has been used to define a representative turbulent inflow, which has been scaled to obtain different TI levels. In order to simulate a turbulent inflow in MIRAS, the velocity-based Mann box is transformed into a particle cloud. This cloud is slowly released one diameter upstream the turbine, and it develops as it convects downstream towards the rotor plane. The released turbulent particles interact freely with the turbine and its wake.

A $22R \times 4R \times 4R$ Cartesian mesh has been employed in all single turbine and tandem cases, with a spacing of 6 m in the X, Y, and Z directions, adding up to a total of 2.8 million cells. A total of 1400 s with a time step size of 0.025 s have been simulated, adding up to 56000 time steps. Each MIRAS simulation in this study uses 80 2.8 GHz processors on a Linux cluster, with an approximate computational time per case of 22 h. The flow has been extracted every time step in 22 planes perpendicular to the flow direction (YZ-planes), from 1R upstream to 20R downstream the rotor plane. Moreover a single XZ-plane is extracted. This plane is defined by the stream-wise direction and the height and is located at the rotor center. To reduce the necessary storage space such planes are defined using 64×64 cells with a constant spacing and are written

TABLE 1 Rigid-body natural frequencies of the WindCrete floater in equilibrium, supporting the IEA Wind 15-MW wind turbine

| Degree of freedom | Natural frequency (Hz) |
|-------------------|------------------------|
| Surge | 0.01221 |
| Heave | 0.03052 |
| Pitch | 0.02441 |
| Yaw | 0.09155 |

out as binary files. This means that in the Y and Z directions the velocity extraction mesh is 2.5 times coarser than the computational mesh and in the X direction the extraction mesh is 17.5 times coarser.

Regarding the wind farm simulations with five turbines in a row, a Cartesian mesh of dimensions $77R \times 8R \times 5.12R$ has been used, which in combination with a cubic cell size of 6 m sums up to more than 25 million cells and a similar number of vortex particles; 2800 s has been simulated with a time step size of 0.025 s, adding up to 112,000 time steps. This simulation length has been chosen to ensure that the flow has developed throughout the entire domain by half of the simulation time. Therefore statistics are extracted using the last 1400 s. One of the key advantages of the present particle-mesh implementation is the use of free boundary conditions to model to domain boundaries, excluding the ground where a no-through condition is used.²⁸ This modeling approach reduces the necessity of using a large mesh in order to avoid the blockage effect as is normally observed in finite volume solvers with a pure Eulerian approach. The total length of the domain is defined by the turbine spacing and the number of turbines, including a 15R spacing downstream the last turbine. The influence of the cross-sectional mesh size is studied in Section 6.

Each MIRAS simulation in this study uses 384 2.9 GHz processors on a Linux cluster, with an approximate computational time per case of 70 h. The flow has been extracted every 32 time steps in a single XZ-plane. This plane, defined by the stream-wise direction and the height, is located at the rotor center and is represented by 256×256 cells with a constant spacing. To model the downstream turbine in HAWC2-BEM via the simplified tandem approach, the flow from the previously introduced extraction mesh at different YZ-planes has been used. Only the second half of the simulated time is employed in the flow analysis, since the first half is disregarded in order to reduce the influence of initial transients.

5 | TANDEM SIMULATIONS

The results obtained from the numerical investigation for tandem are presented in what follows. First, in order to verify the simplified tandem approach, HAWC2-BEM simulations of the downstream turbine are benchmarked against a MIRAS-HAWC2 farm simulation of two turbines in a row. Second, the simplified approach is used in a set of aero-hydro-servo-elastic simulations of a floating wind turbine on the wake of both a bottom-fixed and a floating machine with varying distance between turbines and increasing inflow TI. Finally, the impact in downstream turbines of a prescribed oscillatory motion applied to the first turbine of the row is analyzed.

5.1 | Benchmarking of the simplified tandem methodology

In this section, we verify the HAWC2-BEM simulation of a downstream turbine on full wake operation using the simplified tandem methodology first introduced in Section 3.2. A MIRAS-HAWC2 farm simulation of two turbines in a row is used to benchmark the predicted forces and displacements of WT2 in below-rated conditions, that is, 8 m/s, and under laminar inflow, that is, TI 0%. As shown in Figure 5, a good agreement is obtained between the codes in terms of aerodynamic power, while a general under-prediction of the mean thrust level is observed for BEM, especially during the last 700 s of simulated time where this method also predicts larger load oscillations. Regarding the tower-top side-side (state pos x) and fore-aft (state pos y) displacements, there is a larger amplitude of the displacement predicted by BEM. In order to rule out the effect of the domain size in this code comparison, all the vortex simulations involved were performed with a 50% larger domain in all three directions without significantly reducing differences in the results. To further understand such differences between the predictions of the two aerodynamic/flow models we have computed the aerodynamic damping of both methods for a single turbine with a forced surge motion at a frequency of 0.014 Hz and an amplitude of 5 m. MIRAS-HAWC2 displayed a 18% higher damping ratio compared with HAWC2-BEM, which can explain the smaller response in tower-top fore-aft displacement, especially because the observed response happens at a natural frequency and is therefore very sensitive to the amount of damping. Further, since there is no inflow turbulence in this case, the variations in thrust are mainly due to the fore-aft motion of the rotor, hence the differences observed in thrust amplitude can be attributed to the differences in response.

Even though the differences between the code predictions for WT2 are larger than previously observed for WT1,¹⁹ the overall trends are quite similar. Therefore, we believe that the simplified tandem approach is, in the context of the present study, a reliable alternative to model the downstream turbine at a lower computational cost.

5.2 | Downstream impact of a floating turbine in still water

This section focuses on the impact of the wake generated by the floating IEA-15MW RWT on a downstream machine located at three different distances (10R, 15R, and 19R) and under laminar inflow conditions. These cases where the upstream turbine is free floating are referred to as `UPS-float` and are compared against cases where the upstream turbine is fixed to the sea bottom, which are referred to as `UPS-fixed`. Note that in this section the prescribed floater motion is not used. Following previous research by the authors in Part I of the present study,¹⁹ which showed that the largest differences in the wake of a bottom-fixed and a floating turbine appeared at low wind speeds, the present study is carried

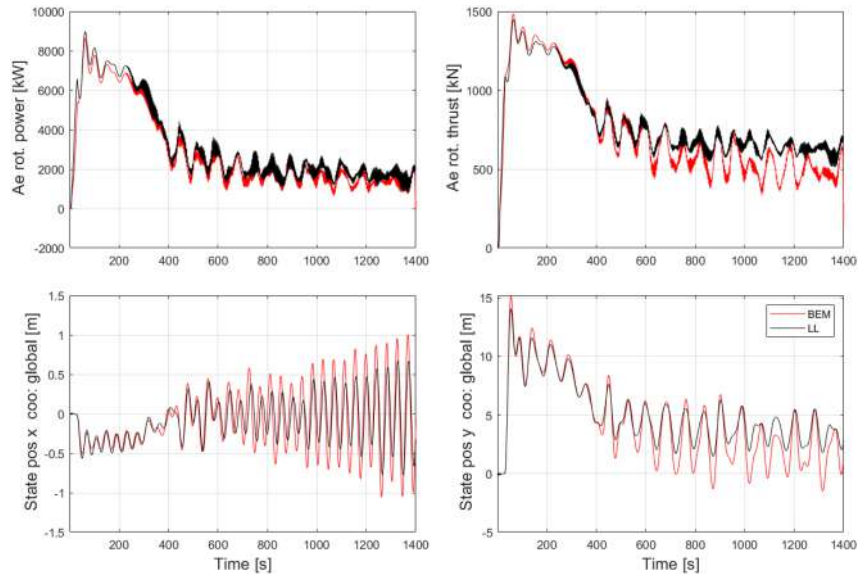


FIGURE 5 Key predicted quantities of a downstream IEA Wind 15MW RWT mounted on the WindCrete platform operating on full wake, comparison between BEM and LL simulations: 8 m/s wind speed, TI 0%, and a distance of 15R to the upstream turbine

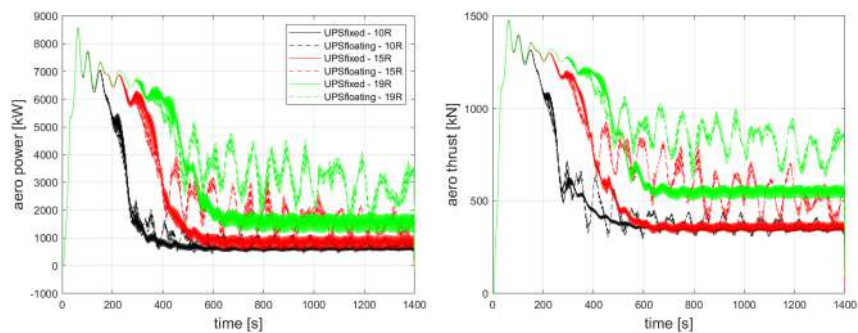


FIGURE 6 Time signals of power and thrust of WT2 located at distances of 10, 15, and 19R downstream WT1. The upstream turbine is considered as bottom-fixed and floating

out in below-rated conditions, that is, 8 m/s, and subject to both laminar and turbulent inflow conditions. In all the simulations presented in this section, the wind turbine controller is active in order to account for a more realistic scenario.

Focusing first in the laminar inflow cases, that is, TI 0%, Figure 6 depicts the power and thrust signal of WT2 during the complete simulated period. As expected, initially all simulations of the downstream turbine show an almost identical behavior as they operate in free incoming flow up to approximately 160 s. At this point, the turbine placed 10R downstream is first hit by the wake of WT1, reducing considerably its power and thrust. The same trend is observed at later times for the turbines placed at the 15R and 19R locations. Differences between the behavior of WT2 for the UPS-floating and UPS-fixed cases are clearly discernible and grow with the increasing spacing between turbines.

In order to analyze in more detail the downstream turbine behavior and how it relates to the upstream machine, a spectral analysis of the thrust signal of WT2 with a 15R spacing has been performed as shown in Figure 7 right. The first 700 s are left out in order to minimize the effect of the initial transients, see Figure 7 left. As expected, compared with the UPS-fixed case, the frequency analysis of WT2 in the UPS-floating case shows much more energy in the low frequency range, with a peak around 0.0144 Hz, which is close to the natural frequency in surge of the WindCrete floater.³¹ This peak is also observed for the UPS-fixed case, although it is slightly moved towards lower frequencies and exhibits

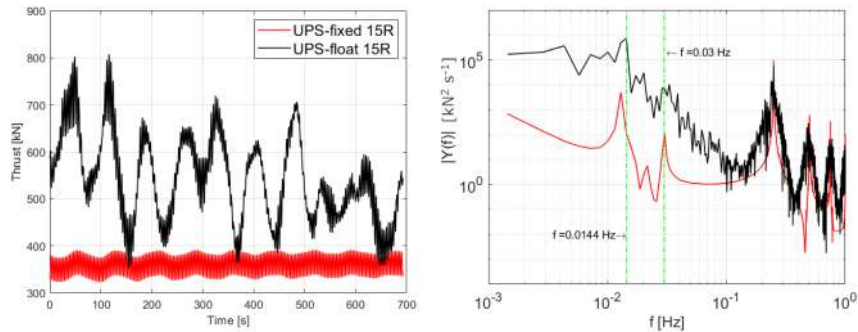


FIGURE 7 Thrust analysis of the floating WT2 located 15R downstream WT1. (left) time signal over the last 700 s and (right) frequency analysis of the thrust. The upstream turbine is accounted as bottom-fixed and floating. Green vertical dash-dotted lines represent the predicted natural frequency of the platform in surge and heave of the floating downstream turbine (see Table 1 for reference of the natural frequencies of the floater in equilibrium, i.e., no-load condition)

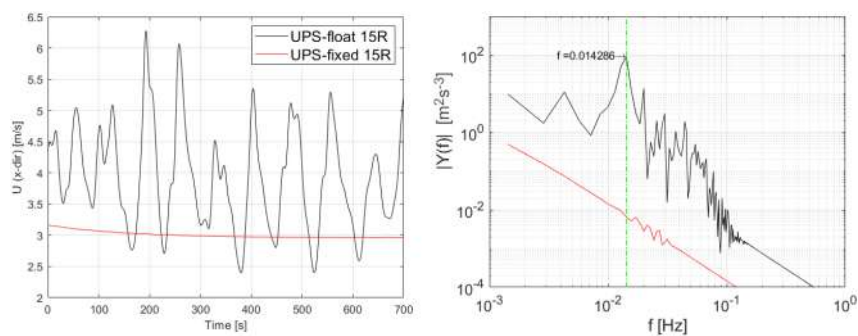


FIGURE 8 Stream-wise velocity at a probe approximately 15R downstream WT1 for the bottom-fixed and floating cases at a height of 150 m. (left) time signal over the last 700 s and (right) frequency analysis. The green vertical dash-dotted lines represent the simulated natural frequency of the platform in surge of the floating downstream turbine (see Table 1 for reference of the natural frequencies of the floater in equilibrium, i.e., no-load condition)

much lower energy since it does not include the contribution of WT1. It is also interesting to remark that WT2 in the UPS-fixed case shows a peak around 0.03 Hz, which is exactly the natural frequency in heave of the WindCrete floater. This has been confirmed by analyzing the time signal of the floater heave motion which undergoes a periodic oscillation with an amplitude of 0.25 m. Although the interaction between thrust and heave motion may seem unlikely, the combination of floater pitch and shaft tilt creates a vertical component of the thrust force, which can excite this vertical motion. Such excitation of the heave degree of freedom (DoF) is masked out by many other frequency motions when operating on the wake of the floating turbine. In this case, the heave motion of the downstream turbine displays a varying amplitude.

Figure 8 shows the time signal and the spectral analysis of the stream-wise component of the velocity in a location 15R downstream WT1 at hub height as computed by MIRAS-HAWC2. It is clear from the figures that the flow downstream a floating turbine is much more unsteady than in the bottom-fixed case. Moreover, the surge natural frequency can be found in the spectral analysis of the UPS-float case around 0.01428 Hz, and it is linked to the large oscillations observed in the time signal.

For the sake of completeness the thrust signal of WT1 is depicted in Figure 9. From the figure, we can discern the relatively large oscillations in thrust that the floating turbine undergoes in comparison with the bottom-fixed one. As earlier observed in WT2, the largest spectral peak in WT1 appears around the surge natural frequency of the floater. However, this peak has a much lower energy content than the equivalent peak observed in WT2, shown in Figure 7 for the UPS-float case. This is because the thrust of WT1 is only affected by its own motion, whereas the thrust of WT2 is affected by the surge motion of both WT2 and WT1 throughout the wake interaction. Finally, it is interesting to note that the natural frequency in heave at 0.03 Hz of the WindCrete floater is also clearly visible in the spectral analysis.

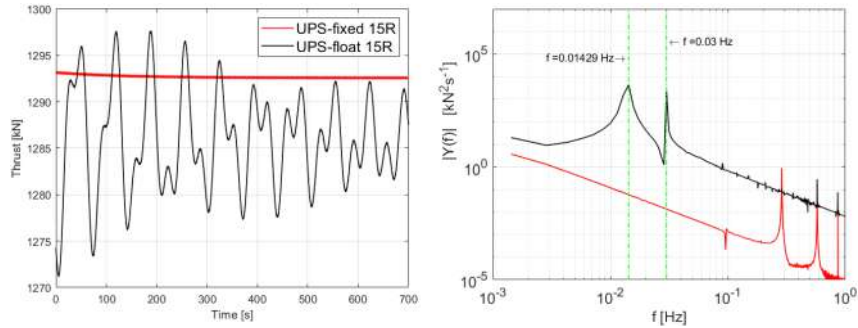


FIGURE 9 MIRAS-HAWC2 thrust analysis of WT1 for the bottom-fixed and floating cases (left) time signal over the last 700 s and (right) frequency analysis. Green vertical dash-dotted lines represent the simulated natural frequency of the platform in surge and heave of the floating downstream turbine (see Table 1 for reference of the natural frequencies of the floater in equilibrium, i.e., no-load condition)

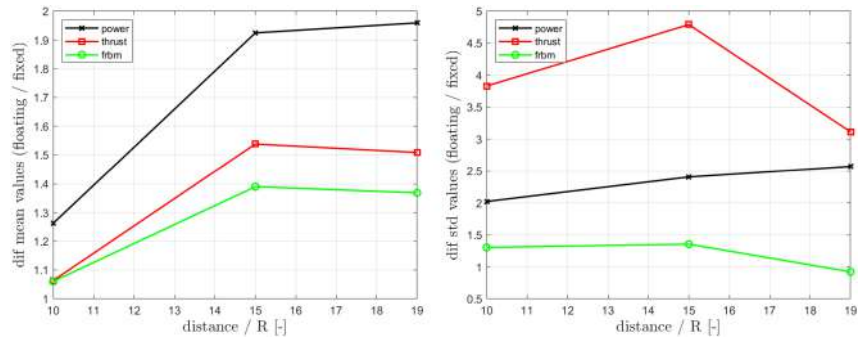


FIGURE 10 Difference in (left) mean and (right) std of power, thrust, and flap-wise root bending moment of the downstream turbine for distances of 10, 15, and 19R. Inflow TI of 0%

The difference in the mean and standard deviation (std) of key sensors of WT2 for the UPS-float cases with respect to the UPS-fixed ones is depicted in Figure 10 as function of the distance to WT1 and in laminar inflow conditions. Differences in power, thrust, and flap-wise root bending moment (flrm) between a turbine operating in the wake of a bottom-fixed or a floating machine grow abruptly from a 10R to a 15R spacing, although they seem to reach a plateau if we further increase the distance between machines. A different picture is seen regarding the std. As expected, a turbine operating in the wake of a floating machine displays a much larger std of the thrust and power signals; however, smaller differences are predicted for the flap-wise root bending moment. From the figure, we can deduce that the gain in power production is much larger than the increase in the blade fatigue loads. However, the large variations in the rotor thrust translates into a much higher tower base fore-aft loading for the turbine operating downstream a floating machine.

5.2.1 | Effect of the inflow turbulence intensity level

In this sub-section we investigate the influence of the inflow TI level in the simplified tandem simulations focusing on both the upstream and downstream turbines. The reader should note once again that the upstream machine is considered as bottom-fixed or floating without waves while the downstream turbine is in all cases considered as floating.

The mean and standard deviation of power and thrust for WT1 and TI of 0%, 4%, 7%, and 10% are presented in Tables 2 and 3 for both the bottom-fixed and floating cases, respectively. We note here that typical values of TI in the offshore environment are 6–8%.⁴² In general, the mean values of both quantities are slightly lower for the floating turbine regardless of the TI. However, the oscillations introduced by the waves (non accounted for here) can considerably modify the power and loading in floating machines. Regarding the std, large differences between the

TABLE 2 Mean, standard deviation, and their ratio for the power and thrust of WT1 in the bottom-fixed as function of the turbulent intensity

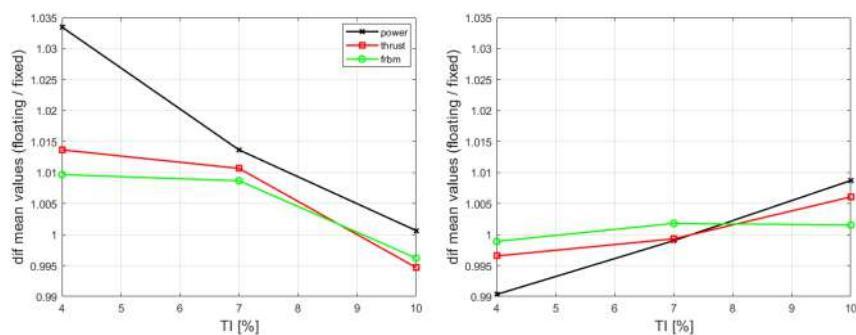
| TI (%) | Bottom-fixed | | | | | |
|--------|--------------|----------|--------------|-----------|----------|--------------|
| | Power | | | Thrust | | |
| | mean (kW) | std (kW) | std/mean (%) | mean (kN) | std (kN) | std/mean (%) |
| 0 | 6863 | 7 | 0.1 | 1292 | 0.1 | 0.0 |
| 4 | 6926 | 235 | 3.3 | 1299 | 26.4 | 2.0 |
| 7 | 7018 | 597 | 8.5 | 1306 | 66.9 | 5.1 |
| 10 | 7126 | 968 | 13.5 | 1311 | 108.0 | 8.2 |

Note: Wind speed of 8 m/s.

TABLE 3 Mean, standard deviation, and their ratio for the power and thrust of WT1 in the floating case as function of the turbulent intensity

| TI (%) | Spar-buoy floater | | | | | |
|--------|-------------------|----------|--------------|-----------|----------|--------------|
| | Power | | | Thrust | | |
| | mean (kW) | std (kW) | std/mean (%) | mean (kN) | std (kN) | std/mean (%) |
| 0 | 6819 | 49 | 0.7 | 1285 | 5.3 | 0.4 |
| 4 | 6862 | 241 | 3.5 | 1290 | 27.4 | 2.1 |
| 7 | 6945 | 590 | 8.4 | 1295 | 67.0 | 5.1 |
| 10 | 7045 | 949 | 13.4 | 1300 | 107.0 | 8.2 |

Note: Wind speed of 8 m/s.

**FIGURE 11** Difference in mean values of power, thrust, and flap-wise root bending moment of WT2 for the UPS-float respect to the UPS-fixed cases. Distances between turbines of (left) 10R and (right) 15R. Turbulent intensity levels of 4, 7, and 10%. Wind speed of 8 m/s

bottom-fixed and floating cases are observed at the TI 0% level. This was expected due to the more dynamic nature of the floating system. It is also observed that such differences are reduced with the increasing turbulence intensity, giving rise to a change in tendency for the cases with TI of 7 and 10%. This can be explained by the increasing variability introduced by the turbulent inflow, which overtake the fluctuations introduced by the floater.

Focusing now on WT2, it has been found that the TI level of the incoming flow plays a key role in the wake development, drastically reducing the differences observed at TI 0% between the UPS-fixed and UPS-float cases. This can be appreciated in Figure 11, which depicts the difference in mean power and loads for the UPS-float cases with respect to the UPS-fixed ones for distances between turbines of 10R and 15R. From the figure, we can appreciate how operating 10R downstream of a floating machine in low turbulence level (i.e., TI = 4%), there is a power gain of approximately 3.5% respect to operating behind a bottom-fixed machine in the same conditions. However, as the turbulence level increases, the power gain linearly decreases, reaching virtually zero for the 10% TI case. Increasing the distance between the turbines to 15R seems to trigger a change in tendency. At low TI levels the turbine operating behind a floating machine shows lower power and loads than the

one operating in the wake of a bottom-fixed one. However, increasing the TI seems to increase the relative power output of the downstream turbine in the UPS-float case respect to the UPS-fixed case. Although these trends are surprising, there is only a $\pm 1\%$ difference between the cases and a clear conclusion cannot be drawn from these results. Note that very similar trends have been observed for a distance between turbines of 19R.

5.3 | Downstream impact of a prescribed harmonic motion in WT1

In an effort to mimic an active response of the turbine wake to wind and waves, and to further investigate its impact in downstream turbines, the motion of WT1 is prescribed to follow a harmonic oscillation in selected DoFs. The surge and pitch DoF have been chosen as the most representative of the oscillatory motion observed in floating wind turbines. First, the surge investigation includes multiple cases with an amplitude of 15 m and frequencies ranging from 0.01419 Hz to 0.11352 Hz. In second place, the pitch investigation includes two different cases, with a pitch amplitude of 6.38° and frequencies of 0.02441 and 0.11352 Hz. The influence of the distance between turbines and the inflow TI level is also investigated in what follows. The simplified tandem methodology described in Section 3.2 has been employed in the investigation, and therefore, WT2 is simulated in HAWC2-BEM with the inflow extracted from a MIRAS-HAWC2 simulation of WT1. WT2 employs the basic DTU Wind Energy controller as described in Section 4. The MIRAS-HAWC2 simulations of WT1 have been performed at the rated wind speed of 10.8 m/s. In order to maximize the impact in downstream turbines, a fixed collective blade pitch of 0° and a fixed rotational speed of 7.56 rpm (rated) have been applied to the upstream machine.

5.3.1 | Prescribed surge motion

Simulations of the upstream turbine have been carried out for a prescribed surge motion of 15 m amplitude and frequencies of 0.01419 (typical surge), 0.02441 (typical pitch), 0.05676 (typical storm sea state), and 0.11352 Hz (typical sea state). A side-view of the iso-vorticity contours for the highest frequency case is shown in Figure 12. Figure 13 provides an overview of the WT1 performance comparing the aerodynamic power and thrust predictions of HAWC2-BEM and MIRAS-HAWC2 during the last surging cycle. The labels t1 to t6 mark different and equally spaced time stamps throughout the cycle, where t1 denotes a time near the beginning and t6 one near the end. It is worth mentioning that the flattened region observed during the backwards motion of the 0.11352 Hz case is directly related with the rotor operating inside its own wake while it is generating a negative thrust force, a sign of a global propeller state as already introduced by Ramos-García et al.¹⁹ In general, the observed trends are very similar to what was found for low-frequency surge motions in the aero-hydro-servo-elastic simulations presented in Part I, where the turbine operation point was not fixed and the generator servo played a small role in regulating the rotor speed.

To investigate the impact of the wake generated by an oscillatory motion applied to WT1 in laminar inflow conditions, a floating turbine placed 10R downstream is simulated via the simplified tandem methodology. Figure 14 depicts the variation during the last 100 s of key quantities of WT2 for the different surge frequencies in WT1. Focusing first on the aerodynamic power and thrust signals, it is observed that the highest frequency motion of the upstream turbine, that is, 0.11352 Hz, enables the largest mean values of power and thrust in the downstream machine. It is also interesting that the low-frequency motions, that is, 0.01419 and 0.02441 Hz, trigger a very different response of the downstream machine. This seems to be related to the proximity of the natural surge and pitch frequencies of the WindCrete floater, which amplifies the response of the turbine when interacting with the incoming wake. Looking at the tower-top fore-aft displacement of WT2 we can see how the low-frequency oscillations in WT1 trigger large and nearly periodic oscillations in the downstream turbine, with the largest oscillations observed when WT1 is surging near the pitch natural frequency of the WindCrete platform, that is, 0.02441 Hz. The amplitude of the oscillations for this case is more than eight times larger than the ones observed for the baseline case without a prescribed motion in WT1, that is, 0 Hz. On the other hand, the highest frequency motion of WT1 induces the largest mean value of the fore-aft displacement in WT2 with the smallest amplitude of oscillation. This fact

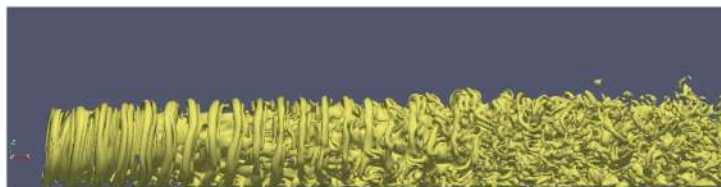


FIGURE 12 Side-view of the iso-vorticity contours on the computational mesh of a MIRAS-HAWC2 simulation of WT1 with the turbine subject to a prescribed harmonic surge of amplitude 15 m and frequency of 0.11352 Hz. Inflow TI level of 0%

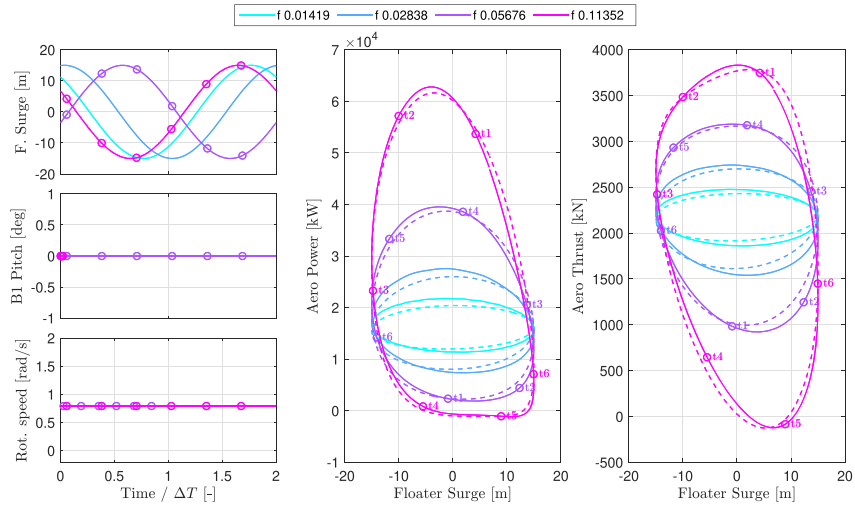


FIGURE 13 Last cycle variation of selected turbine sensors during a prescribed surge motion of the floater with an amplitude of 15 m and various frequencies: 0.01419, 0.02441, 0.05676, and 0.11352 Hz. Solid lines represent MIRAS-HAWC2 results while dashed lines represent HAWC2-BEM predictions. Wind speed of 10.8 m/s, controller off

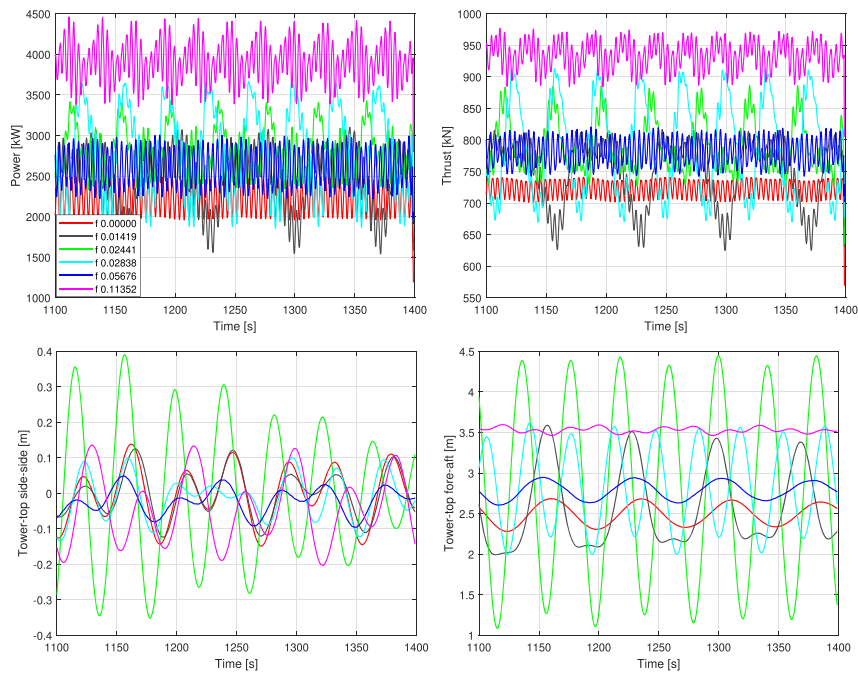


FIGURE 14 Time signals of the (from top to bottom and left to right) power, thrust, tower-top side-side and fore-aft displacements of WT2 located 10R downstream WT1. The upstream turbine is subjected to a prescribed surge motion of 15 m amplitude and frequencies of, 0, 0.0141, 0.02441, 0.05676, and 0.11352 Hz. Wind speed of 10.8 m/s and inflow turbulence intensity of 0%

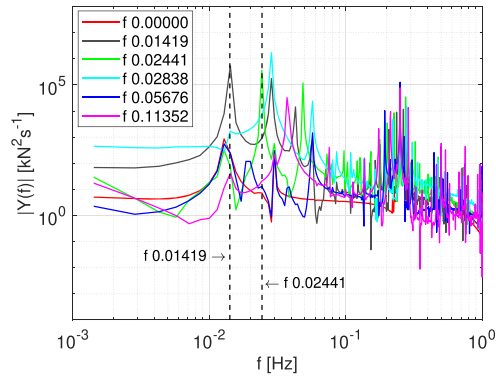


FIGURE 15 Spectral analysis of the thrust signal of WT2 for different surge frequencies of the upstream turbine, 0, 0.01419, 0.02441, 0.05676, and 0.11352 Hz. Wind speed of 10.8 m/s and inflow turbulence intensity of 0% with a 10R spacing between turbines. The reader is referred to Table 1 where the natural frequencies of the floater in equilibrium are shown

surge motion seems to trigger a faster wake breakdown without exciting any of the rigid-body modes of the downstream floater. Regarding the side-side displacement, differences in the frequency of the upstream turbine motion do not have as much influence in the behavior of the downstream turbine, although the 0.02441 Hz case seems to trigger the largest oscillations, which are not periodic.

Figure 15 depicts the spectral analysis of the WT2 thrust signal. The figure shows that low-frequency surge motions of the upstream turbine, that is, 0.01419 and 0.02441 Hz, pump energy into the downstream turbine at the same frequency range creating a resonance effect. Moreover, second and higher harmonics are excited, which could be related to quadratic non-linearities. To further explore this, a simulation of the 0.02441 Hz case has been performed with the downstream turbine fixed to the sea bed in an effort to better understand the response of the floating machine by means of a direct comparison. It has been found that the fixed machine exhibits seven times more energy in the first harmonic peak than the floating turbine; however, the second harmonic is 60% less energetic. Going back to Figure 15 we can conclude that forced motions at higher frequencies do not exhibit such resonance effect in downstream turbines, since the wake disturbances are generated further away from the natural frequencies of the floating system, although the 0.11352 Hz case seems to excite a highly energetic mode at 0.037 Hz, which could be a non-linear effect at the sum of the surge and pitch natural frequencies.

The influence of the inflow TI level in the loads and performance of the second turbine of the row operating in full wake is investigated in what follows. A 15 m amplitude surge case with a low- and a high-frequency motion applied to WT1 has been selected for the investigation, that is, 0.01221 Hz and 0.11352 Hz. The lower frequency has been chosen to be equal to the natural surge frequency of the WindCrete floater while the high one has been selected to be representative of ocean waves. As mentioned earlier, the controller of the upstream turbine has been disabled to reduce the complexity of the cases, but the downstream turbine does operate with a generator and a pitch servo. The predicted power signal of a floating turbine located 10R downstream the surging machine is presented in Figure 16 and compared against the power produced by the same turbine operating downstream a bottom-fixed machine. The figure includes results for inflow TI levels of 0, 4, and 10%. Substantially larger differences are observed between the floating and fixed configurations for the high-frequency oscillation, with the differences decreasing considerably with the increasing TI.

The response of WT2 to a varying distance between turbines and different inflow TI is summarized in Figures 17 and 18. Figure 17 shows the relative mean and standard deviation of WT2 power when operating downstream a surging machine, relative to being downstream a bottom-fixed turbine. From the figure, the power gain observed when operating downstream of a low-frequency surging machine is drastically reduced as soon as inflow turbulence is included, that is, $TI \geq 4\%$. However, when WT1 is oscillating with a high-frequency motion, the observed power gain in WT2 does not completely fade away with the increasing turbulence level. Regarding the influence of the distance between turbines, generally increasing the distance reduces the power gain for the cases with $TI > 0\%$, although the opposite is observed for the $TI 0\%$ cases and a low-frequency surge. Regarding the standard deviation of the power, relative differences between the 10, 15, and 19R cases are reduced as the TI level is increased. It is important to note here that the lowest frequency motion in WT1 triggers the largest variations in the power of WT2 at $TI 0\%$. This is related to an excitation of a mode near the natural surge frequency of the floater once the distance between turbines is large enough.

The relative mean fore-aft tower base bending moment (FATBBM) of WT2 when located downstream a surging machine with respect to operating downstream a fixed turbine is presented in Figure 18 for the low- and high-frequency surge cases. At a 0% TI there is a clear influence of the spacing between turbines in the behavior of the downstream machine, where the largest spacing shows the highest fore-aft tower base bending moment in relative terms. As the inflow turbulence level is increased, differences between the surging and the fixed cases are reduced

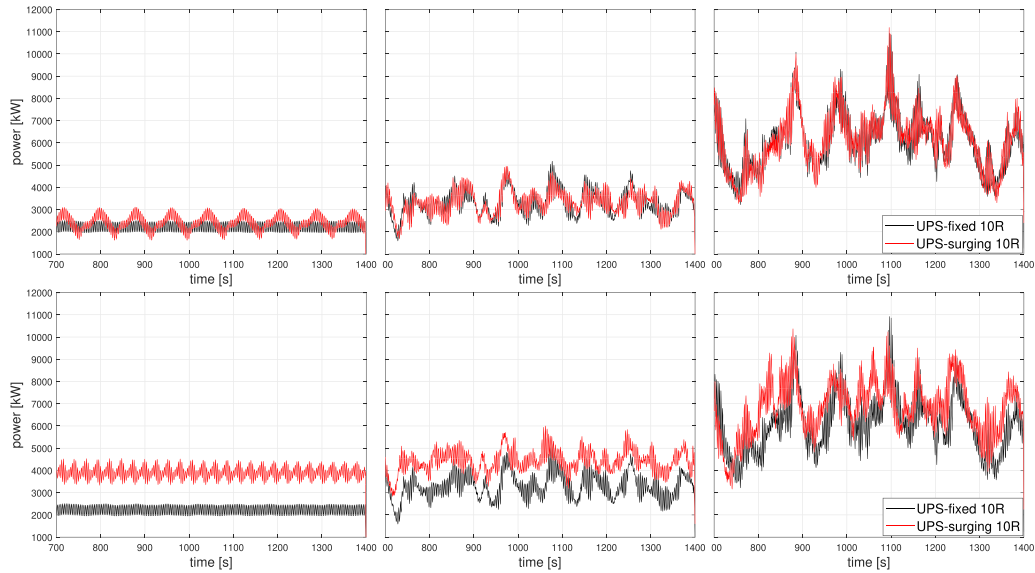


FIGURE 16 Time signal of the aerodynamic power of WT2 located 10R downstream a bottom-fixed machine (black lines) compared with the same turbine located downstream a surging turbine (red lines). The surge motion of WT1 has an amplitude of 15 m and frequencies of (top) 0.01221 Hz and (bottom) 0.11352 Hz. Wind speed of 10.8 m/s and TI levels of (from left to right) 0, 4, and 10%

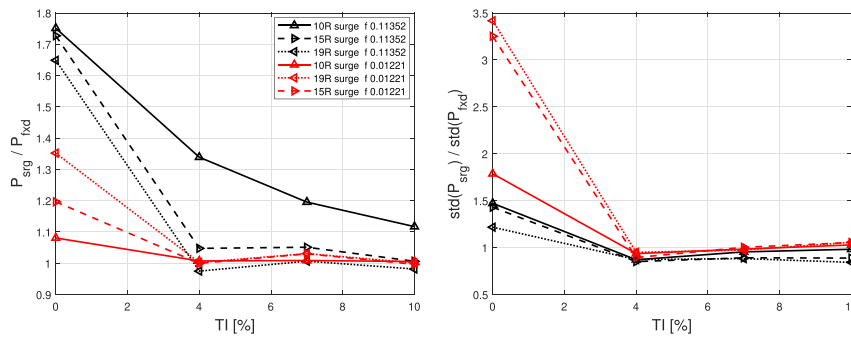


FIGURE 17 Relative (left) mean and (right) std of the power signal for the second turbine of the row with 10R, 15R, and 19R spacing between turbines. Upstream turbine surging with an amplitude of 15 m and frequencies of 0.01221 Hz and 0.11352 Hz. Wind speed of 10.8 m/s

considerably, with exception of the high-frequency surge cases with a spacing of 10R, where relatively large differences in fore-aft tower base bending moment are observed up to the 10% turbulence level.

In order to better assess the influence that the motion of the upstream turbine has upon the motion of WT2 we hereby define the Motion Response Operator (MRO), computed as follows:

$$MRO = \frac{std(x_{dws})}{std(x_{ups})} \tag{5}$$

where x_{ups} is the floater fore-aft displacement of the upstream turbine, which in this case is prescribed, and x_{dws} is the fore-aft displacement of the downstream machine, which in this case is free floating. Figure 19 shows the computed MRO for many of the investigated cases with a prescribed surge in WT1, which include a low and high-frequency surge motion, three different spacings between turbines and four inflow TI levels,

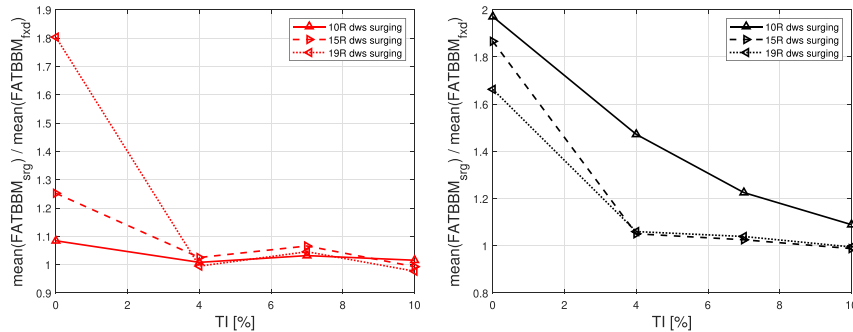


FIGURE 18 Relative mean FATBBM of the second turbine of the row. Distance between turbines of 10R, 15R, and 19R. Upstream turbine oscillating with a surge amplitude of 15 m and frequencies of (left) 0.01221 Hz and (right) 0.11352 Hz. Wind speed of 10.8 m/s

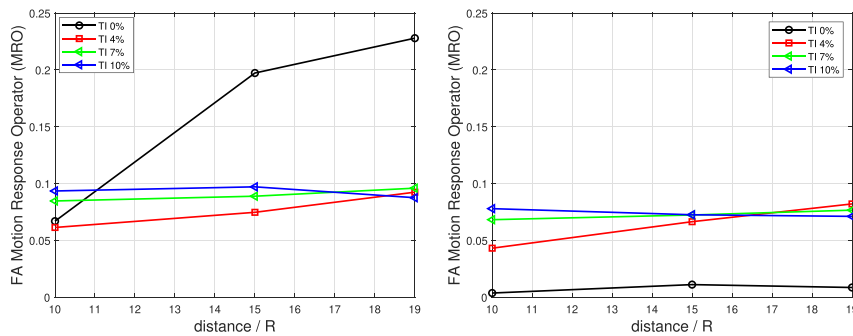


FIGURE 19 Fore-aft motion response operator of the downstream turbine for 10R, 15R, and 19R spacings and TI of 0, 4, 7, and 10%. Upstream turbine surging with an amplitude of 15 m and frequencies of (left) 0.01221 Hz and (right) 0.11352 Hz. Wind speed of 10.8 m/s

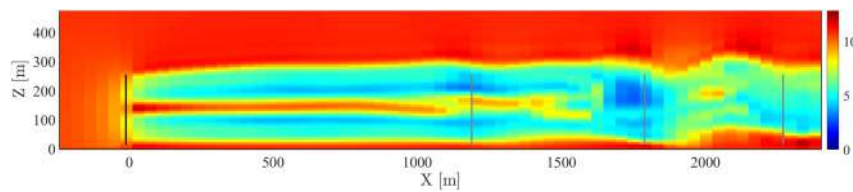


FIGURE 20 Instantaneous stream-wise velocity in the coarse XZ extraction plane for a MIRAS-HAWC2 simulation of a single IEA-15MW-RWT surging with an amplitude of 15 m and a frequency of 0.01221 Hz at a wind speed of 10.8 m/s

summing up a total of 24 simulations. The highest MRO values are obtained for the low-frequency surge motion combined with a 0% turbulence level and the largest distance between turbines. A spectral analysis has shown that, in laminar inflow, a large distance between turbines generate an excitation of the turbine fore-aft motion at the pitch and surge natural frequencies. The clear increase in the MRO between the 10R and 15-19R positions is related to the wake breakdown location, which has been observed between 10 and 15R. The breakdown promotes a larger meandering of the wake, as depicted in Figure 20, triggering a stronger response of the turbines located further downstream. In this way, at 19R WT2 responds with an amplitude of oscillation in fore-aft which is almost a 23% of forced motion applied to WT1, and 2.5 times larger than the MRO of the turbine located 10R downstream.

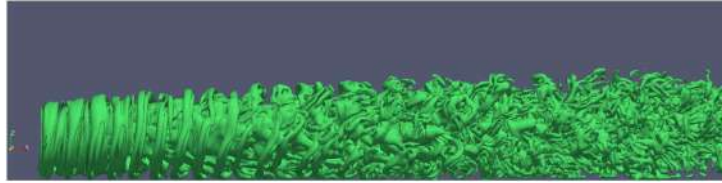


FIGURE 21 Side-view of the iso-vorticity contours on the computational mesh of a MIRAS-HAWC2 simulation of a turbine subject to a prescribed harmonic pitch motion of 6.38° amplitude and frequency of 0.11352 Hz. Inflow turbulence intensity of 0%

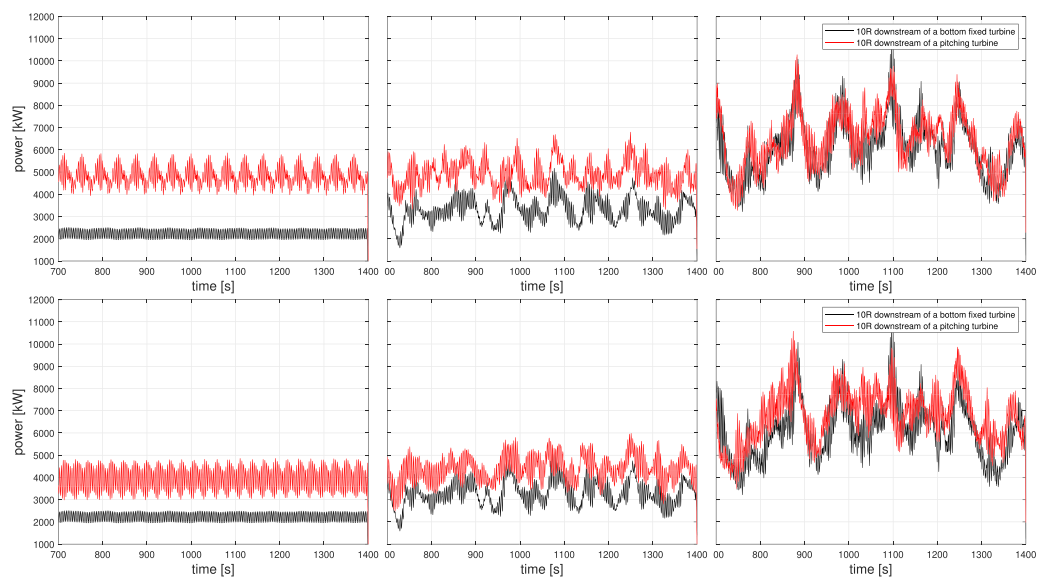


FIGURE 22 Time signal of the aerodynamic power of WT2 located $10R$ downstream a bottom-fixed machine in black lines compared with the same turbine located downstream a pitching turbine in red lines. The pitch motion of WT1 has an amplitude of 6.38° and frequencies of (top) 0.02441 Hz and (bottom) 0.11352 Hz. Wind speed of 10.8 m/s. TI levels of (from left to right) 0 , 4 , and 10%

5.3.2 | Prescribed pitch motion

In this case, MIRAS-HAWC2 simulations of WT1 have been carried out with a prescribed floater pitch motion of 6.38° amplitude and frequencies of 0.02441 and 0.11352 Hz, with the first frequency being representative of the natural pitch frequency of the WindCrest floater and the latter one being representative of ocean waves. Figure 21 shows the side-view of the iso-vorticity contours of the wake of a turbine oscillating with a harmonic pitch motion of 6.38° amplitude and a frequency of 0.11352 Hz with an inflow turbulence intensity of 0% .

Once again the simplified tandem approach introduced in Section 3.2 has been employed to simulate WT2. In this approach, HAWC2-BEM uses the flow extracted from the MIRAS-HAWC2 simulation of WT1.

The influence of the inflow turbulence intensity level in the loads and performance of the downstream turbine is investigated in what follows. As in the surge study, three different spacings as well as four turbulent intensity levels are taken into account. Figure 22 depicts the last 700 s of the downstream turbine power with a distance of $10R$ to WT1. In this case, there is a clear power increase in WT2 for the low-frequency motion in WT1, which does not completely disappear with the increasing TI.

To highlight the influence of the distance between turbines and the TI level on the performance of WT2 when operating downstream of a pitching turbine respect to downstream a fixed machine, the relative mean and standard deviation of the power is depicted in Figure 23. The figure shows that the power gain in WT2 when located on the wake of a pitching turbine is generally larger if WT1 is oscillating with a low

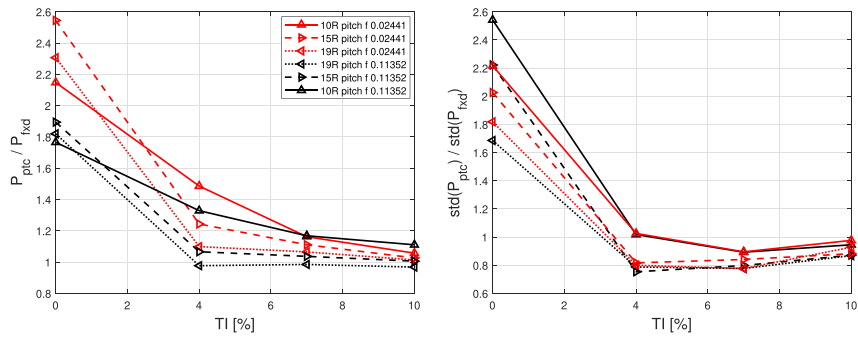


FIGURE 23 Relative (left) mean and (right) std of the power signal for the second turbine of the row with 10R, 15R, and 19R spacing between turbines. Upstream turbine pitching with an amplitude of 6.38° and a frequency of 0.02441 Hz and 0.11352 Hz. Wind speed of 10.8 m/s

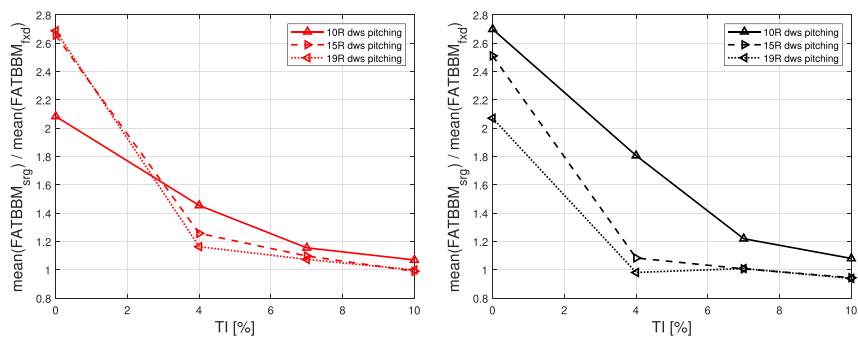


FIGURE 24 Relative mean tower base fore-aft root bending moment (FATBBM) of the second turbine of the row. Distance between turbines of 10R, 15R, and 19R. Upstream turbine moving with a pitch amplitude of 6.38° and frequencies of (left) 0.02441 Hz and (right) 0.11352 Hz. Wind speed of 10.8 m/s

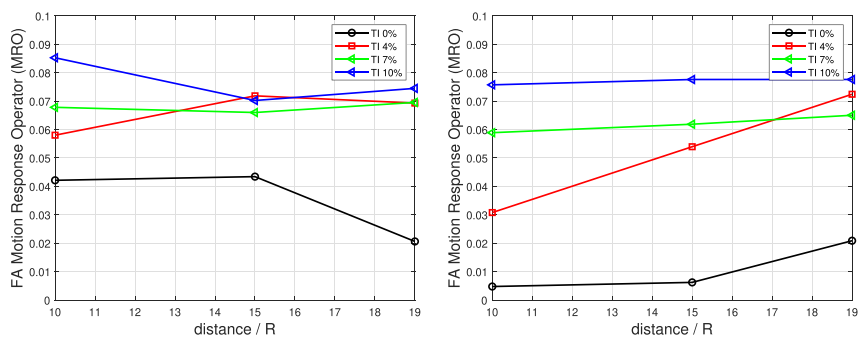


FIGURE 25 Motion response operator of the downstream turbine for 10R, 15R, and 19R spacings and inflow TI of 0, 4, 7, and 10%. Upstream turbine pitching with an amplitude of 6.38° and frequencies of 0.02441 Hz and 0.11352 Hz. Wind speed of 10.8 m/s

frequency. Regarding the standard deviation of the power, very similar trends are observed for the low and high-frequency cases once $TI \geq 4\%$. Moreover, it is observed that for the 15R and 19R spacings the turbine downstream a pitching machine experiences smaller variations in power if $TI \geq 4\%$ compared with the fixed case, with the relative std $< 1\%$. This behavior seems counter-intuitive, since the pitching $WT1$ forces an earlier breakdown of the wake compared with the fixed case, promoting a larger wake meandering, which should increase the power variations in $WT2$.

The relative mean fore-aft tower base bending moment of $WT2$ is presented in Figure 24 for the low- and high-frequency pitch oscillations. Similar trends are observed as the ones mentioned for the power output. The main differences appear for the high-frequency cases where the relative increase in FATBBM is larger than the observed power gain, especially for low TI levels and short distances between turbines.

Figure 25 depicts the fore-aft motion response operator (MRO) for all the simulations with a prescribed pitch motion. Contrary to what has been observed in the surge study, the TI 0% cases display the lowest MRO values independently of the pitching frequency in $WT1$. As the TI level is increased the MRO grows for the 10R spacing. The trends with the increasing distance between turbines are not as clear and vary with the pitch frequency applied to the upstream turbine.

6 | WIND FARM SIMULATIONS

The downstream wake study is now extended to a farm of five floating wind turbines. The turbines are placed in a row and the MIRAS-HAWC2 farm code is used to investigate how the floater motion affects the overall response characteristics of the turbine cluster.

An initial mesh study has been carried out to assess the dependency of the MIRAS-HAWC2 farm predictions with respect to the cross-sectional mesh size. Four different distances from the rotor center to the outer boundary of the auxiliary Cartesian mesh are taken into account, that is, 2R, 3R, 4R, and 5R as sketched in Figure 26. Moreover, a spacing between turbines of 15R, an inflow turbulent intensity of 7% and a wind speed of 8 m/s have been used for the present mesh study.

The relative mean and the coefficient of variation (standard deviation over the mean) for key turbine quantities are depicted in Figure 27 for the different mesh sizes and as function of the turbine position in the row. From the figure, it can be appreciated how the use of a narrow mesh (2R) can be acceptable to simulate cases with up to two turbines, with fairly small disagreements between the predictions. However, as the number of turbines is increased, larger differences appear and it becomes necessary the use of a larger domain. Since free boundary conditions are used in all directions but the ground, these differences can mostly be related to two factors. First, the departure of vorticity outside of the computational domain due to the wake expansion and interaction. Second, changes in the entrainment of vortex structures from outermost areas towards the farm canopy. For the present study of five turbines in a row, the use of a 4R distance to the cross-sectional mesh boundaries has been found acceptable in terms of mesh independence. Therefore, the Cartesian mesh used in the rest of the study has the dimensions of $77R \times 8R \times 5.12R$, with a cell size of 6 m, adding up to a total of more than 25 million cells and a similar number of vortex particles. This number is kept constant throughout the simulations thanks to a continuous particle re-meshing.

In what follows is presented a comparison between a wind farm of bottom-fixed and floating machines in below-rated, rated, and above-rated wind conditions, that is, 8, 10.8, and 15 m/s, respectively. As in the previously presented mesh study, a spacing of 15R and an inflow turbulent intensity of 7% is used. Figure 28 depicts the contour plot of instantaneous stream-wise velocities during the initial phase of the wake development. At this stage it is possible to appreciate from the figures that the undisturbed wakes of the floating turbines present more dynamic vortex structures compared with the wakes generated by bottom-fixed machines. Note that these structures undergo periodic oscillations at the surge natural frequency of the WindCrete platform, as earlier shown in Figure 8. As the flow develops further, differences in the instantaneous velocity contours are less obvious as shown in Figure 29. However, as it will be described in what follows, there are clear differences in the loads and turbine operation between the fixed and floating cases.

Focusing first in below-rated conditions, that is, 8 m/s, clear differences between the fixed and floating cases appear in the low-frequency range, between 0.001 and 0.01 Hz, and for turbines located deep inside the farm. This can be appreciated in the region R1 of the thrust spectral

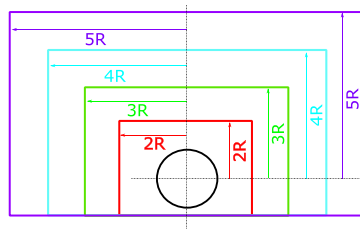


FIGURE 26 Sketch of the different cross sectional mesh sizes considered in the study

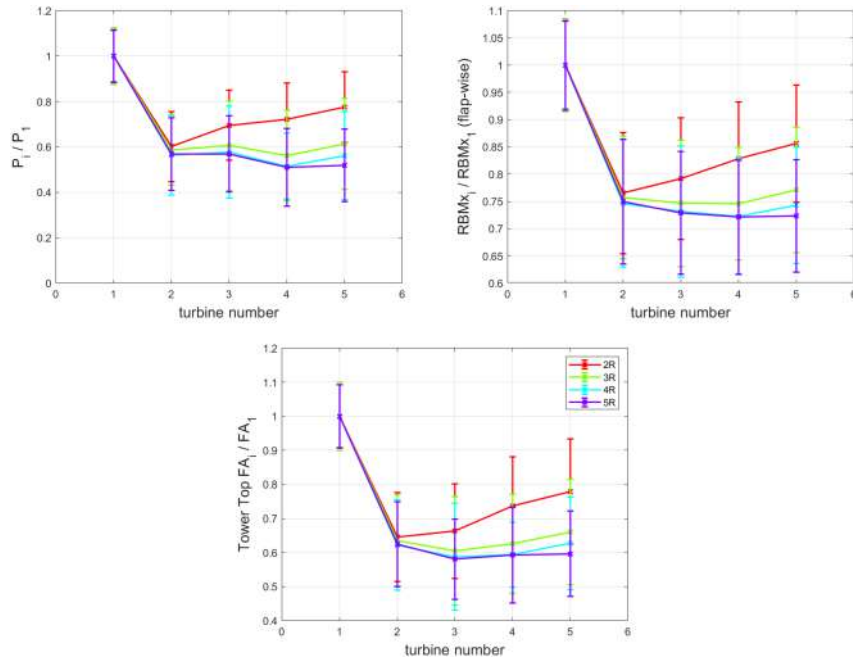


FIGURE 27 Influence of the mesh size on the mean and coefficient of variation of key turbine quantities in function of the turbine position and respect to the first turbine of the row. (Left) Power, (center) blade root flap-wise bending moment, and (right) tower-top fore-aft displacement

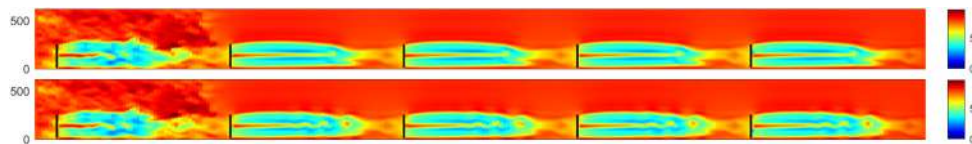


FIGURE 28 Instantaneous stream-wise velocity on the extraction XZ plane for a MIRAS-HAWC2 farm simulation of five turbines with a spacing of 15R. The developing wake during the initialization phase is depicted. (Top) Bottom-fixed IEA-15MW-RWT and (bottom) IEA-15MW-RWT mounted on the WindCrete platform. Wind speed of 15 m/s

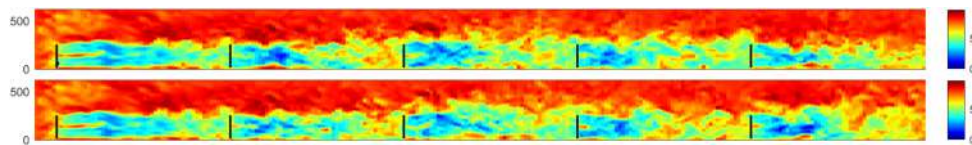


FIGURE 29 Instantaneous stream-wise velocity on the extraction XZ plane for a MIRAS-HAWC2 farm simulation of five turbines with a spacing of 15R. The fully developed wake is depicted. (Top) Bottom-fixed IEA-15MW-RWT and (bottom) IEA-15MW-RWT mounted on the WindCrete platform. Wind speed of 15 m/s

analysis of turbine number four, presented in Figure 30. It can be seen as an initial indication that floating turbines can alter low-frequency modes of the flow inside a wind farm. In addition, differences in the mid-frequency region, between 0.01 and 0.03 Hz (R2), can be seen in all turbines of the row. Note that in this region lay most of the natural frequencies of the WindCrete floater and therefore is expected for the floating turbines

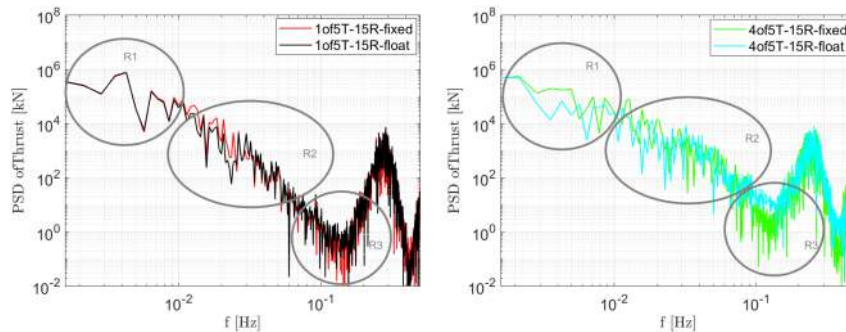


FIGURE 30 Spectral analysis of the thrust signal comparing bottom-fixed with floating turbines in below-rated wind conditions. (Left) First turbine of the row and (right) fourth turbine of the row

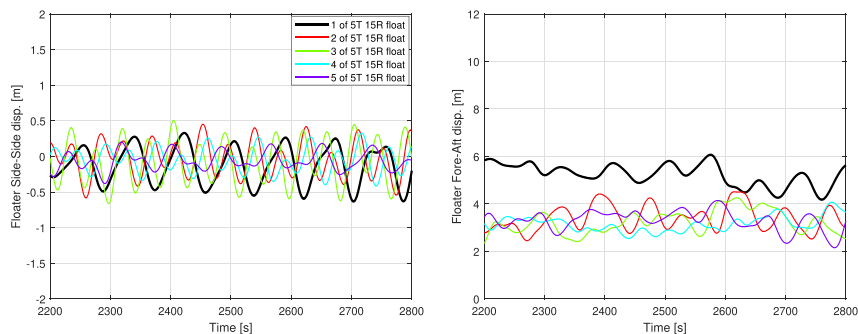


FIGURE 31 Time signal of the floater translations: (left) side-side and (right) fore-aft for the last 600 s simulated of a row of floating turbines in below-rated wind conditions, that is, 8 m/s

response to be different to bottom-fixed machines. The region marked as R3, located just before the blade passing frequency (3P), shows significant differences as well, due to larger variations in the rotational speed of the floating machine, which grow even larger along the row of turbines.

Regarding the motion of the floating machines, Figure 31 depicts the side-side and fore-aft translations of the floater at the still water level. Small differences can be observed depending on the turbine positioning in the row. The first turbine of the row presents a clearly larger mean value of the fore-aft displacement, as expected in below-rated wind conditions, since it is subject to a higher incoming wind speed. Regarding the side-side displacement, the amplitude of the oscillations is slightly reduced deep inside the row of turbines, WT4 and WT5. But what is more interesting is that all downstream turbines display a higher frequency oscillation not observed in WT1. A spectral analysis of the signal has shown that all the downstream turbines but the last one present a more energetic peak at the pitch natural frequency of the WindCrest platform, which seems to be excited, together with a reduction of the peak energy contained at the surge natural frequency. It has also been observed a small excitation of the heave DoF around 0.03 Hz, which grows with the turbine position deeper inside the farm, as can be appreciated in the figure. As previously stated, although the heave motion is in principle unlikely to be excited by the wind, coupling effects and mean displacements in other DoFs can lead to a wind-induced heave response.

Regarding the mean power and thrust of each turbine of the row relative to WT1, presented in Figure 32, there is a small gain in relative power for the second and third turbines. This gain is partially related to the lower power generated by a floating turbine in turbulent conditions, as earlier shown in Section 5.2.1. In terms of absolute power, the second turbine has virtually zero gain respect to the case with bottom-fixed turbines as earlier shown for the equivalent tandem configuration. Moreover, turbines WT4 and WT5 show a lower mean power and thrust in the floating configuration. This lower loading in comparison with the equivalent bottom-fixed turbines could be related to the highest thrust observed in WT3, which generates a higher wake deficit reducing the power available for downstream machines. It is also important to note that in below-rated conditions the torque controller will always try to achieve an optimal rotor speed. However, for a floating turbine the rotor speed will see larger variations due to the oscillatory motion of the rotor, which results in more controller action and larger differences in power.

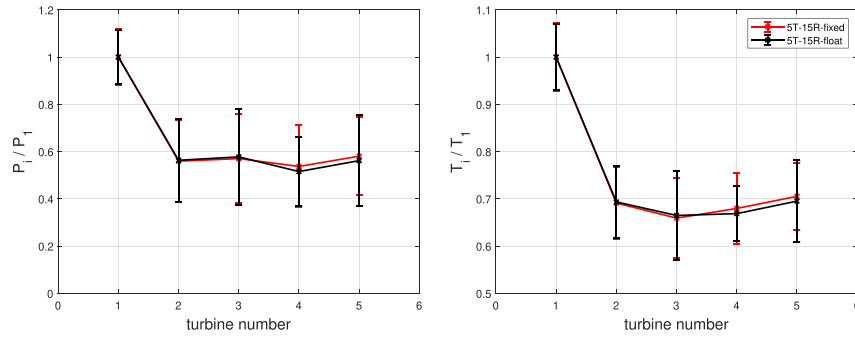


FIGURE 32 Relative mean and standard deviation of the power and thrust for the different turbines of the row in below-rated wind conditions, that is, 8 m/s

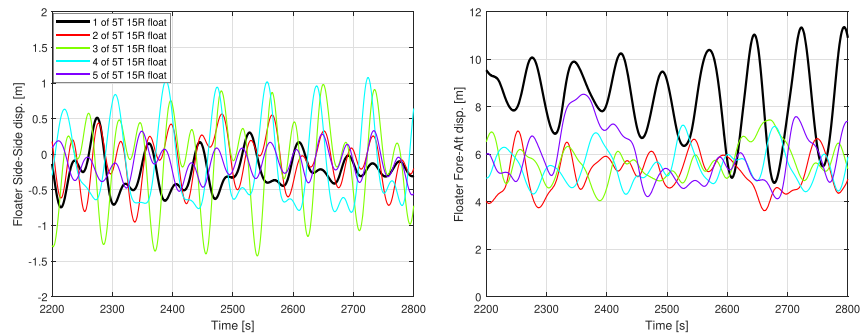


FIGURE 33 Time signal of the floater translations: (left) side-side and (right) fore-aft for the last 600 s simulated of a row of floating turbines at the rated wind speed of 10.8 m/s

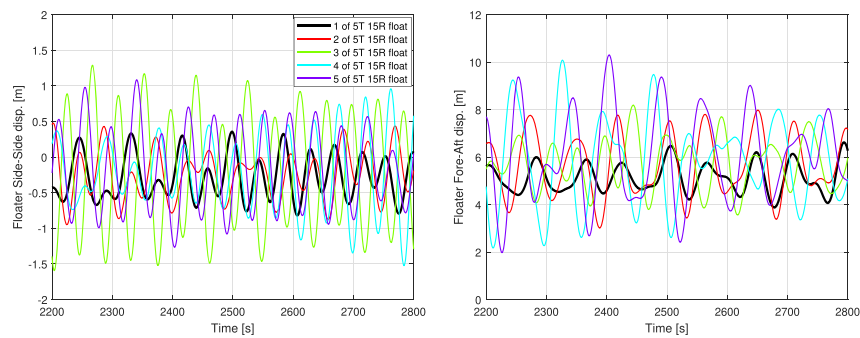


FIGURE 34 Time signal of the floater translations: (left) side-side and (right) fore-aft for the last 600 s simulated of a row of floating turbines in above-rated wind conditions, that is, 15 m/s

At the rated wind speed, that is, 10.8 m/s, larger displacements have been observed along the row of floating wind turbines. This is depicted in Figure 33, where the first turbine of the row exhibits by far the largest amplitude of oscillations in the fore-aft direction. The second turbine of the row operates in lower wind speeds, and therefore, its fore-aft motion is drastically reduced. Further downstream, the turbines present slightly larger oscillations although do not reach the levels attained by the upstream machine. Regarding the side-side displacement, WT3 presents the

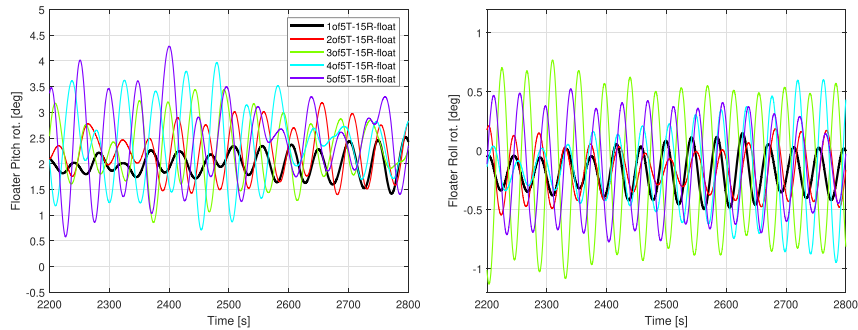


FIGURE 35 Time signal of the floater rotations: (left) pitch and (right) roll for the last 600 s simulated of a row of floating turbines in above-rated wind conditions, that is, 15 m/s

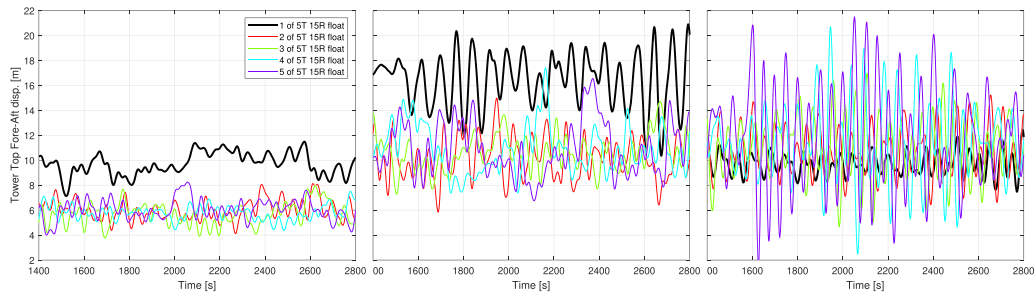


FIGURE 36 Time signal of the tower-top fore-aft displacement for wind speeds of (left) 8, (center) 10.8, and (right) 15 m/s during the last 1400 s of simulated time

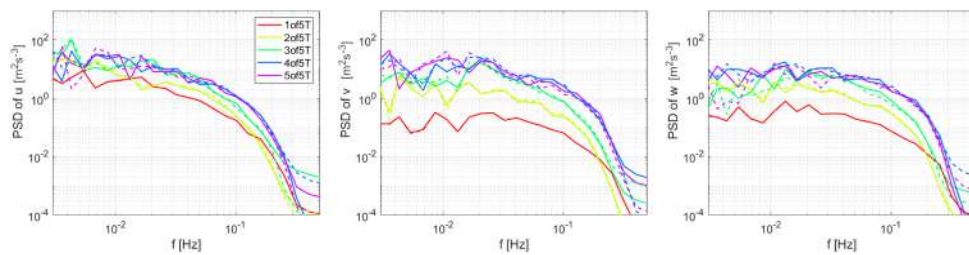


FIGURE 37 Filtered energy spectrum of the three components of the velocity one radius upstream each one of the five turbines of the row at the hub height. From left to right stream-wise, cross-, and vertical component of the velocity. Solid lines represent floating turbines while dashed lines depict bottom-fixed machines. Wind speed of 15 m/s

largest amplitude of oscillation, which seems to be directly related to an excitation of the roll DoF. These differences in the turbine motion do not have a large impact in the turbine aerodynamics, with the spectral analysis of the thrust signal of the different machines showing very similar trends as in the below-rated case (not included for the sake of conciseness). Note that the mean power and thrust loss observed in WT4 and WT5 in below-rated wind conditions is further increased, with their average rotational speed in the fixed case being 2.5% higher than in the floating case.

In above-rated conditions, that is, 15 m/s, large differences between the different turbine positions and types have been observed in both the turbine motion and the loading. The time signal of the floater fore-aft and side-side displacements for all turbines of the row is presented in

Figure 34. From the figure, we see how WT3 undergoes the largest side-side floater displacement, followed closely by WT4 and WT5. What is even more interesting is the turbine motion in the fore-aft direction, in this case the fourth and fifth turbines exhibit very large floater displacements with amplitudes of up to approximately 4 m. This, in combination with the pitch rotation presented in Figure 35, translates into a peak-to-peak tower-top fore-aft maximum displacement of more than 19 m, as can be appreciated from Figure 36. The latter figure depicts the tower-top fore-aft displacement of all turbines in the row under the different wind conditions. It can be appreciated how the turbines located deep inside the farm in above-rated wind conditions undergo much larger oscillations than the others. One could first think that this large increase in the motion of downstream turbines is because they are operating closer to the maximum thrust region. However, this is not the case since WT4 and WT5 in the 15 m/s case are operating at a mean thrust of approximately 1500 kN while WT1 in the rated case (10.8 m/s) is operating with a 30% larger thrust, around 2000 kN. Therefore, the large motion that turbines located deep inside the farm are subjected to must be related to their interaction with the wind farm flow, which is developed to excite some of the floater natural modes. Every time the flow encounters a wind turbine, its energy content increases. This effect is related to the flow interaction with the moving rotor as can be appreciated in Figure 37, which depicts the smoothed-out energy spectrum of the three components of the velocity extracted one radius upstream each turbine of the row. Note that the energy drop observed beyond the 0.1 Hz frequency is related to the sampling frequency of the extracted velocities, which, as noted in Section 4.2, is one sample per 32 times steps. The simulated turbines see a much better resolved turbulent wind at high frequencies than what is shown in the figure. Such high frequencies are not of strong interest in the present analysis since the rigid-body frequencies of the WindCrete floater appear in a much lower frequency range ($<0.09\text{Hz}$)³¹ and it is expected that its motion mainly impacts the flow in that region. As the flow travels down a row of turbines, there is a resonance build-up effect (especially relevant in the lateral and vertical components) that floating machines react to, causing a larger excitation of the last turbines in the row. This phenomenon could be understood as wake-induced vibrations, where the vortices generated by upstream machines induce fluctuations in the downstream turbines. This increase in the energy content of the flow in the low- and mid-frequency range is similarly seen in bottom-fixed machines, although they do not seem to react to it in the same way. This effect can mainly

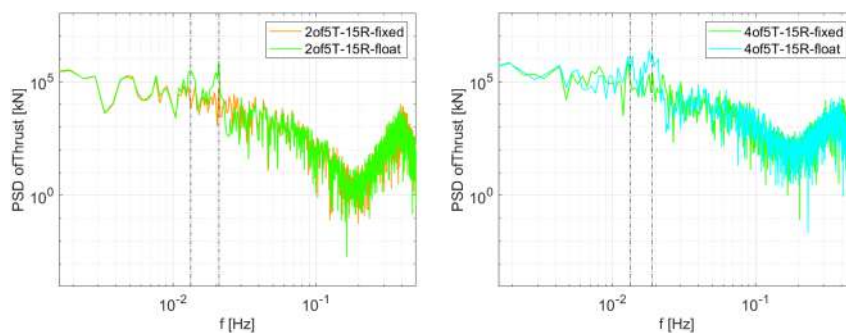


FIGURE 38 Spectral analysis of the thrust signal comparing bottom-fixed with floating turbines in above-rated wind conditions. (Left) WT2 and (right) WT4

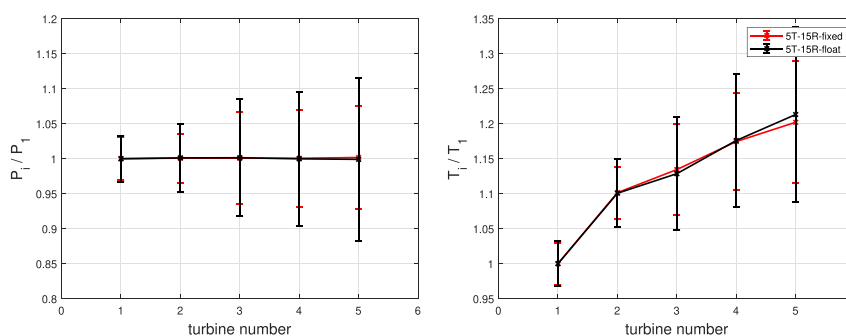


FIGURE 39 Relative mean and standard deviation of the power and thrust for the different turbines of the row in above-rated wind conditions, that is, 15 m/s

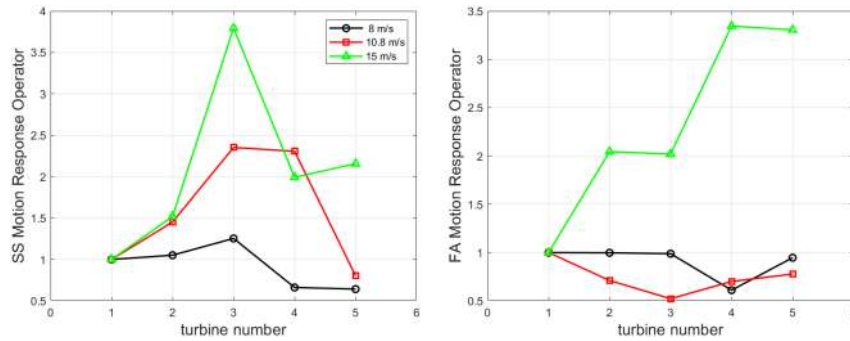


FIGURE 40 Motion response operator for the floater: (left) side-side and (right) fore-aft displacements as function of the turbine position and the wind speed

be observed in above-rated conditions since downstream turbines see a lower incoming wind speed than the upstream machine, which translates into a higher thrust. A higher thrust increases the dynamic response of each machine, thus introducing more energy in the wake and causing more resonance on the next turbine.

To further understand how the floating turbines operate inside the wind farm flow in above-rated conditions, Figure 38 depicts the spectral analysis of the thrust signal for turbines WT2 and WT4. Results of the wind farm with bottom-fixed machines are included in the figure and the main differences with floating turbines are highlighted in what follows. At such high wind speed all floating turbines of the row have an excitation of a mode around 0.021 Hz, which is really close to the natural frequency of the WindCrete floater in pitch. Moreover, selected turbines like the second and the fourth also exhibit an excitation of the surge mode, around 0.014 Hz. It is important to underline that, as was shown in below-rated wind conditions, the further inside the farm the more visible are the differences in the low-frequency response (from 0.001 and 0.01 Hz) between bottom-fixed and floating turbines.

As a final comparison between bottom-fixed and floating machines Figure 39 depicts the relative mean and the standard deviation of the power and thrust as function of the turbine position for the 15 m/s case. The most striking difference between the two configurations is the larger standard deviation observed in all the downstream floating machines. Moreover, the std of both power and thrust signals grow with the turbine position inside the farm. In terms of power, the floating turbines show a 2.9, 18.6, 24.6, 36.3, and 58.5% larger std than the bottom-fixed machines for WT1, WT2, WT3, WT4 and WT5, respectively. Meanwhile, in terms of thrust, the difference in std is slightly lower, with 2.4, 13.0, 17.7, 29.7, and 44.2%.

To better assess the influence that the motion of the first turbine of the row has upon the motion of the downstream machines we have computed the fore-aft and side-side motion response operators for all the floating cases as follows,

$$MRO = \frac{std(x_i)}{std(x_1)} \quad (6)$$

where x_i is the floater fore-aft displacement of turbine number i in the row of turbines, with x_1 being the first turbine of the row and x_5 being the last one. The computed values for wind speeds of 8, 10.8, and 15 m/s are presented in Figure 40. Regarding the side-side MRO, generally the higher the wind speed the larger the response of the downstream turbines to upstream motions with a clear peak at WT3, observed regardless of the wind speed. As already seen in the previous analysis, it seems like the side-side translation and roll rotation of the third turbine of the row are more easily excited by the wind farm flow. This could also be related to the control strategy of virtually constant power in the full-load region, which introduces variations in the generator torque that can excite the roll DoF. In terms of the fore-aft MRO, all wind turbines operating in below-rated conditions show values lower than the unity; however, at 15 m/s, there is a very steep increment of the FA MRO with WT4 and WT5 reaching values of 3.4 and 3.3, respectively. This may be explained by the resonance build-up effect described earlier.

7 | CONCLUSION

In the present work, the impact of the wake generated by a floating wind turbine in downstream machines has been investigated in laminar and turbulent conditions for different configurations of two and five turbines in a row. Throughout the manuscript it has been shown that:

- In a tandem configuration, the second turbine of the row produces more power when operating downstream a floating machine than when operating downstream a fixed one. This power gain is drastically reduced with the increasing turbulent intensity. As an example, for a 10R spacing between turbines and a TI of 4 % there is a power gain of approximately 3.5 %, but as the TI increases to 10% the power gain reduces to virtually zero.
- If the effect of the waves is taken into account through forced oscillations of the upstream machine, the previously mentioned power gain observed in WT2 increases and is less sensitive to the inflow turbulence level. For example, the highest frequency surge case with a spacing of 10R between turbines showed a time-averaged power gain of 34 %, 20 % and 11 % for TI of 4 %, 7 % and 10 %, respectively. On the other hand, the low-frequency surge case showed much smaller gains. Regarding the pitch motion, the low-frequency pitch case showed generally higher power gains, that is, 50%, 19% and 12% for the same TI and turbine spacing.
- In laminar inflow conditions it has been observed that when the upstream turbine surges at a low frequency, the downstream machine draws energy at the same frequency, creating a resonance effect. This effect is the largest at the natural frequency in pitch of the WindCrete platform, that is, 0.02441 Hz, and it is not observed when the upstream turbine oscillates at higher frequencies, that is, 0.05676 and 0.11352 Hz.
- A low-frequency surge motion in the upstream machine seems to generate the largest fore-aft MRO in WT2, reaching values of up to 0.22. This substantial MRO seems to be triggered by a larger wake meandering observed in the far downstream positions. Moreover, if the frequency of oscillation is high, that is, 0.11352 Hz, the downstream turbine response to harmonic oscillations in the upstream turbine is very similar independently of the motion type in WT1 (surge or pitch).
- Wind farm simulations of five turbines in a row have shown that the relative power of WT4 and WT5 in below- and rated wind conditions is considerably reduced in the floating case compared with the bottom-fixed one. This has been attributed to the controller action.
- Farm simulations in above-rated conditions have shown that floating turbines deep inside the farm (WT3, WT4 and WT5) present much larger oscillations than upstream-located turbines. A maximum fore-aft MRO of 3.4 has been computed for WT4. This demonstrates that resonant build-up of motion response can happen through the wake in above-rated wind conditions, where the energy content in the low- and mid-frequency range of the three components of the velocity field increases along the row of turbines.
- Comparing bottom-fixed with floating wind farms in above-rated wind conditions, a larger standard deviation in both power and thrust signals has been observed in all the floating turbines. It has been found that these variations grow with the turbine position inside the farm. For example, a floating WT5 displays a 58.5% larger std in power and a 44.2% larger std in thrust than a bottom-fixed machine located in the same position.

As future work we would like to extend the wind farm investigation to include wave effects and how they affect the interaction between the turbine wakes. Moreover, we would like to account for shared mooring lines between the floaters with the potential of drastically reducing mooring costs at the expense of a more complex system.

We have shown that the interaction between floating wind turbines and their dynamic wakes adds a new level of complexity to the already intricate wind farm flow. We therefore would like to emphasize the need of tailor-made experiments to better understand the physical phenomena involved and to help with the validation of state-of-the-art numerical models.

ACKNOWLEDGEMENTS

This work was carried out as part of the COREWIND project (corewind.eu), which has received funding from the European Union's Horizon 2020 Research and Innovation program under grant agreement no. 815083. This funding is gratefully acknowledged. The authors would also like to acknowledge the support from the Department of Wind Energy, Technical University of Denmark.

PEER REVIEW

The peer review history for this article is available at <https://publons.com/publon/10.1002/we.2738>.

DATA AVAILABILITY STATEMENT

Data available on request due to privacy/ethical restrictions

ORCID

Néstor Ramos-García  <https://orcid.org/0000-0002-8326-2174>

REFERENCES

1. Myhr A, Bjerkseter C, Ågotnes A, Nygaard TA. Levelised cost of energy for offshore floating wind turbines in a life cycle perspective. *Renew Energy*. 2014;66:714-728. <https://www.sciencedirect.com/science/article/pii/S0960148114000469>
2. Maienza C, Avossa AM, Ricciardelli F, Coiro D, Troise G, Georgakis CT. A life cycle cost model for floating offshore wind farms. *Appl Energy*. 2020;266:114716. <https://www.sciencedirect.com/science/article/pii/S0306261920302282>

3. Martínez A, Iglesias G. Mapping of the levelised cost of energy for floating offshore wind in the European atlantic. *Renew Sustain Energy Rev.* 2022; 154:111889. <https://www.sciencedirect.com/science/article/pii/S1364032121011564>
4. Veers P, Dykes K, Lantz E, et al. Grand challenges in the science of wind energy. *Science.* 2019;366(6464):1-17.
5. Lienard C, Boisard R, Daudin C. Aerodynamic behavior of a floating offshore wind turbine. *AIAA J.* 2020;58(9):3835-3847. <https://doi.org/10.2514/1.J059255>
6. Kyle R, Lee YC, Früh W-G. Propeller and vortex ring state for floating offshore wind turbines during surge. *Renew Energy.* 2020;155:645-657. <http://www.sciencedirect.com/science/article/pii/S0960148120304377>
7. Leble V, Barakos GN. Forced pitch motion of wind turbines. *Journal of Physics: Conference Series*, Vol. 753: IOP Publishing; 2016:22042.
8. Jonkman J, Musial W. Offshore code comparison collaboration (OC3) for IEA Task 23 offshore wind technology and deployment. Technical Report NREL/TP-5000-48191, National Renewable Energy Laboratory; 2010.
9. Huang Y, Wan D, Hu C. Numerical study of wake interactions between two floating offshore wind turbines. In: Proceedings of the Twenty-Eighth (2018) International Ocean and Polar Engineering Conference Sapporo, Japan, ISOPE. International Society of Offshore and Polar Engineers; 2018. Proceedings of the Twenty-eighth (2018) International Offshore and Polar Engineering Conference.
10. Wang J, Wang C, Castañeda O, Campagnolo F, Bottasso C. Large-eddy simulation of scaled floating wind turbines in a boundary layer wind tunnel. *J Phys: Conf Ser.* 2018;1037:72032.
11. Johlas H, Martínez Tossas L, Schmidt D, Lackner M, Churchfield M. Large eddy simulations of floating offshore wind turbine wakes with coupled platform motion. *J Phys Conf Ser.* 2019;1256:12018.
12. Xiao S, Yang D. Large-eddy simulation-based study of effect of swell-induced pitch motion on wake-flow statistics and power extraction of offshore wind turbines. *Energies.* 2019;12(7):1246.
13. Wise A, Bachynski EE. Analysis of wake effects on global responses for a floating two-turbine case. *J Phys: Conf Ser.* 2019;1356:12004.
14. Jonkman JM, Annoni J, Hayman G, Jonkman B, Purkayastha A. Development of fast.farm: a new multi-physics engineering tool for wind-farm design and analysis. In: 35th wind energy symposium. American Institute of Aeronautics and Astronautics; 2017. <https://arc.aiaa.org/doi/abs/10.2514/6.2017-0454>
15. Wise A, Bachynski EE. Wake meandering effects on floating wind turbines. *Wind Energy.* 2020;23(5):1266-1285.
16. van Binsbergen DW, Wang S, Nejad AR. Effects of induction and wake steering control on power and drivetrain responses for 10 MW floating wind turbines in a wind farm. *J Phys: Conf Ser.* 2020;1618:22044.
17. Nanos EM, Letizia S, Clemente DJB, et al. Vertical wake deflection for offshore floating wind turbines by differential ballast control. *J Phys: Conf Ser.* 2020;1618:22047.
18. Kopperstad KM, Kumar R, Shoele K. Aerodynamic characterization of barge and spar type floating offshore wind turbines at different sea states. *Wind Energy.* 2020;23(11):2087-2112. <https://onlinelibrary.wiley.com/doi/abs/10.1002/we.2547>
19. Ramos-García N, Kontos S, Pegalajar-Jurado A, González Horcas S, Brednose H. Investigation of the floating IEA wind 15 MW RWT using vortex methods part I: flow regimes and wake recovery. *Wind Energy.* 2022;25(3):468-504. <https://onlinelibrary.wiley.com/doi/abs/10.1002/we.2682>
20. Manolas D, Riziotis V, Papadakis G, Voutsinas S. Hydro-servo-aero-elastic analysis of floating offshore wind turbines. *Fluids.* 2020;5:200.
21. Li Z, Dong G, Yang X. Onset of wake meandering for a floating offshore wind turbine under side-to-side motion. *J Fluid Mech.* 2022;934.
22. Rockel S, Peinke J, Hölling M, Cal RB. Wake to wake interaction of floating wind turbine models in free pitch motion: an eddy viscosity and mixing length approach. *Renew Energy.* 2015;85:666-676.
23. Jacobsen A, Godvik M. Influence of wakes and atmospheric stability on the floater responses of the hywind scotland wind turbines. *Wind Energy.* 2020;24(2):149-161.
24. Fu S, Jin Y, Zheng Y, Chamorro LP. Wake and power fluctuations of a model wind turbine subjected to pitch and roll oscillations. *Appl Energy.* 2019; 253:113605.
25. Ramos-García N, Sørensen JN, Shen WZ. Three-dimensional viscous-inviscid coupling method for wind turbine computations. *Wind Energy.* 2016; 19(1):67-93.
26. Sessarego M, Ramos-García N, Sørensen JN, Shen WZ. Development of an aeroelastic code based on three-dimensional viscous-inviscid method for wind turbine computations. *Wind Energy.* 2017;20(7):1145-1170. <https://onlinelibrary.wiley.com/doi/pdf/10.1002/we.2085>
27. Ramos-García N, Hejlesen MM, Sørensen JN, Walther JH. Hybrid vortex simulations of wind turbines using a three-dimensional viscous-inviscid panel method. *Wind Energy.* 2017;20(11):1871-1889.
28. Ramos-García N, Spietz HJ, Sørensen JN, Walther JH. Vortex simulations of wind turbines operating in atmospheric conditions using a prescribed velocity-vorticity boundary layer model. *Wind Energy.* 2019;21(11):1216-1231.
29. Larsen TJ, Hansen AM. *Hawc2 - user manual*. DTU-Risø-R-1597; 2015.
30. Gaertner E, Rinker J, Sethuraman L, et al. Definition of the IEA Wind 15-Megawatt Offshore Reference Wind Turbine. tech. rep., National Renewable Energy Laboratory; 2020.
31. Mahfouz MY, Salari M, Hernández S, et al. COREWIND D1.3: Public design and FAST models of the two 15MW floater-turbine concepts. tech. rep., University of Stuttgart; 2020.
32. Ramos-García N, Sessarego M, Horcas SG. Aero-hydro-servo-elastic coupling of a multi-body finite-element solver and a multi-fidelity vortex method. *Wind Energy.* 2021;24(5):481-501. <https://onlinelibrary.wiley.com/doi/abs/10.1002/we.2584>
33. Madsen HA, Larsen TJ, Pirrung GR, Li A, Zahle F. Implementation of the blade element momentum model on a polar grid and its aeroelastic load impact. *Wind Energy Sci.* 2020;5(1):1-27. <https://www.wind-energ-sci.net/5/1/2020/>
34. Øye S Dynamic stall simulated as a time lag of separation. In: Proc. of EWEC, Thessaloniki, Greece; 1994.
35. Bæk P. Unsteady flow modeling and experimental verification of active flow control concepts for wind turbine blades. *Ph.D. Thesis*: Technical University of Denmark; 2012.
36. Hejlesen MM, Rasmussen JT, Chatelain P, Walther JH. A high order solver for the unbounded poisson equation. *J Comput Phys.* 2013;252:458-467.
37. Shabana AA. *Computational Dynamics, Second Edition*: John Wiley & Sons, Inc; 2001.
38. Vigarà F, Cerdán L, Durán R, et al. COREWIND D1.2: Design Basis. tech. rep., ESTEYCO; 2019.

39. Hansen MH, Henriksen LC. *Basic DTU Wind Energy Controller*. Denmark: DTU Wind Energy; 2013. Contract Number: EUDP project Light Rotor; Project Number 46-43028-Xwp3 The report number is DTU-Wind-Energy-Report-E-0028 and not DTU-Wind-Energy-Report-E-0018 as stated inside the report.
40. Henriksen L, Tibaldi C, Bergami L. DTU wind energy technical report. technical report, DTU Wind Energy; 2015.
41. Gözcü O, Verelst DR. The effects of blade structural model fidelity on wind turbine load analysis and computation time. *Wind Energy Sci*. 2020;5(2): 503-517. <https://wes.copernicus.org/articles/5/503/2020/>
42. Barthelmie R, Hansen OF, Enevoldsen K, et al. Ten years of meteorological measurements for offshore wind farms. *J Solar Energy Eng*. 2005;127: 170-176.

How to cite this article: Ramos-García N, González Horcas S, Pegalajar-Jurado A, Kontos S, Bredmose H. Investigation of the floating IEA wind 15-MW RWT using vortex methods Part II: Wake impact on downstream turbines under turbulent inflow. *Wind Energy*. 2022;25(8): 1434-1463. doi:[10.1002/we.2738](https://doi.org/10.1002/we.2738)

8 Summary and conclusions

8.1 Sub-conclusion on wave forcing

An accelerated method for inviscid second order wave loads is presented based on QTFs determined by a potential flow panel code. The accuracy and efficiency of the method is tested by simulating the loads of mild and severe sea states on the WindCrete spar-buoy floater. The method is implemented in FORTRAN as part of the HAWC2 software and in Matlab, to be included in Matlab based optimizers. The study shows that:

- The accelerated method scales with $O(n)$ cost compared to the $O(n^2)$ cost of the double sum method.
- When using 8 modes the error of the accelerated method is below 5% in the translational degrees of freedom and around 18% for roll and pitch. When 30 modes are used the error drops below 1% for all degrees of freedom.
- The efficiency gains of the method are highly dependant on the programming language of choice. High gains are achieved in Matlab where for-loops are computationally expensive. When simulating an one hour time series the accelerated method decreases the computational cost by approximately 92% and 72% for 8 and 30 modes respectively. Similar results are expected in a Python implementation where for-loops have a similar cost with Matlab. In a FORTRAN implementation we observed a 60% decrease in cost for an one hour time series and 8 modes. However the cost increased by 24% when we used 30 modes due to the fast for-loop executions that FORTRAN provides.
- Concluding, the method is suitable for use as part of software that uses simplified models for the response calculation, e.g. optimization tools. It then provides good accuracy with a decreased cost.

8.2 Sub-conclusion on farm response

The new capabilities of HAWC2Farm in simulating floating wind turbine farms with shared mooring, under turbulent wind and irregular waves including second order wave loads, are presented using a two turbine design with a shared anchor. The DLC61 is selected as case study to investigate the effect of second order waves on the response of the farm. We also compared the response of the individually moored turbine to the response of the two turbine design. The investigation has shown that:

- The second order wave loads don't have a significant effect on the mooring line loads both for the single and the two turbine design. This could be attributed to the taut mooring line design that is less sensitive to wave drift loads.
- The surge motion of the shared mooring design is significantly larger compared to the individually moored turbine. As a result, the maximum mooring line force is increased by 21%.
- The second order hydrodynamic model gives larger surge motions than the first order hydrodynamic model for both designs. However, second order wave load effects are not as large as in the surge direction for the floater motions in other directions.
- The upwind turbine in the shared mooring case experienced higher exceedance probability for large amplitudes in surge and heave than the downwind turbine.
- The turbines in the shared mooring line design slides slowly in roll and pitch direction. The convergence of this slide might be further investigated by some analyses with very long simulation times.

- The second order wave loads increased the fore-aft tower bottom moments and accelerations by 7%. The shared mooring design has slightly lower tower top accelerations and tower bottom moments than the single turbine case.
- The upwind turbine in the shared mooring line design has higher probability of large fore-aft moments than the downwind turbine.

8.3 Sub-conclusion on wake effect of floater motion

A detailed investigation of the floating IEA Wind 15 MW reference wind turbine and its wake has been carried out under a large variety of conditions. The main numerical approach relied on the in-house multi-fidelity vortex solver **MIRAS**, equipped with a Lifting Line (**LL**) aerodynamic model and coupled with the multi-body finite-element solver **HAWC2**. The turbine behaviour predicted by the **MIRAS-HAWC2** coupling has been compared against the **HAWC2-BEM** lower fidelity method. In the study it has been shown that:

- The aero-hydro-servo-elastic simulations showed the largest differences between the codes appeared at high wind speeds under regular waves. Regarding the influence of the wave characteristics, in general it has been found that differences between **BEM** and **LL** methods are more sensitive to variations in wave frequency than in wave amplitude, with the **BEM** predictions deviating considerably from the **LL** solution at high wave frequencies, where **BEM** over-predicts the maximum amplitude of the motion by more than a 50 %.
- The analysis of the effect of mean tilt in the wake development has confirmed that a positive tilt angle deflects the wake upwards, promoting the wake stretching and helping break down the cylindrical wake shape, which leads to a faster wake recovery. The recovery has been quantified as function of the downwind position for three tilt angles. For a tilt angle of 10 degrees, the recovery is 0.52 at a distance of 12 rotor radii, relative to a value of 0.45 for the 0 degree case.
- During the parametric study under prescribed pitch motion it was found that the largest relative differences between the codes appear during the backward motion of the rotor, where the **BEM** method can violate the momentum balance assumption. Regarding the rotor flow, it has been observed that the outer part of the blades are more prone to local vortex ring state in below-rated conditions and high frequency motions.
- Wake recovery is enhanced by the pitch motion, since the rotor motion accelerates the mixing and breakdown of the tip vortices. A relation between short time intervals of large FA blade tip displacements and a faster break down of the wake has been demonstrated. It was further found that in terms of the wake recovery, slow oscillations have shown to be more beneficial than high frequency ones. The latter ones can produce a stronger and more stable wake, which recovers slower than in the steady case without motion.
- It has been shown that a pitching wind turbine can transition throughout all possible rotor states. Moreover, inverted rotor states have been identified and defined during a cycle with high frequency pitch motion. In this regime negative thrust and strong blade oscillations can occur during the motion cycle.
- Regarding the surge investigation, it has been found that a surging rotor has, in general, a very similar behavior to a pitching one. However, there are clear differences in the generated wake due to the translatory nature of the surge movement. The wake of a surging turbine seems to be less prone to local vortex ring state compared to the wake of a pitching turbine. Additionally, an accordion-like effect has been clearly identified in some of the presented cases. Regarding the wake recovery, the amplitude of the surge motion does not have a strong effect in the recovery of the wake for the investigated frequencies.

Overall the study demonstrates the applicability of vortex solvers to supplement and detail the engineering calculations offered by BEM methods for the loads and energy yield of floating wind turbines. The generic nature of the study allows generalization to arbitrary floater designs, based on their natural frequencies in surge and pitch and the associated typical motion amplitudes.

8.4 Sub-conclusion on comparison between MIRAS-HAWC2 farm and FAST.Farm

A preliminary comparative study of MIRAS-HAWC2 farm and FAST.Farm using the floating IEA Wind 15 MW reference wind turbine is carried out. Statistical differences in power and wake wind fields are investigated at two TIs, with and without floating effects for 8 m/s average inflow wind speed. In the study it has been shown that:

- When effects from floating motions are taken into account, only minimal changes observed in upwind turbines. However, FAST.Farm predicted up to 14% higher power production in downwind turbine, whereas MIRAS-HAWC2 farm predicted a similar power performance.
- Statistical analysis of the wake wind field shows under prediction of wake mixing in FAST.Farm compared to MIRAS-HAWC2 farm at low ambient TI. This leads to higher velocity deficit and smaller wake diameter. At higher ambient TI, FAST.Farm wake wind fields exhibit higher turbulence in the wake.
- In all load cases, FAST.Farm wake wind fields exhibit deflection of wake in vertical direction. This is a significant difference compared to MIRAS wake wind fields, where wake is still concentrated at hub level.
- Wake deficit in FAST.Farm simulations observed to be deflected further with the inclusion of floating effects, which could explain high power production. In the higher fidelity MIRAS-HAWC2 farm, the deflection was less and velocity deficit differences were localized.

Although this limited study does not propose generalized differences between the two tools, it identifies several differences that can be analysed in a larger comparative study, where uncertainties related to medium fidelity floating wind farm simulations can be better determined.

8.5 Sub-conclusion on wind tunnel wake measurements

A wind tunnel test campaign has been carried out to investigate the wake-flow response of a 1:100 scale model of the IEA 15 MW turbine subjected to imposed platform motion. The wake was measured at a distance of 2.3D, imposing motion in 5 directions (surge, sway, roll, pitch, yaw) with frequency equal to the wave frequency at the Gran Canaria site; the inflow was steady. The experiment has shown that:

- the average axial-velocity in the wake in correspondence of the rotor disk is slightly lower with motion compared to the fixed case. In the motion conditions at hand, the wake recovery appears to be slower than for a bottom-fixed turbine. This is in agreement with simulations in MIRAS-HAWC2;
- the turbulence kinetic energy in the wake is generally lower with motion than for a bottom-fixed turbine. The wake is more stable, and the lower flow mixing may explain the lower wake recovery;
- axial velocity in the wake of the floating turbine has oscillations at the same frequency of the imposed motion. These are due to the dynamic inflow created by motion and the effect of wake meandering. The additional oscillations in the wake velocity should be taken into account because, thinking to a floating farm, they represent an additional forcing for waked turbines. If platform motion occurs at the natural frequency of platform modes, velocity fluctuations

in the wake are expected at these frequencies, and can be a source of resonant excitation for downstream units.

8.6 Sub-conclusion on floating farm response

The impact of the wake generated by a floating wind turbine in downstream machines has been investigated in laminar and turbulent conditions for different configurations of two and five turbines in a row. It has been shown that:

- In a tandem configuration, the second turbine of the row produces more power when operating downstream a floating machine than when operating downstream a fixed one. This power gain is drastically reduced with the increasing turbulent intensity. As an example, for a 10R spacing between turbines and a TI of 4 % there is a power gain of approximately 3.5 %, but as the TI increases to 10% the gain reduces to virtually zero.
- If the effect of the waves is taken into account through forced oscillations of the upstream machine, the previously mentioned power gain observed in WT2 increases, and is less sensitive to the inflow turbulence level. For example, the highest frequency surge case with a spacing of 10R between turbines showed a time averaged power gain of 34 %, 20 % and 11 % for TI of 4 %, 7 % and 10 % respectively. On the other hand, the low frequency surge case showed much smaller gains. Regarding the pitch motion, the low frequency pitch case showed generally higher gains, i.e. 50 %, 19 % and 12 % for the same TI and turbine spacing.
- In laminar inflow conditions it has been observed that when the upstream turbine surges at a low frequency the downstream machine draws energy at the same frequency, creating a resonance effect. This effect is the largest at the natural frequency in pitch of the WindCrete platform, i.e. 0.02441 Hz, and it is not observed when the upstream turbine oscillates at higher frequencies, i.e. 0.05676 and 0.11352 Hz.
- A low frequency surge motion in the upstream machine seems to generate the largest fore-aft MRO in WT2, reaching values of up to 0.22. This substantial MRO seems to be triggered by a larger wake meandering observed in the far downstream positions. Moreover, if the frequency of oscillation is high, i.e. 0.11352 Hz, the downstream turbine response to harmonic oscillations in the upstream turbine is very similar independently of the motion type in WT1 (surge or pitch).
- Wind farm simulations of five turbines in a row have shown that the relative power of WT4 and WT5 in below- and rated wind conditions is considerably reduced in the floating case compared to the bottom-fixed one. This has been linked to the controller action.
- Farm simulations in over-rated conditions have shown that floating turbines deep inside the farm (WT3, WT4 and WT5) present much larger oscillations than more upstream located turbines. A maximum fore-aft MRO of 3.4 has been computed for WT4. This could be due to a resonance like build-up effect in above rated wind conditions, where the energy content in the low and mid frequency range of the three components of the velocity field increases along the row of turbines.
- Comparing bottom-fixed with floating wind farms in above rated wind conditions, a larger standard deviation in both power and thrust signals has been observed in all the floating turbines. It has been found that these variations grow with the turbine position inside the farm. For example, a floating WT5 displays a 58.5% larger std in power and a 44.2 % larger std in thrust than a fixed machine located in the same position.

References

- AAGAARD MADSEN, HELGE, LARSEN, TORBEN JUUL, PIRRUNG, GEORG, LI, ANG & ZAHLE, FREDERIK 2020 Implementation of the blade element momentum model on a polar grid and its aeroelastic load impact. *Wind Energy Science* **5**, 1–27.
- BORG, MICHAEL, HANSEN, ANDERS MELCHIOR & BREDMOSE, HENRIK 2016 Floating substructure flexibility of large-volume 10mw offshore wind turbine platforms in dynamic calculations. *Journal of Physics: Conference Series* **753**, 082024.
- BREDMOSE, HENRIK & PEGALAJAR-JURADO, ANTONIO 2020 An $o(n \log n)$ method for for second-order wave loads on a vertical pile. 35th International Workshop on Water Waves and Floating Bodies (IWWF 2020) ; Conference date: 26-04-2020 Through 29-04-2020.
- BREDMOSE, HENRIK, RINKER, JENNIFER, SKRZYPINSKI, WITOLD, ZAHLE, FREDERIK, MENG, FANGZHONG, DYKES, KATHERINE, GAERTNER, EVAN, BARTER, GARRETT, BERTOLOTTI, PIETRO, SETHURAMAN, LATHA & SHIELDS, MATT 2020 Definition of the 15 mw reference wind turbine. *Tech. Rep.* D1.1. Corewind.
- COUDOU, N, MOENS, M, MARICHAL, Y, BEECK, J VAN, BRICTEUX, L & CHATELAIN, P 2018 Development of wake meandering detection algorithms and their application to large eddy simulations of an isolated wind turbine and a wind farm. *Journal of Physics: Conference Series* **1037**, 072024.
- DUARTE, T., SARMENTO, A. J. N. A. & JONKMAN, J. 2014 Effects of second-order hydrodynamic forces on floating offshore wind turbines .
- FONTANELLA, A., BAYATI, I., MIKKELSEN, R., BELLOLI, M. & ZASSO, A. 2021 UnafLOW: a holistic wind tunnel experiment about the aerodynamic response of floating wind turbines under imposed surge motion. *Wind Energy Science* **6** (5), 1169–1190.
- FREDDY J. MADSEN, ANTONIO PEGALAJAR-JURADO, HENRIK BREDMOSE 2021 Form modelling of extreme response waves for floaters. EERA DeepWind'2021.
- FU, SHIFENG, JIN, YAQING, ZHENG, YUAN & CHAMORRO, LEONARDO P. 2019 Wake and power fluctuations of a model wind turbine subjected to pitch and roll oscillations. *Applied Energy* **253**, 113605.
- GHADIRIAN, AMIN, BREDMOSE, HENRIK & SCHLØER, SIGNE 2017 Prediction of the shape of in-line wave force and free surface elevation using first order reliability method (form). , vol. 137, pp. 162–176. Elsevier, 14th Deep Sea Offshore Wind Ramp;D Conference, EERA DeepWind'2017 ; Conference date: 18-01-2017 Through 20-01-2017.
- GÖZCÜ, OZAN, KONTOS, STAVROS & BREDMOSE, HENRIK 2022 -Submitted Dynamics of two floating wind turbines with shared anchor and mooring lines. TORQUE 2022 ; Conference date: 01-06-2022 Through 03-06-2022.
- GÖZCÜ, OZAN, KONTOS, STAVROS, BREDMOSE, HENRIK, BAILEY, TOM & BORISADE, FRIEDEMANN 2021 Corewind d1.4: Methods for multiple floaters and dynamic cables at farm level. *Tech. Rep.* D1.4. Corewind.
- HANSEN, MORTEN HARTVIG & ZAHLE, FREDERIK 2011 *Aeroelastic Optimization of MW Wind Turbines. Denmark. Forskningscenter Risø. Risø-R 1803(EN)*. Danmarks Tekniske Universitet, Risø Nationallaboratoriet for Bæredygtig Energi.
- JONKMAN, J & SHALER, K 2020 FAST . Farm User ' s Guide and Theory Manual (April).

- LARSEN, TORBEN J. & HANSEN, ANDERS M. 2020 How 2 hawc2, the user's manual. *Tech. Rep.*. DTU Wind.
- LEE, CH 1995 Wamit theory manual. *Tech. Rep.* 95-2. Massachusetts Institute of Technology Department of Ocean Engineering.
- MAHFOUZ, MOHAMMAD YOUSSEF, MOLINS, CLIMENT & PAU, TRUBAT 2020a Corewind d1.3: Public design and fast models of windcrete 15mw floater-turbine concepts. *Tech. Rep.*. Corewind.
- MAHFOUZ, M. Y., MOLINS, C., TRUBAT, P., HERNÁNDEZ, S., VIGARA, F., PEGALAJAR-JURADO, A., BREDMOSE, H. & SALARI, M. 2021 Response of the international energy agency (iea) wind 15 mw windcrete and activefloat floating wind turbines to wind and second-order waves. *Wind Energy Science* **6** (3), 867–883.
- MAHFOUZ, MOHAMMAD YOUSSEF, SALARI, MOHAMMAD, HERNÁNDEZ, SERGIO, VIGARA, FERNANDO, MOLINS, CLIMENT, TRUBAT, PAU, BREDMOSE, HENRIK & PEGALAJAR-JURADO, ANTONIO 2020b Public design and fast models of the two 15mw floater-turbine concepts. *Tech. Rep.* D1.3. Corewind.
- NATARAJAN, ANAND, HANSEN, MORTEN HARTVIG & WANG, SHAOFENG 2016 *Design Load Basis for Offshore Wind turbines: DTU Wind Energy Report No. E-0133*. DTU Wind Energy Report No. E-0133.
- NREL 2021 OpenFAST. Version 3.0.0.
- PEGALAJAR-JURADO, ANTONIO & BREDMOSE, HENRIK 2020 Accelerated hydrodynamic analysis for spar buoys with second-order wave excitation. In *Proceedings of the ASME 2020 39th International Conference on Ocean, Offshore and Arctic Engineering*, , vol. 9: Ocean Renewable Energy. United States: American Society of Mechanical Engineers, 39th International Conference on Ocean, Offshore and Arctic Engineering (OMAE2020) ; Conference date: 03-08-2020 Through 07-08-2020.
- RAINEY, R. C. T. 1989 A new equation for calculating wave loads on offshore structures. *Journal of Fluid Mechanics* **204**, 295–324.
- RAINEY, R. C. T. 1995 Slender-body expressions for the wave load on offshore structures. *Proceedings: Mathematical and Physical Sciences* **450** (1939), 391–416.
- RAMOS-GARCÍA, NÉSTOR, KONTOS, STAVROS, PEGALAJAR-JURADO, ANTONIO, GONZÁLEZ HORCAS, SERGIO & BREDMOSE, HENRIK 2022 Investigation of the floating iea wind 15 mw rwt using vortex methods part II: Wake impact on downstream turbines under turbulent inflow, *under review*. *Wind Energy* **25** (8), 1434–1463.
- RINKER, JENNIFER, GAERTNER, EVAN, ZAHLE, FREDERIK, SKRZYPIŃSKI, WITOLD, ABBAS, NIKHAR, BREDMOSE, HENRIK, BARTER, GARRETT & DYKES, KATHERINE 2020 *Comparison of loads from HAWC2 and OpenFAST for the IEA Wind 15 MW Reference Wind Turbine*. *Journal of Physics: Conference Series* **1618** (5), 1–13.
- SHALER, KELSEY & JONKMAN, JASON 2021 *FAST.Farm development and validation of structural load prediction against large eddy simulations*. *Wind Energy* **24** (5), 428–449.
- VIGARA, FERNANDO, CERDAN, LARA, DURAN, RUBEN, MUNOZ, SARA, LYNCH, MATTIAS, DOOLE, SIOBHAN, MOLINS, CLIMENT, TRUBAT, PAU & GUANCHE, RAUL 2019 *Design basis*. *Tech. Rep.* D1.2. Corewind.